Modelling of Calcium Handling in Genetically Modified Mice

By

Liren Li

A thesis submitted in partial fulfillment of the requirements for the degree

of

DOCTOR OF PHILOSOPHY

Supervised by Professor Nicolas Smith and Professor Barbara Casadei

Computational Biology Group, Department of Computer Science

Worcester College

University of Oxford

Trinity Term, 2011

To a Mouse

By Robert Burns

Wee, sleekit, cow’rin, tim’rous beastie,	Small, crafty, cowering, timorous little beast,
O, what a panic’s in thy breastie!	O, what a panic is in your little breast!
Thou need na start awa sae hasty	You need not start away so hasty
Wi bickering brattle!	With argumentative chatter!
I wad be laith to rin an’ chase thee,	I would be loath to run and chase you,
Wi’ murdering pattle.	With murdering plough-staff.
I’m truly sorry man’s dominion	I’m truly sorry man’s dominion
Has broken Nature’s social union,	Has broken Nature’s social union,
An’ justifies that ill opinion	And justifies that ill opinion
Which makes thee startle	Which makes thee startle
At me, thy poor, earth born companion	At me, thy poor, earth born companion
An’ fellow mortal!	And fellow mortal!

Abstract

This thesis develops biophysically-based data-driven mathematical models of intracellular calcium dynamics in ventricular myocytes for both normal and genetically modified mouse hearts, based on species- and temperature-consistent experimental data. The models were subsequently applied to quantitatively examine the changes in calcium dynamics in mice with cardiomyocyte-specific knockout (KO) of the cardiac sarco/endoplasmic reticulum ATPase (SERCA2) gene, to determine the contributing mechanisms which underlie the ultimate development of heart failure in these animals. In Chapter 1, with emphasis on calcium dynamics and calcium regulation in heart failure, an overview of cardiac electrophysiology, excitation-contraction coupling and mathematical models of cardiac electrophysiology is provided. In Chapter 2, models of calcium dynamics in the ventricular myocytes from the C57BL/6 mouse heart at a physiological temperature is developed and validated based on species- and temperature-consistent measurements. In Chapter 3, the C57BL/6 model framework is re-parameterised to experimental data from the control and SERCA2 KO mice at 4 weeks after gene deletion. The models are then used to quantitatively characterise changes in calcium dynamics in the KO animals and the role of the compensatory mechanisms. In Chapter 4, the model framework is extended to include differential distributions of ion channels in the sarcolemma and the calcium dynamics in the sub-sarcolemmal space, with parameters in these sub-components fitted to experimentally measured calcium dynamics from the control and KO cardiomyocytes at 7-week after gene deletion. Finally in Chapter 5, conclusions are drawn, the limitations of this study are discussed, and the future extensions to this study are described.

Acknowledgements

The writing of this dissertation has been one of the most significant academic challenges I have ever had to face. It would not have been possible to complete this work without the generous help, guidance and support from so many people, to only some of whom it is possible to give particular mention here.

I owe my deepest gratitude to Miguel Bernabeu for his enthusiastic encouragement and unceasing patience throughout the past four years. I am grateful to my two supervisors, Professor Nicolas Smith and Professor Barbara Casadei. I am most indebted to Nic for guiding me from the preliminary to the concluding stages of my work. His knowledge and commitment to the highest standards inspired and motivated me. I would also like to give my deepest thanks to Dr. Steven Niederer, who went out of his way to give guidance and invaluable suggestions on my research despite his many other academic and professional commitments. I would also like to thank my collaborator Dr. William Louch, who was extremely supportive in terms of experimental data collection and providing experimentalist insight into the project. I also received very useful advice from a number of people at various stages of my research, including Dr. Pawel Swietach, Dr. Jonathan Cooper and Dr. Yinhua Zhang. In addition, I want to thank my friends in Oxford: Hristina Palikareva, Ramon Granell, Matthew Hague, Shibin Zhang and Jun Zhao, to name a few, with whom I have spent the most memorable four years of my life.

Finally, to my family in China: my parents Weibo Li and Hongyu Duan, and my grandparents Qingfang Wang and Qiang Duan, who have supported, encouraged and believed in me, in all my endeavours: I owe you everything.

Contents

List of Figures

List of Tables

List of Symbols

E-C	Excitation-Contraction
HF	Heart Failure
KO	Knockout
FF	Flox/Flox
TG	Transgenic
WT	Wild-Type
bpm	Beats Per Minute
LV	Left Ventricle
SERCA	Sarco/Endoplasmic Reticulum Ca^{2+} ATPase
NCX	Na^{+}/Ca^{2+} Exchanger
NHE	Na^{+}/H^{+} Exchanger
LCC	L-type Ca^{2+} Channels
PMCA	PlasmaMembrane Ca^{2+} ATPase
NKA	Na^{+}/K^{+} ATPase
RyR	Ryanodine Receptor

PLB	Phospholamban
SR	Sarcoplasmic Reticulum
T-tubules	Transverse tubules
jc	Junctional space
sl	Sub-sarcolemmal space
ds	Dyadic space
Tn-Tm	Troponin-Tropomyosin complex
CaMKII	Ca^{2+}-Calmodulin Kinase II
FDAR	Frequency Dependent Acceleration of Relaxation
V_m	Transmembrane potential
AP	Action Potential
APD	Action Potential Duration
TTP	Time To Peak
$[Ca^{2+}]_i$	Intracellular Ca^{2+} concentration
$\Delta[Ca^{2+}]_i$	$[Ca^{2+}]_i$ transient magnitude
$[Ca^{2+}]_p$	Peak $[Ca^{2+}]_i$ during a $[Ca^{2+}]_i$ transient
RT_{50}	Time to half decay of the $[Ca^{2+}]_i$ transient
$[Na^+]_i$	Intracellular Na^+ concentration
$[K^+]_i$	Intracellular K^+ concentration
$[Ca^{2+}]_{sl}$	Ca^{2+} concentration in the sub-sarcolemmal space
$[Ca^{2+}]_{jc}$	Ca^{2+} concentration in the junctional space
$[Ca^{2+}]_{total}$	Total cytosolic Ca^{2+} concentration

$[Na^+]_o$	Extracellular Na^+ concentration
$[Ca^{2+}]_{ds}$	Ca^{2+} concentration in the dyadic space
$CSQN_{tot}$	Total concentration of calsequestrin in the SR
I_{CaL}	L-type Ca^{2+} current
I_{Na}	Fast Na^+ current
I_{ks}	Slow delayed rectifier K^+ current
I_{kr}	Rapid delayed rectifier K^+ current
$I_{k,tof}$	Rapidly inactivating transient outward K^+ current
I_{kur}	Rapidly activating slowly inactivating K^+ current
I_{kss}	Non-inactivating steady-state K^+ current
I_{k1}	Time-independent K^+ current
I_{Nab}	Persistent Na^+ current
I-V	Current-Voltage relationship
KO-I_{CaL}	SERCA2 KO model (4-week) with I_{CaL} clamped to have the same time course as that seen in the FF model
KO-NCX	SERCA2 KO model (4-week) with maximum activity of NCX reduced to the same level as that in the FF model
KO-ICaL-NCX	SERCA2 KO model (4-week) in which both the I_{CaL} and the NCX were adjusted to the levels in the FF model
TG*	Model of transgenic mice with NCX over-expression without allosteric NCX regulation by Ca^{2+}
H-H	Hodgkin-Huxley
LRd	Luo-Rudy model of guinea-pig cardiac electrophysiology

HRd	Hund-Rudy model of canine cardiac electrophysiology
ODE	Ordinary Differential Equation
SEM	Standard Error of Mean
RMSD	Root Mean Square Deviation

For a full list of parameter definitions, see Appendices.

Chapter 1

Introduction

For an average adult with a life-span of 80 years, their heart will have to maintain rhythmic beating for over three billion cycles. During each heartbeat, the chambers of the heart are activated by an electrical impulse that propagates across the heart. The activation wave is initiated by a group of pacemaking cells located in the right atria of the heart. These activation waves then spread throughout the ventricles via the specialised Purkinje fibre conduction system. The arrival of the activation wave at each myocyte causes a depolarisation of the cell membrane that initiates an action potential, which ultimately leads to concerted myocardial contraction and relaxation through a process termed excitation-contraction coupling (E-C coupling). Numerous inter-dependent cellular pathways regulate E-C coupling, with intracellular calcium (Ca^{2+}) handling playing, arguably, one of the most important roles, as myofilaments are activated in a calcium-dependent manner. This coupling means that the dynamic rise and fall of intracellular free Ca^{2+} concentration directly influence myocardial contraction and cardiac function.

The breakdown/disruption of E-C coupling has been closely linked to heart failure (HF), which is a prevalent and complex pathology. Many of the underpinning mechanistic aspects of HF remain to be fully understood. The condition is underpinned by a depressed cardiac contractile function, while altered cellular Ca^{2+} handling is believed to play a

central role in its development [76, 157, 170, 85, 23]. Recently, genetically modified mice have enabled studies of changes in individual Ca^{2+} handling mechanisms that may be important to the genesis of cardiac diseases. The combination of consistent data from experimental models of cardiac physiology and pathophysiology with mathematical modelling provides an integrated framework to further investigate the interactions and quantify the effects of these changes on global Ca^{2+} dynamics in HF. This thesis follows this approach to develop a data-driven, biophysically-based model of Ca^{2+} dynamics in the ventricular myocytes of genetically modified mice, in order to elucidate the key alterations in Ca^{2+} handling that lead to the development of HF in these animals.

There are three main stages to the development of the models. In Chapter 2, a model of Ca^{2+} dynamics in normal murine ventricular myocytes (C57BL/6 mice) is developed and validated against a range of experimental observations based on species- and temperature-consistent experimental data. In Chapter 3, this model framework is used to study Ca^{2+} handling in genetically modified mice with cardiomyocyte-specific knockout (KO) of the sarco/endoplasmic reticulum Ca^{2+} ATPase (SERCA2) gene at 4 weeks after gene deletion. Finally in Chapter 4, the framework is extended to include a detailed description of Ca^{2+} dynamics in the sub-sarcolemmal compartment, and used to analyse changes in Ca^{2+} handling in SERCA2 KO mice through time from the 4-week time point to the 7-week time point to reveal the mechanisms that lead to the development of HF.

1.1 Overview of Cardiac Electrophysiology and Intracellular Calcium Handling

In the following section, we first provide a general overview of cardiac electrophysiology and E-C coupling, followed by detailed descriptions of each individual Ca^{2+} handling mechanisms and the species-dependent features of E-C coupling in the heart that are im-

portant for this study. We then review the current understanding of Ca^{2+} handling in HF and the use of transgenic mouse models in HF studies. For a more detailed overview of cardiac electrophysiology and Ca^{2+} handling see Bers 2001 [19].

1.1.1 Cardiac Action Potential

The surface membrane of a cardiac cell is called the sarcolemma. On either side of the sarcolemma, the intracellular and extracellular environments consist of a solution of dissolved salts that dissociate into Na^{+}, K^{+} and Ca^{2+} ions, etc. An important property of the sarcolemma is its selective permeability, such that each ion species are unevenly distributed between the intracellular and extracellular spaces, resulting in concentration gradients across the membrane. The uneven distribution of ions across the sarcolemma also creates an electrical gradient. The equilibrium potential (Nernst potential) for a particular ion S, at which its electrical gradient is balanced by its concentration gradient is expressed as:

$$\mathrm{E_s} = \frac{\mathrm{RT}}{\mathrm{zF}} \cdot \ln(\frac{[\mathrm{S}]_\mathrm{o}}{[\mathrm{S}]_\mathrm{i}}) \tag{1.1}$$

where R is the gas constant, T is the temperature (K), z is the valence of the ion, F is Faraday's constant and $[\mathrm{S}]_\mathrm{i}$ and $[\mathrm{S}]_\mathrm{o}$ are the intracellular and extracellular concentrations of S respectively. In quiescent cardiac myocytes, the resting membrane is typically at -80 mV, which is determined by the intracellular and extracellular concentrations of the ions and the permeabilities of the membrane to these ions [69, 92].

Another crucial property of the sarcolemma is its capacity to respond to electrical depolarisation through the brief opening and closing of highly specific ion channels and electrogenic transporters to produce changes in its transmembrane potential. With each heartbeat, the cell membrane is depolarised and an action potential (AP) is initiated as a result of a complex interplay of multiple ion channels and transporters in the myocardium.

The AP waveform is not only formed by transmembrane ionic currents but also acts as a driving potential that in turn modulates the dynamics of the very same ion channels and transporters. A typical AP consists of five phases, each of which is associated with the opening of specific ion channels, as described below.

Five Phases of the Action Potential

As shown in Fig. 1.1, the initial depolarisation phase (Phase 0) is due to the opening of voltage-gated fast Na^+ channels ($\mathrm{I_{Na}}$) when the transmembrane voltage reaches the activation threshold of the channel between -70 and -60 mV. Upon depolarisation, Na^+ channels change their structural conformation within submilliseconds and positively charged Na^+ current flows rapidly into the cell due to the large Na^+ concentration gradient and the negative transmembrane potential, leading to further depolarisation. Depolarisation also triggers the channels to close rapidly and become inactivated for a short period during which the cell membrane is not excitable. The early repolarisation of the AP (phase 1) is primarily caused by the rapidly activating and inactivating transient outward K^+ current named $\mathrm{I_{k,to}}$. Following this initial repolarisation is a plateau phase (phase 2), which results from a prolonged influx of Ca^{2+} ions, as the voltage-gated L-type Ca^{2+} channels (LCCs) open upon depolarisation. This flow of Ca^{2+} ions plays a crucial role in cardiac E-C coupling, as it initiates a series of intracellular events that ultimately lead to myocardial contraction (see later). Another current that contributes to the plateau phase is the net inward current through NCX in Ca^{2+} extrusion mode [20] (see later). Thereafter, the outward flow of K^+ ions is the major factor causing repolarisation (phase 3) that is complex in origin and determines the duration of the AP. The large number of K^+ channels can be divided into two molecular families: the voltage-gated channels and the inward rectifier channels. The voltage-gated outward K^+ channels, such as the rapid delayed rectifier $\mathrm{I_{kr}}$ and the rapidly activating slowly inactivating K^+ current $\mathrm{I_{kur}}$, are chiefly responsible for repolarisation, fully activated at around -10 mV and deactivated by full repolarisation [19]. The inward rectifier K^+ channels, such as the time-independent

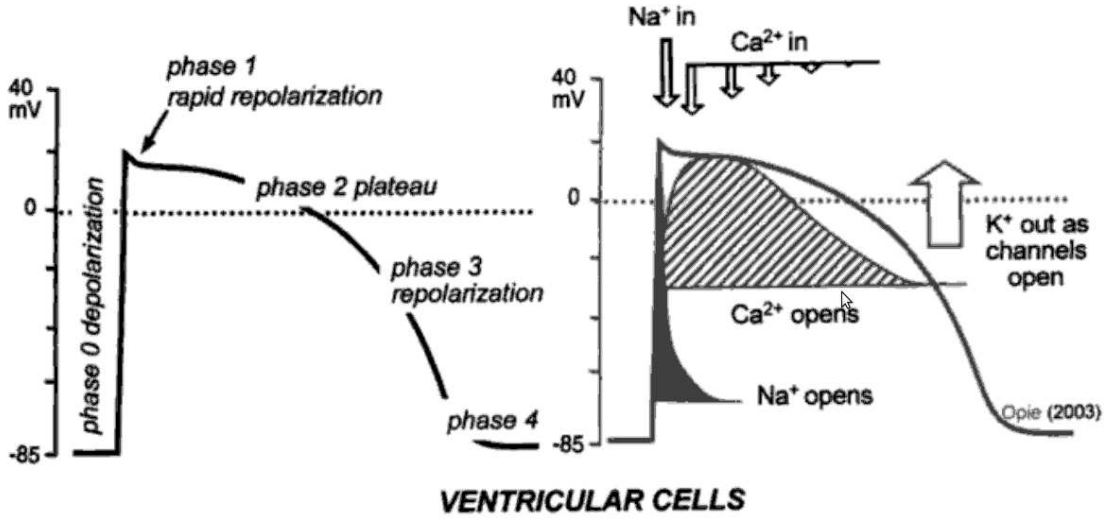

FIGURE 1.1: A schematic of AP phases (left) and currents (right), adapted from [149]. The rapid entry of Na^{+} accounts for the rapid depolarisation phase. Ca^{2+} channels open at depolarisation and Ca^{2+} entry sustains the plateau phase. Then K^{+} channels open and outward flow of K^{+} leads to repolarisation and sets the membrane potential back to the resting state.

K^{+} current $\mathrm{I_{k1}}$, help to regulate resting membrane potential and contribute to late phase 3 repolarisation. $\mathrm{I_{k1}}$ closes upon depolarisation and reopens during repolarisation to help terminate an AP and reset the membrane potential to the resting state (phase 4) [19]. A number of other mechanisms, such as the flow of negatively charged Cl^{-} ions and the voltage- and Ca^{2+}-dependent inactivation of Ca^{2+} channels, are also believed to play a role in the return of the membrane potential back to its resting level. The individual ionic channels involved in the initiation and shaping of the AP are shown schematically in Fig. 1.2. In murine ventricular myocytes, the AP typically has a very short duration and lacks a prominent plateau phase, compared to other mammalians such as rabbits and guinea-pigs, which is thought to result from a much more significant early repolarisation due to a greater $\mathrm{I_{k,to}}$ [106].

The cell membrane invaginates and forms an extensive tubular network called transverse (T) tubules which allows the AP to penetrate rapidly to the interior of the cell [149]. Next to the T-tubules inside the cell lies the terminal cisternae of the sarcoplasmic retic-

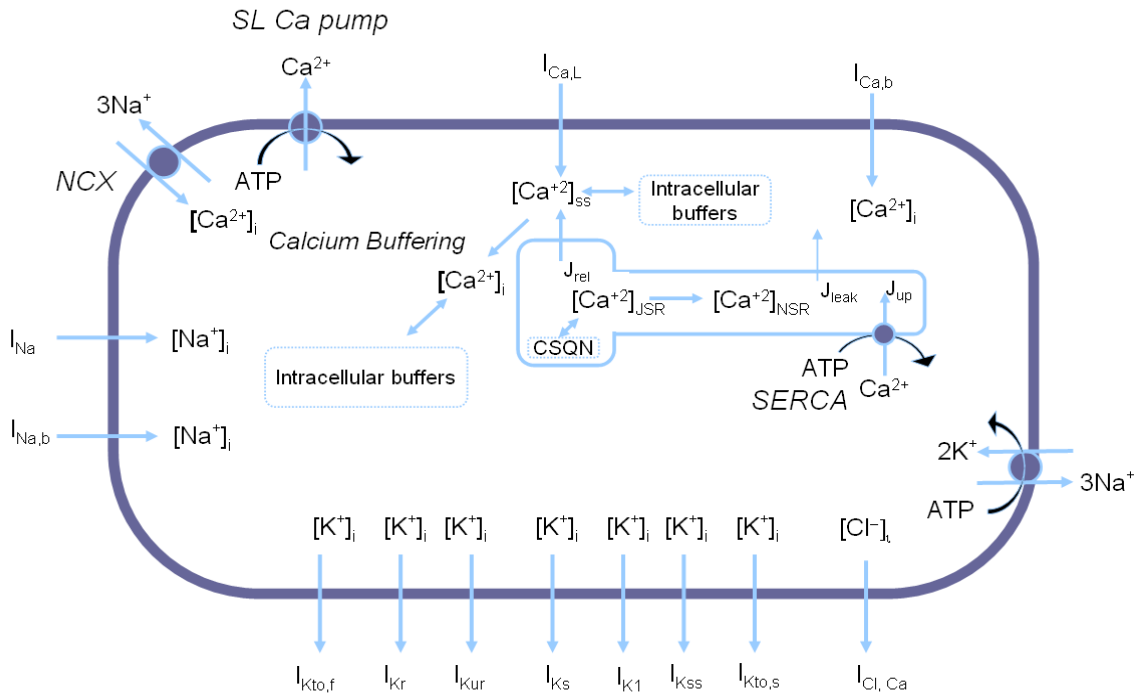

FIGURE 1.2: A schematic of the cardiomyocytes showing sarcolemmal ionic channels and transporters, as well as intracelllar Ca^{2+} dynamics

ulum (SR), forming a closely coupled structure called the dyad. As the AP travels along the sarcolemma and along the T-tubules, Ca^{2+} entry through LCCs due to depolarisation induces rapid release of Ca^{2+} from the SR into the dyadic space, i.e. the space between the T-tubules and the terminal cisternae of the SR, which then diffuses into the cytosol.

The ionic concentration gradients across the sarcolemma, required for the movement of ions during an AP, are in turn maintained by a number of membrane exchangers and pumps. The Na^+/K^+ ATPase (NKA) is a key transporter that establishes a low intracellular Na^+ concentration ($[Na^+]_i$) and a high intracellular K^+ concentration ($[K^+]_i$) by moving three Na^+ ions out and two K^+ ions into the cell using the energy of one ATP molecule [162]. As such the pump is electrogenic extruding one net charge per cycle. The Na^+/Ca^{2+} exchanger (NCX) is another important transporter that maintains the Ca^{2+} concentration gradient. This exchanger is a reversible counter-transport system that, when in forward (Ca^{2+} extrusion) mode, uses the energy provided by the inward flux of Na^+

ions down their electrochemical gradient to extrude Ca^{2+} ions with a generally accepted stoichiometry of 3:1 [164], thus moving one net charge into the cell per cardiac cycle.

1.1.2 The Role of Calcium in E-C Coupling

As mentioned previously, Ca^{2+} entry via voltage-dependent opening of LCCs during phase 2 of the AP is a crucial event that initiates E-C coupling. This Ca^{2+} influx increases the concentration of Ca^{2+} in the dyadic space. Ca^{2+} then binds to and activates the ryanodine receptors (RyRs), which are Ca^{2+} release channels located on the SR, triggering further release of a much greater number of Ca^{2+} ions from the SR [60]. This process of a small amount of Ca^{2+} entry leading to a greater Ca^{2+} release is termed Ca^{2+}-induced-Ca^{2+}-release or CICR. As Ca^{2+} diffuses from the dyadic space into the cytosol, the transient rise in free cytosolic Ca^{2+} concentration is named a $[Ca^{2+}]_i$ transient.

Importantly, Ca^{2+} is highly buffered in cardiac myocytes. While the free $[Ca^{2+}]_i$ transient in cardiac myocytes may rise from 0.1 μM at diastole to a peak near 1 μM during systole, it takes 100 μM Ca^{2+} added to the cytosol to produce this change [19]. This buffering capacity in addition to the Ca^{2+} regulatory sites on troponin C (see below) is a result of numerous Ca^{2+}-binding ligands. Specifically, in the cytosol the major binding sites include SERCA, calmodulin, ATP, creatine phosphate, and in the SR Ca^{2+} is substantially buffered by calsequestrin.

The myofilaments, which are the end effector of E-C coupling, are activated in a [Ca^{2+}]-dependent manner. The main contractile machinery are the thin (actin) and thick (myosin) filaments. At rest when $[Ca^{2+}]_i$ is low, the acto-myosin interaction is blocked by sterical hindrance where the thin filament regulatory proteins tronopin-tropomyosin (Tn-Tm) complex blocks the myosin binding sites on actin preventing the cross bridges from binding and generating tension. As $[Ca^{2+}]_i$ rises during a $[Ca^{2+}]_i$ transient, Ca^{2+}

ions bind to the Ca^{2+}-binding subunit of troponin (troponin C or TnC) on the low-affinity Ca^{2+}-binding site (site II) and enable the movement of the TnT-Tm complex to allow acto-myosin interaction and tension generation.

Relaxation occurs as Ca^{2+} is removed from the cytosol, lowering $[Ca^{2+}]_i$ such that Ca^{2+} dissociates from TnC. Ca^{2+} removal is achieved either via Ca^{2+} extrusion from the cell or Ca^{2+} uptake into intracellular Ca^{2+} stores. Two mechanisms are known to be responsible for the extrusion of Ca^{2+} from the myoctes: the NCX as mentioned previously and the plasma membrane Ca^{2+} ATPase (PMCA). The majority of the Ca^{2+} entering the cytosol during a $[Ca^{2+}]_i$ transient is taken up back into the SR via the SR Ca^{2+} ATPase (SERCA), although the exact percentage contribution is species-dependent (below). In mice, SERCA contributes to approximately 90% of total cytosolic Ca^{2+} removal, while the contribution of NCX is roughly 9% and the remaining 1% has been attributed to slow mechanisms such as Ca^{2+} extrusion through PMCA and mitochondrial Ca^{2+} uptake [116].

Ca^{2+} loading of the mitochondria is widely accepted to be essential for the process of matching cellular energy production and demand [130]. However, there remains significant debate over the role of mitochondrial Ca^{2+} uptake in regulating Ca^{2+} dynamics on the beat-to-beat time-scale [150]. Experimental studies by Bassani et al., using the oxidative phosphorylation uncoupler FCCP to inhibit mitochondrial Ca^{2+} uptake during caffeine-induced contractures, indicated that mitochondrial Ca^{2+} uptake was 50-folds slower than Ca^{2+} removal by NCX [11]. In addition, it has also been proposed that mitochondria do not respond rapidly to transient changes in $[Ca^{2+}]_i$ due to the low Ca^{2+} affinity of the uptake mechanism [65]. Therefore, a previously proposed theory was that beat-to-beat changes in mitochondrial Ca^{2+} concentration ($[Ca^{2+}]_m$) were small and mitochondria Ca^{2+} accumulation occurred on a much slower time scale than that of the $[Ca^{2+}]_i$ transient [150]. However, recent advances in experimental techniques

have enabled more accurate measurements of $[Ca^{2+}]_m$. A study by Robert et al. [167], using targeted molecular probes for mitochondrial Ca^{2+}, showed rapid and transient oscillations in mitochondrial free Ca^{2+} concentration in synchrony with $[Ca^{2+}]_i$ changes. This coupling was thought to result from the proximity of mitochondria to the RyRs meaning the mitochondria sensed microdomains of highly elevated $[Ca^{2+}]_i$. Nevertheless, it is still unclear whether mitochondrial Ca^{2+} uptake plays a significant role in excitation-contraction coupling, since changes in total mitochondrial Ca^{2+} could not be measured by these molecular probes. Furthermore, acute mitochondrial inhibition would also lead to a range of cellular effects in addition to affecting Ca^{2+} transport, which in turn would complicate the interpretation of results. Therefore, within the scope of this thesis, mitochondrial Ca^{2+} uptake during the $[Ca^{2+}]_i$ transient has been assumed to play a relatively small role under physiological conditions, compared to SERCA, NCX and PMCA.

Finally, the control of $[Ca^{2+}]_i$ is achieved through the careful balancing of Ca^{2+} fluxes through the various transporters and channels. At steady state, Ca^{2+} entry and Ca^{2+} efflux balance each other over each heart beat such that there is no net sarcolemmal Ca^{2+} flux and the SR Ca^{2+} content is maintained [50]. When Ca^{2+} entry exceeds Ca^{2+} efflux, the net influx of Ca^{2+} leads to increased SR loading and a greater amount of Ca^{2+} to be released with each beat. At a higher level of $[Ca^{2+}]_i$, L-type Ca^{2+} channels inactivate faster and Ca^{2+} extrusion via NCX is enhanced, thereby bringing the $[Ca^{2+}]_i$ transient to a new steady state.

1.1.3 Intracellular Calcium Handling Mechanisms

The various Ca^{2+} transporters important for the regulation of $[Ca^{2+}]_i$ are presented in Fig. 1.2. The following sections provide a more detailed description of the properties of each of the Ca^{2+} handling mechanisms.

L-type Calcium Channels

The LCCs are the most prominent sarcolemmal Ca^{2+} channels in cardiac muscle. This inward L-type Ca^{2+} current (I_{CaL}) contributes to the plateau phase of the AP and carries a small influx of Ca^{2+} into the cell triggering further SR Ca^{2+} release via the process of CICR. I_{CaL} is therefore directly and indirectly involved in the activation of contraction in the heart.

I_{CaL} is rapidly activated by depolarisation, reaching its peak within a few milliseconds [90]. Its activation is voltage-dependent with the activation threshold at approximately -40 mV. Inactivation of the current is both voltage- and Ca^{2+}-dependent. It has been shown that the voltage-dependent inactivation process occurs on a relatively slow time-scale, with a time to half inactivation ($t_{1/2}$) at approximately 150 ms as measured using Ba^{2+} as the charge carrier. On the other hand, Ca^{2+}-dependent inactivation is a much faster process with a $t_{1/2}$ less than 20 ms under normal conditions [143]. Ca^{2+}-dependent inactivation results from the rise in local [Ca^{2+}] in the dyadic space due to (1) Ca^{2+} entering via the channel itself and (2) SR Ca^{2+} release. The fact that LCCs respond to local [Ca^{2+}] has been demonstrated experimentally where Ca^{2+}-dependent inactivation was observed even in the presence of a high concentration of EGTA, a Ca^{2+} buffer which abolishes $[Ca^{2+}]_i$ transient and SR Ca^{2+} release, as EGTA can not prevent the rise in dyadic Ca^{2+} concentration [79].

The amount of Ca^{2+} entry via I_{CaL} is relatively small compared to the amount of SR Ca^{2+} release it triggers, although the exact contribution is species-dependent (see later). In mouse ventricular myocytes, Ca^{2+} entry through LCCs contribute to less than 10% of total Ca^{2+} increase during an AP [19, 125].

SR Calcium Release Channels

The SR Ca^{2+} release channel, the RyR, is a tetrameric structure located in the junctional SR and spans the gap between the SR and the sarcolemmal membrane [202]. Its close proximity to the sarcolemmal L-type Ca^{2+} channel is crucial for the process of CICR as it enables fast activation of SR Ca^{2+} release via I_{CaL}.

The elementary events underlying SR Ca^{2+} release are the spontaneous local increases in [Ca^{2+}], termed Ca^{2+} sparks, resulting from stochastic openings of the RyR at rest [36]. During CICR, the rise in local [Ca^{2+}] due to I_{CaL} increases the open probability of the RyR. The spatial and temporal summation of thousands of Ca^{2+} sparks synchronised by the AP in turn leads to the global $[Ca^{2+}]_i$ transient. Activation of SR Ca^{2+} release occurs rapidly upon Ca^{2+} entry through LCCs during an AP, with only a few milliseconds of delay between peak I_{CaL} and peak SR Ca^{2+} release flux as measured in rat ventricular myocytes [182]. SR Ca^{2+} release is not an all-or-none process but graded as a function of the $[Ca^{2+}]_i$ that triggers CICR [59, 60, 61]. The amount of Ca^{2+} released from the SR during CICR is also much greater compared to the amount of Ca^{2+} entry through I_{CaL} (high gain). In murine ventricle, the amount of total SR Ca^{2+} release can be over 15 times of the integrated triggering I_{CaL}. Therefore, in cardiac muscle, SR Ca^{2+} release contributes to the majority of the Ca^{2+} required for the generation of the $[Ca^{2+}]_i$ transient and thus contraction. RyR activation has been found to decline in a time-dependent manner after local [Ca^{2+}] is raised rapidly [78, 175]. This phenomenon is thought to limit the inherently positive feedback in CICR and help to terminate SR Ca^{2+} release.

Apart from activation by Ca^{2+}, SR Ca^{2+} release is altered by a number of other modulators. For example, caffeine is a common experimental tool used to probe SR Ca^{2+} release. A low dose of caffeine ($\sim$500 μM) is known to moderately increase the open probability of the RyR whereas a high concentration of caffeine ($\sim$10mM) causes sus-

tained opening of the RyR and hence complete depletion of SR Ca^{2+} content [54]. Thus caffeine application is a routine procedure used to assess SR Ca^{2+} content in intact cardiomyocytes [4, 173]. In addition, tetracaine is an inhibitor of RyR release. By quantifying changes in diastolic $[Ca^{2+}]_i$ in the presence and absence of tetracaine, one can assess the amount of SR Ca^{2+} leak at rest [177].

SR Calcium ATPase

In vertebrates, three distinct genes encode SERCA 1, 2 and 3, which in turn produce more than 10 isoforms [153]. SERCA1 protein is found in fast twitch muscle, SERCA2a is expressed predominantly in slow twitch muscle and cardiac muscle [131, 29], and SERCA2b and SERCA3 are ubiquitously expressed in muscle and non-muscle cells [153]. The cardiac isoform of SERCA (SERCA2a) is the main contributor to Ca^{2+} removal from the cytosol during relaxation in cardiac muscle. Two Ca^{2+} ions are transported into the SR for each ATP molecule consumed. The transport reaction starts with the binding of two Ca^{2+} ions and one ATP molecule on the cytosolic side of the pump. Phosphorylation of ATP then induces a conformational change and the release of the Ca^{2+} ions into the SR lumen [40].

The transport rate of SERCA is dependent on $[Ca^{2+}]_i$ and is modulated by a number of factors. Specifically, phospholamban (PLB), an endogenous inhibitor of SERCA present at a high concentration in ventricular myocytes, decreases the activity of the pump by lowering its affinity to intracellular Ca^{2+}. Such inhibitory effects are removed upon PLB phosphorylation [109]. PLB can be phosphorylated by cAMP-dependent protein kinase (PKA) at serine-16 and by Ca^{2+}/calmodulin-dependent protein kinase activities [181]. PLB phosphorylation by PKA increases the Ca^{2+}-affinity of SERCA, thereby enhancing SR Ca^{2+} uptake and SR Ca^{2+} content [174].

Phosphorylation of phospholamban by Ca^{2+}-calmodulin kinase II (CaMKII) is thought by some groups to contribute to frequency-dependent acceleration of relaxation

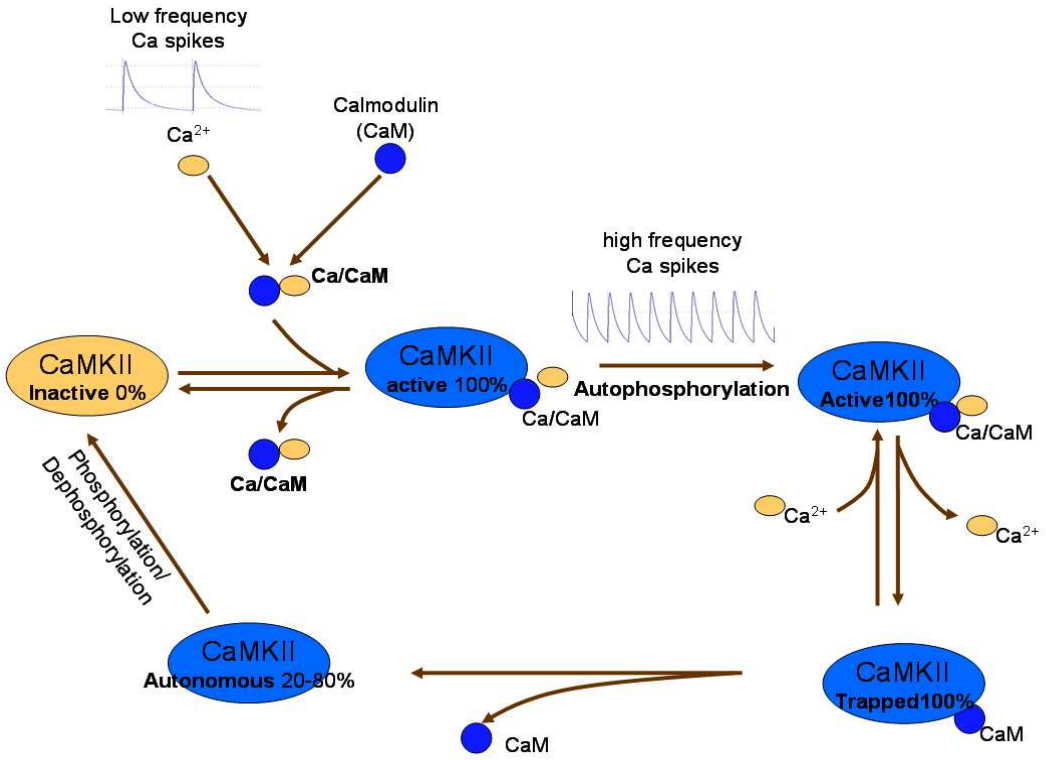

FIGURE 1.3: A schematic of the CaMKII regulating pathways, and underlying mechanisms of frequency-decoding.

(FDAR), a phenomenon describing the up-regulated SERCA activity at higher pacing frequencies [113]. However, findings from other groups suggest that CaMKII may act directly on SERCA [209] instead of via PLB. Regardless of the underlying mechanisms, FDAR is thought to be important for the rate-dependent shortening of the twitch duration and $[\mathrm{Ca}^{2+}]_{\mathrm{i}}$ transient duration in the heart [93]. From a physiological point of view this effect is important in speeding relaxation at high heart rates, allowing the heart to refill more rapidly between beats. The following section provides a brief overview of the current understanding of CaMKII regulating pathways and the effects of CaMKII on SERCA activity.

CaMKII Regulation of SERCA

CaMKII is a protein kinase that is activated upon binding of the Ca^{2+}/calmodulin complex. It can be further autophosphorylated at high $[\mathrm{Ca}^{2+}]_{\mathrm{i}}$ levels through inter-subunit

reactions that require calmodulin [82]. Autophosphorylation of the kinase makes it Ca^{2+} independent by "trapping" bound calmodulin (calmodulin off-rate is reduced 1000-fold [30]) and enabling the kinase to remain partially active even after calmodulin dissociates. Autophosphorylation is a cooperative process with positive feedback, *i.e.* it potentiates the response of the kinase to sequential $[\mathrm{Ca}^{2+}]_\mathrm{i}$ transients and enables the kinase to detect $[\mathrm{Ca}^{2+}]_\mathrm{i}$ transient frequency. Fig. 1.3 shows the regulating pathways described above. An earlier hypothesis about the involvement of CaMKII in cardiac FDAR is that at higher pacing frequencies, CaMKII becomes highly active and phosphorylates PLB [19]. As discussed previously, PLB phosphorylation leads to accelerated Ca^{2+} uptake through SERCA and thus faster relaxation. At lower frequency, CaMKII becomes less active, and PLB remains inhibitory to SERCA, slowing down the rate of $[\mathrm{Ca}^{2+}]_\mathrm{i}$ decline. Indeed, CaMKII inhibitors were found to abolish FDAR in rat, ferret and mouse myocytes [14, 116, 156], and the effect was reversed if SR Ca^{2+} uptake was prevented with thapsigargin or caffeine, indicating that FDAR is SERCA-dependent. However, whether there is involvement of PLB phosphorylation in FDAR is controversial. Although increased levels of PLB phosphorylation have been found to correlate with increasing pacing frequency and FDAR [80], Li et al. [116] and DeSantiago et al. [45] both found that PLB knockout mice still exhibited FDAR which was abolished by CaMKII inhibitors. To summarise, CaMKII has been implicated in FDAR via enhanced SR Ca^{2+} uptake. It is still not clear whether CaMKII acts directly on SERCA or via PLB phosphorylation.

Na^{2+}/Ca^{2+} Exchanger

It is generally accepted that the role of NCX in cardiac cells is to maintain diastolic $[\mathrm{Ca}^{2+}]_\mathrm{i}$ by way of Ca^{2+} extrusion. The direction and amplitude of $\mathrm{I_{NCX}}$ is governed by the transmembrane potential (V_m) as well as the intra- and extracellular concentrations of Ca^{2+} and Na^{+} ions. The potential at which $\mathrm{I_{NCX}}$ is zero, or at which the electrochemical gradients for Na^{+} and Ca^{2+} are equal, is called the reversal potential ($\mathrm{E_{NCX}}$). It follows

that:

$$E_{NCX} = 3E_{Na} - 2E_{Ca} \tag{1.2}$$

where E_{Na} and E_{Ca} are the Nernst potentials for Na^+ and Ca^{2+}, respectively, as defined in Eq. 1.1.

Under physiological conditions, E_{NCX} is approximately -40 mV during diastole, assuming typical values of $[Na^+]_o$ = 145 mM, $[Na^+]_i$ = 10 mM, $[Ca^{2+}]_o$ = 1.4 mM and $[Ca^{2+}]_i$ = 0.1 μM. Since V_m is at approximately -80 mV, NCX operates in forward mode where Ca^{2+} extrusion and hence an inward I_{NCX} is thermodynamically favoured. However, since $[Ca^{2+}]_i$ is low, the amplitude of I_{NCX} is relatively small. During depolarisation of a cardiac AP when V_m becomes greater than E_{NCX}, the exchanger switches briefly to the reverse mode leading to a Ca^{2+} influx and an outward I_{NCX}. As $[Ca^{2+}]_i$ rises due to CICR, E_{NCX} becomes more positive. The shift in E_{NCX} and the decrease in V_m during repolarisation again favour Ca^{2+} extrusion and an inward I_{NCX} which is significantly greater in amplitude than during diastole, thus facilitating the decay of $[Ca^{2+}]_i$ and relaxation.

In addition to playing a crucial role in trans-sarcolemmal Ca^{2+} extrusion, NCX has also been implicated in triggering SR Ca^{2+} release, although the experimental evidence remains debated (for a comprehensive review see [26]). For example, Kohomoto et al. [108] reported ryanodine-sensitive Ca^{2+} release through reverse mode NCX when I_{CaL} was blocked by nifedipine, indicating Ca^{2+} entry through reverse mode NCX may activate CICR. Leblanc and Hume [114] also observed tetrodotoxin (I_{Na} blocker)-sensitive SR Ca^{2+} release in the absence of Ca^{2+} entry through I_{CaL}. They proposed that Na^+ entry through I_{Na} may elevate subsarcolemmal Na^+ concentration substantially, enhancing Ca^{2+} entry through NCX to an extent sufficient to trigger CICR. On the other hand, Evans and Cannell [57] failed to demonstrate activation of SR Ca^{2+} release through I_{Na}-

stimulated reverse mode NCX, and suggested that the SR Ca^{2+} release observed by other groups may result instead from Ca^{2+} entry through I_{CaL} due to a loss of voltage control or incomplete blockage of I_{CaL}. In addition, the authors demonstrated through thermodynamic considerations and simulation study that, to enable SR Ca^{2+} release through reverse mode NCX, local [Na^+] must reach a level substantially higher than the bulk $[Na^+]_i$, which is only possible if NCX are tightly packed around the Na^+ channels with highly restricted Na^+ diffusion. Therefore, under physiological conditions, Ca^{2+} entry through I_{CaL} is by far the most dominant trigger for SR Ca^{2+} release, although NCX-mediated Ca^{2+} influx may become important under conditions such as an elevated $[Na^+]_i$ level or increased SR Ca^{2+} content.

Plasma Membrane Calcium ATPase

The plasma membrane Calcium ATPase (PMCA) belongs to the same ATPase family as the NKA and SERCA. Through PMCA, Ca^{2+} ions are extruded from the cytosol against its electrochemical gradient using the energy released from ATP hydrolysis. In the meantime, protons are co-transported into the cell although the exact stoichiometry of protons per Ca^{2+} remains debated and is likely to be between 1-2 H^+ per Ca^{2+} [146]. PMCA has a relatively high affinity for Ca^{2+} [12], but its transport rate is considerably slower compared to the other Ca^{2+} handling proteins such as SERCA and NCX [19]. In mice, it has been reported that less than 10% of total Ca^{2+} extrusion can be attributed to PMCA under physiological conditions [116]. However, in mice with cardiac-specific NCX knockout, only modestly reduced cardiac function was observed despite the complete ablation of NCX function, possibly due to stimulation of PMCA by Ca^{2+}/calmodulin or by phosphorylation [88]. Therefore, while PMCA is not a major Ca^{2+} transporter on a beat-to beat basis, it may become important when other Ca^{2+} removal mechanisms are compromised [125].

1.1.4 Species-dependent Features of the Heart

Many aspects of cardiac function are species-dependent. For example, while human hearts typically function at around 60 beats per minute (bpm), smaller animals tend to have a much faster heart rate. The mouse heart rate ranges between 400 and 800 bpm. These differences in heart rate lead to significant physiological consequences, such as different intracellular ion homeostasis conditions that in turn result in different responses under pathological conditions.

Significant variations in Ca^{2+} handling properties have been observed in different species. Yuan et al. [213] recorded greater I_{CaL} in rat ventricular myocytes, compared to rabbits, under voltage-clamp conditions suggesting a larger steady-state I_{CaL} in rats. However, in AP clamp experiments, total Ca^{2+} entry through LCCs in rabbits was twice as large as that observed in rats, since the triangular waveform of APs in rat and mouse ventricular myocytes limits the duration of I_{CaL} during an AP. As a result, I_{CaL} contributes significantly more towards total $[\mathrm{Ca}^{2+}]_i$ increases in the rabbit ventricle (23%) than in rat and mouse ventricles (7-8%) [19].

Another example of species-dependent variations in Ca^{2+} handling is the contributions of NCX and SERCA to $[\mathrm{Ca}^{2+}]_i$ regulation. As mentioned previously, the levels of $[\mathrm{Na}^{+}]_i$ and $[\mathrm{Ca}^{2+}]_i$ play an important role in setting E_{NCX}, which in turn determines NCX activity during an AP. During diastole, Yao et al. [212] found that in mice, the concentration of $[\mathrm{Na}^{+}]_i$ at resting state was so high (about 16 mM) that NCX appeared to be near its equilibrium potential and contributed to very little diastolic Ca^{2+} extrusion (E_{NCX} = -76 mV, based on values of $[Na^+]_o$ $[Na^+]_i$ = 15.6 mM, $[Ca^{2+}]_o$ = 1.08 mM and $[Ca^{2+}]_i$ = 0.1 μM). In rabbits, on the other hand, Ca^{2+} extrusion via NCX is thermodynamically favoured at rest due to a much lower $[Na^+]_i$ (8 mM), hence the predicted E_{NCX} is much more positive to the transmembrane potential [179]. During relaxation,

SERCA is generally dominant over the NCX in terms of Ca^{2+} removal, but the ratio varies between 2-3:1 in rabbits and guinea-pigs [13] to greater than 10:1 in rats and mice [13, 156].

The frequency-dependent effects on force and $[\mathrm{Ca}^{2+}]_{\mathrm{i}}$ transient also vary among different species. An increase in stimulation frequency produces an increase in force and $[\mathrm{Ca}^{2+}]_{\mathrm{i}}$ transients (a positive force- and $[\mathrm{Ca}^{2+}]_{\mathrm{i}}$- frequency relationship) in isolated myocardial preparations from most mammalian species [13, 110]. However, in rat and mouse hearts, both positive [112] and negative [49] frequency-dependent effects have been observed. Whether the force- and $[\mathrm{Ca}^{2+}]_{\mathrm{i}}$-frequency relationship is positive or negative depends on the interaction of a number of processes. At higher pacing frequencies, SR Ca^{2+} content is generally enhanced due to frequency-dependent up-regulation of SERCA. In addition, Ca^{2+} extrusion through NCX is decreased due to a decreased driving force resulting from increased Na^{+} influx and hence $[\mathrm{Na}^{+}]_{\mathrm{i}}$ elevation. Furthermore, frequency-dependent facilitation of $\mathrm{I}_{\mathrm{CaL}}$ may also lead to a higher fractional release, and when combined with the higher SR Ca^{2+} content, result in a positive frequency response of the $[\mathrm{Ca}^{2+}]_{\mathrm{i}}$ transient [112]. However, frequency-dependent reduction in $\mathrm{I}_{\mathrm{CaL}}$ has been observed in mice. For example, Antoons et al. recorded a 45% reduction in peak $\mathrm{I}_{\mathrm{CaL}}$ in mouse ventricular myocytes [7]. Such a reduction could offset the effect of a greater SR Ca^{2+} content and thus cause an overall decrease in the magnitude of the $[\mathrm{Ca}^{2+}]_{\mathrm{i}}$ transient and hence a negative frequency response.

Despite significant variations among different species, the fundamental processes involved in E-C coupling remain the same. E-C coupling is a well-tuned integrated process that is also species-dependent. Its crux lies in the changing concentration of Ca^{2+} in the cytosol during an AP, which then initiates a chain of processes that eventually lead to contractions. The dynamic and delicate balance of Ca^{2+} fluxes during an AP is a key factor governing normal ventricular functions.

1.1.5 Calcium Handling in Heart Failure

HF is one of the most important causes of mortality in industrialised societies [1]. In the simplest terms, HF is characterised by a decreased contractile function and thus the inability of the heart to provide sufficient cardiac output to meet the metabolic demands of the body. Clinically, a number of risk factors have been associated with the development of HF, including hypertension, coronary heart disease and diabetes etc. [87]. The development of HF can result from both a progressive decline in contractile function and/or sudden cardiac death due to arrhythmias [19]. While numerous other factors contribute to the development of HF, intrinsic contractile dysfunction occurs at the myocyte and trabecular level, and the genesis of arrhythmias are also frequently attributed to changes in cellular Ca^{2+} handling and transmembrane ionic currents. In the following section, we will provide a brief overview of the current understanding of Ca^{2+} handling in HF, relevent to this thesis.

At the cellular level, HF is characterised by reduced twitch force and cell contraction paralleled by a decrease in the $[\mathrm{Ca}^{2+}]_{\mathrm{i}}$ transient magnitude ($\Delta[\mathrm{Ca}^{2+}]_{\mathrm{i}}$) [76, 23]. Other characteristics include the slowing down of relaxation and decay of the $[\mathrm{Ca}^{2+}]_{\mathrm{i}}$ transient, a decreased SR Ca^{2+} content, as well as a prolonged AP duration [85, 157, 23]. These alterations are underpinned by changes in the expression and function of multiple Ca^{2+} handling proteins.

Although Ca^{2+} current through LCCs is the initiating event of CICR, changes in $\mathrm{I}_{\mathrm{CaL}}$ have not been consistently observed, despite the universally observed reduction in $\Delta[\mathrm{Ca}^{2+}]_{\mathrm{i}}$ in HF. Some studies have reported no changes in peak $\mathrm{I}_{\mathrm{CaL}}$ and its voltage-dependence in both animal and human models of HF [151, 138], while others have reported decreases its expression level [191, 52]. It is therefore thought that changes in

[1] www.heartstats.org

I_{CaL} may not play a key role in the reduction in $\Delta[Ca^{2+}]_i$ despite all studies reporting a decrease in $\Delta[Ca^{2+}]_i$.

Observations on changes in RyR activity in HF have also been mixed with various studies reporting either increased [64, 25], unchanged [169] or decreased RyR activity [198, 32]. Several studies have also reported changes in the regulation of RyR. Marx et al. reported hyper-phosphorylated RyR2 (the cardiac isoform) in human failing heart with increased RyR open probability at rest and decreased coordinated gating, indicating that diastolic SR Ca^{2+} leak may be increased which may contribute to a lower SR Ca^{2+} content [135]. Gómez et al. reported a decreased ability of I_{CaL} to trigger SR Ca^{2+} release in failing rat hearts [70]. However, Eisner et al. [195, 54] have shown that alterations in RyR gating only transiently affect $[Ca^{2+}]_i$ which gradually returns to the same steady-state level. Therefore, the increased diastolic SR Ca^{2+} leak may be a more significant contribution to decreased E-C coupling in HF.

The process of SR Ca^{2+} uptake through SERCA plays a key role in determining the rate of decay of the $[Ca^{2+}]_i$ transient and hence relaxation, which in turn is crucial for diastolic filling at the whole-heart scale. Ca^{2+} uptake into the SR also replenishes SR Ca^{2+} stores so that Ca^{2+} can be released again during the next cardiac cycle. In almost all animal and human HF models, reductions in the expression and function levels of SERCA have been reported [214, 85, 171, 170]. In addition, the expression level of phospholamban (PLB) is either unchanged [207, 171] or decreased [139]. Even in the case where PLB expression is decreased, the extent of reduction is proportionally less compared to SERCA, such that there is generally a decreased SERCA:PLB ratio [139]. This would mean a more pronounced inhibition of SERCA by PLB and a further reduction in SR Ca^{2+} uptake. The decrease in SERCA activity in HF models is believed to play a fundamental role in both the slowing down of relaxation (or decay of the $[Ca^{2+}]_i$ transient) and the reduction in $\Delta[Ca^{2+}]_i$ since Ca^{2+} removal is impaired and less Ca^{2+} is

available in the SR for CICR.

Again, as outlined above, the primary trans-sarcolemmal Ca^{2+} extrusion mechanism is through NCX. Increased NCX activity has been reported for both human patients [188, 85] and animal models of HF [86], and is thought to facilitate $[\mathrm{Ca}^{2+}]_{\mathrm{i}}$ decay in the presence of an impaired SERCA function. However, as Ca^{2+} extrusion through NCX competes with SR Ca^{2+} uptake through SERCA, NCX up-regulation also leads to a reduced SR Ca^{2+} content and hence a lower $[\mathrm{Ca}^{2+}]_{\mathrm{i}}$ peak. In human models of HF, the important role of NCX in maintaining diastolic function has been demonstrated by Hassenfuss et al. [85]. In their study in which failing hearts were grouped according to their diastolic function, it was found that the group with preserved diastolic function also had increased protein levels of NCX. In contrast, in hearts where NCX protein level was unchanged, diastolic function was severely compromised. As mentioned previously, the direction of Ca^{2+} transport through NCX is dependent on a number of conditions, including membrane potential and the concentration gradients of Ca^{2+} and Na^{+}. Therefore, when $[\mathrm{Ca}^{2+}]_{\mathrm{i}}$ is sufficiently low, NCX up-regulation could also cause a greater Ca^{2+} influx during an AP [19]. However, this effect is unlikely to play an important role in murine hearts which have very short AP durations.

The dependence of Ca^{2+} transport through NCX on $[\mathrm{Na}^{+}]_{\mathrm{i}}$ means that Ca^{2+} handling and intracellular Na^{+} homeostasis are intimately linked (for a comprehensive review see [142]. Many studies have reported elevated $[\mathrm{Na}^{+}]_{\mathrm{i}}$ in both human and animal models of HF [47, 200, 158]. $[\mathrm{Na}^{+}]_{\mathrm{i}}$ elevation lowers the driving force for Ca^{2+} extrusion through NCX and may increase Ca^{2+} entry through NCX during the AP, thereby enhancing SR Ca^{2+} content and the $[\mathrm{Ca}^{2+}]_{\mathrm{i}}$ transient magnitude. Therefore, it is thought that increased $[\mathrm{Na}^{+}]_{\mathrm{i}}$ may have inotropic effects and help to maintain contractile function in HF [47, 200]. However, a study by Pieske et al. revealed that failing human myocardium was characterised by a higher $[\mathrm{Na}^{+}]_{\mathrm{i}}$ and a higher diastolic force at lower pacing frequencies, with

a similar systolic force compared to the non-failing myocardium. In addition, while non-failing myocardium showed a positive force-frequency relationship without changes in diastolic tension, failing myocardium showed a negative relationship with significant increases in diastolic tension as frequency was increased [158], suggesting that failing hearts with $[\mathrm{Na}^{+}]_{\mathrm{i}}$ elevation may be prone to diastolic $[\mathrm{Ca}^{2+}]_{\mathrm{i}}$ overload and thus compromised diastolic function.

1.1.6 Genetically Modified Animal Models

The development of recombinant DNA technology has allowed the introduction of exogenous genetic material first into bacteria, then eukaryotic cells in culture, and most recently whole animals [83]. These advances have given birth to genetically engineered animals. In particular, genetically modified mice have become a popular candidate for studying heart diseases, including those associated with Ca^{2+} mishandling in HF. Through addition or deletion of genes, these models allow the identification of genes that are important for HF and evaluation of molecular and cellular mechanisms responsible for the development and progression of the disease [43, 116, 212, 4].

While transgenic mouse models enable the study of each Ca^{2+} handling mechanism in isolation, the complex compensatory mechanisms and the overall effects on global Ca^{2+} dynamics require an integrated understanding of the dynamic inter-play between the different Ca^{2+} handling components. With a large amount of experimental data in mice now becoming available, mathematical modelling has the potential power to rationalise the data and provide an integrated understanding of the mouse heart in the presence of genetic manipulations.

We now present a brief overview of previously published mathematical models of cardiac electrophysiology and Ca^{2+} handling, and describe the motivation for this thesis.

1.2 Mathematical Modelling of Cardiac Electrophysiology

1.2.1 Overview

The heart is an example of how a highly complex system can be better understood through the use of mathematical modelling. Traditionally, cardiac research has taken the reductionist approach, collecting data from isolated building blocks of the cardiac system, such as in isolated myocytes and myocardial tissue [168]. Whilst such approach enables us to gain a better understanding of individual aspects of the system, mathematical modelling offers a novel method to integrate these discrete components into a physiologically functioning system of the heart.

Mathematical modelling of cardiac cellular electrophysiology has undergone significant development over the last five decades driven by parallel technological advances that provide improved experimental techniques and ever-increasing computational power. The spectrum of electrophysiological models now available encompasses simple polynomial-based models of electrical activation [96] through to biophysically based models of Ca^{2+} dynamics within the dyadic subspace associated with CICR [178, 27]. These models typically use a system of ordinary differential equations (ODEs) to simulate the waveform of an AP. Various cellular components underlying the AP are included in the model, such as changes in ionic concentrations, electrical activity of ion channels and the resulting ionic currents.

In almost all electrophysiology models, the cell membrane is viewed as an electrical circuit (the equivalent circuit model), comprised of a capacitor in parallel with resistors that represent ionic currents, as shown in Fig. 1.4. The total membrane current is the sum

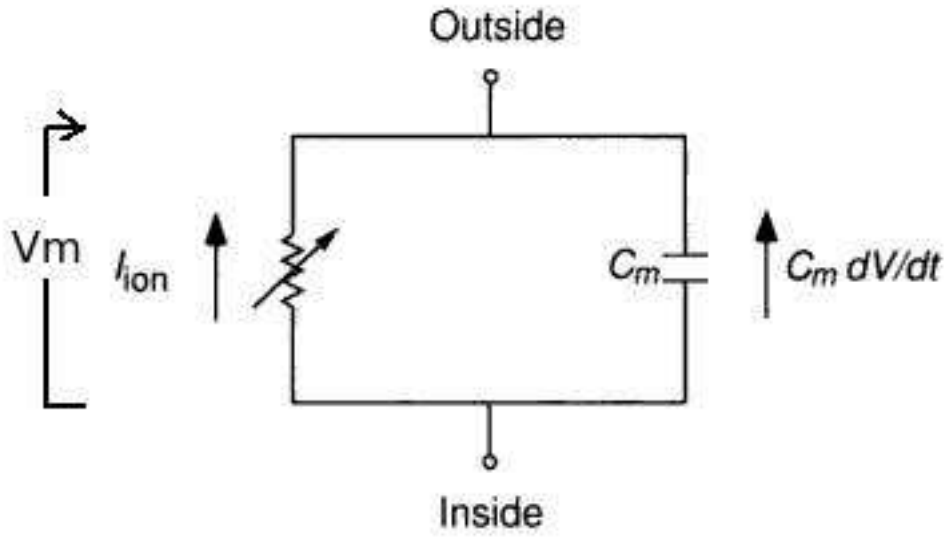

FIGURE 1.4: Simplified equivalent circuit for a patch of cardiac membrane, adapted from [101]. The cell membranes is viewed as a capacitor in parallel with a resistor. I_{ionic} represents the summation of all ionic currents. In the absence of externally applied stimulus, total membrane current is zero, such that I_{ionic} is balanced by the capacitive currents.

of the capacitive current and the ionic current:

$$I_m = C_m \frac{dV_m}{dt} + I_{ionic} \tag{1.3}$$

where I_m is the total membrane current, I_{ionic} is the sum of the transmembrane ionic currents, C_m is the capacitance of the cell membrane per unit area, and V_m is the transmembrane voltage. In the absence of an externally applied current, I_m is equal to zero, thus:

$$C_m \frac{dV_m}{dt} + I_{ionic} = 0 \tag{1.4}$$

The transmembrane current is either ion-specific or non-selective, and there are two main groups: inward (negative) currents which depolarise, and outward (positive) currents which repolarise the membrane. As outlined previously, during an AP, the major

depolarising currents are Na^+ and Ca^{2+} currents, and the most important repolarising currents are the K^+ current group, all of which are sensitive to changes in $\mathrm{V_m}$.

The large number of cell models currently available can be loosely classified into two categories. Models in the first category aim to reproduce the AP based on experimental information about the voltage- and time- dependence of ion channel conductance. The ion channel kinetics are based on the classic Hodgkin-Huxley model of the squid giant axon [91], as outlined below. The second category includes more recent models that use the Markov formulation to represent single ion-channel states explicitly and claim to provide a more accurate representation of the ion channel. Formulations for the Markov models will be discussed in a later section.

1.2.2 The Hodgkin-Huxley Formulation

The first computational model of the AP was developed by Alan Hodgkin and Andrew Huxley [91], who characterised the voltage-dependent properties of the ion channel conductance in excitable cells of the squid giant axon. Axonal AP morphology was reproduced with mathematical descriptions of the macroscopic transmembrane currents generated by a large ensemble currents, consisting of mainly Na^+ and K^+ currents, with representations of the actual underlying mechanisms for the voltage-dependent kinetics of the channels.

The general form of the models using the Hodgkin-Huxley (H-H) formalism is as follows:

$$\mathrm{C_m}\frac{\mathrm{dV_m}}{\mathrm{dt}} = -\sum_{\mathrm{s}} \mathrm{I_s} \tag{1.5}$$

$$\mathrm{I_s} = \overline{\mathrm{G}}_{\mathrm{s}} \prod_{\mathrm{i}=1}^{\mathrm{n}} \mathrm{x_s^i} \cdot (\mathrm{V_m} - \mathrm{V_s}) \tag{1.6}$$

$$\frac{dx_s^i}{dt} = \frac{x_{s\infty}^i(V_m) - x_s^i}{\tau_s^i(V_m)} \tag{1.7}$$

where I_s is the current carried by an ionic species through a particular ion channel. The original H-H model included the depolarising fast Na^+ current (I_{Na}), the repolarising K^+ current (I_K), and a leakage current (I_L). The magnitude of each ionic current is determined by the conductance of the channel and the difference between the transmembrane potential (V_m) and the Nernst potential (V_s) for the particular ion.

The conductance of a particular ion channel is in turn determined by the maximal conductance ($\overline{G}_s$) and the voltage and time dependent gating variables (x_s) that vary between 0 and 1. These describe the activation, inactivation and recovery of the channel. $x_{s\infty}$ is the steady-state value of x_s, and τ_s is the time constant describing the return of x_s to its steady-state following a voltage perturbation. The voltage dependence of both $x_{s\infty}$ and τ_s can be determined from experimental data [91].

1.2.3 Development of Cardiac Electrophysiology Models

While the first mathematical model of the AP was developed by Hodgkin and Huxley [91] for the squid giant axon, the field of cardiac electrophysiology has been pioneered by Denis Noble, who was the first to adapt the H-H formulations to describe cardiac Purkinje fibre APs in 1962 [147]. As more extensive experimental data from cardiac cells became available, an improved model for the Purkinje cells was later developed by McAllister et al. in 1975 [137], which included a Ca^{2+} current and three different types of time-dependent K^+ currents. In 1977, Beeler and Reuter [16] developed an AP model for cardiac ventricular myocytes. Similar to the previous models, this model relied on the H-H formulation to describe ion channel kinetics, assuming constant $[Na^+]_i$ and $[K^+]_i$. Dynamic changes in $[Ca^{2+}]_i$ were also included into the Beeler-Reuter model, as in cardiac myocytes, Ca^{2+} entry through I_{CaL} contributes to the plateau phase of the AP and triggers CICR (see section 1.1.2), which in turn affects AP morphology.

The first model to include dynamic changes in $[\mathrm{Na}^+]_\mathrm{i}$ and $[\mathrm{K}^+]_\mathrm{i}$ was the DiFrancesco-Noble model for the Purkinje fibre AP, developed in 1985 [51]. This is also the first model to include the various ion exchangers and transporters, *i.e.* the NCX, NKA and SERCA, which are crucial for intracellular ion homeostasis. In addition, a model of SR Ca^{2+} release was included to account for CICR. Using this model, the stoichiometry of NCX was predicted to be 3:1 in order to maintain resting $[\mathrm{Ca}^{2+}]_\mathrm{i}$ at a physiological level, as opposed to the 2:1 stoichiometry more widely accepted at that time. This model prediction was later confirmed experimentally in the guinea-pig heart [103].

Following the approach of DiFrancesco and Noble, a similar model for the ventricular myocytes was developed by Luo and Rudy (LRd) for guinea pig ventricular AP [128], which included detailed descriptions of intracellular Ca^{2+} regulation such as SR Ca^{2+} release, SR Ca^{2+} uptake, trans-sarcolemmal Ca^{2+} extrusion as well as intracellular Ca^{2+} buffering. This model was then followed by the development of a number of models for other cell types and species [163, 152, 27].

While these models have been extremely useful for characterising whole-cell behaviours, one of the limitations with the H-H formulation is that the gating parameters do not represent specific kinetic states of ion channels and are assumed to be independent, which is often not a valid assumption. For example, the Na^+ channel is more likely to inactivate when it is open than when it is closed. The inter-dependence between channel states is a consequence of molecular interactions and specific channel movements that have been characterised experimentally [15, 8]. To represent the dependence of a given transition of a channel on its present conformation, Markov-type models have been used in more recent models.

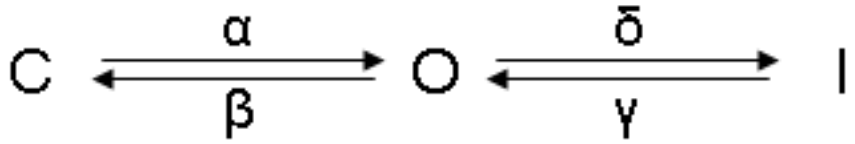

FIGURE 1.5: Markov formulation for a simple three-state channel. Inter-dependent channel gating occurs as inactivation can only occur from the open state.

1.2.4 Markov Models for Computing the Action Potential

For a simple hypothetical channel with three states: open (O), closed (C) and inactivated (I) (Fig. 1.5), we can use the following first-order differential equations to describe the rate of change of occupancy in these states.

$$\frac{\mathrm{dC}}{\mathrm{dt}} = -\alpha \mathrm{C} + \beta \mathrm{O} \tag{1.8}$$

$$\frac{\mathrm{dO}}{\mathrm{dt}} = \alpha \mathrm{C} + \gamma \mathrm{I} - (\beta + \delta)\mathrm{O} \tag{1.9}$$

$$\mathrm{O} + \mathrm{I} + \mathrm{C} = 1 \tag{1.10}$$

where O, C and I are the probabilities that the channel is in the open, closed or inactivated state respectively, and α, β, δ and γ are the voltage dependent transition rates between these states. In this scheme, inactivation can only occur from the open state, and the assumption of independent gating no longer applies.

Models that use Markov formulation are typically more computationally expensive, as they tend to have a large number of state variables. Therefore, whole-ventricle simulations using Markov-formulation have largely been confined to the smaller mouse and rabbit hearts [41]. It should also be noted that the H-H and Markov representations of currents can be used interchangeably. Markov models are often used to describe the major

currents during an AP, such that the effects of molecular interactions that determine channel dynamics can be more accurately represented. Examples of models that use Markov formulation include Clancy and Rudy 1999 (depolarising Na^+ current $\mathrm{I_{Na}}$) [38], Clancy and Rudy 2001 (repolarising K^+ current $\mathrm{I_{kr}}$) [39], and Bondarenko 2004 (L-type Ca^{2+} current $\mathrm{I_{CaL}}$) [27].

1.2.5 Modelling Intracellular Calcium Handling

While the earlier cardiac myocyte models are able to capture AP morphology with detailed descriptions of membrane currents, the intracellular Ca^{2+} handling system is often described using a phenomenological model of CICR without accounting for the underlying mechanisms involved [51, 128]. Spatial distribution of Ca^{2+} within the cell is ignored in these models and SR Ca^{2+} is assumed to be released directly into the bulk cytosol during CICR. However, as described previously, Ca^{2+} entry through LCCs and the subsequent CICR through RyRs occur in a sub-cellular domain called the dyad, where there is a tight coupling between the T-tubules and the junctional SR. As outlined in section 1.1.3, the inter-dependent properties of $\mathrm{I_{CaL}}$ and CICR play a crucial role in determining the shape of the $[\mathrm{Ca}^{2+}]_\mathrm{i}$ transient. With additional experimental evidence concerning the RyRs and LCCs becoming available in the last twenty years [78, 71, 97], a number of biophysically-based mathematical formulations for intracelluar Ca^{2+} handling have been developed [98, 102, 185].

From this work, the recent models of CICR can be generally categorised into either common pool models or local control models. Common pool models [184] are formulated such that all Ca^{2+} influx through LCCs and SR Ca^{2+} release flux are directed into the same compartment [98, 152]. In some of these models, Ca^{2+} is released into the dyadic space and subsequently diffuses into the cytosol. However, even with the detailed spatial distribution of Ca^{2+}, as long as the trigger Ca^{2+} and the Ca^{2+} released from the SR

reside in the same compartment, such models produce all-or-none regenerative calcium releases inconsistent with experimental observations of graded release, due to the positive feedback of rising [Ca^{2+}] on RyR activation. This issue can be overcome by using a phenomenological formulation defining SR Ca^{2+} release flux as an explicit function of sarcolemmal Ca^{2+} influx [27, 58].

On the other hand, the local control models [185, 89, 72] include a detailed mechanistic description of discrete dyadic Ca^{2+} release sites which are independently regulated by local [Ca^{2+}], thereby interrupting the positive feedback loop. The stochastic opening of RyRs within each release site results in Ca^{2+} sparks and graded release is achieved through statistical recruitment of these Ca^{2+} sparks. These models were initially developed to investigate properties of local Ca^{2+} release at the level of the dyadic space [185, 35, 166], and become computationally intensive when integrated into a whole-cell model. In addition, these models often involve a large number of parameters which can not be readily determined experimentally, and details of the actual mechanism for triggering RyR opening remain to be fully understood through future experiments. Therefore, this thesis follows the phenomenological approach to describe graded CICR.

1.2.6 Previous Model of Mouse Ventricular Electrophysiology

Previously, Bondarenko, et al. [27] have published a biophysically based model of mouse ventricular AP, incorporating information from recent advances in molecular biology on the structure and function of ion channels. This model includes descriptions of ionic currents, intracellular ion homeostasis and the corresponding changes in transmembrane potential. Markov models are used for the fast Na^{+} current (I_{Na}), the L-type Ca^{2+} current (I_{CaL}) and the rapid delayed rectifier K^{+} current (I_{kr}), and Hodgekin-Huxley formulation is used for the other ion channels. While the Bondarenko model is able to reproduce murine APs that agree with experimental measurement in duration and amplitude, several

limitations with this model preclude its direct use to quantitatively study Ca^{2+} handling in transgenic mouse heart as explained below.

Following the approach of Niederer et al. [144] to investigate the experimental data dependencies of the Bondarenko model [27], we found significant heterogeneities in the data sources used to determine its model parameters, as shown in Fig. 1.6-1.7. These figures show the hereditary tree for each of the model components, depicting the parent model and the associated species from which the mathematical formulation and the parameter values are adapted (see figure legend for details). While many of the ion channel formulations, including the fast Na^{+} current (I_{Na}) and the various K^{+} currents ($\mathrm{I}_{\mathrm{k,tof}}$, $\mathrm{I}_{\mathrm{k,tos}}$, $\mathrm{I}_{\mathrm{kur}}$ and $\mathrm{I}_{\mathrm{kss}}$ etc.), were derived from murine left ventricular (LV) myocytes, the intracellular Ca^{2+} handling system was based mostly on the Jafri et al. model for guinea pigs [98]. No direct experimental measurements in mice were used to re-fit these parameters, and very little explanation is provided in this paper on how the parameter values were chosen. Furthermore, the Bondorenko et al. model characterises the murine AP at 25°C. However, to simulate murine cardiac myocytes at more physiological conditions requires the re-parameterisation of the model to capture the faster ion channel kinetics at higher temperatures. Recently more data has become available that now allows such a model at a physiologically relevant temperature to be developed.

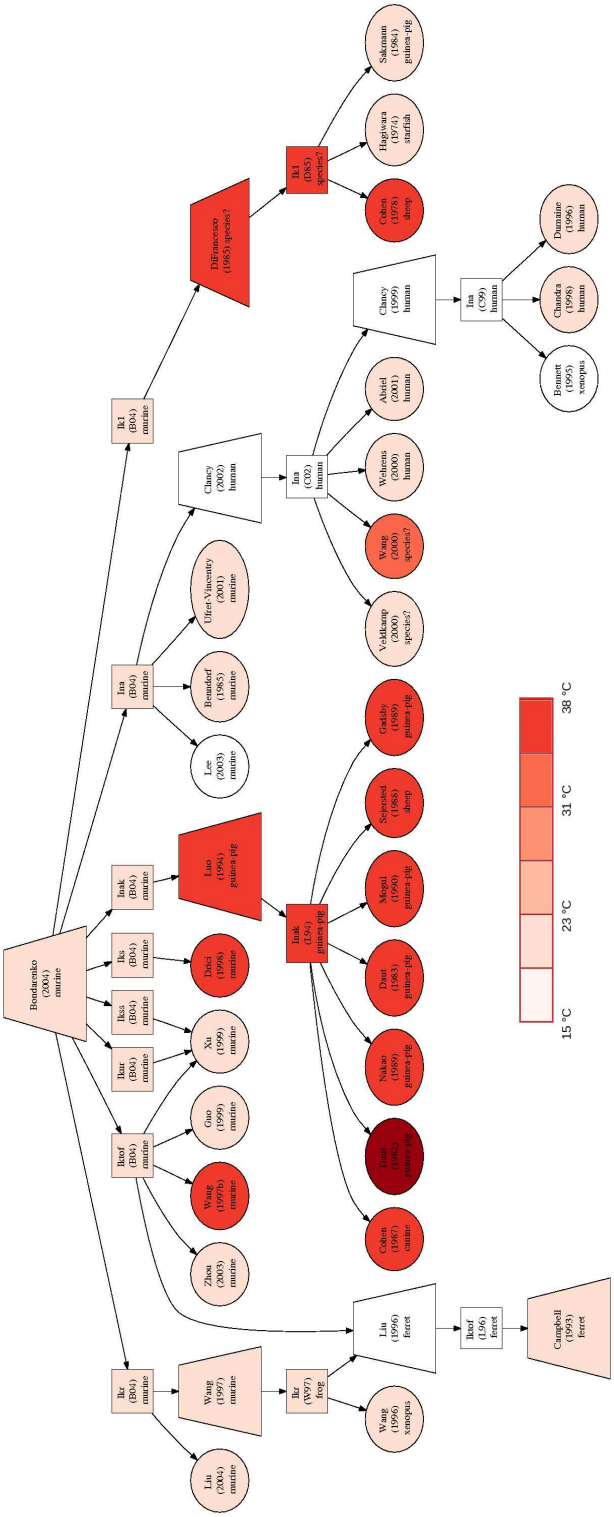

FIGURE 1.6: "Phylogenetic" schematic for the transmembrane current components of the Bondarenko model. Trapezoidal, square and oval shapes represent mathematical models, the components of a model and the experimental work for which the formulation of a component was based on, respectively.

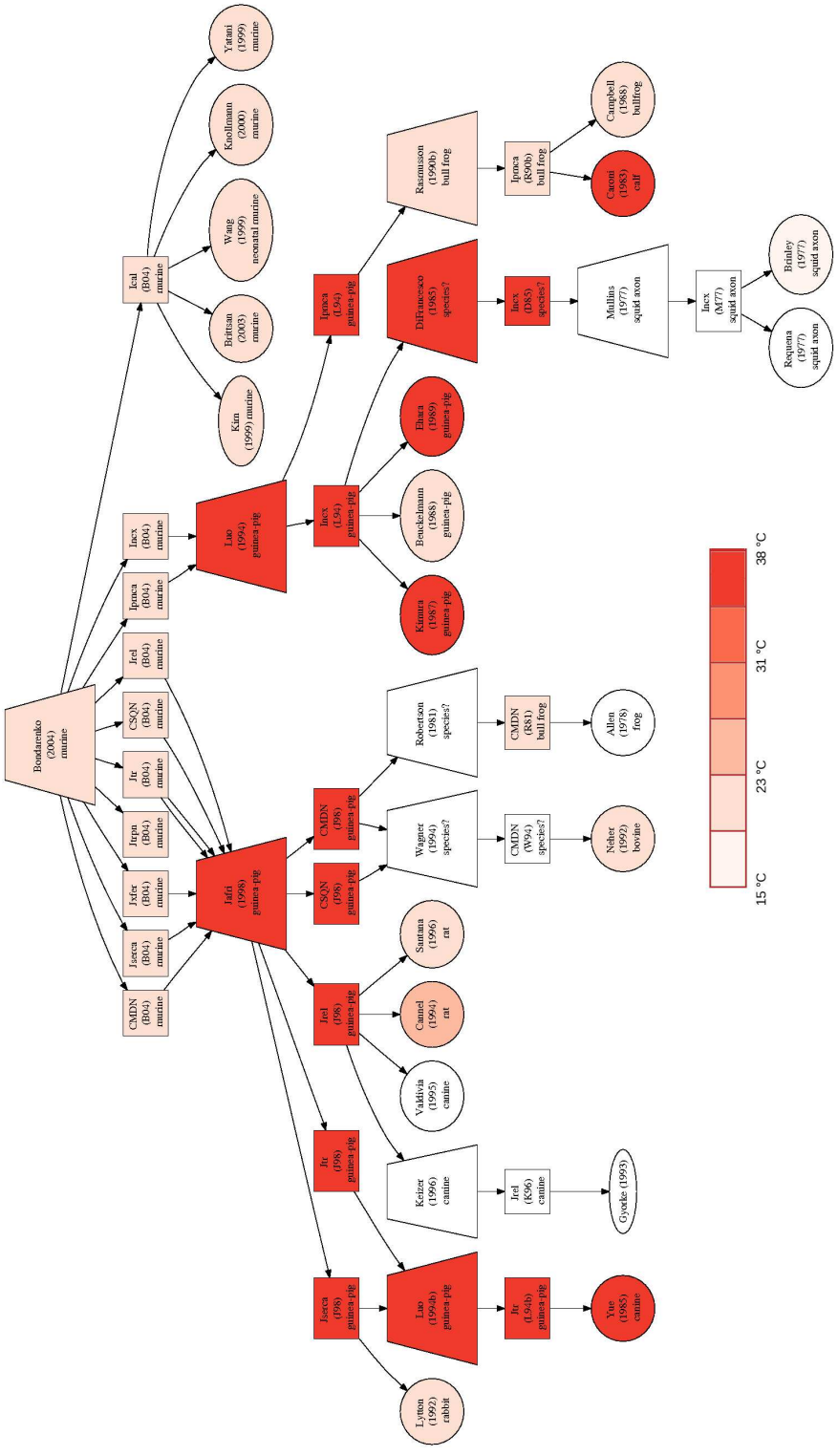

FIGURE 1.7: "Phylogenetic" schematic for Ca^{2+} handling components of the Bondarenko model. Trapezoidal, square and oval shapes represent mathematical models, the components of a model and the experimental work for which the formulation of a component was based on, respectively.

Furthermore, some properties of simulated Ca^{2+} dynamics and AP kinetics in the Bondarenko model were found to be inconsistent with experimental observations. Specifically, reviewing the model behaviour, the time to half decay of the simulated $[\mathrm{Ca}^{2+}]_{\mathrm{i}}$ transients using the Bondarenko model paced at a lower pacing frequency (0.5 Hz: 49 ms) is less than 50 ms, which is significantly shorter than that reported experimentally (175 $\pm$ 25 ms) at the same pacing frequency and under similar extracellular ion concentrations [67]. In addition, at 1 Hz, simulated Ca^{2+} flux through PMCA is similar in magnitude to that through SERCA and significantly greater than that through NCX. In the model, the percentage contribution of SERCA, NCX and PMCA to total Ca^{2+} removal is 46.1$\%$, 6.5$\%$ and 47.4$\%$ respectively, which is not consistent with experimental observations in mouse that SERCA is responsible for over 90$\%$ of total Ca^{2+} removal and PMCA less than 1$\%$ [116]. Finally, APs simulated using the Bondarenko model do not reproduce AP duration restitution properties, i.e. decreasing AP duration with decreasing diastolic interval. Such phenomenon has been observed experimentally in intact mouse heart [106], and is believed to be an important factor underlying cardiac arrhythmia [68].

Finally, it is also worth noting that the original formulation of the Bondarenko model does not account for the ionic concentration changes introduced by the stimulus current, which is required for charge conservation and to avoid gradual drift in the variables [42, 94]. Following the approach of Hund et al. [94], we have assigned the stimulus current to be a K^{+} carrier in all the simulations discussed in the following paragraph.

The limitations of the Bondarenko et al. as explained above concerning its heterogeneous sources of experimental data and the temperature difference were the main motivations for the development a new temperature- and species-consistent model of murine electrophysiology. In light of the above limitations, we now present the first part of the thesis which develops a species- and temperature-consistent model of Ca^{2+} dynamics in murine ventricular myocytes, which forms the basis for the subsequent simulation studies

of SERCA2 KO mice.

Chapter 2

A Data-driven Biophysically-based Electrophysiology Model of the C57BL/6 Mouse Left Ventricular Myocytes

2.1 Introduction

As outlined in Chapter 2, genetically modified mice have become a popular tool for understanding the mechanisms leading to cardiac diseases, including those associated with Ca^{2+} handling dysfunction [43, 116, 212, 4]. With the large amount of experimental murine data now becoming available, mathematical modelling has the potential power to rationalise the data and provide an integrated understanding of the heart. However, the only widely adopted existing mouse electrophysiology model has components that were developed using data sourced from a range of temperatures, and furthermore, its Ca^{2+} handling components were based on experimental data from other species, thus precluding its direct application to quantitatively examine Ca^{2+} handling in transgenic mouse hearts. Therefore, the focus of this chapter was to develop a species- and temperature-consistent

model of Ca^{2+} dynamics in the ventricular myocytes of the C57BL/6 mice, with the aim of quantitatively capturing the experimentally observed Ca^{2+} handling properties. Simulation results were validated against experimentally observed frequency response of Ca^{2+} dynamics, AP shape, the dependence of AP duration on cycle length and electrical restitution.

To demonstrate the importance of using data-driven models that take into account species-dependent variations, the C57BL/6 model was then applied to analyse Ca^{2+} handling in mice over-expressing the canine cardiac NCX. As mentioned in section 1.1.5 "Calcium Handling in Heart Failure", altered NCX activity and expression have been associated with HF [188, 85, 86]. Motivated by this observation, using transgenic mice, the effects of over-expression of NCX have been studied by several groups [1, 165, 193, 192, 212]. In ventricular myocytes from mice with heterozygous over-expression of the canine cardiac NCX, an unchanged [1, 193, 192] or a slightly higher [212] $[\mathrm{Ca}^{2+}]_{\mathrm{i}}$ transient magnitude, a faster rate of decay of the $[\mathrm{Ca}^{2+}]_{\mathrm{i}}$ transient and an unchanged [1, 212] or enhanced [193, 192] SR Ca^{2+} content have often been observed. Furthermore, allosteric regulation of NCX by $[\mathrm{Ca}^{2+}]_{\mathrm{i}}$ has been reported, which appears to be absent in wild-type murine heart [206]. Using the mathematical model, we were able to investigate the mechanisms underlying the observed changes in global Ca^{2+} handling and the significance of allosteric regulation by simulating and comparing Ca^{2+} dynamics in the normal and NCX over-expressing murine hearts, with and without allosteric regulation.

The model developed in this chapter forms the foundation element for the next two chapters, in which we use modelling to further investigate altered Ca^{2+} handling at a more systemic scale, in mice with cardiomyocyte-specific conditional knockout of the SERCA2 gene.

2.2 Experimental Procedures

In the following section, the methods and materials used for collecting experimental data are described. These experiments were carried out by collaborators Idigo, W., Zhang, Y. H. and Casadei, B. from the department of Cardiovascular Medicine, University of Oxford [118].

2.2.1 Isolation of Myocytes

Left ventricular (LV) myocytes were isolated using a standard enzymatic dispersion technique. Briefly, the heart was initially perfused for three minutes with a nominally Ca^{2+}-free solution, followed by a further 8-9 minutes with an enzyme-containing solution (collagenase, 1 mg/ml, Worthington Biochemical Co., Ca^{2+} 0.05mmol/L). Unless specified otherwise, myocytes were superfused with a modified Tyrode solution containing in mmol/L: NaCl 134, KCl 5.4, $MgCl_2$ 1.2, $CaCl_2$ 1.4, glucose 11.1, HEPES 5, at pH equal to 7.4 (adjusted with NaOH). The LV free wall was isolated and placed in a separate flask containing fresh enzyme solution. Myocytes were harvested following further five and ten minute digestion periods, washed twice and resuspended in storage solution containing in mmol/L: NaCl 120, KCl 5.4, MgSO4 5, $CaCl_2$ 0.2, Napyruvate 5, glucose 20, taurine 20, Hepes 10, at pH equal to 7.4 (adjusted with NaOH). The myocyte suspension was stored at room temperature and cells were used within eight hours of isolation. All protocols were in accordance with the *Home Office Guidance on the Operation of Animals (Scientific Procedures) Act, 1986* (H.M.S.O).

2.2.2 Measurement of Calcium Transients

The $[\mathrm{Ca}^{2+}]_{\mathrm{i}}$ transient was evaluated in Fura-2AM -loaded (5 μmol/L, Molecular Probes) LV myocytes field-stimulated at 0.5, 1 and 3 Hz or exposed to caffeine (10 mmol/L for 10 s) after loading the SR by a train of more than 50 stimuli at 3 Hz. Although the basal frequency of 3 Hz is slower than the typical heart rate of a mouse (10 Hz), it is the highest

frequency at which synchronised $[Ca^{2+}]_i$ transient and contraction could be consistently observed. Fluorescence was excited at 365 and 380 nm and monitored at 510 nm (IonOptix Corp) and the amplitude of the $[Ca^{2+}]_i$ transient was calculated as the difference between diastolic and peak Ca^{2+} fluorescence. The $[Ca^{2+}]_i$ transients from individual myocytes were obtained by averaging the recordings over a stable period of approximately 10 s, to provide characteristic $[Ca^{2+}]_i$ transients for analysis.

2.2.3 Measurement of Calcium Current

L-type Ca^{2+} current (I_{CaL}) was measured using the whole-cell configuration of the patch-clamp technique (Axopatch 200A, Axon Instruments), in the presence of 1 mmol/L 4-aminopyridine (4-AP) to block the fast transient outward K^+ currents. I_{CaL} current was elicited by 200 ms step depolarisations from a holding potential of -40 mV to a range of test potentials at a stimulation frequency of 1 Hz. Peak inward current was measured with respect to the current at -40 mV. The average cell membrane capacitance (C_m), measured by applying a -10 mV pulse from a holding potential of -40 mV for 50 ms, was 139 pF. All experiments were conducted at 35°C.

2.2.4 Calibration

The ratiometric fluorescence was converted into free $[Ca^{2+}]_i$ using the following equation proposed by Grynkiewicz et al. [73]:

$$[Ca^{2+}]_i = K_d \cdot \frac{R - R_{min}}{R_{max} - R} \cdot \frac{F_{max380}}{F_{min380}} \tag{2.1}$$

where $[Ca^{2+}]_i$ is the concentration of free cytosolic Ca^{2+} ions, R is the fluorescence ratio recorded at the two excitation wavelengths (F_{365} and F_{380}), K_d is the dissociation constant (0.251 μM), R_{min} (0.909) and R_{max} (2.695) are the fluorescence ratios under Ca^{2+}-free and Ca^{2+}-saturating conditions respectively, and F_{max380} (326.286) and F_{min380} (83.543) are the maximum and minimum fluorescence intensities, exciting at 380nm.

2.3 Model Derivation

MATLAB (The MathWorks, Matick, MA) was used for all data analysis and parameter fitting. All error bars shown represent the standard error of the mean (SEM). For parameter fitting, we used either a subspace trust region method ('lsqcurvefit' function) or the unconstrained nonlinear optimisation function based on the Nelder-Mead Simplex method ('fminsearch' function).

2.3.1 Calcium flux through NCX (Wild-Type Murine)

Current through the NCX (I_{NCX}) is modeled using the formulation from Weber et al. [206]:

$$I_{NCX} = \frac{V_{NCX}^{max}}{1 + (\frac{K_{mallo}}{[Ca^{2+}]_i})^2} \cdot \frac{[Na^+]_i^3 \cdot [Ca^{2+}]_o \cdot e^{\frac{\eta V_m F}{RT}} - [Na^+]_o^3 \cdot [Ca^{2+}]_i \cdot e^{\frac{(\eta-1)V_m F}{RT}}}{\left\{ \begin{array}{l} K_{mCao} \cdot [Na^+]_i^3 + K_{mNao}^3 \cdot [Ca^{2+}]_i \\ +K_{mNai}^3 \cdot [Ca^{2+}]_o \cdot (1 + \frac{[Ca^{2+}]_i}{K_{mCai}}) \\ +K_{mCai} \cdot [Na^+]_o^3 \cdot \left[1 + (\frac{[Na^+]_i}{K_{mNai}})^3)\right] \\ +[Na^+]_i^3 \cdot [Ca^{2+}]_o + [Na^+]_o^3 \cdot [Ca^{2+}]_i \end{array} \right\} \cdot (1 + k_{sat} \cdot e^{\frac{(\eta-1)V_m F}{RT}})} \quad (2.2)$$

where V_m is the transmembrane voltage, V_{NCX}^{max} is the maximal flux through the exchanger, K_{mallo} is the affinity for allosteric $[Ca^{2+}]_i$, η is the energy barrier position controlling V-dependence of I_{NCX}. K_{mCao}, K_{mCai}, K_{mNao}, K_{mNai} are transport affinities for Ca^{2+} and Na^+ inside and out. k_{sat} (0.27) assures saturation at very negative V_m, F is the Faraday's constant (96.5 C/mmol), R is the universal gas constant (8.314 $J{\cdot}mol^{-1}{\cdot}K^{-1}$) and T is the absolute temperature (308 K). K_{mallo} was set to zero as allosteric regulation of the exchanger by $[Ca^{2+}]_i$ was not observed in wild type mouse ventricular myocytes [206]. The relationship between I_{NCX} and the flux of Ca^{2+} ions through the channel (J_{NCX}) into the cytosol is defined by:

$$J_{NCX} = 2 \cdot I_{NCX} \cdot \frac{C_m}{2V_{myo}F} \quad (2.3)$$

where C_m is the average cell membrane capacitance (139 pF) and the myoplasmic volume of the murine ventricular myocyte (V_{myo}) was set at 22x10^{-6} μL [148].

Caffeine-induced SR Ca^{2+} release is a commonly used experimental protocol to investigate the function of NCX. As mentioned in section 1.1.3 "SR Calcium Release Channels ", a high concentration of caffeine causes depletion of SR Ca^{2+} content [54]. Assuming that no net Ca^{2+} re-uptake into the SR occurs, the rate of decay of the total cytosolic Ca^{2+} concentration ($[Ca^{2+}]_{total}$) is equal to the net flux of Ca^{2+} across the sarcolemma ($J_{sarcolemma}$). To infer the rate of sarcolemmal Ca^{2+} extrusion, the time courses of caffeine-induced $[Ca^{2+}]_i$ transients from individual myocytes (N = 18) were first averaged and converted to free $[Ca^{2+}]_i$ using Eq. 2.1. $[Ca^{2+}]_i$ was then converted to the total cytosolic Ca^{2+} concentration ($[Ca^{2+}]_{total}$) using a fast buffering approximation proposed by Trafford and Eisner [196]:

$$[Ca^{2+}]_{total} = a + \frac{B_{max} \cdot [Ca_i^{2+}}{K_{d,buffer} + [Ca^{2+}]_i} \tag{2.4}$$

where $K_{d,buffer}$ (0.60 μM) is the affinity of the buffer, B_{max} (109 μM) is the concentration of the buffer, and a is an arbitrary offset [196]. Since this equation represents the total amount of cytosolic Ca^{2+} buffering, the original calcium buffering equations in the Bondarenko model (Eqs. A16 and A17 in ref. [27]) have been removed in our new formulation. The time derivative of $[Ca^{2+}]_{total}$ in Eq. 2.4 determines $J_{sarcolemma}$. Assuming that the contribution of PMCA to the decay is comparatively small [116], we attributed 90% of the total Ca^{2+} extrusion to NCX and 10% to PMCA [116]. J_{PMCA} takes the same form as that used by Bondarenko et al.. The fitted values of maximum pump rate (I_{PMCA}^{max}) and affinity for Ca^{2+} ($K_{m,PMCA}$) are 0.096 pA/pF and 0.289 μM respectively. The $[Ca^{2+}]_i$-dependence of J_{NCX} was fitted according to Eqs. 2.6 and 2.3 as follows.

To determine $[Na^+]_i$, parameters for NKA were first adjusted according to experimental measurements of the pump current at 35 °C by Berry and colleagues [18]. Specifically,

the Hill coefficient was set to 2.4 and the affinity of the pump to Na^+ was adjusted to 16.6 mM. The maximum pump current (I_{NKA}^{max}) was then determined to be 2.486 pA/pF, such that amplitude at 0 mV in 5 mM $[K^+]_i$ and 50 mM $[Na^+]_o$ is 1.4 pA/pF. These new parameter values were incorporated into the AP framework paced at 1 and 3 Hz, to obtain $[Na^+]_i$ values of 10 and 12.5 mM respectively. $[Na^+]_i$ in quiescent murine myocytes has been reported to be between 14.9 and 17.1 mM at 25 ^oC [212]. However, the activity of the pump is expected to be enhanced at higher temperatures, resulting in a lower $[Na^+]_i$, meaning our estimates remain consistent with cellular functioning at 35 ^oC. In addition, we also assumed that V_m remained constant during caffeine application at -80 mV. The validity of this assumption was confirmed as the experimental protocol was reproduced in our model, i.e. the simulated transmembrane potential was -79.1 mV during caffeine application. For parameterisation, $[Na^+]_i$ was set at 12 mM. Extracellular ion concentrations, set to be consistent with the experimental set-up, were $[Na^+]_o$ (134 mM) and $[Na^+]_o$ (1.4 mM). Other constants include: F (96.5 C/mmol), R (8.314 J·mol^{-1} ·K^{-1}), T (308 K), C_m (139 pF), V_{myo} (22$\times 10^{-6}$ μL).

Initially for the fit, V_{NCX}^{max} only was allowed to vary, and we set all other parameters to the same values as those used by Weber et al. [206]. Fig. 2.1A shows a caffeine induced $[Ca^{2+}]_i$ transient, expressed as fura-2AM ratio, from a single myocyte with prior pacing at 3 Hz. The average time course of the transient, expressed as free cytosolic Ca^{2+} concentration converted using Eq. 2.1, is shown in Fig. 2.1B. $[Ca^{2+}]_i$ was then converted to $[Ca^{2+}]_{total}$ using Eq. 2.4. After taking into account the small background Ca^{2+} leak current and assuming that the contribution of PMCA to the decay is comparatively small [116], we attributed 90% of the total Ca^{2+} extrusion to NCX. The dependence of J_{NCX} on $[Ca^{2+}]_i$ can then be shown by plotting J_{NCX} against the corresponding $[Ca^{2+}]_i$ at each point in time, as shown in Fig. 1C. The simulated J_{NCX} as a function of $[Ca^{2+}]_i$, with the fitted (see sensitivity analysis details below) maximum exchanger rate (V_{NCX}^{max}: 3.939 pA/pF), is shown as the solid line in Fig. 2.1C. The Root Mean Square Deviation

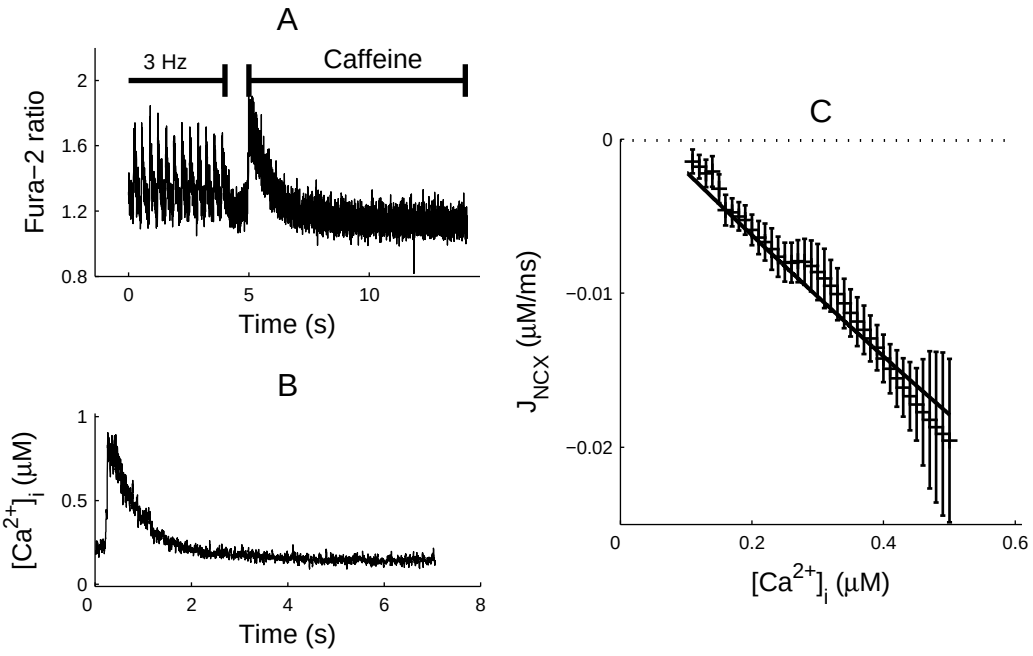

FIGURE 2.1: Characterisation of NCX. A: Top panel: representative caffeine-induced $[\mathrm{Ca}^{2+}]_{\mathrm{i}}$ transient fluorescence ratio recordings, taken from a single myocyte. Bottom panel: average decay of caffeine-induced $[\mathrm{Ca}^{2+}]_{\mathrm{i}}$ transients (n=18), with the fluorescence ratio converted to free $[\mathrm{Ca}^{2+}]_{\mathrm{i}}$. B: Experimentally observed J_{NCX} (circles), and fitted J_{NCX} (line) plotted as a function of $[\mathrm{Ca}^{2+}]_{\mathrm{i}}$.

(RMSD) between the predicted J_{NCX} and the values calculated from experimental data was 1.219×10^{-3} μM/ms.

In the original formulation proposed by Weber et al. [206], there are a total of seven parameters. Taking into account of the Haldane relationship [206], i.e. $K_{\mathrm{mCai}} \cdot K^3_{\mathrm{mNao}} = K^3_{\mathrm{mNai}} \cdot K_{\mathrm{mCao}}$ and hence $K^3_{\mathrm{mNao}} = K^3_{\mathrm{mNai}} \cdot K_{\mathrm{mCao}}/K_{\mathrm{mCai}}$, there are now six free parameters as listed in Table 2.1. We then carried out sensitivity analysis on these parameters following the approach by Fink et al. [63]. Briefly, we defined variable y as the RMSD between the predicted and experimentally calculated J_{NCX}, representing the quality of the fit, and y = y(p) where p is the parameter we are interested in. It follows that at $p = p_0$, $y_0 = y(p_0)$, and at $p = p_0 + \Delta p$, we defined $\Delta y = y(p_0 + \Delta p) - y(p_0)$. The sensitivity ($\sigma_{y,p}$)

of y with respect to the parameter p at p_0 is defined as follows:

$$\sigma_{y,p}(p_0) = \lim_{\Delta p \to 0} \frac{\Delta y / y_0}{\Delta p / p_0} \tag{2.5}$$

Using this method and by setting p_0 to be the original parameter value used by Weber et al. (except for V_{NCX}^{max}, which was set to be the fitted value), and Δp to be 5% of p_0, the sensitivity of RMSD to each parameter is listed in Table 2.1.

TABLE 2.1: Parameters in the NCX model and the corresponding sensitivity of the quality of fit to experimentally observed J_{NCX}.

Parameter Number	Parameter Name	Sensitivity
1	V_{NCX}^{max}	3.270
2	η	0.5536
3	$K_{m,Cao}$	0.0518
4	$K_{m,Cai}$	1.581
5	$K_{m,Ni}$	0.929
6	k_{sat}	1.56

It can be seen that the quality of the fit is most sensitive to V_{NCX}^{max} and moderately sensitive to $K_{m,Cai}$ and k_{sat}. It is insensitive to η, $K_{m,Cao}$ and $K_{m,Nai}$ under this protocol. To check whether allowing more parameters to vary would give a better fit, we tried fitting the three most sensitive parameters $K_{m,Cai}$, k_{sat} and V_{NCX}^{max}, yielding an RMSD of 1.211×10^{-3} μM/ms. The quality of fit is only marginally better than that obtained by fitting V_{NCX}^{max} only (RMSD: 1.219×10^{-3} μM/ms), and the differences between the fits were not visually detectable (not shown). For this reason, we did not vary the values for $K_{m,Cai}$, k_{sat} in the final model. Thus Eq. 2 can be simplified by setting parameters $K_{m,Cao}$ and $K_{m,Nai}$ to be constants and making use of the relation $K_{mNao}^3 = K_{mNai}^3 \cdot K_{mCao}/K_{mCai}$. Parameter η was kept as a variable as it governs the voltage-dependence of the exchange current. The

simplified formulation can be written as:

$$I_{NCX} = \frac{V_{NCX}^{max}}{1 + (\frac{K_{mallo}}{[Ca^{2+}]_i})^2} \cdot \frac{[Na^+]_i^3 \cdot [Ca^{2+}]_o \cdot e^{\frac{\eta V_m F}{RT}} - [Na^+]_o^3 \cdot [Ca^{2+}]_i \cdot e^{\frac{(\eta-1)V_m F}{RT}}}{\left\{ \begin{array}{l} [Na^+]_i^3 \cdot (1400 + [Ca^{2+}]_o + \frac{K_{mCai} \cdot [Na^+]_o^3}{12000^3}) \\ +[Ca^{2+}]_i \cdot \left[\frac{12000^3}{K_{mCai}} \cdot (1400 + [Ca^{2+}]_o) + [Na^+]_o^3\right] \\ +12000^3 \cdot [Ca^{2+}]_o + K_{mCai} \cdot [Na^+]_o^3 \end{array} \right\} \cdot (1 + k_{sat} \cdot e^{\frac{(\eta-1)V_m F}{RT}})} \tag{2.6}$$

2.3.2 Calcium Flux through SERCA

The $[Ca^{2+}]_i$-dependence of Ca^{2+} flux through SERCA (J_{SERCA}) was determined by integrating the NCX model fitted above with the decay phase of the $[Ca^{2+}]_i$ transients elicited by field-stimulation at a range of frequencies. The sources of $[Ca^{2+}]_i$ are assumed to be I_{CaL} and SR Ca^{2+} release, whereas the $[Ca^{2+}]_i$ sinks are SERCA, NCX and PMCA. The inactivation time constant for the LCC is faster than 40 ms (see next section), whereas CICR was assumed to have a duration of no more than 80 ms based on studies performed in rats [182]. Therefore, the effects of Ca^{2+} influx through I_{CaL} and Ca^{2+} release through RyRs can be neglected when analysing the later part of the $[Ca^{2+}]_i$ transient. Thus, to characterise SERCA, Ca^{2+} fluxes were calculated after 70 ms (3 Hz) or 90 ms (0.5 and 1 Hz) had elapsed from the peak of the $[Ca^{2+}]_i$ transient.

At each frequency, the ensemble flux of Ca^{2+} ions (J_{total}) during the decay of the transient was calculated using the same method as was described previously for the caffeine-induced $[Ca^{2+}]_i$ transient. Sarcolemmal Ca^{2+} flux, $J_{sarcolemma}$, estimated from the NCX and PMCA models derived above, was then subtracted from J_{total} to give the net flux of Ca^{2+} ions into the SR (J_{SERCA}). Here we have relied on the assumption that the Ca^{2+} efflux due to mitochondria uptake is minimal under physiological conditions [19]. To

summarise, J_{SERCA} is obtained from:

$$J_{SERCA} = J_{total} - J_{sarcolemma} \text{ for t } > \text{ 70 ms (90 ms) post-peak at 3 Hz (0.5, 1 Hz)} \tag{2.7}$$

In the current study, net flux of Ca^{2+} ions into the SR is assumed to be made up of two components, Ca^{2+} uptake through SERCA (J_{up}) and a non-SERCA-mediated Ca^{2+} leak flux (J_{leak}) mostly attributed to Ca^{2+} sparks through RyR channels. The formulation of the J_{up} model was adopted from Jafri et al. [98] , giving the following equations:

$$J_{SERCA} = J_{up} - J_{leak} \tag{2.8}$$

$$J_{up} = -V_{up} \cdot \frac{[Ca^{2+}]_i^{nH}}{K_{m,up}^{nH} + [Ca^{2+}]_i^{nH}} \tag{2.9}$$

where the negative sign denotes Ca^{2+} movement from the intracellular space to the SR, V_{up} is the maximum pump rate of SERCA at saturating $[Ca^{2+}]_i$, $K_{m,up}$ is the Ca^{2+} affinity of SERCA, and the Hill coefficient nH (equal to two) is set to be consistent with experimental findings [129]. J_{leak} is in turn defined as:

$$J_{leak} = V_{leak} \cdot ([Ca^{2+}]_{NSR} - [Ca^{2+}]_i) \tag{2.10}$$

where V_{leak} determines the dependence of J_{leak} on the Ca^{2+} concentration gradient between the network SR and the cytosol ($[Ca^{2+}]_{NSR}$-$[Ca^{2+}]_i$).

Fig. 2.2A (top panel) shows an example of experimental recordings from a myocyte field-stimulated at 3 Hz. The average $[Ca^{2+}]_i$ transient from individual myocytes (N=22) is shown in Fig. 2.2A (bottom panel). The total ensemble flux of Ca^{2+} ions (J_{total}) during

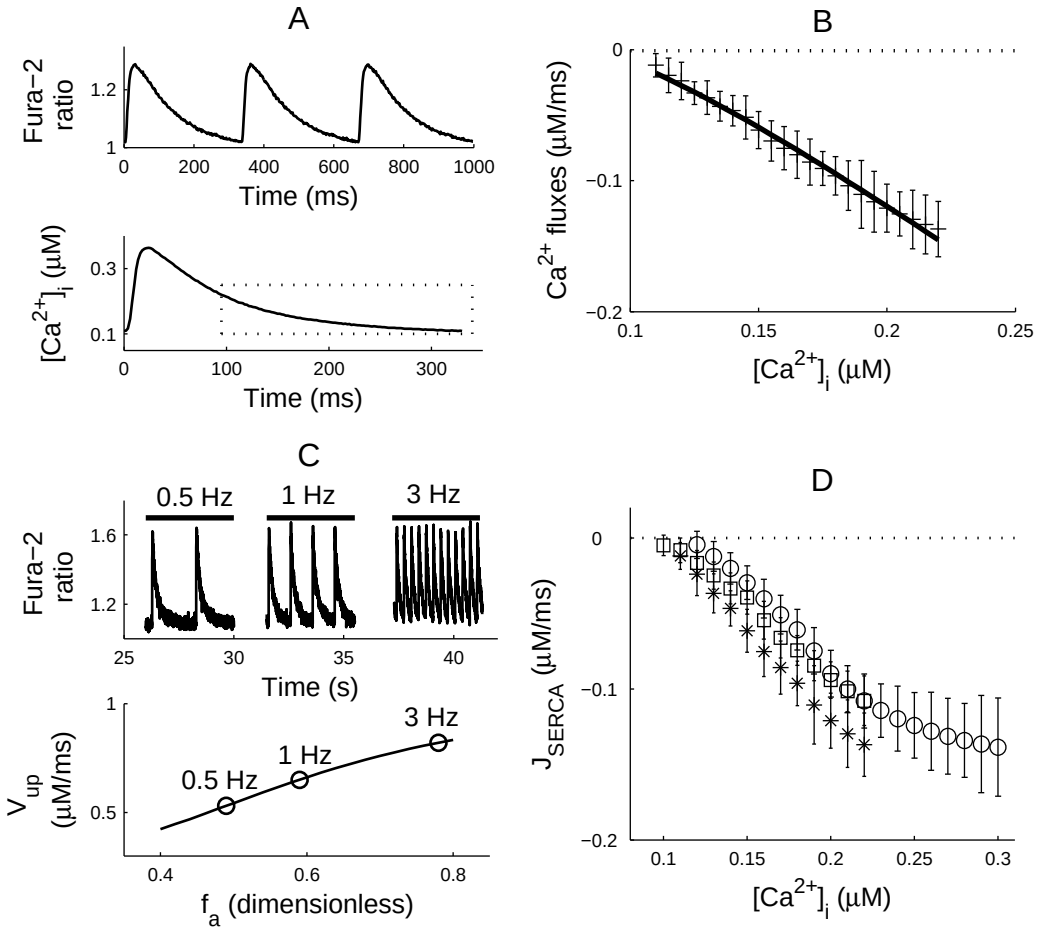

FIGURE 2.2: Characterisation of frequency-dependent SERCA. A: Top panel: representative 3Hz field-stimulated $[\mathrm{Ca}^{2+}]_\mathrm{i}$ transients fluorescence ratio recordings, taken from a single myocyte Bottom panel: 3 Hz $[\mathrm{Ca}^{2+}]_\mathrm{i}$ transient (n=22), with the fluorescence ratio converted to free $[\mathrm{Ca}^{2+}]_\mathrm{i}$. B: Experimentally measured (circles) and fitted (line) $\mathrm{J_{SERCA}}$ at 3 Hz. C: Top panel: experimental recordings of $[\mathrm{Ca}^{2+}]_\mathrm{i}$ transients, measured as the fluorescence ratio, at 0.5, 1 and 3 Hz field stimulations from one myocyte. Bottom panel: SERCA uptake rate ($\mathrm{V_{up}}$) plotted against the corresponding level of active CaMKII ($\mathrm{f_a}$) (circles) at 0.5, 1 and 3 Hz. This was then used to fit parameters in Eqs. 12-14. D: $\mathrm{J_{SERCA}}$ at 0.5 (circles), 1 (squares) and 3 Hz (asterisks) show increased rate of Ca^{2+} uptake at 3 Hz.

the decay of the $[\mathrm{Ca}^{2+}]_\mathrm{i}$ transient was calculated using the same method as was described previously for the caffeine-induced $[\mathrm{Ca}^{2+}]_\mathrm{i}$ transient. Sarcolemmal Ca^{2+} flux, $\mathrm{J_{sarcolemma}}$,

estimated from the NCX and PMCA models derived above, was then subtracted from J_{total} to give the net flux of Ca^{2+} ions into the SR (J_{SERCA}). J_{SERCA} was then used to re-parameterise $K_{m,up}$, V_{up} and provide an estimate of J_{leak}. Fig. 2.2B shows the experimentally derived J_{total} (points) compared with the fitted J_{total} (dotted line) consisting of J_{NCX}, J_{PMCA}, J_{up} and J_{leak}. The SR leak rate V_{leak} then determined in a way such that in whole-cell simulations at 3 Hz, J_{leak} is close to that estimated from parameter fitting. J_{leak}, V_{up} and $K_{m,up}$ were fitted to J_{SERCA} at 3 Hz, yielding J_{leak}equal to 0.037 μmol/L cytosol per millisecond, V_{up} equal to 0.82 μM/ms and $K_{m,up}$ equal to 0.412 μM.

An important assumption underlying the Jafri et al. [98] formulation of SERCA is that V_{up} and $K_{m,up}$ remain constant across a range of pacing frequencies. In our model, fitting J_{up} to experimental data recorded at different pacing frequencies, suggested that J_{up} was up-regulated at 3 Hz, compared to 0.5 and 1 Hz (N = 22). Fig. 2.2C (top panel) shows an indicative example of an experimental recording of the frequency response of $[Ca^{2+}]_i$ transients from one myocyte. Fig. 2.2D shows the frequency-dependent changes in the $[Ca^{2+}]_i$-dependence of J_{up}, with J_{up} reaching a greater magnitude (more negative) for a given level of $[Ca^{2+}]_i$ at 3 Hz, compared to lower frequencies. The values for V_{up} at 0.5 and 1 Hz were determined by fitting J_{up} according to Eq. 2.9. This yielded V_{up} values of 0.55 μM/ms and 0.65 μM/ms for 0.5 and 1 Hz, respectively. Existing literature supports the finding that Ca^{2+} uptake rate through SERCA becomes faster at higher frequencies to facilitate frequency-dependent acceleration of relaxation (FDAR) [93]. FDAR is thought to involve calcium/calmodulin kinase II (CaMKII) through phosphorylation of key Ca^{2+} regulatory proteins such as phospholamban [113] and SERCA [209], although the exact mechanism remains debated [80, 116] as discussed in section 1.1.3 “CaMKII Regulation of SERCA”. Picht and colleagues [156] recently carried out quantitative analysis of cytosolic Ca^{2+} removal during $[Ca^{2+}]_i$ decline and found that in mice, increases in the level of active CaMKII at higher pacing frequencies led to the elevation of SERCA Ca^{2+} uptake by way of accelerating V_{up} without affecting its affinity.

To model the frequency-dependence of J_{up}, the CaMKII regulatory pathway was incorporated into our model using the formulation proposed by Hund and Rudy (HRd) for canine ventricular myocytes [95]. Many of the parameter values used in the HRd model have been taken from a mathematical model of CaMKII function in the brain, as experimental data for its neuronal isoform is much more abundant than that for the cardiac isoform. We decided to use almost identical parameter values as those in the HRd model, since there is no sufficient data available, to our knowledge, to allow re-parameterisation. While highly simplified in its description of CaMKII dynamics and computationally efficient, the HRd model is able to produce steady-state $[\mathrm{Ca}^{2+}]_{\mathrm{i}}$ transients for a wide range of pacing frequencies that agree with experimental measurements [95].

The state variables f_a, f_b, and f_t in our model correspond to $\mathrm{CaMK}_{\mathrm{active}}$, $\mathrm{CaMK}_{\mathrm{bound}}$ and $\mathrm{CaMK}_{\mathrm{trap}}$ in the HRd model respectively. Parameters f_0, α, β correspond to CaMK_0, α_{CaMK} and β_{CaMK} in the HRd model respectively. Specifically, the fractional occupancies of bound CaMKII (f_b) and trapped CaMKII (f_t) are described below, and the total fractional occupancy of active CaMKII (f_a) is given by the sum of f_b and f_t:

$$f_b = f_0 \cdot (1 - f_t) \cdot \frac{1}{1 + \frac{K_{m,CaM}}{[Ca^{2+}]_{ds}}} \tag{2.11}$$

$$\frac{df_t}{dt} = \alpha \cdot f_b \cdot (f_b + ft) - \beta \cdot f_t \tag{2.12}$$

$$f_a = f_b + f_t \tag{2.13}$$

where f_0 (5%) is the fractional occupancy at equilibrium of the low affinity calmodulin-binding sites, $K_{m,CaM}$ (0.7 μM) is the concentration of $[Ca^{2+}]$ for half-maximal activation of the kinase [215]. α (0.05 ms^{-2}) is the autophosphorylation rate and β, assumed to be 2.0x10^{-4} ms^{-1}, is the rate of dephosphorylation. Minor modifications to the HRd model for CAMKII include: (1) The value for $K_{m,CaM}$ was changed from the original value of

1.5 μM to 0.7 μM, as more recent studies suggest half maximal activation of CaMKII occurs at 0.5 -1 μM free Ca^{2+} [215]. (2) The value for β was changed from 0.00068 ms^{-1} to 0.0002 ms^{-1}, to avoid large oscillations in f_a over each cardiac cycle, which was seen when the original value was used in our simulations.

Then the dependence of J_{up} on CaMKII was modelled by defining V_{up} from Eq. 2.9 as a function of the fractional occupancy of active CaMKII, as shown in Fig. 1.1.3C (bottom panel).

$$J_{up} = -V_{up} \cdot \frac{[Ca^{2+}]_i^{nH}}{K_{m,up}^{nH} + [Ca^{2+}]_i^{nH}} \tag{2.14}$$

$$V_{up} = (\Delta V_{up,CaMK} + 1) \cdot \overline{V_{up}} \tag{2.15}$$

$$\Delta V_{up,CaMK} = \overline{\Delta V_{up,CaMK}} \frac{f_a^n}{K_{m,CaMK}^n + f_a^n} \tag{2.16}$$

where $\overline{V_{up}}$ is the maximal uptake rate in the absence of CaMKII, $\overline{\Delta V_{up,CaMK}}$ denotes the maximum CaMKII-dependent increase in V_{up}, $K_{m,CaMK}$ is the half-saturation coefficient and n is the Hill coefficient. The line of best fit for V_{up} plotted over f_a for each frequency yields $\overline{V_{up}}$ (0.396 μM/ms), $\overline{\Delta V_{up,CaMK}}$ (2.998), $K_{m,CaMK}$ (1.244) and n (2.583).

2.3.3 L-type Calcium Current

An example of the experimentally recorded transmembrane currents elicited by test potentials between -30 and 20 mV is shown in Fig. 2.3A. The fast Na^+ current (I_{Na}) was inactivated by applying a holding potential of -40 mV and the transient outward K^+ currents were blocked due to the presence of 4-AP (see Materials and Methods). Therefore, the peak transmembrane current measured at each test potential, as shown in Fig. 2.3B, could be taken as a good approximation of I_{CaL}. This assumption was validated using the final model (See: section 2.3.4 “Simulated Transmembrane Current during Voltage Clamp”).

Under the particular experimental protocol used, the decay phase of the transmembrane current consisted of both I_{CaL} and the late K^+ currents, such as the slow delayed rectifier (I_{ks}) and the rapid delayed rectifier (I_{kr}), which are insensitive to 4-AP. It was therefore not possible to directly acquire the inactivation kinetics of the channel. As an approximation, we used the formulations proposed by Bondarenko et al. [27], with re-parameterised parameter values (see below), to approximate the magnitudes and time courses of the late K^+ currents, and subtracted them from the experimentally recorded transmembrane current. The remaining current was assumed to consist of I_{CaL} only and fitted to a single exponential function to give the time constant of decay (τ) at each test potential, shown in Fig. 2.3C.

The original formulation for the LCC in the Bondarenko [27] model consists of eight channel states with multiple pathways between different states. The complexity of this formulation is problematic given that only a limited set of experimental data is available to parameterise the model. We therefore used a simpler formulation, with a smaller number of parameters, which was still able to reproduce our experimental observations.

We chose a modified version of the LCC model developed by Hinch et al. [89] for rat ventricular myocytes, which is a simplification of the Jafri et al. [98] model. In this formulation, transitions from the closed state C to the open state O and vice versa are governed by voltage-dependent transition rates α_+ and α_-, respectively. Transition from the closed state C to the inactivated state I is a function of Ca^{2+} concentration in the dyadic space ($[Ca^{2+}]_{ds}$), which reflects its Ca^{2+}-dependent nature. A schematic of the LCC is shown in Fig. 2.4. The transition rates are defined the same way as proposed by Hinch et al. [89] with nine parameters.

The voltage-dependent inactivation gate y in the original Jafri 1998 model [98] is

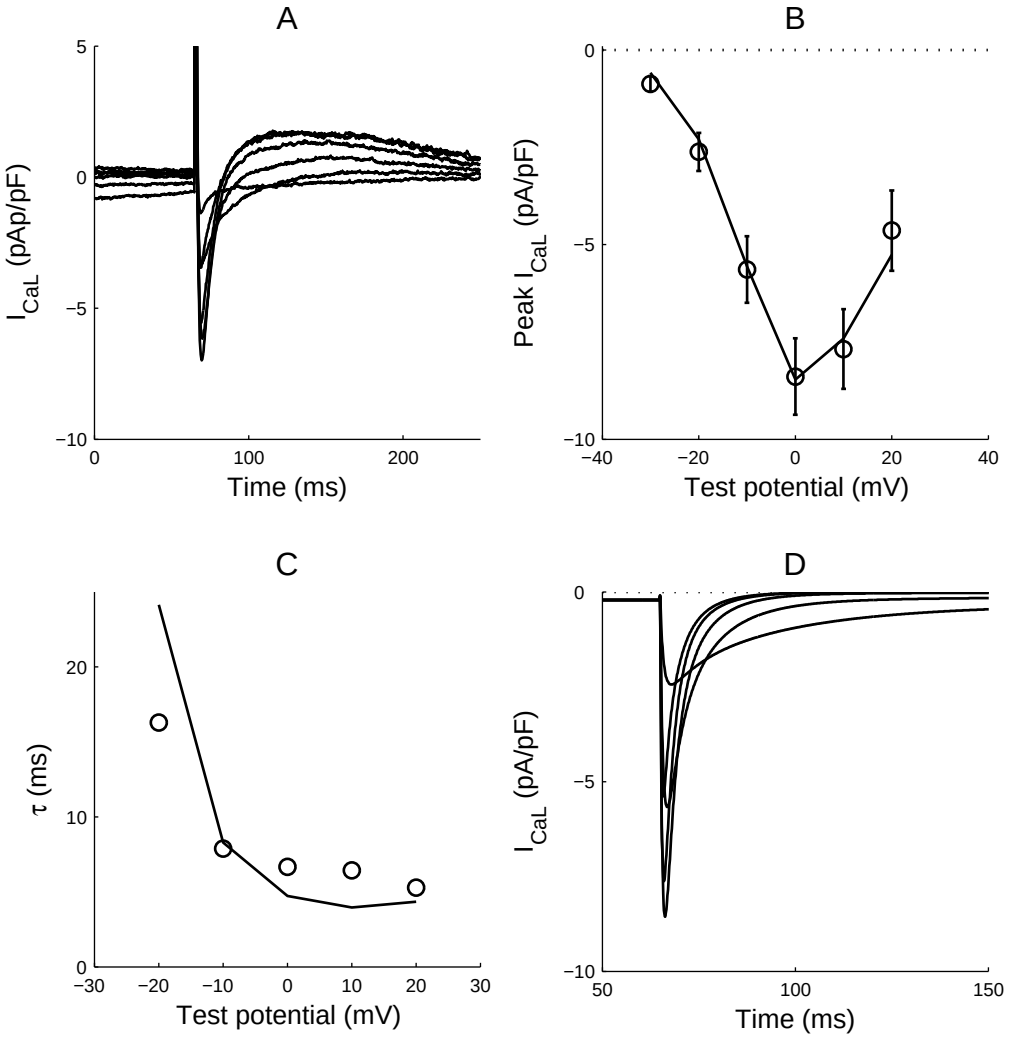

FIGURE 2.3: Parameterisation of the LCC. A: Examples of transmembrane currents measured for a range of test potentials between -30 and 20 mV, in increment of 10 mV. B: Experimentally measured (circles) and simulated current-voltage relationship (line). C: Inactivation time constant (τ) estimated from experimental recordings (circles) and simulated results (line). D: Simulated I_{CaL} at test potentials between -20 and 20 mV.

retained here to capture the voltage-inactivation kinetics of the channel, with the following formulation:

$$\frac{\mathrm{dy}}{\mathrm{dt}} = \frac{\mathrm{y}_\infty - \mathrm{y}}{\tau_\mathrm{y}} \tag{2.17}$$

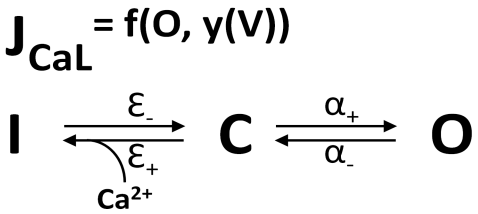

FIGURE 2.4: Schematic of the L-type Ca^{2+} model. Ca^{2+} flux through LCCs is governed by the proportion of the channels in the open state (O) and the voltage-inactivation gate y. State O is represented using a Markov model with three states: the open state (O), the closed state (C) and the Ca^{2+}-dependent inactivated state (I). Voltage-dependent inactivation y is described using a Hodgkin-Huxley formulation (Eqs 2.17-2.19).

$$\mathrm{y}_{\infty} = \frac{1}{1 + \mathrm{e}^{(\mathrm{V}+\mathrm{C}_1)/\mathrm{C}_2}} + \frac{\mathrm{C}_3}{1 + \mathrm{e}^{(-\mathrm{V}+\mathrm{C}_4)/\mathrm{C}_5}} \tag{2.18}$$

$$\tau_{\mathrm{y}} = \mathrm{C}_6 + \frac{\mathrm{C}_7}{1 + \mathrm{e}^{(\mathrm{V}+\mathrm{C}_8)/\mathrm{C}_9}} \tag{2.19}$$

which has nine parameters (C_1 to C_9), yielding a total of 18 parameters. The flux of Ca^{2+} through the L-type Ca^{2+} channel into the dyadic space is then governed by:

$$\mathrm{J}_{\mathrm{CaL}} = \overline{\mathrm{P}_{\mathrm{CaL}}}\delta \mathrm{VOy}\frac{[\mathrm{Ca}^{2+}]_{\mathrm{e}} \cdot \mathrm{e}^{-\delta \mathrm{V}} - [\mathrm{Ca}^{2+}]_{\mathrm{ds}}}{1 - \mathrm{e}^{-\delta \mathrm{V}}} \tag{2.20}$$

where $\mathrm{P}_{\mathrm{CaL}}$ is the permeability of the channel and δ = zF/RT, with z being the valance of Ca^{2+}, F being the Faraday constant (96.5 C·mmol^{-1}), R being the universal gas constant (8.314 J mol^{-1}K^{-1}) and T being the absolute temperature in Kelvin (K). This yields the following equation for the L-type Ca^{2+}current ($\mathrm{I}_{\mathrm{CaL}}$):

$$\mathrm{I}_{\mathrm{CaL}} = 2 \cdot \mathrm{J}_{\mathrm{CaL}}\frac{\mathrm{V}_{\mathrm{ds}}\mathrm{F}}{\mathrm{A}_{\mathrm{cap}}\mathrm{Cm}} \tag{2.21}$$

where V_{ds} is the volume of the dyadic space, set to 2.2×10^{-8} μL to keep the same myoplasmic and dyadic space volume ratio as that in the Bondarenko model.

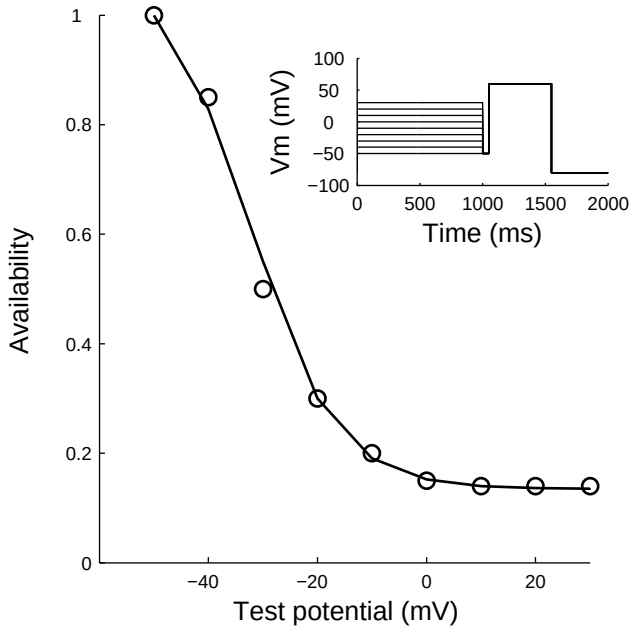

FIGURE 2.5: Experimentally measured (circles) availability-voltage relationship of I_{CaL} in the presence of Ba^{2+} in adult mouse ventricular myocytes [143] under the standard double-pulse voltage-clamp protocols (inset). Availability was measured as the amplitude of the current elicited by the test pulse divided by the amplitude of the current elicited by the prepulse step at -50 mV. Superimposed is the fitted relationship from the model (line).

Hinch et al. [89] fitted V_L and ΔV_L to the I-V curve of the current. However, it is likely that other 16 parameters also need to be re-assessed due to differences between the rat and mouse. Therefore, the parameter values have been identified as follows.

First, some of the parameters governing the voltage-dependent inactivation can be determined from experimental data obtained with Ba^{2+} as the charge carrier for LCC [143]. Using double-pulse voltage-clamp protocols as shown in Fig. 2.5, Nguemo et al. [143] measured the availability-voltage relationship of the current in the presence of Ba^{2+} in adult mouse ventricular myocytes at 37^{o}C. The above measurements were used to fit parameters C_1, C_2 and C_7, yielding C_1 equal to 33 mV, C_2 equal to 8.23 mV and C_3 equal to 315 ms.

TABLE 2.2: Parameters in the LCC model and the corresponding sensitivities of the quality of fit to experimentally observed I-V relationship and inactivation kinetics of the current

Parameter number	Parameter name	Sensitivity of I-V	Sensitivity of τ
1	Φ_L	8.079	2.223
2	t_L	2.761	-0.411
3	τ_L	1.039	-1.257
4	K_L	0.055	-1.348
5	P_{CaL}	5.776	-0.619
6	a	6.228	1.375
7	b	0.474	-0.015
8	C_3	-0.404	0.017
9	C_4	0.041	0.010
10	C_5	1.995	0.002
11	C_6	-0.555	-0.627
12	C_8	-0.774	-0.497
13	C_9	-0.956	0.348

Second, we carried out a sensitivity analysis, similar to that used for the NCX model, to examine the importance of the other 13 parameters in determining the quality of the fit to the experimentally measured I-V curve and the experimentally calculated voltage-dependent inactivation time constant (τ) of the current. As shown in Table 2.2, the I-V curve and the inactivation kinetics are both very sensitive to parameters Φ_L, a, P_{CaL} and t_L. Further visual investigation (not shown) revealed that parameters Φ_L and t_L determines the slope of the I-V curve while parameters a and P_{CaL} only scale the I-V curve. The inactivation kinetics are also very sensitive to K_L,τ_L, C_6, C_8 and C_9. Both the I-V curve and the inactivation kinetics are insensitive to parameters b, C_3, C_4, C_5.

Therefore, we fitted P_{CaL} (2.5 ms^{-1}), Φ_L (1.798) and t_L (1.5), along with V_L (0 mV) and ΔV_L (6.449 mV) to the I-V curve as shown in Fig. 2.3B, with inclusion of the NCX and SERCA models fitted previously and the conductivities of the K^+ currents set to zero. Parameters K_L (0.3 μM), τ_L (1150 ms), C_6 (8 ms), C_8 (30 mV) and C_9 (4 mV) were then fitted to the experimentally calculated voltage-dependent inactivation time constant (τ) of the current, shown in Fig. 3C. In addition, parameter b (0.4) was chosen such that the magnitude of the current elicited by field stimulation at 3 Hz was approximately 50$\%$ of that at 0.5 Hz according to experimental observations in mouse ventricular myocytes [7]. Finally, parameters C_3, C_4, C_5 were set to be the same values as those proposed by Jafri et al. [98]. Simulated time courses of the current elicited by test potentials between -20 and 20 mV in 10 mV intervals are shown in Fig. 2.3D.

2.3.4 Simulated Transmembrane Current during Voltage Clamp

We have used a voltage clamp protocol to measure the current-voltage relationship of I_{CaL} (See "Experimental Procedures"). To test whether the observed transmembrane current at each test potential was indeed a close approximation to I_{CaL} with minimal contamination by other currents, we used our final model to simulate the magnitude of the currents other than I_{CaL} under the same protocol. Fig. 2.6A shows the simulated time course of the sum of transmembrane currents other than LCC (I_{other}), during a 200 ms voltage clamp from a holding potential -40 mV to a range of test potentials. I_{other} was normalised to its magnitude at -40 mV. As experimentally measured I_{CaL} reached its peak approximately 4 ms after the onset of depolarization, we examined the magnitude of I_{other} at 4 ms after the onset of depolarization, as shown in Fig. 2.6B. At test potentials between -20 and 10 mV, simulated I_{other} was less than 5$\%$ of the total transmembrane current measured indicating negligible contamination of the measurement. At test potential equal to -30 and 20 mV, simulated outward I_{other} had a comparable order of magnitude to I_{CaL} although

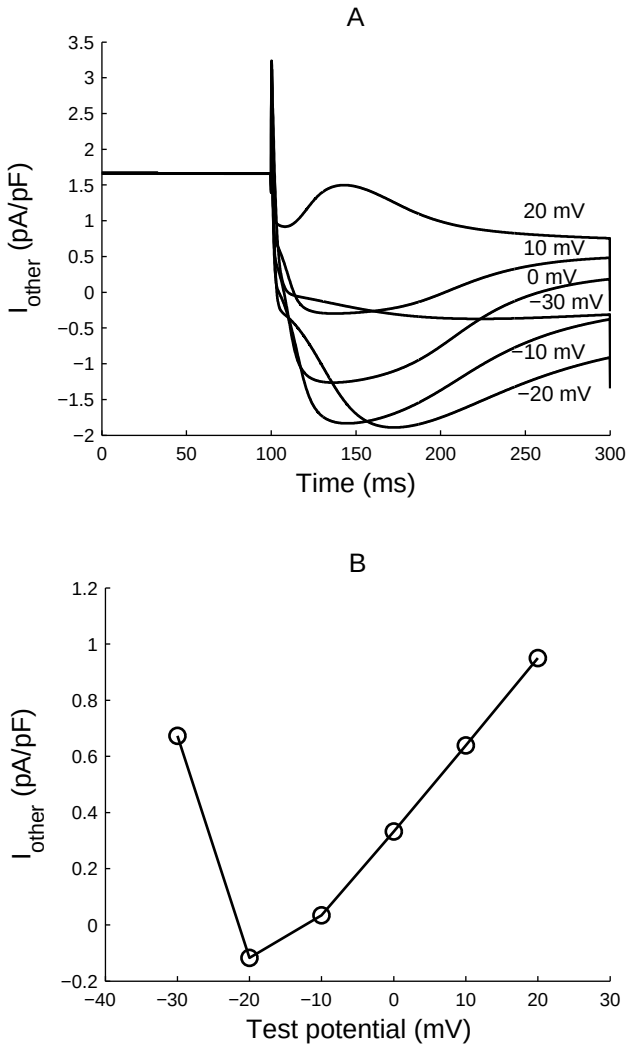

FIGURE 2.6: Simulated sum of transmembrane currents not carried by LCC (I_{other}). The same voltage clamp protocol as that used experimentally to measure I_{CaL} was applied to the final model. (A): Simulated time courses of the sum of the currents (I_{other}) during a 200 ms voltage clamp from -40 mV to a range of test potentials as indicated. (B): Simulated magnitude of I_{other} within 4 ms after the onset of depolarisation to each test potential.

was still significantly smaller. Therefore, possible contamination of I_{CaL} measurements by the presence of other transmembrane currents may be small.

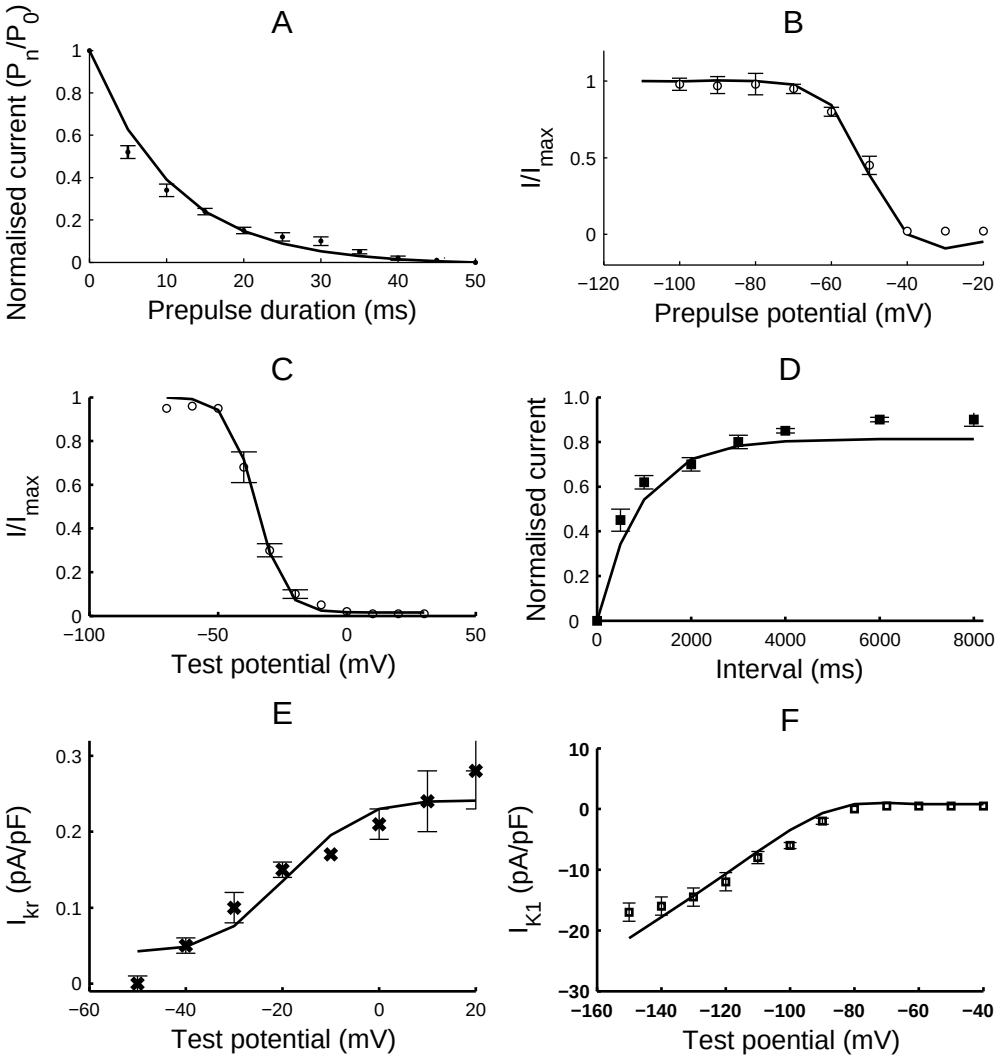

FIGURE 2.7: Fitting of individual K^+ currents. A: $I_{k,tof}$: Experimentally observed inactivation kinetics (dots) [33] and simulated results (line), obtained from a 500 ms depolarisation to +30 mV preceded by a -40 mV inactivating prepulse of varying durations. B: $I_{k,tof}$: experimentally observed (triangles) [33] and simulated (line) voltage-dependence of steady-state inactivation obtained by a two-pulse voltage-clamp protocol. C: I_{kur}: experimentally observed steady-state inactivation (dots) [217] and simulated results (line), produced by a 40 mV depolarisation preceded by various prepulse potential between -60 and 30 mV. D: I_{kur}: experimentally observed recovery from steady-state inactivation (filled squares) [217] and simulated results (line). E: I_{kr}: experimentally measured current-voltage relationship (crosses), produced from step depolarisations to various test potentials between -50 and 20 mV [115], and simulation results (line). F: I_{k1}: experimentally measured current-voltage relationship [105] (open squares) and simulation results (line).

2.3.5 Other Transmembrane Currents

To ensure temperature-consistency of the model, formulations of other transmembrane currents including the various K^+ currents and the fast Na^+ current (I_{Na}) were fitted to experimental measurements at a more physiological temperature, with the fitted NCX, SERCA and LCCs components incorporated. The mathematical formulations of these currents were the same as those proposed by Bondarenko et al [27]. There are seven types of K^+ currents with different kinetics in the Bondarenko model, six of which are considered here: the rapidly inactivating transient outward K^+ current ($I_{k,tof}$), the rapidly activating slowly inactivating K^+ current (I_{kur}), the non-inactivating steady-state K^+ current (I_{kss}), the rapid delayed rectifier (I_{kr}), the slow delayed-rectifier (I_{ks}) and the time-independent K^+ current (I_{k1}). We have chosen to exclude the slow inactivating transient outward K^+ current ($I_{k,tos}$) since it is only found in the septum region of the heart [210] and the cardiomyocytes used in this study (see 2.2 "Experimental Procedures") were from the LV free wall. Parameters for I_{ks} were kept the same as those used in the Bondarenko [27] model as its expression in murine heart was questionable and the magnitude was relatively small [10, 37]. Whenever possible, each of these currents was parameterised individually using the appropriate experimental data from literature as explained below. When direct measurements were not available, parameters were fitted to the ensemble K^+ current [53] and validated using experimentally measured AP durations (APDs).

For $I_{k,tof}$, the kinetics of the inactivation state $i_{to,f}$ can be re-written as:

$$i_{to,f} = \frac{i_{to,f,ss} - i_{to,f}}{\tau_{i_{to,f}}} \tag{2.22}$$

The inactivation time constant $\tau_{i_{to,f}}$ was fitted to experimentally measured time course of inactivation shown in Fig. 2.7A, yielding:

$$\tau_{i_{to,f}} = 9.66 + \frac{10.94}{1 + e^{\frac{1+54.1}{5}}} \tag{2.23}$$

The proportion of the channel that is inactivated at steady-state ($i_{to,f,ss}$) was fitted to the experimentally measured voltage-dependence of steady-state inactivation, shown in Fig. 2.7B, yielding

$$i_{to,f,ss} = \frac{1}{1 + e^{\frac{1+54.1}{5}}} \tag{2.24}$$

The voltage dependence of the activation of $I_{k,tof}$ was fitted to experimentally measured transient and sustained components of the ensemble outward K^+ currents [53]:

$$\begin{aligned} \alpha_a &= 0.18064 \cdot e^{0.03577 \cdot (V_m + 45)} \\ \beta_a &= 0.395 \cdot e^{-0.06237 \cdot (V_m + 45)} \end{aligned} \tag{2.25}$$

where α_a and β_a are the voltage-dependent rate constants for activation.

For I_{kur}, the proportion of the channel that is inactivated at steady-state (i_{ss}) was fitted to the experimentally measured voltage-dependence of steady-state inactivation corrected for the presence of divalent ions Co^{2+}, as shown in Fig. 2.7C. The time constant of inactivation τ_{iur} was fitted to the experimentally measured recovery from steady-state inactivation, shown in Fig. 2.7D. Other parameters were the same as those in the Bondarendo et al. model [27].

$$\begin{aligned} i_{ss} &= \frac{1}{1 + e^{\frac{V_m + 42.1}{5.4}}} \\ \tau_{iur} &= 643 + \frac{1000}{1 + e^{\frac{V_m + 42.1}{5.4}}} \end{aligned} \tag{2.26}$$

For I_{kr}, the conductance of the channel and the rate constants from the state C_{K2} to state O_K (α_{a1}) and from state O_K to state I_K (α_i) were fitted to the experimentally measured current-voltage relationship [115], as shown in Fig. 2.7E.

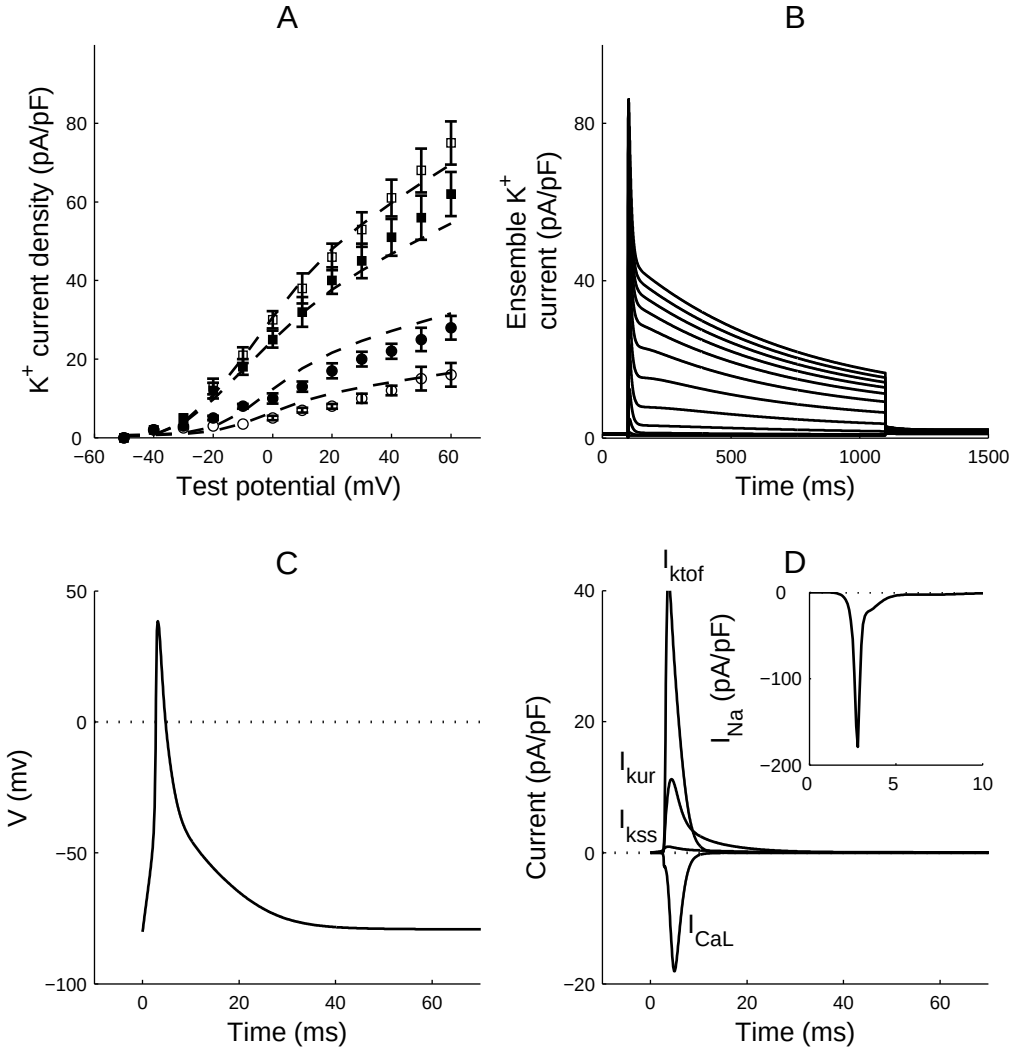

FIGURE 2.8: Fitting of ensemble K^+ currents and AP kinetics. A: Experimentally recorded current-voltage relationships for transient component measured at 300 ms (filled squares) and 1000 ms (open squares) after depolarisation and sustained components measured at the same time points (filled circles and open circles, respectively). Currents were elicited by a 1 s step depolarisation from -80 mV to a range of test potentials [53] and simulation results. B: Simulated time courses of K^+ currents under protocol in A. C: Simulated AP paced at 1 Hz. D: Simulated time courses of major K^+ current during the AP in C. Inset: time course of the fast Na^+ current during the AP in C.

$$\begin{aligned} \alpha_{\mathrm{a1}} &= 0.0335 \cdot \mathrm{e}^{0.0109\mathrm{V_m}} \\ \alpha_{\mathrm{i}} &= 0.0703 \cdot \mathrm{e}^{0.0287(\mathrm{V_m}+5)} \end{aligned} \tag{2.27}$$

For I_{k1}, the conductance of the channel (G_{k1}) (0.35 mSμF) was fitted to experimentally recorded current-voltage relationship [105], as shown in Fig. 2.7F.

Finally, experimentally measured transient and sustained components of the ensemble outward K^+ currents [53], as shown in Fig. 2.8A-B, was used to parameterise the conductance of $I_{k,tof}$ (G_{ktof}: 0.535 mS/μF), I_{kur} (G_{kur}: 0.250 mS/μF) and I_{kss} (G_{kss}: 0.060 mS/μF). It was also used to fit the voltage-dependence of variable a_{ss} which governs the steady-state activation of I_{kur} and I_{kss}:

$$a_{ss} = \frac{1}{1 + \mathrm{e}^{-(\mathrm{V_m}+6.19/9.6)}} \tag{2.28}$$

Due to its large magnitude and fast kinetics, experimental data on the activation and inactivation kinetics of I_{Na} done at physiological temperatures are very limited and we did not fit I_{Na} explicitly. To determine the scope of variations resulting from uncertainty in I_{Na}, a sensitivity analysis of AP shape to the conductance of I_{Na} (G_{Na}) was carried out. A 50% increase in G_{Na} caused a 25% increase in the maximum upstroke velocity of the AP (V_{max}), a 10% increase in AP overshoot, a 3% decrease in APD_{25}, a 5% increase in APD_{90} and a 1.5% increase in $[Na^+]_i$. Therefore, G_{Na} was adjusted to match the experimentally measured V_{max} (177 V/s) [44].

2.3.6 RyR Calcium Release and Intra-SR Buffering Parameters

The rate of SR Ca^{2+} release through the ryanodine receptors (RyRs) during CICR was fitted to match the experimentally measured time-to-peak (TTP) of the $[Ca^{2+}]_i$ transient at 3 Hz (25 $\pm$ 1 ms). Parameters determining the rate of changes in P_{ryr} (first and second constants in Eq. A15 in the Bondarenko model [27], termed $A_{P_{RyR}}$ and $B_{P_{RyR}}$ respectively in Table B.1) have been adjusted from 0.04 and 0.1 respectively, to 0.01 and 2.0, respectively, such that the peak opening probability of RyRs is higher with a shorter opening duration.

$$\frac{dP_{RyR}}{dt} = -0.03 \cdot P_{RyR} - 2.0 \cdot \frac{I_{CaL}}{7.0} \cdot e^{\frac{-(V_m-5.0)^2}{648.0}} \tag{2.29}$$

The total concentration of calsequestrin ($CSQN_{tot}$) was set to 50 mM or 175 μmol Ca^{2+} binding sites per liter cytosol, close to the estimates by Bers [19] of the range between 175 and 350 μmol per litre cytosol. The affinity of calsequestrin to Ca^{2+} (K_m^{CSQN}) was set to 630 μM according to measurements found in literature [176].

2.3.7 Background Calcium Current

The background Ca^{2+} current is formulated as linear leakage current:

$$\begin{aligned} I_{Cab} &= G_{Cab} \cdot (V_m - E_{CaN}) \\ E_{CaB} &= \frac{RT}{2F} \cdot \ln(\frac{[Ca^{2+}]_o}{[Ca^{2+}]_i}) \end{aligned} \tag{2.30}$$

where G_{Cab} is the conductance of the channel and E_{CaN} is the Ca^{2+} Nernst potential. G_{Cab} (7.0 $\times 10^{-4}$ mS/μF) was set such that simulated diastolic $[Ca^{2+}]_i$ levelw was 0.10 μM at 3Hz, close to the experimentally measured level (0.11 $\pm$ 0.01 μM). Simulated diastolic Ca^{2+} influx through I_{Cab} is 0.0047 μM/ms.

2.3.8 Volumes of Intracellular Compartments

With the myoplasmic volume set to be 2.2×10^{-6} μL, the volumes of intracellular compartments were determined by their percentage of the cell volume. Using stereological techniques with electron microscopy, Bossen and colleagues [28] reported the volume fractions of the mitochondria and total SR to be 37.5 and 0.87% of the total cell volume, respectively, in murine left ventricular myocytes. Assuming myoplasm to be 62.5% of the total volume, the fractional volume of total SR is thus 1.4% of myoplasm. In the same study, the volume fraction of the junctional SR was reported to be 0.22% of the total cell volume, equivalent to 25% of the total SR. Accordingly, the volumes of the junctional and network SR were set to be 7.7×10^{-8} and 2.31×10^{-7} μL respectively. The volume of the dyadic space is reportedly near 0.1% of cell volume [19], and thus was set to be 2.2×10^{-8} μL.

2.3.9 Canine Cardiac NCX Over-expression Model

To characterise NCX function in transgenic (TG) mice with canine cardiac NCX over-expression, the TG NCX formulation was parameterised based on studies by Weber et al. [206] and Terracciano et al. [193]. According to the study by Weber et al. [206], at $[Ca^{2+}]_i$ equal to 10 mM, the affinity for allosteric regulation (K_{mAllo}) in TG mice was estimated to be 0.15 μM. For this reason, we set K_{mAllo} in our TG model to be 0.15 μM. We then fitted the NCX parameters (15.0 pA/pF) and η (0.6) in the TG model to the current-voltage relationship measured by Terracciano et al. [193] at room temperature, since to our knowledge no data at 35°C have been published. In their study, I_{NCX} were recorded under a voltage-ramp protocol, where the membrane was depolarised from a holding potential of -75 mV to -40 mV for 200 ms, followed by a voltage ramp to 80 mV and back to -120 mV at a velocity of 50 mV/s.

2.3.10 Phylogenesis of the Current Model

The phylogenesis of the current model, shown in Fig. 2.9-2.10, can be compared to that of the Bondarenko et al. [27] model in Fig. 1.6 and 1.7. Such analysis further reveals that the current model is an significant improvement from the previously published model in terms of species- and temperature-consistency. Therefore, it provides a more reliable basis to use for quantitative analysis of Ca^{2+} dynamics in normal and genetically modified mouse models.

2.4 Results

2.4.1 Model Validation (Wild-type Murine)

Action Potential Kinetics

At a pacing frequency of 1 Hz (Fig. 2.8C), resting potential during diastole was -80 mV, close to experimental values of -79 and -80 mV [33, 53, 105]. The overshoot potential was 38.5 mV, compared to 40 and 46 mV reported by Brouillette et al. [33] and Knollmann et al. [105], respectively. At 1 Hz pacing frequency, the simulated AP duration to 50% repolarisation (APD_{50}) was 2.92 ms, compared to experimental values of 1.7 [99], 2.5 [33], 4.7 [53] and 6.0 ms [105]. APD_{90} was 19.2 ms, compared to experimentally reported values of 23.6 [75], 25 [105, 123] , 15 [33] and 15.4 [99] ms . Table 2.3 lists experimentally measured AP characteristics, and the corresponding strain of mice, cell type and temperature.

Validating RyR Model

In the proposed model, the properties of the RyR, an important modulator for CICR, were not measured directly. Instead, we adapted the formulation used in the Bondarenko

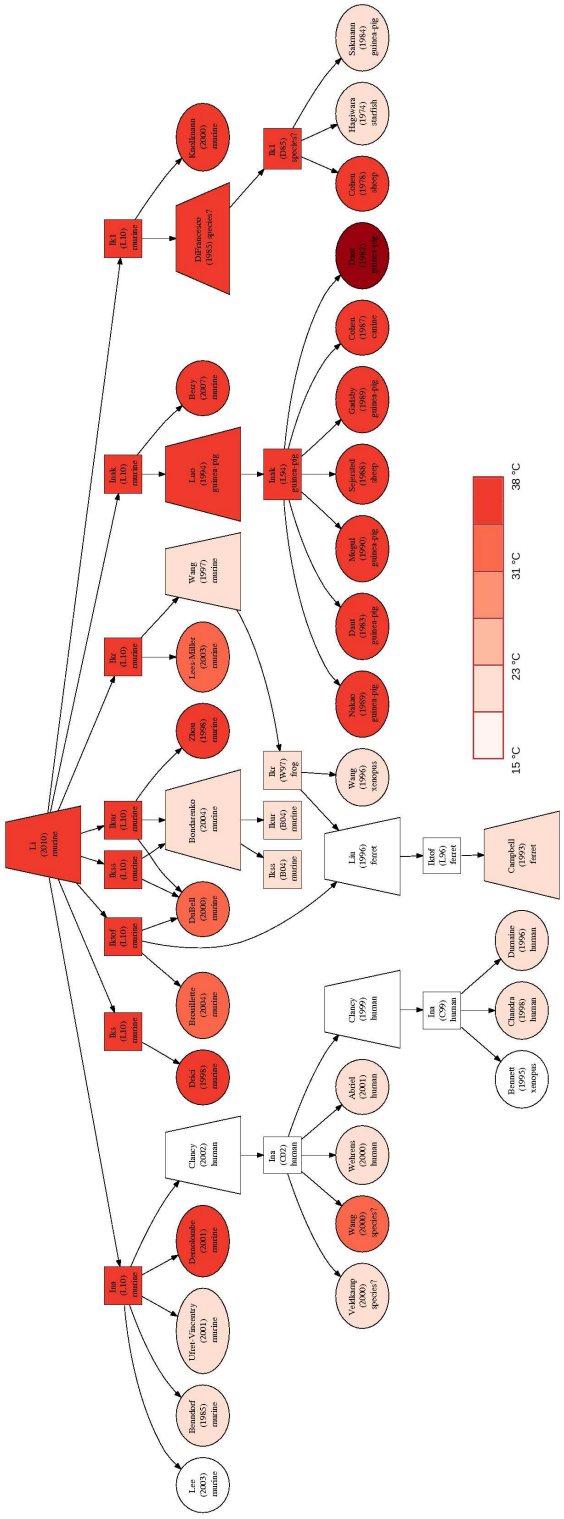

FIGURE 2.9: "Phylogenetic" schematic for the transmembrane current components of the C57/BL/6 model.Trapezoidal, square and oval shapes represent mathematical models, the components of a model and the experimental work, respectively.

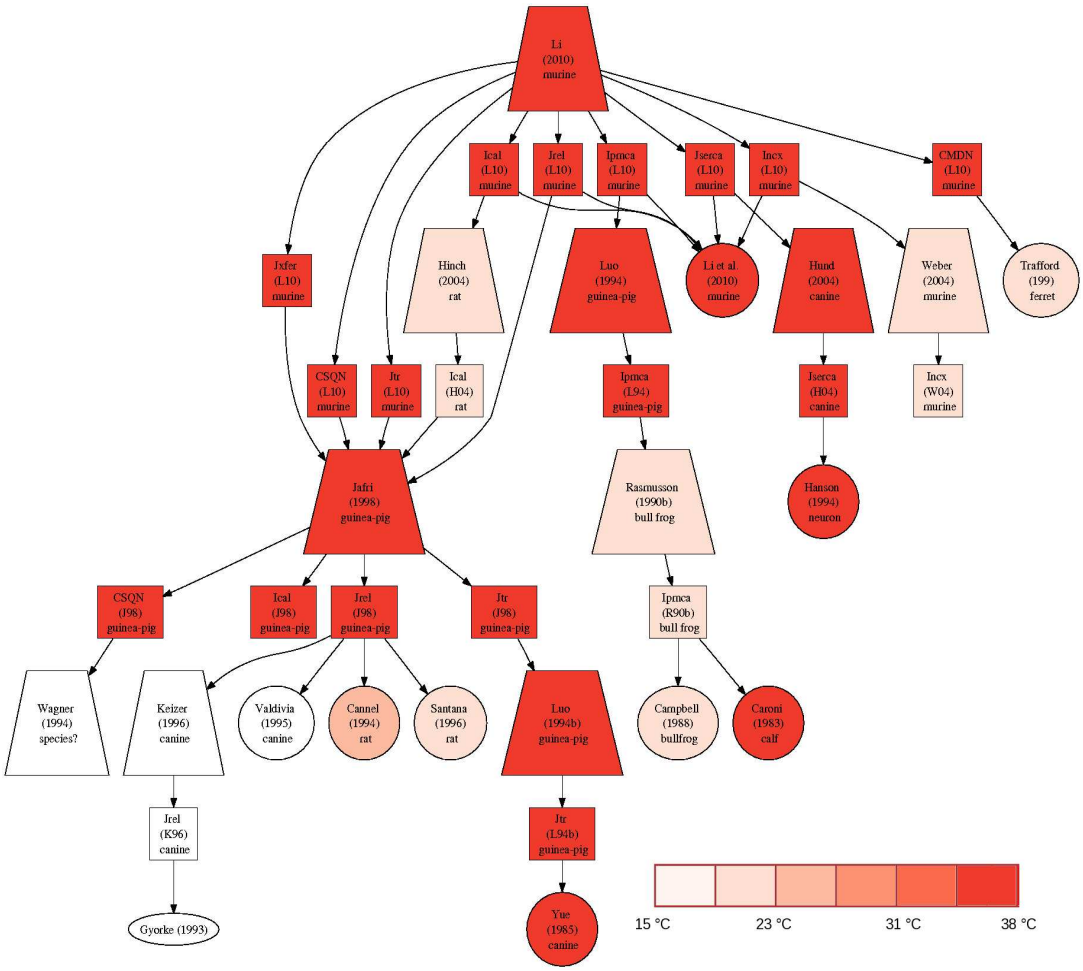

FIGURE 2.10: "Phylogenetic" schematic for Ca^{2+} handling components of the C57BL/6 model. Trapezoidal, square and oval shapes represent mathematical models, the components of a model and the experimental work, respectively.

model with some adjustments to parameter values to match the experimentally observed time-to-peak of the $[Ca^{2+}]_i$ transient. Here we show that our model is able to qualitatively reproduce key characteristics of CICR.

The first set of simulations test the ability of our model to capture the property of graded release, which refers to the observation that SR Ca^{2+} release is proportional to the influx of trigger Ca^{2+}. Fig. 2.11A shows the time courses of I_{CaL} (top panel) and the $[Ca^{2+}]_i$ transient (middle panel) in response to a 200 ms step depolarization from a holding potential of -50 mV to 0 mV. And Fig. 2.11A (bottom panel) shows the peak

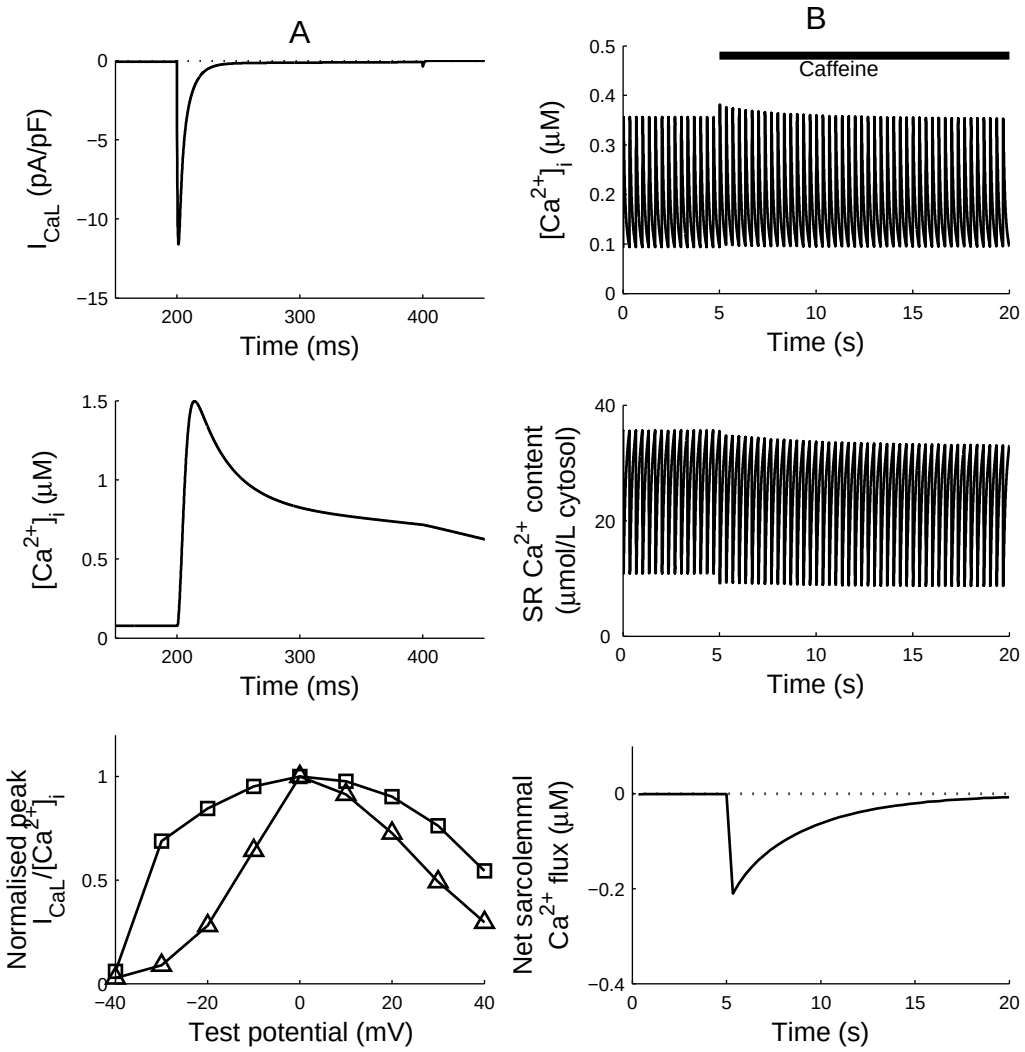

FIGURE 2.11: Properties of simulated CICR. A: Graded response of Ca^{2+} release. Top panel: simulated $\mathrm{I_{CaL}}$ in response to a 200 ms step depolarisation from a holding potential of -50 mV to a test potential of 0 mV. Middle panel: simulated $[\mathrm{Ca}^{2+}]_\mathrm{i}$ transient under the same protocol as described in A. Bottom panel: peak $\mathrm{I_{CaL}}$ (triangles) and peak $[\mathrm{Ca}^{2+}]_\mathrm{i}$ (squares) as a function of test potential, normalised to their respective values at 0 mV. B: Effects of increasing RyR open probability. Top panel: simulated $[\mathrm{Ca}^{2+}]_\mathrm{i}$ transient in response to a 100% increase in RyR open probability, to mimic the effects of a low dose of caffeine. Middle panel: changes in total SR Ca^{2+} content before and after caffeine application. Bottom panel: net sarcolemmal Ca^{2+} flux over each cardiac cycle before and after caffeine application.

TABLE 2.3: Experimentally observed AP characteristics. APD_{50} and APD_{90}, AP duration at 50% and 90% repolarisation, respectively; RV, right ventricle; LV, left ventricle.

Source	Strain cell type	T °C ^oC	Frequency Hz	Resting V mV	Overshoot mV	APD_{50} ms	APD_{90} ms
[105]	CH3/DBA Ventricle	36	1	-79	46	6.4 ± 0.4	25 ± 1.3
[33]	CD1/RV Ventricle	32	1	-80	40	2.5	15
	CD1 Ventricle	32	5	-80	—	4.73 ± 0.03	17.1 ± 0.32
[99]	Hybrid Ventricle	37	Unknown	—	61	1.7 ± 0.2	15.4 ± 1.2
[123]	C57BL/6 LV	35	1	—	—	—	25 ± 1
[75]	C57BL/6 LV	35	1	—	—	—	23.6 ± 1.8
Model	C57BL/6	35	1	-81	38.5	2.9	19.2

I_{CaL} and $[Ca^{2+}]_i$ as a function of the test potential between -40 and 40 mV. The peak I_{CaL} shows a voltage-dependence with a maximum at 0 mV, and the peak $[Ca^{2+}]_i$ follows the same qualitative trend.

The second set of model simulations aim to reproduce the auto-regulation observations of Eisner et al. [54], who demonstrated the transient nature of the cell's response to an increase in the open probability of the RyRs. In their study, a low concentration of caffeine was applied to field-stimulated ventricular myocytes. This produced a transient increase

in the amplitude of the systolic $[Ca^{2+}]_i$ transient which gradually returned to the same steady-state level as that of the control. To validate our model, we repeated the same protocol in our simulations by doubling the open probability of the RyR (PO_1 + PO_2) during steady-state pacing at 3 Hz. The magnitude of the simulated $[Ca^{2+}]_i$ transient, as shown in Fig. 2.11B (top panel), increased upon application of caffeine and gradually decreased over time until it returned to the magnitude prior to caffeine application. As can be seen in Fig. 2.11B (middle panel), there was a decrease in total SR Ca^{2+} after caffeine application which did not recover over time. When examining the net sarcolemmal Ca^{2+} flux in Fig. 2.11B (bottom panel), we found that the loss of Ca^{2+} from the SR was due to a net Ca^{2+} efflux immediately after caffeine application resulting from the simultaneous transient increase in $[Ca^{2+}]_i$ transient. As SR Ca^{2+} decreased, the $[Ca^{2+}]_i$ transient also decreased until a new balance point was established where there was zero net sarcolemmal flux. The above simulation results were consistent with those observed by Eisner et al. [54], and further validate the ability of our model to capture CICR characteristics.

Calcium Dynamics versus Pacing Frequency

TABLE 2.4: Comparison of $[Ca^{2+}]_i$ transients characteristics between experimental and simulated values.

$[Ca^{2+}]_i$ transient dynamics		Experimental values	Simulated values
Diastolic $[Ca^{2+}]_i$ (μM)	0.5 Hz	0.10 ± 0.02	0.06
	1 Hz	0.09 ± 0.01	0.06
	3 Hz	0.11 ± 0.01	0.10
Peak $[Ca^{2+}]_i$ (μM)	0.5 Hz	0.50 ± 0.09	0.48
	1 Hz	0.36 ± 0.05	0.37
	3 Hz	0.37 ± 0.06	0.36
RT_{50}	0.5 Hz	96 ± 6	94
	1 Hz	94 ± 6	88
	3 Hz	67 ± 3	65

As shown in Fig. 2.12A-B, simulated $[Ca^{2+}]_i$ transients paced at 0.5, 1 and 3 Hz were in good agreement with experimental measurements. Overall, a slightly negative frequency response of the $[Ca^{2+}]_i$ transient magnitudes was observed experimentally, with peak

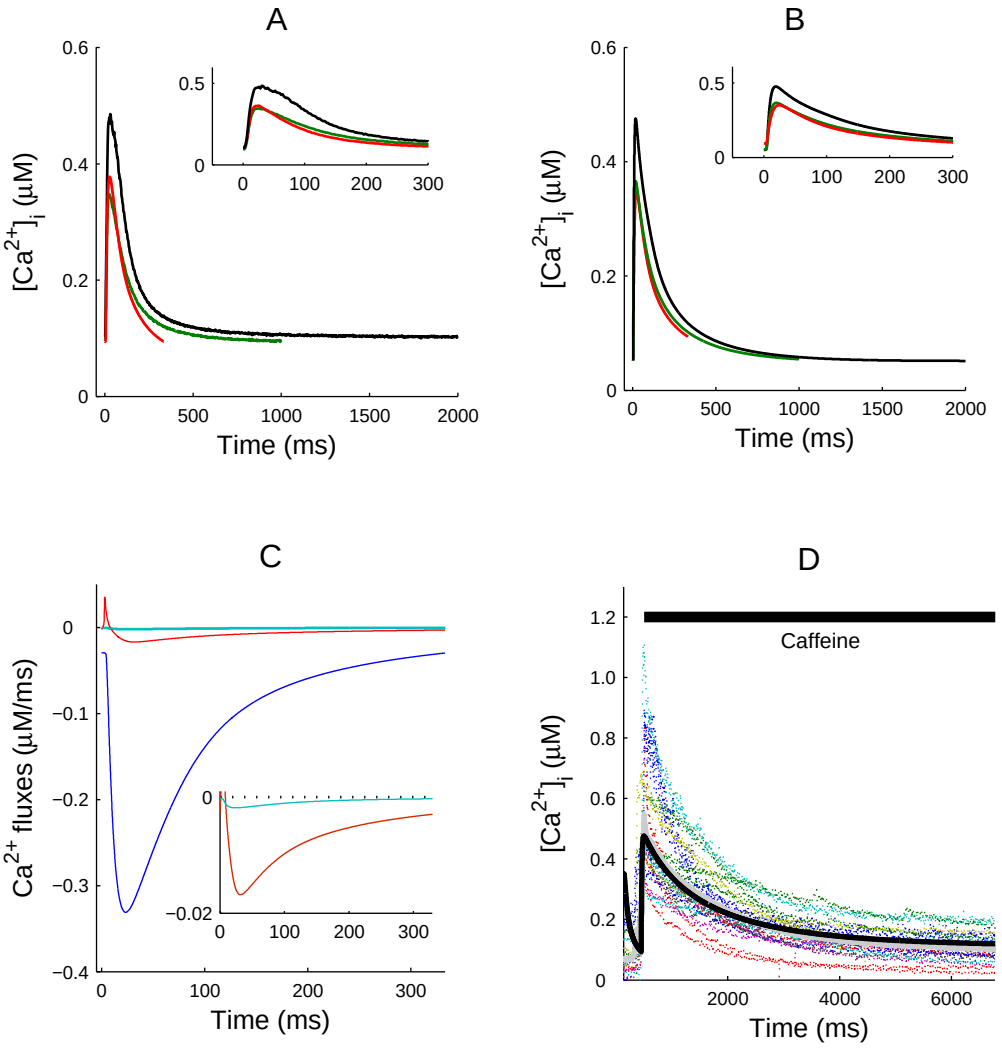

FIGURE 2.12: Comparison between experimentally observed and simulated $[Ca^{2+}]_i$ transients. A: Experimentally recorded $[Ca^{2+}]_i$ transients at 0.5, 1 and 3 Hz. B: Simulated $[Ca^{2+}]_i$ transients at 0.5, 1 and 3 Hz. C: Time courses of Ca^{2+} fluxes through SERCA (blue), NCX (red) and PMCA (green) during a cardiac cycle at 3 Hz. D: Simulated caffeine-induced $[Ca^{2+}]_i$ transient (black) following field-stimulation at 3 Hz, compared with experimentally recorded caffeine-induced $[Ca^{2+}]_i$ transients from 18 individual myocyte (dotted lines) and the average transient (grey).

$[Ca^{2+}]_i$ decreasing from 0.50 $\pm$ 0.09 μM at 0.5 Hz to 0.37 $\pm$ 0.06 μM at 3 Hz. This compared well with simulated peak $[Ca^{2+}]_i$ values of 0.48 μM at 0.5 Hz and 0.36 μM at 3 Hz. Consistent with our analysis of frequency-dependent SERCA function, the time to half relaxation (RT_{50}) was shortened from 96 $\pm$ 6 ms at 0.5 Hz to 67 $\pm$ 3 ms at 3 Hz, which were closely matched by simulated values of 94 and 65 ms respectively. A summary of simulated and experimental $[Ca^{2+}]_i$ transients parameters are listed in Table 2.4.

The time courses of Ca^{2+} fluxes through SERCA, NCX and PMCA during one cardiac cycle at 3 Hz are shown in Fig. 2.12C. The percentage contribution of SR Ca^{2+} uptake to total Ca^{2+} removal, calculated as the ratio between the integral of J_{serca} over one cardiac cycle and the integral of the sum of the fluxes, was 93.4%. NCX and PMCA contributed to 5.9% and 0.7% respectively.

A simulated caffeine-induced $[Ca^{2+}]_i$ transient is shown in Fig. 2.12D. A train of field-stimulation at 3 Hz was applied to the model prior to caffeine application until limit-cycle had been reached. The effects of caffeine application were replicated by setting the open probability of RyR to one, and increasing the rate SR Ca^{2+} leak to 0.1 ms^{-1}, causing a rapid and complete release of Ca^{2+} from the SR. Experimentally recorded transients from individual myocytes and the average transient are also shown in the same plot for comparison. Peak $[Ca^{2+}]_i$ of the simulated transient was 0.49 μM compared to the experimental average of 0.55 μM. The time constant of decay of the simulated transient was 1.27 s compared to 1.36 s recorded experimentally.

Effects of Cycle Length and Restitution

The effects of pacing frequency on the shape of steady-state APs are shown in Fig. 2.13A-B, with pacing frequency increasing from 0.5 to 10 Hz in the direction indicated by the arrow. There were no significant differences in the upstroke and early repolarisation

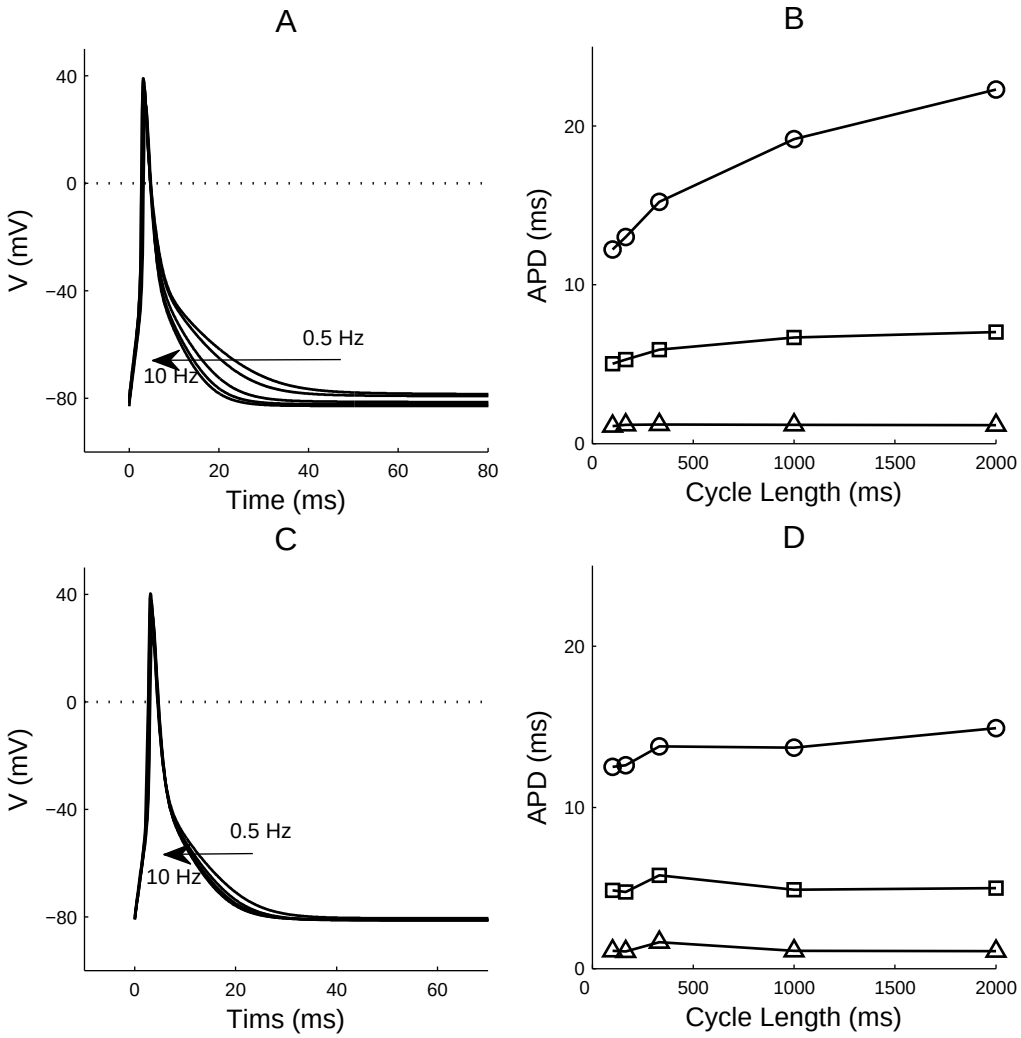

FIGURE 2.13: Effects of pacing frequency on steady-state AP. A: Effects of pacing frequency on the shape of steady-state AP, with pacing frequency increasing from 0.5 to 10 Hz in the direction indicated by the arrow. B: Changes in APD_{25} (triangles), APD_{70} (squares) and APD_{90} (circles) with increasing cycle length. C: Effects of pacing frequency on the shape of steady-state AP in the absence of I_{NCX}. D. Changes in APD_{25} (triangles), APD_{70} (squares) and APD_{90} (circles) with increasing cycle length in the absence of I_{NCX}.

phases (APD_{25}) between different frequencies. However late repolarisation, measured by APD_{75} and $APD_{90,}$ was progressively prolonged with increasing cycle length, which matched qualitatively with experimental characterisation of AP at various cycle lengths in intact murine hearts. It has been suggested that in murine and rat ventricular myocytes, the inward current through the electrogenic NCX during the later phase of the AP is responsible for shaping APD_{90} [104]. To test whether our model agrees with this literature, we eliminated I_{NCX} by setting V_{NCX}^{max} to zero in our model. APs in the absence of I_{NCX} over the same range of frequencies as previously are plotted in Fig. 2.13C, and the corresponding APDs in Fig. 2.13D. It was evident that at longer cycle lengths, late repolarisation was faster in the case without I_{NCX}, with APD_{90} at 0.5 Hz decreasing from 22.3 to 14.9 ms, whereas at shorter cycle lengths, repolarisation dynamics were less affected by the presence of I_{NCX}. The frequency-dependent prolongation in APD_{70} and APD_{90} with increasing cycle length was much attenuated in the absence of I_{NCX}. Therefore, our model results matched well with the finding that I_{NCX} plays a role in shaping the later repolarisation phase of the AP.

The electrical restitution of the AP is shown in Fig. 2.14A, where S1 stands for the last trace of a pacing train at a cycle length of 300 ms, followed by a premature beat (S2) with various S1-S2 intervals ranging between 70 and 1000 ms. Fig. 2.14B shows the relationship between APD_{90} and S1-S2 interval, with APD_{90} gradually lengthening from 14.8 ms at 70 ms S1-S2 interval to 16.5 ms at 1000 ms S1-S2 interval. This was also in qualitative agreement with experimental observations reported by Knollmann et al. in intact murine heart [106]. The effects of a premature beat on I_{CaL} and $[Ca^{2+}]_i$ is shown in Fig. 2.14. The APs during the last cycle of the pacing train followed by a premature beat 100 ms later are shown in Fig. 2.14C, where there was a slight reduction in overshoot during S2 compared to S1 (30.5 *versus* 35.8 mV), a slower upstroke (V_{max}: 132 *versus* 168 V/s) and a faster repolarisation with APD_{70} decreasing from 5.7 ms during S1 to 5.65 ms during S2 and APD_{90} from 14.9 to 14.4 ms. The changes in the AP shape was mirrored

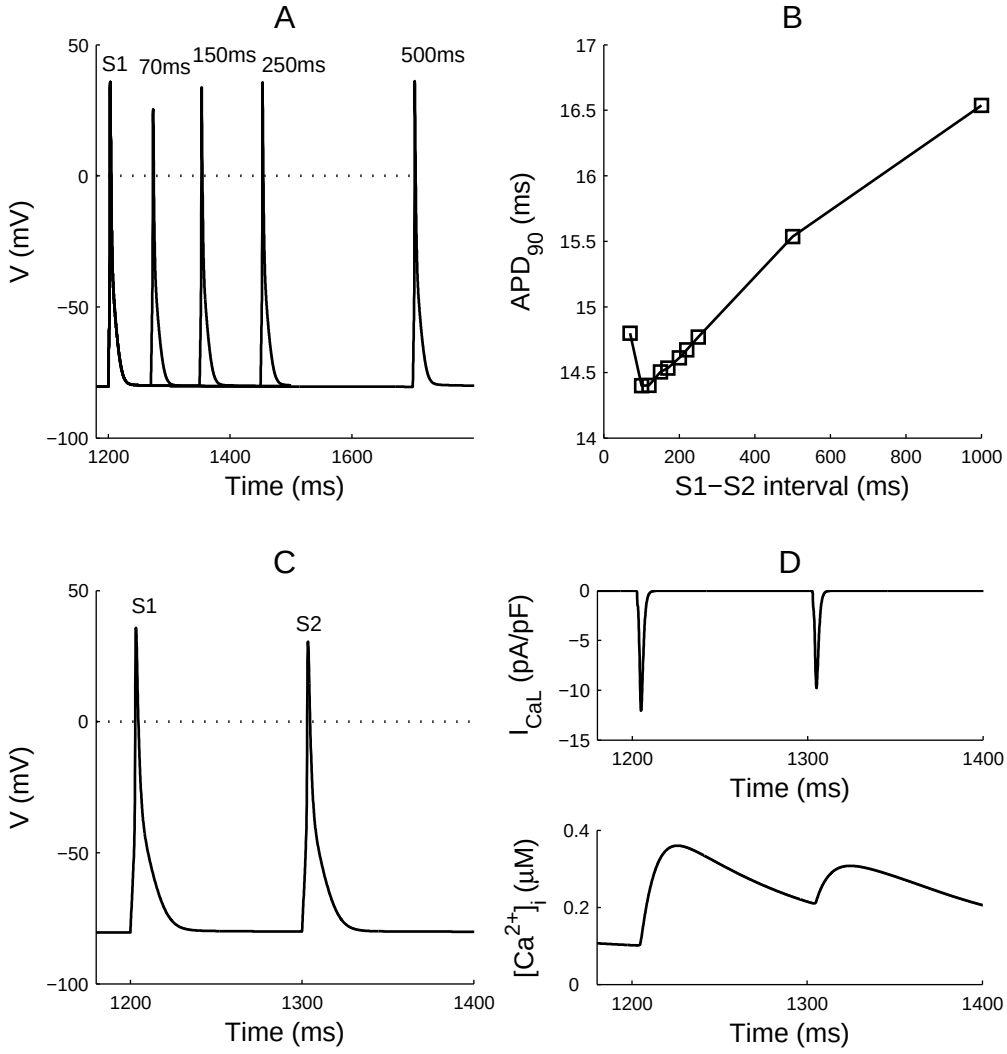

FIGURE 2.14: Electrical restitution of AP. A: Simulated AP in response to a premature beat. S1 stands for the last trace of a pacing train at a cycle length of 150 ms, followed by a premature beat (S2) with various S1-S2 intervals ranging between 70 and 250 ms. B: The relationship between APD_{90} and S1-S2 interval, with APD_{90} gradually lengthening from 12.86 ms at 70 ms S1S2 interval to 13.4 ms at 250 ms S1-S2 interval. C: Simulated AP during the last cycle of the pacing train (S1) followed by a premature beat 70 ms later (S2). D: Top panel: simulated I_{CaL} during S1 and S2. Bottom panel: simulated $[Ca^{2+}]_i$ transient during S1 and S2.

by a decrease in the magnitude of I_{CaL} from 12.0 pA/pF during S1 to 9.8 pA/pF S2, shown in Fig. 2.14D (top panel). The reduction in Ca^{2+} in turn triggered a smaller amount of Ca^{2+} release from the SR hence a smaller $[Ca^{2+}]_i$ transient shown in Fig. 2.14D (bottom panel).

2.4.2 Calcium Handling in Mice Over-expressing the Canine Cardiac NCX

As mentioned in section 2.1, NCX over-expression in mice has been used by several groups to assess the function of NCX in cardiac E-C coupling. As a case study to demonstrate the application of the framework developed in this chapter, we incorporated measurements of NCX function from TG mice and examined its impact on Ca^{2+} handling and the significance of allosteric regulation of NCX function by $[Ca^{2+}]_i$.

Current-Volgate Relationship of I_{NCX}

The extracellular ion concentrations $[Na^+]_o$, $[K^+]_o$, and $[Ca^{2+}]_o$ were adjusted to 140, 6 and 1 mM respectively, to match the experimental set-up of Terracciano et al. [193]. $[Na^+]_i$ (9.6 mM) and $[Ca^{2+}]_i$ (0.135 μM in WT, 0.159 μM in TG) were fixed to the same values as those observed experimentally. The voltage-clamp protocol and the simulated I_{NCX} in the WT and TG models are shown in Fig. 2.15A. The simulated current-voltage relationships are shown in Fig. 2.15B. At positive potentials, simulated I_{NCX} in the TG model was on average 2.7 times the magnitude of the WT model. At negative potentials, the differences in I_{NCX} were less significant, with an average ratio of 1.5, consistent with experimental observations that the statistically significant difference in I_{NCX} diminishes towards more negative potentials .

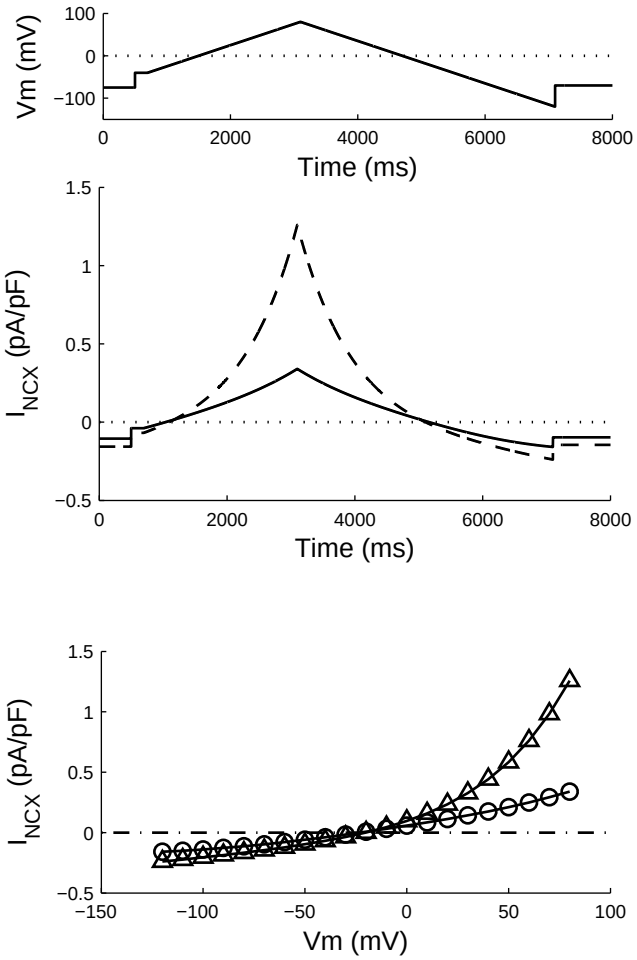

FIGURE 2.15: Simulated current-voltage relationship of I_{NCX} in the WT and TG models. Top: the voltage-clamp protocol used by Terracciano et al. [193] to measure the current-voltage relationship of I_{NCX} in ventricular myocytes isolated from the TG and WT mice. Middle: simulated time courses of I_{NCX} in the WT (solid line) and TG (dashed line) models under the voltage-clamp protocol described above. Bottom: Simulated current-voltage relationships of I_{NCX} in the WT (circles) and TG (triangles) models, under the voltage-clamp protocol described at the top.

Field-stimulated and Caffeine-induced Calcium Transients

Experimentally measured $[Ca^{2+}]_i$ transients, as shown in Table 2.5, show quite significant variations across different groups resulting from, at least partially, differences in the experimental set-up. For example, experiments have been carried out at room temperature [1, 193, 212] or 37°C [192]; $[Ca^{2+}]_i$ transients were elicited by either depolarising pulses or field stimulation at frequencies ranging from 0.25 [212], 0.5 [193] to 1 Hz [192], and perfusion solutions with different $[Na^+]_o$, $[K^+]_o$ and $[Ca^{2+}]_o$ have been used. However, ventricular myocytes from NCX over-expressing mice have been consistently characterised by a 2- to 3-fold increase in the forward function of NCX [193, 192, 212], an unchanged [1, 193, 192] or a slightly higher $[Ca^{2+}]_i$ transient magnitude [212], a faster rate of decay of the $[Ca^{2+}]_i$ transient elicited by either field-stimulation or caffeine, and an unchanged [1, 212] or enhanced [193, 192] SR Ca^{2+} content.

To validate our models, the protocol described by Terracciano et al. [193] was reproduced in both the WT and TG models. Results are compared with those reported by Terracciano et al. [193], as well as other studies [1, 212, 192]. The extracelluar ion concentrations in both the WT and TG models have also been adjusted according to the experimental set-up. The models were initially paced at 0.5 Hz until limit cycle was reached, 2 seconds after cessation of stimulation, the transmembrane was clamped at -75 mV and the effects of caffeine application were simulated by setting the open probability of RyR to one, and increasing the rate SR Ca^{2+} leak to 0.1 ms^{-1}, causing a rapid and complete release of Ca^{2+} from the SR.

Simulated $[Ca^{2+}]_i$ transients during 0.5 Hz field-stimulations are shown in Fig. 2.16A. The magnitude of $[Ca^{2+}]_i$ transient was 0.28 μM in the TG model, 22% higher compared to the WT model (0.23 μM). In general, $[Ca^{2+}]_i$ transient by field-stimulation in the TG mice has been found to be of a similar magnitude or with a slight increasing trend

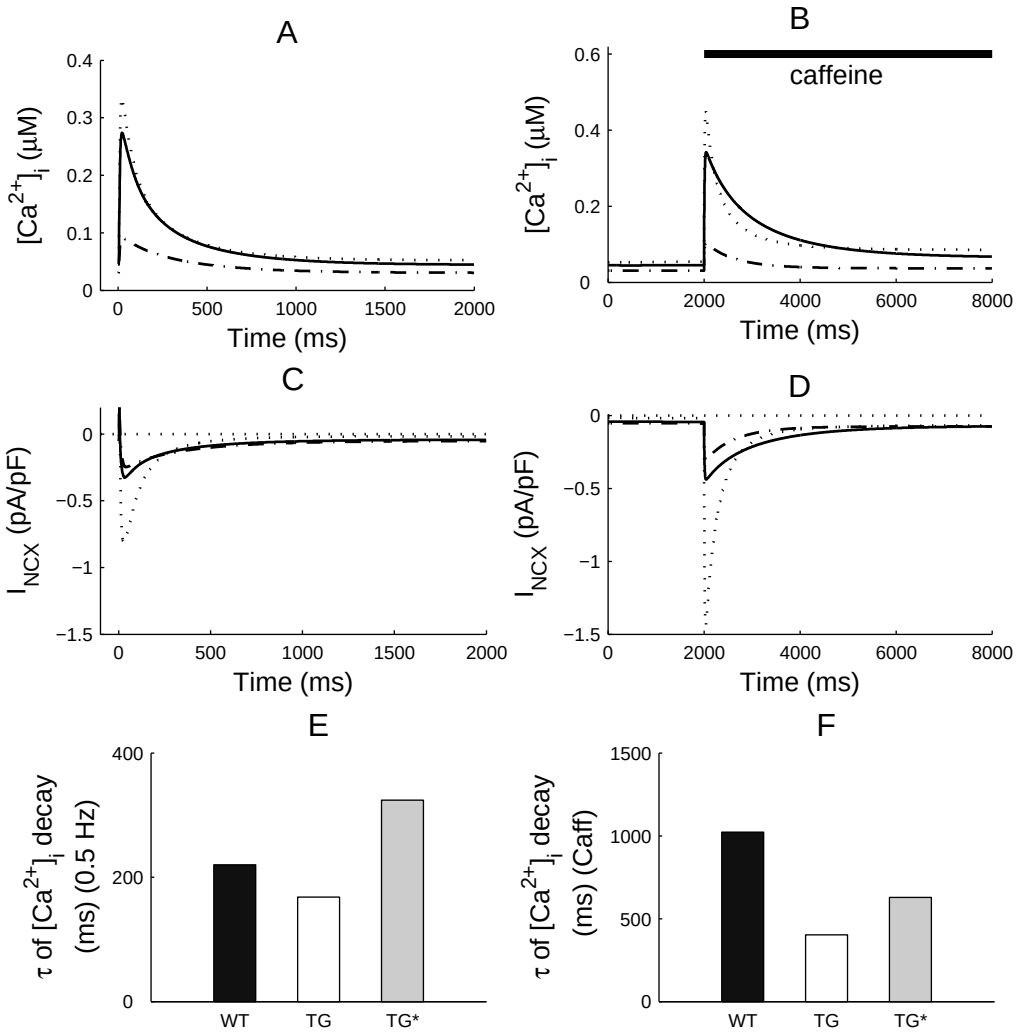

FIGURE 2.16: Simulated field-stimulated $[\mathrm{Ca}^{2+}]_\mathrm{i}$ transient and application of caffeine in the TG model. A: Simulated $[\mathrm{Ca}^{2+}]_\mathrm{i}$ transients elicited by field-stimulation at a pacing frequency of 0.5 Hz, in the WT model (solid line), the TG model (dotted line), and the TG* model (dashed line). B: Simulated $[\mathrm{Ca}^{2+}]_\mathrm{i}$ transients elicited by application of caffeine, in the WT model (solid line), the TG model (dotted line), and the TG* model (dashed line). C: Time courses of $\mathrm{I_{NCX}}$ during 0.5 Hz field stimulation, in the WT model (solid line), the TG model (dotted line), and the TG* model (dashed line). D: Time courses of $\mathrm{I_{NCX}}$ during caffeine application, in the WT model (solid line), the TG model (dotted line) and the TG* model (dashed line). E: Time constant of decay (τ) of the $[\mathrm{Ca}^{2+}]_\mathrm{i}$ transients by field-stimulation and caffeine application, in the WT model (black), the TG model (white) and the TG* model (grey). F: Simulated AP at 0.5 Hz in the WT model (solid line), the TG model (dotted line) and the TG* model (grey).

TABLE 2.5: Percentage changes of Ca^{2+} handling in TG mice relative to control. * = p $<$ 0.05 *versus* ventricular myocytes from WT. [193]: C57BL/6 mice. Heterozygous NCX over-expression. Isolated ventricular myocytes. 22^{o}C. [1]: C57BL/6 mice. Heterozygous NCX over-expression. Isolated LV myocytes. 25^{o}C. [212]: C57BL/6 mice. Heterozygous NCX over-expression. Isolated ventricular myocytes. 22^{o}C. [192]: C57BL/6 mice. Heterozygous NCX over-expression. Isolated ventricular myocytes. 37^{o}C.

		Terracciano et al. [193]	Adachi-akahane et al. [1]	Yao et al. [212]	Terracciano et al. [192]	Model
$[Ca^{2+}]_i$ transient by field-stimulation at 0.2 Hz [212], 0.5 [193] and 1 [192] Hz, or by depolarising pulses [1]	Diastolic $[Ca^{2+}]_i$	92	107	90	—	117
	$\Delta[Ca^{2+}]_i$	71	94	155	95	122
	RT_{50}	72*	—	—	67*	74
	τ	—	—	77	—	76
Caffeine-induced $[Ca^{2+}]_i$ transient	$\Delta[Ca^{2+}]_i$	—	107	79	177*	133
	Peak I_{NCX}	299*	308*	288*	252*	327
	$\int I_{NCX}$	176*	—	108	—	113
	RT_{50}	—	—	27*	—	34
	τ	—	40*	—	—	39
I-V relationship of I_{CaL}		—	97	100	—	100
I-V relationship of I_{NCX}		Significant ↑	—	—	—	2.7-fold ↑ on average at positive potentials

compared to that in the WT mice (See Table 3). Simulated peak forward mode I_{NCX} (Fig. 2.16C) during the $[Ca^{2+}]_i$ transient was 0.81 pA/pF in the TG model, compared to 0.33 pA/pF in the WT model, corresponding to a 2.5-fold increase in I_{NCX} magnitude. The decay of the $[Ca^{2+}]_i$ transient was faster in the TG model, with a 30% decrease in RT_{50} (92 *versus* 125 ms) and τ (168 *versus* 220 ms). Terracciano et al. [193] reported a 38% decrease in RT_{50}. In other studies of the TG mice, a 33% decrease in RT_{50} and a 23%

decrease in τ have been reported [192].

Simulated caffeine-induced $[Ca^{2+}]_i$ transients are shown in Fig. 2.16B. The magnitude of the $[Ca^{2+}]_i$ transient in the TG model was 0.40 μM, compared to 0.30 μM in the WT model, indicating a greater SR Ca^{2+} load in the TG model. This was in qualitative agreement with the 69$\%$ increase in caffeine-induced $[Ca^{2+}]_i$ transient magnitude reported by Terracciano et al. [193]. In other studies, some reported a 77$\%$ increase [192] while others observed no statistically significant difference in caffeine-induced $[Ca^{2+}]_i$ transient magnitude [1, 212]. Simulated peak I_{NCX} (Fig. 2.16D) during caffeine-application was 1.44 pA/pF in the TG model, compared to 0.44 pA/pF in the WT model, corresponding to a 3-fold increase in I_{NCX} magnitude. A 2-fold increase in I_{NCX} magnitude during caffeine application was reported by Terracciano et al. [193], whereas a 2.4-fold increase and a 3-fold increase have been reported in other studies. The rate of decay of the simulated caffeine-induced $[Ca^{2+}]_i$ transient was 61$\%$ faster in the TG model (τ: 402 *versus* 1022 ms). Although not quantified by Terracciano et al. [193], τ is reportedly 73$\%$ and 60$\%$ faster in the TG mice according to Yao et al. [212] and Adachi-akahane et al. [1] respectively.

Effects of Allosteric Regulation

To determine whether the presence of allosteric regulation in the canine cardiac NCX, which is absent in WT mice, plays a significant role in Ca^{2+} handling in the TG mice, we replaced the current formulation of NCX in the TG model with an alternative formulation (TG*) without allosteric regulation, i.e. V_{NCX}^{max} was set to 9.75 pA/pF to represent a 2.5-fold increase in maximum NCX activity, and all other parameters values were the same as those in the WT model. In contrast to previous observations, field-stimulated $[Ca^{2+}]_i$ transient magnitude (Fig. 2.16A) was significantly lower in the TG* model compared to the WT model (0.06 *versus* 0.23 μM). Caffeine-induced $[Ca^{2+}]_i$ transient magnitude (Fig. 2.16B) was only 23$\%$ of the level in WT (0.07 *versus* 0.30 μM) indicating a dramatic

loss of SR Ca^{2+}. Despite the increase in V_{NCX}^{max}, inward I_{NCX} magnitudes during field-stimulation (Fig. 2.16C) was lower in the TG* model during systole (0.25 *versus* 0.33 pA/pF) and slightly higher during diastole (0.052 *versus* 0.043 pA/pF). Consistent with the lower caffeine-induced $[Ca^{2+}]_i$ transient magnitude, I_{NCX} during caffeine application (Fig. 2.16D) was also lower in the TG* model (0.30 *versus* 0.44 pA/pF), reflecting a significant reduction in SR Ca^{2+} content. When comparing the rates of decay of the $[Ca^{2+}]_i$ transient, the time constant in the TG* model was longer during field-stimulation (324 *versus* 220 ms) and shorter during caffeine-application (628 *versus* 1022 ms).

2.4.3 Sensitivity Analysis of the Whole-cell Model

Using a similar approach to that for NCX parameters (Eq. 2.5), the sensitivity of important ensemble model behaviors to the estimated parameters was investigated using a sensitivity analysis with results shown in Table 2.6. We have focused on seven metrics for characterising model behaviors including diastolic $[Ca^{2+}]_i$, magnitude of the transient ($\Delta[Ca^{2+}]_i$) at 3 Hz, RT_{50} of the transient at 3 Hz, resting V_m, peak V_m during an action potential at 3 Hz, APD_{50} and APD_{90}. For each metric, y_0 was defined as the model output with the original parameter value ($y(p_0)$). Δy was defined as the change in the output due to a 5% increase in the parameter value. Simulation results were obtained after running the model for at least 100 s until limit cycle was reached.

Compared to the other estimated parameters, diastolic $[Ca^{2+}]_i$ is most sensitive to τ_{tr}, $\Delta[Ca^{2+}]_i$ to τ_{xfer} and G_{Nab}. RT_{50} is most sensitive to τ_{tr}, τ_{xfer} and k_a^-. Key AP characteristics were not found to be sensitive to any of the estimated parameters. Further investigation showed that diastolic $[Ca^{2+}]_i$ increased by 0.6% following a 5% increase in τ_{tr}. $\Delta[Ca^{2+}]_i$ decreased by 1.7% and increased by 1.5% following a 5% increase in τ_{xfer} and G_{Nab} respectively. RT_{50} decreased by 0.5%, increased by 1.2% and decreased by 0.5% following a 5% increase in τ_{tr}, τ_{xfer} and k_a^-, respectively. Therefore, while model

TABLE 2.6: Sensitivity of model ensemble behaviors to estimated parameters. Bold numbers indicate model behavior is most sensitive to these parameters.

Parameter	Diastolic $[Ca^{2+}]_i$	$\Delta[Ca^{2+}]_i$	RT_{50}	Resting V_m	Overshoot	APD_{50}	APD_{90}
v_{rel}	1.42×10^{-2}	4.05×10^{-2}	1.37×10^{-3}	2.28×10^{-5}	2.84×10^{-4}	-1.37×10^{-2}	3.95×10^{-4}
τ_{tr}	**0.126**	-6.58×10^{-2}	-0.102	-5.55×10^{-4}	-6.33×10^{-4}	6.54×10^{-3}	4.97×10^{-3}
τ_{xfer}	-4.5×10^{-2}	**-0.345**	0.244	-9.37×10^{-5}	2.07×10^{-3}	-6.50×10^{-2}	-5.87×10^{-2}
k_a^+	6.78×10^{-4}	-3.81×10^{-2}	5.12×10^{-2}	-7.35×10^{-5}	-3.73×10^{-5}	2.90×10^{-4}	-1.98×10^{-3}
k_a^-	-3.09×10^{-3}	7.33×10^{-2}	-0.108	-1.17×10^{-4}	5.59×10^{-5}	-3.52×10^{-3}	2.09×10^{-3}
k_b^+	-6.86×10^{-4}	-9.24×10^{-5}	-2.82×10^{-4}	-1.17×10^{-4}	-3.26×10^{-5}	-6.84×10^{-4}	-4.10×10^{-4}
k_b^-	7.52×10^{-4}	2.30×10^{-4}	2.73×10^{-5}	-3.04×10^{-5}	-1.86×10^{-5}	3.24×10^{-4}	2.76×10^{-6}
$k+_c$	7395×10^{-3}	6.04×10^{-3}	-6.15×10^{-2}	-1.37×10^{-4}	-1.49×10^{-4}	4.76×10^{-3}	1.96×10^{-4}
k_c^-	-8.72×10^{-3}	2.49×10^{-2}	1.74×10^{-2}	-4.05×10^{-5}	1.49×10^{-4}	-7.05×10^{-3}	1.17×10^{-4}
n	-3.56×10^{-3}	4.85×10^{-3}	1.86×10^{-2}	-4.05×10^{-5}	1.40×10^{-5}	-2.06×10^{-3}	-3.71×10^{-4}
m	-8.32×10^{-4}	-2.27×10^{-2}	2.64×10^{-2}	-6.08×10^{-5}	3.73×10^{-5}	-1.97×10^{-3}	-2.31×10^{-3}
G_{Nab}	6.73×10^{-2}	**0.300**	-4.49×10^{-2}	-2.12×10^{-2}	-3.41×10^{-2}	-7.05×10^{-2}	6.06×10^{-3}
G_{ks}	0	0	-5.93×10^{-6}	-2.79×10^{-5}	-9.31×10^{-6}	-7.80×10^{-5}	-8.03×10^{-5}
$G_{Cl,Ca}$	1.90×10^{-4}	8.97×10^{-4}	-1.99×10^{-4}	-8.11×10^{-5}	-1.19×10^{-3}	2.92×10^{-4}	-3.86×10^{-6}
$K_{m,Cl}$	-1.79×10^{-4}	-8.45×10^{-4}	1.72×10^{-4}	4.05×10^{-5}	1.08×10^{-3}	-5.95×10^{-4}	-3.29×10^{-4}
E_{CL}	9.48×10^{-5}	4.59×10^{-4}	-1.01×10^{-4}	5.83×10^{-5}	-5.87×10^{-4}	6.06×10^{-5}	-4.65×10^{-5}
$CSQN_{tot}$	-7.92×10^{-3}	4.02×10^{-2}	2.53×10^{-2}	2.89×10^{-4}	-9.92×10^{-4}	1.51×10^{-2}	-3.42×10^{-3}
K_m^{CSQN}	7.20×10^{-3}	4.09×10^{-2}	5.69×10^{-3}	-2.69×10^{-4}	7.27×10^{-4}	-1.20×10^{-2}	3.12×10^{-3}

behaviors were not found to be highly sensitive to any of these estimated parameters, they may be moderately affected by the rate of Ca^{2+} transfer from the network SR to the junctional SR, the rate of Ca^{2+} transfer from the dyadic space to cytosol, the conductance of the background Na^+ channel, and the RyR rate constant governing its transition from state O_1 to C_1.

2.5 Discussion

Species- and temperature-dependent differences in Ca^{2+} dynamics are well known. However, previous modeling studies often have the limitation of using heterogeneous experimental data to develop model components (Fig. 1), which precludes the model's potential to reliably interpret experimental observations. The first objective of this thesis, therefore, was to use consistent experimental data, whenever possible, to parameterise model components; and provide a transparent link between parameters and experimental data. All the measurements on $[\mathrm{Ca}^{2+}]_{\mathrm{i}}$ transients and $\mathrm{I}_{\mathrm{CaL}}$ were obtained in our own laboratory from LV ventricular myocytes obtained at 35°C. Other transmembrane currents and AP measurements were taken from existing literature, from murine ventricular myocytes at a temperature between 32 and 35°C.

Simulated $[\mathrm{Ca}^{2+}]_{\mathrm{i}}$ dynamics showed good agreement with experimental observations. The description of the RyR in our model was consistent with experimental observations. Firstly, graded response of Ca^{2+} release could be reproduced using our model, which showed a bell-shaped voltage-relationship with both peak $\mathrm{I}_{\mathrm{CaL}}$ and peak $[\mathrm{Ca}^{2+}]_{\mathrm{i}}$ transient occurring at around 0 mV. Secondly, increasing the open probability of the RyR units, by means of caffeine for example, produced a transient increase in $[\mathrm{Ca}^{2+}]_{\mathrm{i}}$ transient which returned gradually to control level, similar to that observed experimentally by Eisner et al. [54]. Net sarcolemmal flux and SR Ca^{2+} content also followed the same changes as those described by Eisner et al. [54], i.e. a transient net sarcolemmal Ca^{2+} efflux led to a sustained loss of SR Ca^{2+} content which reset the balance point of Ca^{2+} dynamics after caffeine application.

In order to achieve temperature consistency across different model components, we have also re-fitted the K^{+} and Na^{+} channels to experimental data at physiological temperatures close to 35°C. Experimentally measured AP shape and duration were used

to validate the fitting process. There was good agreement in AP characteristics between simulation and experimental data, including resting potential, overshoot, maximum upstroke velocity and AP durations to 25, 50 and 90% repolarisation. With increasing cycle length, steady-state APD increases in agreement with observations made by other groups [9, 106, 189]. This was shown to be strongly affected by the presence of the NCX current in our model, which was also seen experimentally [104]. Therefore our model is capable of representing the interactions and feedback loops between Ca^{2+} dynamics and sarcolemmal electrophysiology at physiological pacing frequencies and temperatures under steady state conditions.

The second aim of this section of work was to apply our model to investigate the effects of heterozygous over-expression of canine NCX in transgenic mice. It is worth noting that the more recent findings by Weber et al. [206] on allosteric regulation are not fully consistent with those reported previously by Maxwell et al. [136], who observed allosteric $[\mathrm{Ca}^{2+}]_{\mathrm{i}}$ regulation of NCX in both the control and transgenic mice. This indicates that the lack of $[\mathrm{Ca}^{2+}]_{\mathrm{i}}$ regulation observed by Weber et al. [206] in wild-type preparations may be due to species- and/or preparation-dependent differences. However, as the study by Weber et al. [206] was conducted under more physiological conditions (in intact myocytes and allowing dynamic $[\mathrm{Ca}^{2+}]_{\mathrm{i}}$ regulation) compared to previous measurements obtained in membrane patches, we have parameterised the current models based on their measurements.

Our simulations results from the TG model were consistent with the experimentally observed 2.7-fold increase in NCX activity [1, 192, 193, 212], assessed from the current-voltage relationship and the rate of decay of the caffeine-induced $[\mathrm{Ca}^{2+}]_{\mathrm{i}}$ transient. At the pacing frequency of 0.5 Hz, simulated $[\mathrm{Ca}^{2+}]_{\mathrm{i}}$ transient magnitude in the TG model was 18% greater compared with the WT model with a 22% faster rate of $[\mathrm{Ca}^{2+}]_{\mathrm{i}}$ decay, and a 27% increase in SR Ca^{2+} load. These results were in agreement with experimental

studies [1, 192, 193, 212].

No difference in the time course of I_{CaL} was observed between the WT and TG models stimulated at 0.5 Hz (not shown here), so the total amounts of Ca^{2+} entry through sarcolemma are the same between WT and TG models. The balance of Ca^{2+} entry and extrusion over each heartbeat therefore requires that Ca^{2+} extrusion through NCX should also be the same in the two models. Indeed, our calculations of the integral of J_{NCX} showed the same amounts of Ca^{2+} extrusion. This has occurred despite the over 2-fold increase in the magnitude of J_{NCX} in the TG model, which was compensated by a lower diastolic J_{NCX}. The reason behind the decrease in J_{NCX} during diastole was not a lower diastolic $[Ca^{2+}]_i$, as diastolic $[Ca^{2+}]_i$ was in fact slightly higher in the TG model at 0.5 Hz. But this may be explained by the presence of allosteric regulation by $[Ca^{2+}]_i$ in the TG mice, which has not been found in the WT mice [206]. According to the NCX formulation, with an estimated K_{mAllo} of 0.15 μM [206] and an diastolic $[Ca^{2+}]_i$ of 0.05 μM in our models, the maximum exchange rate of NCX could be as low as a tenth of V_{NCX}^{max} during diastole in the TG model. However, during systole when $[Ca^{2+}]_i$ is high, the maximum exchange rate approaches V_{NCX}^{max} so peak I_{NCX} is considerably higher in the TG model.

The less competitive diastolic J_{NCX} and the higher diastolic $[Ca^{2+}]_i$ promote Ca^{2+} uptake into the SR through SERCA. This means that more Ca^{2+} is available for CICR and hence a higher $[Ca^{2+}]_i$ transient magnitude in the TG model. The greater $[Ca^{2+}]_i$ transient magnitude in turn facilitates SR Ca^{2+} uptake, the consequences of which are two-fold. Firstly, higher J_{SERCA} along with the enhanced systolic J_{NCX} results in a faster decay of the $[Ca^{2+}]_i$ transient. Secondly, it increases the relative contribution of SERCA and hence decreases that of NCX in the TG model. Although a difference in diastolic $[Ca^{2+}]_i$ has not been detected experimentally [1, 193, 212], Terracciano et al. [193] speculated that a slightly higher diastolic $[Ca^{2+}]_i$ would promote SR uptake and SR Ca^{2+} loading in the

TG mice, although the difference might be smaller than can be measured.

In contrast with the increased $[Ca^{2+}]_i$ transient magnitude and SR Ca^{2+} load, and the faster decay kinetics of $[Ca^{2+}]_i$ both during field-stimulation and caffeine-application observed in the TG model, results from the TG* model show different characteristics of Ca^{2+} handling. When allosteric regulation was removed, the enhanced NCX activity alone caused significantly decreased $[Ca^{2+}]_i$ transient magnitude and SR Ca^{2+} content compared with the WT model. This occurs as J_{NCX} is enhanced during both diastole and systole in the absence of allosteric regulation, therefore shifting the balance away from SR Ca^{2+} uptake and towards sarcolemmal Ca^{2+} extrusion. This in turn leads to a net loss of Ca^{2+} and a lowered systolic $[Ca^{2+}]_i$ to a point where sarcolemmal Ca^{2+} influx and efflux are again in balance. The decrease in $[Ca^{2+}]_i$ transient magnitude also decreases J_{SERCA} such that the rate of decay of the $[Ca^{2+}]_i$ transient is slightly slower in the TG* model during 0.5 Hz field stimulation. The above simulation results suggest the presence of allosteric regulation in the canine cardiac NCX could be a key factor underlying the observed increases in $[Ca^{2+}]_i$ transient magnitude and SR Ca^{2+} content in the TG mice.

Chapter 3

Calcium Dynamics in the Ventricular Myocytes of SERCA2 KO Mice: A Modelling Study

3.1 Introduction

As discussed in the Chapter 1, disruption to $[\mathrm{Ca}^{2+}]_{\mathrm{i}}$ homeostasis resulting from abnormalities in Ca^{2+} handling is believed to be an important mechanism underlying HF [62, 161, 84, 121, 157]. In particular, decreases in the expression level of SERCA and thus SR Ca^{2+} transport have been reported in both animals models with pressure overload-induced hypertrophy [62, 161] and in failing human myocardium [84, 121, 157]. In this chapter, we apply the C57BL/6 model framework developed in Chapter 2 to investigate the genetically modified mouse model with cardiomyocyte-specific, conditional excision of the *Serca2* gene [4].

Global knockout of *Serca2* has previously been shown to be lethal [154]. On the other hand, genetically modified mice, in which cardiomyocyte-specific excision of the *Serca2* gene can be induced at any age, allow investigation into the effects of major reduction

in SERCA2 expression with more specificity. Data from this experimental model shows that at 4 weeks following gene excision (KO), cardiac function was only moderately impaired compared to the *Serca2*$^{flox/flox}$ (FF) control despite a reduction in SERCA2 protein expression level to less than 5% of normal values. Given that SR Ca^{2+} uptake in healthy controls accounts for over 90% of Ca^{2+} removal in the mouse heart under physiological conditions [116], these findings have sparked significant debate over how these animals can survive with such a dramatic reduction in SERCA function [197]. It has been hypothesized that enhanced Ca^{2+} fluxes through LCCs, NCX and PMCA act as compensatory mechanisms in the KO myocytes to shift the reliance of the $[\mathrm{Ca}^{2+}]_{\mathrm{i}}$ transient generation from SR Ca^{2+} release to sarcolemmal Ca^{2+} fluxes [4]. However, whether all of these compensatory changes are crucial and their relative contributions in maintaining cardiac function remain to be fully investigated. Furthermore, while the rate of decay of the $[\mathrm{Ca}^{2+}]_{\mathrm{i}}$ transient in the KO is significantly slower compared to FF at a low pacing frequency (1 Hz), it is only minimally affected at physiologically relevant pacing rates [4]. These observations motivate further investigation to elucidate the mechanisms underpinning Ca^{2+} handling in both the FF and KO animal models.

Trafford [197] has conducted a preliminary simulation study using the Bondarenko et al. murine AP model [27]. Simulation results showed an increased diastolic $[\mathrm{Ca}^{2+}]_{\mathrm{i}}$, a decreased rate of decay of the $[\mathrm{Ca}^{2+}]_{\mathrm{i}}$ transient which became less profound at higher frequencies, and finally a prolonged action potential [197]. However, Trafford assumed a simple linear correlation between the expression and activity of the proteins, an assumption which deserves further validation. It is also worth noting that the Bondarenko model [27] was developed based on experimental data obtained at room temperature (25 ^{o}C), while the study on SERCA2 KO mice [4] was carried out at 37 ^{o}C. The formulation of Ca^{2+} dynamics in the Bondarenko model [27] was derived from a previous model of guinea-pig ventricular myocytes [98], which assumes constant SERCA uptake rate at different frequencies, and hence does not account for FDAR observed experimentally in

both FF and KO mice (see below). Thus while mathematical modelling provides a potentially promising and quantitative framework for analysing the mechanisms underlying the observed Ca^{2+} handling, for the reasons outlined above, the characteristics of the $[\mathrm{Ca}^{2+}]_{\mathrm{i}}$ transients simulated using the Bondarenko model are unlikely to be a good representation of those observed experimentally by Andersson et al.[4].

Here, we have re-parameterised the model of Ca^{2+} dynamics developed in Chapter 2 to experimental measurements obtained from the FF and KO cardiomyocytes, to enable direct comparison between simulation results and experimental data. Using this model, we examine the underlying changes in Ca^{2+} handling and the relative contributions of the compensatory mechanisms present in the SERCA2 KO mice.

3.2 Materials and Methods

All experimental measurements described below were provided by collaborators, Louch W. E., Andersson, K. B., Christensen, G. and Sejersted, O.M., from the Institute for Experimental Medical Research, Oslo University Hospital Ullevål in Norway [117].

All animal use was approved by the Norwegian National Committee for Animal Welfare under the Norwegian Animal Welfare Act, which conforms to the *Guide for the Care and Use of Laboratory Animals* published by the US National Institutes of Health (NIH publication No. 85-23, revised 1996). The *Serca2*$^{flox/flox}$ Tg(αMHC-MerCreMer) mouse (KO) was employed, which allows for inducible, cardiomyocyte-specific disruption of the *Serca2* gene in adult mice [4]. *Serca2* gene excision in 8-10 week old mice was accomplished by inclusion of taxomifen base powder (RM1 FG SQC, 811004, Scanbur BK) in the feed (100mg/200 g) for 7 days [6, 125]. *Serca2*$^{flox/flox}$ mice (FF) served as controls [4, 5]. Tamoxifen administration triggers *Serca2* gene excision exclusively in the cardiomyocytes of KO animals [4]. Hearts were harvested at 4 weeks following tamoxifen

treatment.

3.2.1 Cardiomyocyte Experiments

Cardiomyocytes were enzymatically isolated [4, 126], plated on laminin-coated coverslips, and placed in a perfusion chamber on the stage of an inverted microscope. $[\mathrm{Ca}^{2+}]_{\mathrm{i}}$ transient measurements were recorded in fluo-4 AM (Invitrogen Molecular Probes, Eugene,OR, USA) loaded myocytes during field stimulation (3 ms biphasic pulse, 25% above threshold). Cells were perfused with HEPES Tyrode solution containing (in mM): 140 NaCl, 1 $CaCl_2$, 0.5 $MgCl_2$, 5.0 HEPES, 5.5 glucose, 0.4 NaH2PO4 and 5.4 KCl (pH 7.4, 37^{o}C), and an LSM 510 microscope (Zeiss GmbH, Jena, Germany) was used to record $[\mathrm{Ca}^{2+}]_{\mathrm{i}}$ transients in line-scan mode [126].

Patch-clamp experiments were conducted with an Axoclamp 2B amplifier (Axon Instruments, Foster City, CA, USA), pCLAMP software (Axon Instruments), and low resistance pipettes (1-2 MΩ). $\mathrm{I}_{\mathrm{CaL}}$ was recorded during 200 ms voltage steps from -50 mV to a range of potentials, with an internal solution containing (in mM) 130 CsCl, 0.33 $MgCl_2$, 4 Mg-ATP, 0.06 EGTA, 10 HEPES, and 20 TEA, and an extracellular solution containing (in mM) 20 CsCl, 1 $MgCl_2$, 135 NaCl, 10 Hepes, 10 D-glucose, 4 4-aminopyridine, and 1 $CaCl_2$ [4, 125]. Diastolic $[\mathrm{Ca}^{2+}]_{\mathrm{i}}$ was measured by whole-cell photometry (Photon Technology International, Monmouth Junction, NJ) in cells pipette-loaded with a solution containing (in mM): 0.1 fura-2 salt (Invitrogen Molecular Probes), 120 K-aspartate, 0.5 $MgCl_2$, 10 NaCl, 0.06 EGTA, 10 HEPES, 10 glucose, 25 KCl and 4 K_2-ATP (pH 7.2) [4, 125]. Fura-2 fluorescence ratios (F_{340}/F_{380}) were calibrated to $[\mathrm{Ca}^{2+}]_{\mathrm{i}}$, and calculated diastolic values were then used to calibrate $[\mathrm{Ca}^{2+}]_{\mathrm{i}}$ transients recorded in fluo-4 loaded cells [4, 125, 36].

SR Ca^{2+} content was measured by rapidly switching the extracellular solution to one

containing 10 mM caffeine, and measuring either the magnitude of the elicited $[Ca^{2+}]_i$ transient or the integral of the elicited Na^+-Ca^{2+} exchange current [4, 125]. The SR-dependent component of the $[Ca^{2+}]_i$ transient was estimated by comparing the magnitude of $[Ca^{2+}]_i$ transients in the presence and absence of caffeine [4, 125].

3.3 Model Derivation

Similar to the methods presented in Chapter 2, MATLAB (The MathWorks, Matick, MA) was used for all data analysis and parameter fitting. Intracellular Ca^{2+} buffering was accounted for using Eq. 2.4, as proposed by Trafford et al. [196]. Paramaterisation for NCX and PMCA followed the same approach as presented in Chapter 2. Briefly, parameters for sarcolemmal Ca^{2+} fluxes, i.e. fluxes through NCX (J_{NCX}) and PMCA (J_{PMCA}), were fitted to the decay phase of the caffeine-induced $[Ca^{2+}]_i$ transient following field-stimulation at 1 Hz. The relative contributions of NCX and PMCA to sarcolemmal Ca^{2+} removal ($J_{sarcolemma}$) were determined based on previously published experimental observations by Li et al. [116]. In indo 1-AM loaded mouse ventricular myocytes, using caffeine to block SR Ca^{2+} uptake and Na^+ and Ca^{2+}-free solution to block Ca^{2+} extrusion via NCX, and by analysing the rate constants of decay of the $[Ca^{2+}]_i$ transients, the fractions of Ca^{2+} removed from the cytosol via SERCA, NCX and the slow mechanisms (PMCA and mitochondria) were estimated to be 90.3, 9.2 and 0.5% respectively, or alternatively NCX and PMCA contributed to approximately 95 and 5% of sarcolemmal Ca^{2+} extrusion. Because indo 1 compartmentalisation was thought to cause a possible underestimation of the slow mechanisms of Ca^{2+} extrusion, the above analysis was repeated using twitch relaxation data estimating the contributions of NCX and PMCA to be approximately 74 and 26% respectively [116]. Based on these observations, we assigned 80 and 20% of $J_{sarcolemma}$ to J_{NCX} and J_{PMCA} respectively.

For fitting the KO data, a slight modification was introduced to account for the

suspected change in the percentage contributions of NCX and PMCA to the sarcolemmal Ca^{2+} flux in the KO cardiomyocytes. Specifically, we set the maximum rate of J_{PMCA} in the KO model to be 145% of the fitted FF value, consistent with the percentage increase in its protein expression level observed experimentally. The affinity of PMCA to Ca^{2+} was assumed to be unchanged. The difference between $J_{sarcolemma}$ and the estimated J_{PMCA}, during the caffeine-induced $[Ca^{2+}]_i$ transient, was then attributed to J_{NCX} and used to fit the model of NCX.

Fig. 3.1 shows the process of parameterisation of NCX in the FF and KO models. Representative caffeine-induced $[Ca^{2+}]_i$ transients recorded in the FF and KO cardiomyocytes are shown in Fig. 3.1A. The experimentally calculated $J_{sarcolemma}$ and the corresponding fitted $J_{sarcolemma}$ are plotted as a function of $[Ca^{2+}]_i$ in Fig. 3.1B. Using the fitted parameter values for NCX and PMCA, the decay of the $[Ca^{2+}]_i$ transients have been calculated and superimposed onto the experimental measurements in Fig. 3.1A. Our analysis of the decay of the caffeine-induced $[Ca^{2+}]_i$ transients showed that for the same level of $[Ca^{2+}]_i$, $J_{sarcolemma}$ was significantly greater in the KO compared to the FF. Based on the assumptions that NCX and PMCA contributed to 80 and 20% of Ca^{2+} extrusion respectively in the FF and that the functional activity of PMCA was increased by 45% in the KO equivalent , the fitted value for the maximum exchange rate of NCX (V_{NCX}^{max}) increased from 1.06 pA/pF in the FF Model to 3.63 pA/pF in the KO model, consistent with our previous finding of an increased NCX activity in the KO cardiomyocyte. This corresponded to a 3.5-fold increase in the functional activity of NCX. Other fitted parameters governing the exchanger activity were not found to be significantly different from the FF model and thus were assumed to remain unchanged.

The fitted NCX and PMCA parameters were then used to predict $J_{sarcolemma}$ during field-stimulations at 1 and 6 Hz. $[Na^+]_i$ was set to be 10 and 15 mM at 1 and 6 Hz respectively, based on simulation results using the C57BL/6 model and are within the range of

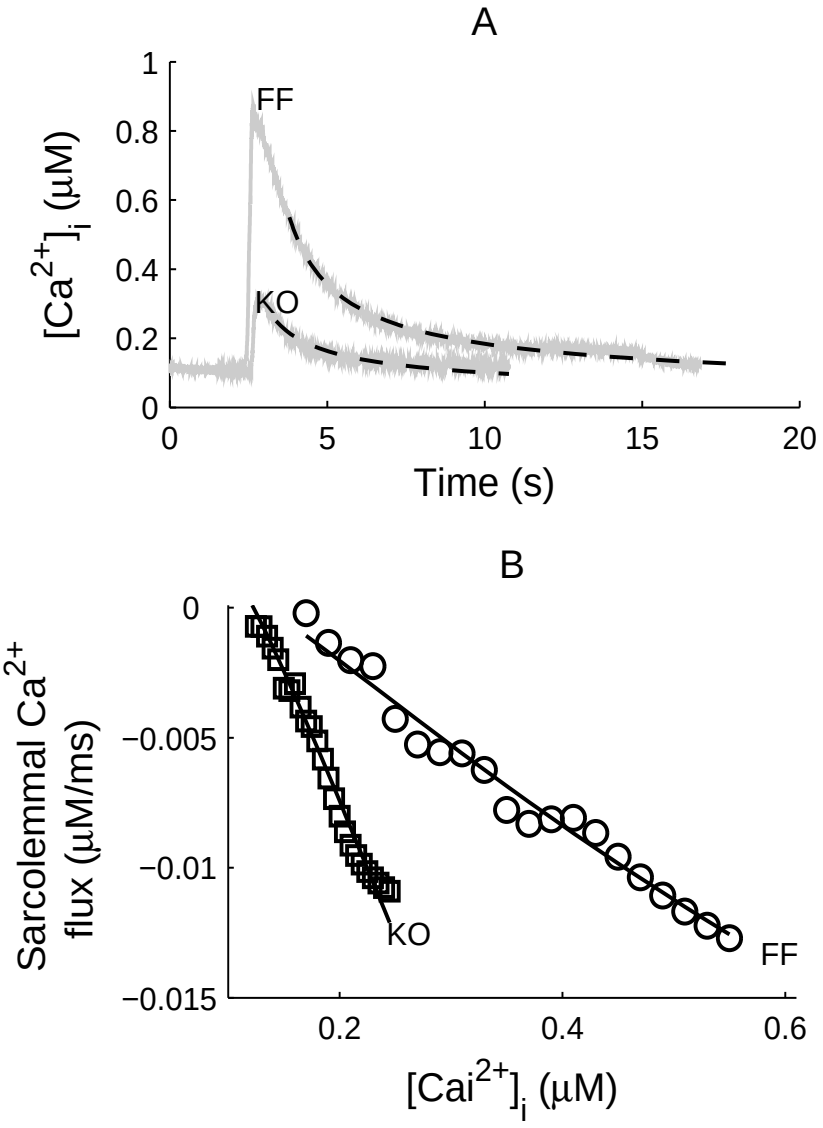

FIGURE 3.1: Parameterisation of NCX in the FF and KO models. A: Average experimentally recorded caffeine-induced $[\mathrm{Ca}^{2+}]_\mathrm{i}$ transients in isolated ventricular myocytes from the SERCA2 FF and KO mice as indicated. Simulated decay of the $[\mathrm{Ca}^{2+}]_\mathrm{i}$ transients (dashed lines) using the fitted parameter values for NCX and PMCA are superimposed. B: The experimentally calculated total fluxes of Ca^{2+} through the sarcolemma ($\mathrm{J}_\mathrm{sarcolemma}$) plotted as a function of $[\mathrm{Ca}^{2+}]_\mathrm{i}$ obtained from the FF myocytes (circles) and KO myocytes (squares). The fitted $\mathrm{J}_\mathrm{sarcolemma}$ in the FF model (solid line) and KO model (dashed line) are superimposed.

published experimental values [212]. During the late phase (90 ms and 60 ms post-peak at 1 Hz and 6 Hz respectively) of the decay of the field-stimulated $[\mathrm{Ca}^{2+}]_\mathrm{i}$ transient, net Ca^{2+} uptake through SERCA ($\mathrm{J}_\mathrm{SERCA}$) was calculated as the difference between total

Ca^{2+} flux (J_{total}) and the predicted $J_{sarcolemma}$, which was then used to fit the maximum uptake rate of SERCA (V_{up}), the Ca^{2+} affinity of the pump ($K_{m,up}$) and the SR Ca^{2+} leak flux (J_{leak}), yielding values of 0.162 μM/ms, 0.322 μM and 0.0088 μM/ms, respectively, at 1 Hz. The RMSD between fitted and measured J_{SERCA} was 3.04 $\times$ 10^{-4} μM/ms. The rate of SR Ca^{2+} leak (V_{leak} = 2 $\times$ 10^{-5} ms^{-1}) in the model was then set such that SR Ca^{2+} leak flux in the whole-cell simulation was at the same level as the estimated J_{leak}.

At 6 Hz, J_{SERCA} was found to be significantly greater compared to 1 Hz, given the same level of $[Ca^{2+}]_i$. To account for FDAR, V_{up} was re-fitted while setting $K_{m,up}$ to be the same as 1 Hz and J_{leak} (0.02 μM/ms) to be the simulated level when the model was paced at 6 Hz, yielding a V_{up} of 0.42 μM/ms with an RMSD of 1.2 $\times$ 10^{-3} μM/ms. $K_{m,up}$ was assumed to remain unchanged at different pacing frequencies, based on the recently published finding that FDAR is a result of an increase in V_{up} without a change in its affinity to Ca^{2+} [156].

Similarly for the KO at 1 and 6 Hz, V_{up} had fitted values of 0.078 and 0.23 μM/ms respectively. J_{leak} had values of 0.0084 and 0.023 μM/ms respectively (V_{leak} = 6 $\times$ 10^{-3} ms^{-1}). Including $K_{m,up}$ in the fitting process at 1 Hz did not improve the quality of the fit (RMSD = 5.74 $\times$ 10^{-6} μM/ms *versus* 5.88 $\times$ 10^{-6} μM/ms for free $K_{m,up}$ *versus* fixed $K_{m,up}$). Therefore, $K_{m,up}$ (0.322 μM) was assumed to be unchanged between the FF and KO in the final model. The increase in V_{up} with increasing frequency was then incorporated into our framework using a simple phenomenological model of the CaMKII-regulatory pathway as previously [118], for both the FF and KO models, using Eqs. 2.15-2.16.

The process of parameterising SERCA in the FF and KO models is shown in Fig. 3.2. Representative recordings of $[Ca^{2+}]_i$ transients, paced at 1 and 6 Hz, are shown in Fig. 3.2A and C, respectively. The corresponding fluxes of Ca^{2+} through SERCA (J_{SERCA})

at 1 and 6 Hz are shown in Fig. 3.2B and D, respectively. At 1 Hz, J_{SERCA} in the KO cardiomyocytes was measurable over only a limited range of $[Ca^{2+}]_i$ due to the small magnitude of its $[Ca^{2+}]_i$ transient. For the same level of $[Ca^{2+}]_i$, J_{SERCA} in the KO was on average 67% lower than the FF value at 1 Hz (Fig. 3.2B inset). During parameterisation, the reduction in J_{SERCA} was found to be associated with an over 60% decrease in V_{up} and an increase in V_{leak} consistent with the increased Ca^{2+} spark frequency observed experimentally in the KO at an earlier time point [187]. No significant difference was found in $K_{m,up}$, i.e. allowing $K_{m,up}$ to change between the FF and KO did not improve the quality of the fit. Therefore, $K_{m,up}$ was assumed to be unchanged. At the higher pacing frequency of 6 Hz, J_{SERCA} increased approximately threefold in both the FF and KO, indicating that FDAR is present in both experimental models. The decay of the $[Ca^{2+}]_i$ transients predicted from the model using the fitted values of SERCA, NCX and PMCA were superimposed to the experimental recordings in Fig. 3.2A and C.

The formulation for I_{CaL} was parameterised based on the I-V relationship and the time course of the current during a voltage clamp at -10 mV. The time to half inactivation of the simulated I_{CaL} during a voltage clamp at -10 mV was 4.09 ms in the FF model and 8.89 ms in the KO model, compared to the experimental values of 4.79 $\pm$ 0.26 and 9.10 $\pm$ 0.84 ms in the FF and KO cardiomyocytes respectively. The integrals of the aforementioned simulated currents were 0.092 and 0.23 pC/pF in the FF and KO models respectively, compared to 0.105 $\pm$ 0.0006 and 0.205 $\pm$ 0.02 pC/pF in the FF and KO cardiomyocytes measured experimentally. The simulated and experimentally measured I-V relationship of the I_{CaL} for test potentials between -40 and 60 mV are shown in Fig. 3.3A. It can be seen that at test potentials between -20 and 20 mV, peak I_{CaL} current density during voltage clamp was greater in magnitude in the KO myocytes compared to the FF. The simulated and experimentally recorded time courses of the current at -10 mV test potential are shown in Fig. 3.3B.

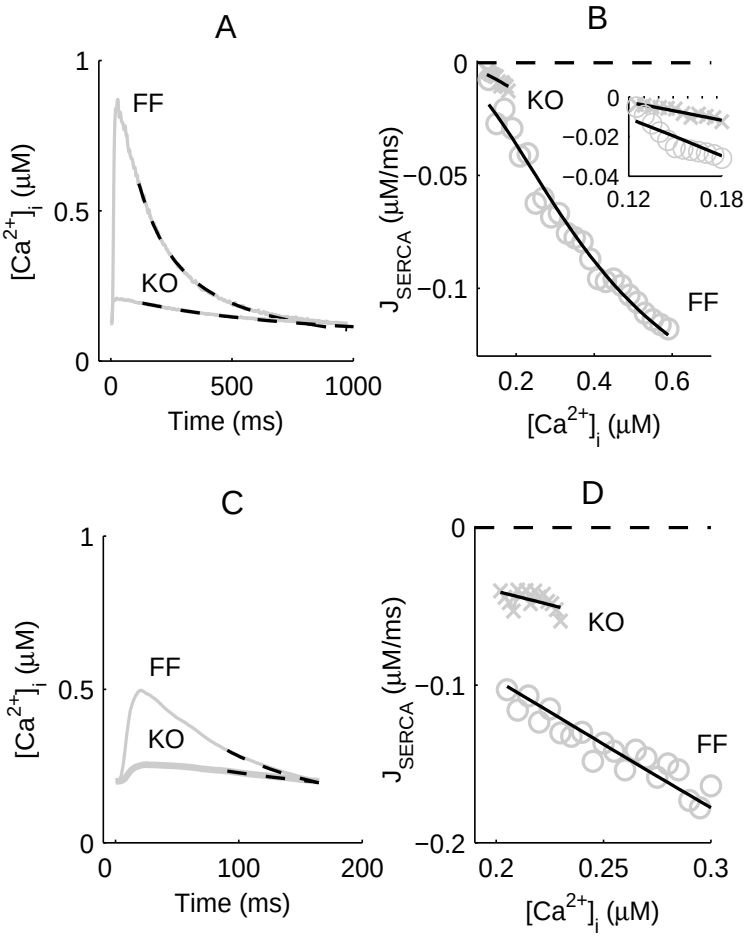

FIGURE 3.2: Parameterisation of SERCA in the FF and KO models. A: Average experimentally recorded $[\mathrm{Ca}^{2+}]_\mathrm{i}$ transients, paced at 1 Hz, in isolated ventricular myocytes from the SERCA2 FF and KO mice as indicated. Simulated decay of the $[\mathrm{Ca}^{2+}]_\mathrm{i}$ transients (dashed lines) using the fitted parameter values for SERCA (1 Hz), NCX and PMCA are superimposed. B: Ca^{2+} flux through SERCA ($\mathrm{J_{SERCA}}$) at 1 Hz, plotted as a function of $[\mathrm{Ca}^{2+}]_\mathrm{i}$, for FF (circles) and KO (crosses) mice. Fitted ($\mathrm{J_{SERCA}}$) are superimposed. Inset: an enlarged view comparing SERCA activity in the KO and FF. C: Average experimentally recorded $[\mathrm{Ca}^{2+}]_\mathrm{i}$ transients, paced at 6 Hz, in isolated ventricular myocytes from the SERCA2 FF and KO mice as indicated. Simulated decay of the $[\mathrm{Ca}^{2+}]_\mathrm{i}$ transients (dashed lines) using the fitted parameter values for SERCA (6 Hz), NCX and PMCA are superimposed. D: Ca^{2+} flux through SERCA ($\mathrm{J_{SERCA}}$) at 6 Hz, plotted as a function of $[\mathrm{Ca}^{2+}]_\mathrm{i}$, for FF (circles) and KO (crosses) mice. Fitted ($\mathrm{J_{SERCA}}$) are superimposed.

The Ca^{2+} dynamics models for the FF and KO cardiomyocytes described above were then coupled with the sarcolemmal ionic currents from the C57BL/6 model framework introduced in Chapter 2. A list of all the parameters and their values are provided in the

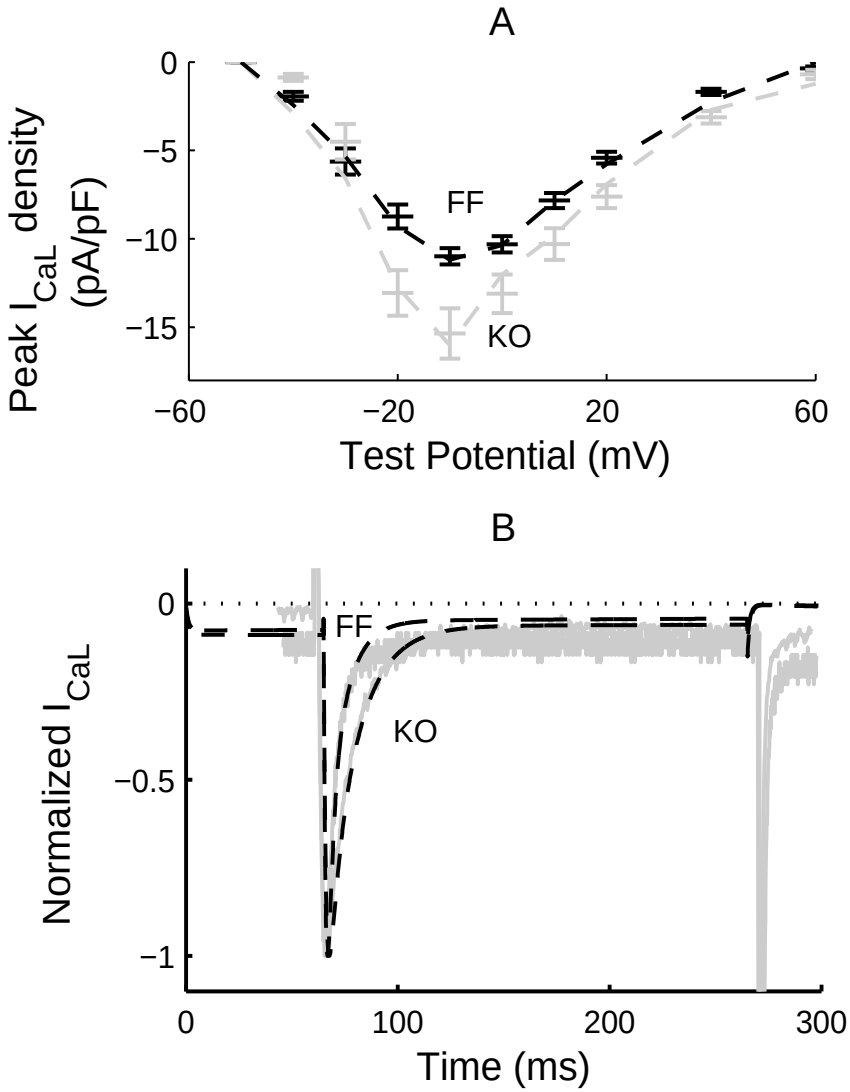

FIGURE 3.3: Parameterisation of I_{CaL}. A: Experimentally recorded current-voltage relationship of I_{CaL} for test potentials between -40 and 60 mV (see section 3.2) in the FF (black) and KO (grey) myocytes. The fitted I-V relationship (dotted lines) is superimposed. B: The time courses of the I_{CaL} at the test potential of -10 mV, showing slower inactivation kinetics with SERCA2 KO with the time constant (τ) of decay increasing from 5.5 ms in the FF myocytes to 12.8 ms in the KO myocytes. The fitted time courses (dotted lines) are superimposed.

Appendices.

3.4 Results

3.4.1 Model Validation

To validate the models, we compared simulation results with experimentally measured field-stimulated $[Ca^{2+}]_i$ transients, caffeine-induced $[Ca^{2+}]_i$ transients and experimentally estimated SR function. For all simulation results, the model was run for at least 100 s or until the limit cycle was reached.

Experimentally measured $[Ca^{2+}]_i$ transients in the FF and KO myocytes at pacing frequencies of 1 and 6 Hz (Fig. 3.4A and C) were compared with simulation results at these frequencies (Fig. 3.4B and D). Key characteristics are summarised in Table 3.1. At 1 Hz, simulated diastolic $[Ca^{2+}]_i$ in the FF and KO models were similar, consistent with experimental measurements. $\Delta[Ca^{2+}]_i$ was decreased in the KO model by 88% and RT_{50} increased by 105% from the FF values, compared with changes of 85 and 118% measured experimentally. At 6 Hz, simulated diastolic $[Ca^{2+}]_i$ in the FF and KO models were again very similar, consistent with experimental measurements. Simulated $\Delta[Ca^{2+}]_i$ in the KO model was decreased by 74% from the FF value, compared to 75% measured experimentally. This was paralleled by an increased RT_{50} in both the model and experimental measurements (30% and 20% increase, respectively). It is worth noting that at the more physiological frequency of 6 Hz, the decrease in the rate of decay of the $[Ca^{2+}]_i$ transient in the KO model was less pronounced than at 1 Hz, as indicated by the significantly smaller percentage change in RT_{50} between KO and FF models. Simulated SR Ca^{2+} contents in the KO and FF models at 0.5 Hz were 8.2 and 61.0 μmol per L cytosol, respectively, corresponding to a 87% reduction in SR Ca^{2+} loading. This was consistent with the 87% reduction in the magnitude of the caffeine-induced $[Ca^{2+}]_i$ transient observed experimentally in the KO cardiomyocytes.

TABLE 3.1: Comparison between experimental measured and simulated $[Ca^{2+}]_i$ transients

$[Ca^{2+}]_i$ Transient Characteristics	FF Experiment	FF Model	KO Experiment	KO Model
Magtnidue at 1 Hz (μM)	0.786 ± 0.145	0.720	0.098 ± 0.031	0.090
Magtnidue at 6 Hz (μM)	0.290 ± 0.029	0.323	0.066 ± 0.007	0.085
Diastolic $[Ca^{2+}]_i$ at 1 Hz (μM)	0.139 ± 0.024	0.110	0.127 ± 0.014	0.128
Diastolic $[Ca^{2+}]_i$ at 6 Hz (μM)	0.204 ± 0.036	0.219	0.190 ± 0.025	0.207
Time to half decay at 1 Hz (ms)	131 ± 10	128	285 ± 18	269
Time to half decay at 6 Hz (ms)	54 ± 1	48	65 ± 2	60

The contribution of the SR to the $[Ca^{2+}]_i$ transient can be estimated experimentally from the difference in the magnitudes of the transients before and during sustained caffeine treatment. By this method, the contribution of SR to the transient was estimated to be 88% in the FF cardiomyocytes and 30% in the KO cardiomyocytes at 0.5 Hz. In our model, SR contribution could be calculated more directly as the ratio between the integral of J_{SERCA} and the integral of the sum of the removal fluxes through SERCA, NCX and PMCA over one cardiac cycle. The integral of these Ca^{2+} removal fluxes at 0.5 Hz are shown in Fig. 3.4 E-G. The percentage contribution of SERCA to Ca^{2+} removal was 86% in the FF model and 36% in the KO model, consistent with experimental estimates. The contributions of NCX in the FF and KO models were 12% and 58% respectively, while the contributions of PMCA were 2% and 6% respectively.

3.4.2 Quantitative Analysis of Changes in Calcium Handling with SERCA2 KO

Simulated APs elicited by field-stimulations at 1 and 6 Hz are plotted in Fig. 3.5A and B, respectively. At the lower pacing frequency of 1 Hz, there was a slight prolongation in late repolarisation in the KO model, APD_{90} repolarisation equal to 24.4 ms, compared

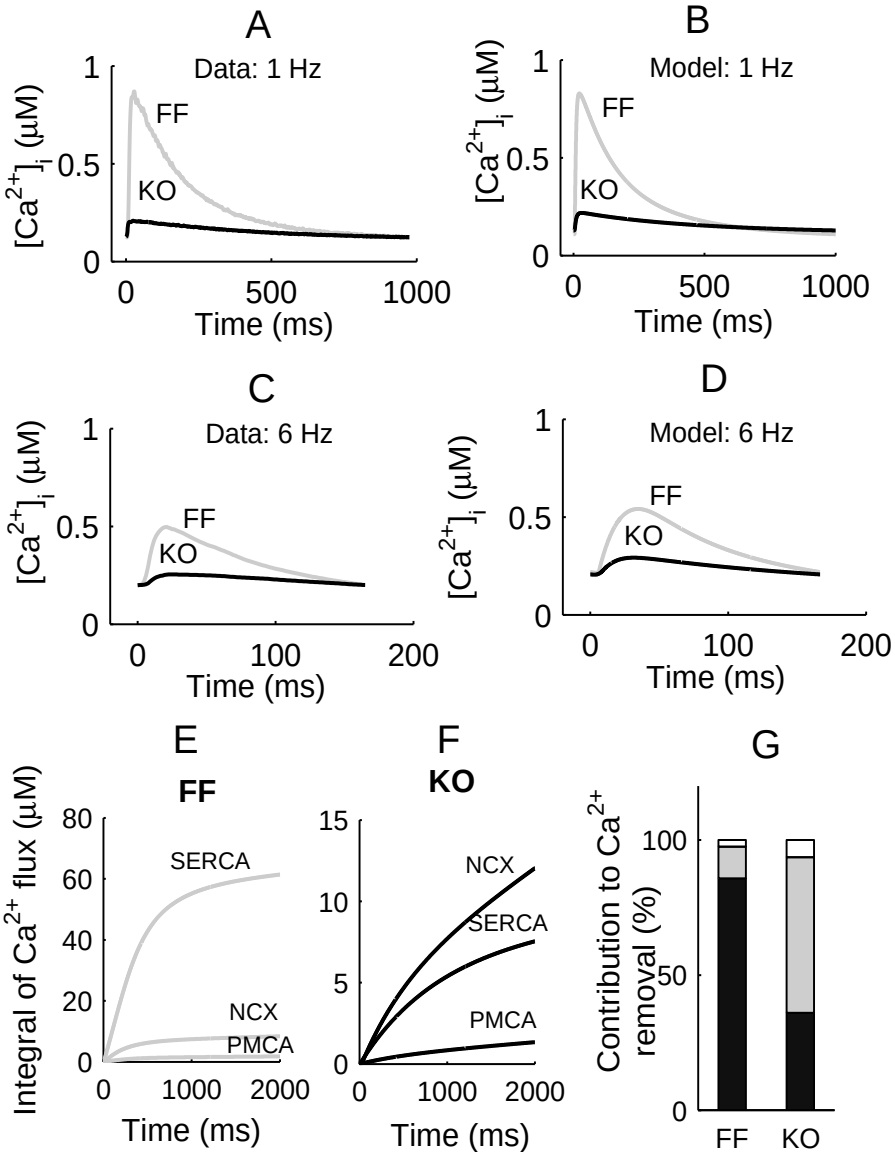

FIGURE 3.4: Comparison between experimentally measured and simulated $[\mathrm{Ca}^{2+}]_\mathrm{i}$ transients. A: Average experimentally measured $[\mathrm{Ca}^{2+}]_\mathrm{i}$ transients at 1 Hz in the FF (grey) and KO (black) myocytes. B: Simulated $[\mathrm{Ca}^{2+}]_\mathrm{i}$ transients at 1 Hz in the FF (grey) and KO (black) models. C: Average experimentally measured $[\mathrm{Ca}^{2+}]_\mathrm{i}$ transients at 6 Hz in the FF (grey) and KO (black) myocytes. D: Simulated $[\mathrm{Ca}^{2+}]_\mathrm{i}$ transients at 6 Hz in the FF (grey) and KO (black) models. E: Time courses of the integrals of the Ca^{2+} fluxes through SERCA, NCX and PMCA in the FF model over one cardiac cycle at 0.5 Hz. F: Time courses of the integrals of the Ca^{2+} fluxes through SERCA, NCX and PMCA in the KO model over one cardiac cycle at 0.5 Hz. G: Percentage contributions of SERCA, NCX and PMCA to Ca^{2+} removal in the FF and KO models.

to 18.9 ms in the FF model, in agreement with a tendency towards AP prolongation previously reported at this time point following SERCA2 knockout [125]. At the higher

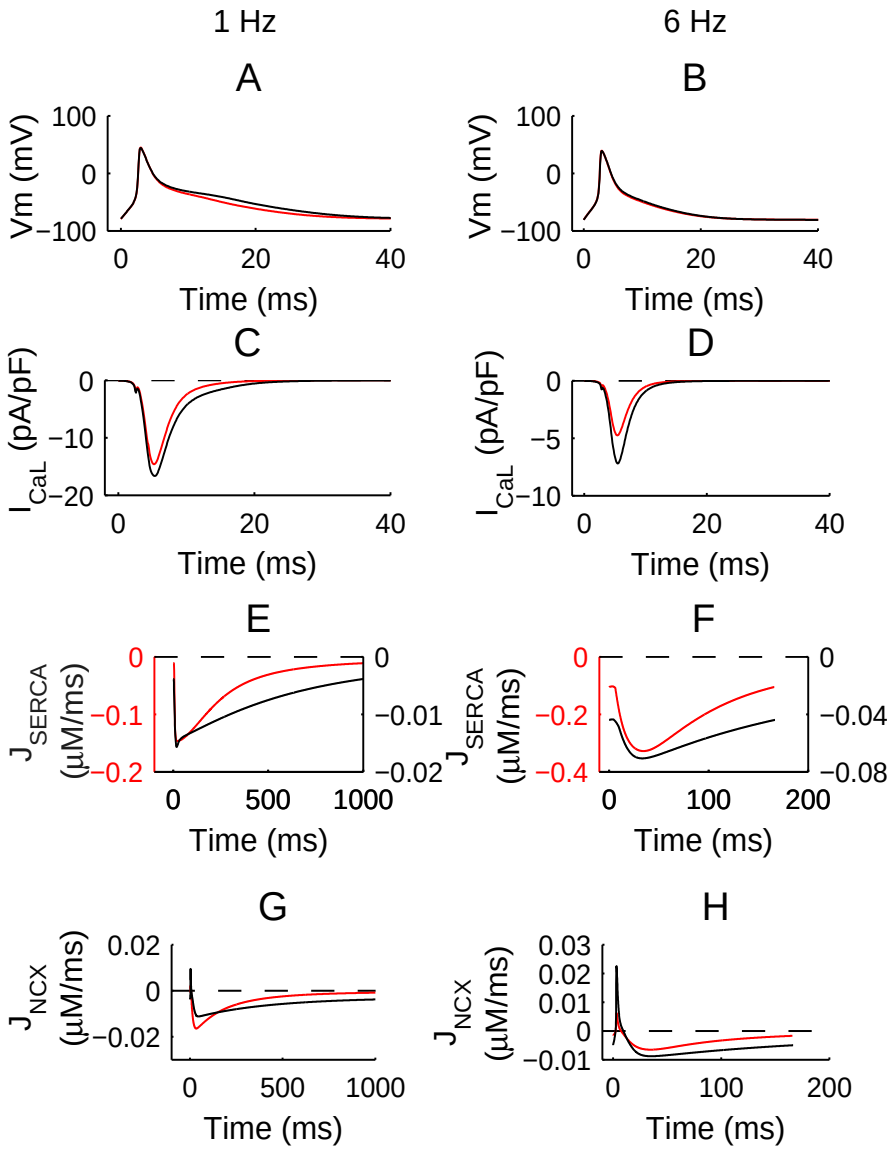

FIGURE 3.5: Simulated Ca^{2+} dynamics in the FF (red) and KO (black) models at 1 and 6 Hz. A-B: Simulated AP at 1 (A) and 6 Hz (B) . C-D: Simulated time courses of I_{CaL} at 1 (C) and 6 Hz (D). E-F: Simulated time courses of Ca^{2+} uptake through SERCA (J_{SERCA}) at 1 (E) and 6 Hz (F). G-H: Simulated time courses of Ca^{2+} extrusion through NCX (J_{NCX}) at 1 (G) and 6 Hz (H).

pacing frequency of 6 Hz, repolarisation was faster compared to the same model at 1 Hz and the differences in APDs between the models were diminished, with the APD_{90} equal to 12.2 and 13.1 ms respectively.

Simulated time courses of I_{CaL} during the above APs are plotted in Fig. 3.5C and

D, showing an enhanced I_{CaL} in the KO model, with both greater magnitude and slower inactivation kinetics. At 1 Hz (Fig. 3.5C), maximum I_{CaL} current density increased from 15.6 pA/pF in the FF model to 17.5 pA/pF in the KO model. The integral of the current over the duration of the AP increased by 33% at 1 Hz from 0.12 pC/pF in the FF model to 0.16 pC/pF, and by 49% at 6 Hz (Fig. 3.5D).

Simulated time courses of J_{SERCA} are shown in Fig. 3.5E and F for one cardiac cycle at 1 and 6 Hz, respectively (note difference in figure scale for FF and KO). At 1 Hz, peak J_{SERCA} during systole in the KO model was 0.015 μMms, compared to 0.14 μM/ms in the FF model, corresponding to an 89% decrease in systolic SERCA activity. During diastole, J_{SERCA} in the KO model was 0.0036 μMms compared to 0.0094 μM/ms in the FF model, corresponding to a 62% decrease in diastolic SERCA activity. The total amount of Ca^{2+} uptake, calculated as the integral of J_{SERCA} over one cardiac cycle, decreased from 49.2 μM in the FF model to 7.4 μM in the KO model, corresponding to an 84% decrease. At 6 Hz with SERCA2 KO, J_{SERCA} decreased by 73 and 61% of control values during systole and diastole respectively, and total Ca^{2+} uptake decreased by 71%.

Simulated time courses of J_{NCX} are plotted in Fig. 3.5G and H for 1 and 6 Hz, respectively. During an AP, there is a very brief period where Ca^{2+} influx via NCX is thermodynamically favored. This Ca^{2+} influx, corresponding to positive values of J_{NCX}, was greater in the KO model compared to FF model. At 1 Hz, the magnitude of the influx was relatively small, equal to 0.0018 μM/ms in the FF model and increasing 5-fold to 0.0089 μM/ms in the KO model. At 6 Hz, the elevation of $[Na^+]_i$ resulted in an enhanced Ca^{2+} influx through reverse mode NCX. Peak Ca^{2+} influx was 0.0055 μM/ms in the FF model and increased 3.6-fold to 0.020 μM/ms in the KO model. These results show that Ca^{2+} entry through reverse mode NCX was significantly enhanced in the KO model, although its magnitude was relatively small compared to Ca^{2+} entry through I_{CaL}.

When comparing Ca^{2+} extrusion through NCX in forward mode, J_{NCX} in the KO model was lower during systole and higher during diastole compared to the FF model. Quantitative analysis showed that peak systolic J_{NCX} in the KO model was 0.011 μM/ms compared to 0.017 μM/ms in the FF model, corresponding to a 35% decrease. This moderate reduction in NCX activity occurred despite a 73% decrease in peak $[Ca^{2+}]_i$. Diastolic J_{NCX} was 0.0041 μM/ms in the KO model compared to 0.0009 μM/ms in the FF model, corresponding to a 4.5-fold increase. At 6 Hz, both systolic and diastolic J_{NCX} was higher in the KO model. During systole, J_{NCX} was 0.009 μM/ms in the KO model compared to 0.007 μM/ms in the FF model, corresponding to a 33% increase. During diastole, J_{NCX} was 0.0052 μM/ms in the KO model compared to 0.0019 μM/ms in the FF model, corresponding to a 2.5-fold increase.

Simulated $[Na^+]_i$ at 1 Hz in the KO model was 9.9 mM and rose to 13.7 mM at 6 Hz, compared to values of 9.3 and 13.2 mM, respectively, in the FF model. The relatively small increase in $[Na^+]_i$ between the FF and KO models are consistent with experimental measurements, in which no statistically significant difference in $[Na^+]_i$ between the FF and KO mice was observed [125]. NKA plays an important role in regulating $[Na^+]_i$. The formulation of NKA used in our model has previously been parameterised to data from mouse ventricular myocytes at 37 ^{o}C [118, 18]. Experimental data on NKA activity plotted as a function of $[Na^+]_i$ show that NKA is half-activated at $[Na^+]_i$ equal to 16.6 mM. At the $[Na^+]_i$ levels predicted by our model, NKA activity lies in the steep part of the curve, indicating a high level of sensitivity that will quickly compensate changes in $[Na^+]_i$. Furthermore, as shown above, despite the over three-fold increase in the maximum exchange rate of NCX, the actual NCX activity over one cardiac cycle did not increase significantly in the KO mice due to the dramatic reduction in $[Ca^{2+}]_i$. Therefore, the increase in Na^+ influx through NCX in the KO mice was limited.

3.4.3 Graded Reduction of the Maximum Uptake Activity of SERCA

In order to better understand the changes that occur in Ca^{2+} handling of the KO cardiomyocytes, we carried out a series of simulation studies based on our model. We first tested the sensitivity of the peak and diastolic $[Ca^{2+}]_i$ to a series of graded reductions in SERCA uptake activity in both the FF and KO model. V_{up} was reduced from 95% of its FF value (calculated from the decay of the experimentally measured $[Ca^{2+}]_i$ transient in the FF at 1 and 6 Hz) to 0 (or until alternans appeared) in 5% increments. In all simulations, the LCCs, NCX and all other parameters were kept unchanged from their original values.

As shown in Fig. 3.6, at the more physiologically relevant pacing frequency of 6 Hz, peak $[Ca^{2+}]_i$ appeared to be insensitive to decreases in SERCA activity. Diastolic $[Ca^{2+}]_i$, on the other hand, increased dramatically with decreasing SERCA activity. With the FF model, diastolic $[Ca^{2+}]_i$ almost tripled when SERCA activity was reduced to zero. In the KO model, a similar trend was observed, although the extent of increase in diastolic $[Ca^{2+}]_i$ was smaller. These results suggest that at a physiologically relevant pacing frequency, a reduction in SERCA activity has a much stronger effect on diastolic $[Ca^{2+}]_i$ than on peak $[Ca^{2+}]_i$.

3.4.4 Contributions of the Compensatory Mechanisms

Experimental observations have suggested that in SERCA2 KO cardiomyocytes, transsarcolemmal Ca^{2+} fluxes are enhanced to compensate for the dramatically impaired SR function [4, 125]. Specifically, an enhanced I_{CaL} may increase the amount of Ca^{2+} entry into the cell, and increased Ca^{2+} extrusion through up-regulated NCX and PMCA may facilitate Ca^{2+} removal during the decay of the $[Ca^{2+}]_i$ transient. These compensatory mechanisms are thought to shift the reliance of the $[Ca^{2+}]_i$ transient generation towards sarcolemmal Ca^{2+} fluxes and away from SR Ca^{2+} release [4, 125].

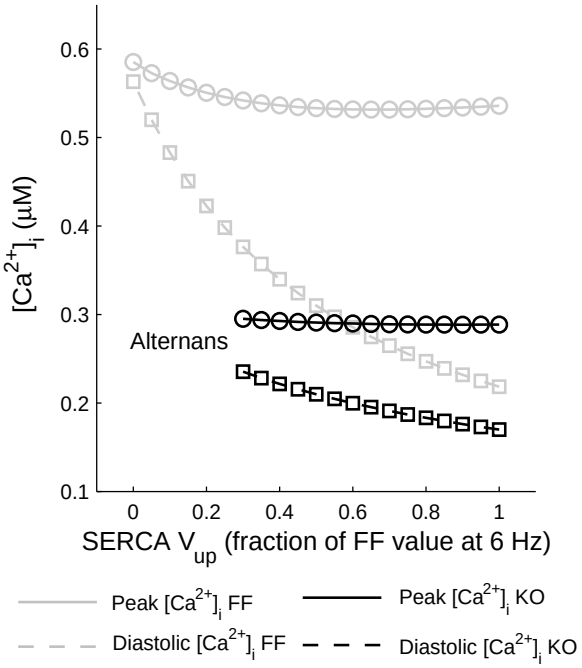

FIGURE 3.6: Changes in peak (circles and solid lines) and diastolic $[\mathrm{Ca}^{2+}]_{\mathrm{i}}$ (squares and dashed lines) in response to graded reductions in the maximum uptake activity of SERCA in the FF (grey) and KO (black) models.

A quantitative investigation into the contribution of each compensatory mechanism to Ca^{2+} handling in the KO mice was carried out using in-silico perturbations of our models. The first in-silico perturbation involved simulating the KO model with $\mathrm{I_{CaL}}$ clamped to have the same time course as that seen in the FF model, which will be referred to as the KO-$\mathrm{I_{CaL}}$ model. The second perturbation involved reducing the maximum activity of NCX in the KO model to the same level as that in the FF model, which will be referred to as the KO-NCX model. The third perturbation, in which both the $\mathrm{I_{CaL}}$ and the NCX were adjusted to the levels in the FF model, was designed to test the combined effects of these two compensatory mechanisms and will be referred to as the KO-ICaL-NCX model.

The resulting Ca^{2+} dynamics from these three perturbations were then compared to those observed in the control KO model, as shown in Fig. 3.7. These simulations

were performed at 1Hz, as opposed to 6Hz. Simulations at 6Hz resulted in unstable responses, which were attributed to the 5non-physiological combintations of parameter values in these models. It can be seen that in the absence of an increased I_{CaL}, simulated $\Delta[Ca^{2+}]_i$ and SR Ca^{2+} content decreased by 28% and 15%, respectively, from the KO values. Furthermore, diastolic $[Ca^{2+}]_i$ decreased by 9% and RT_{50} increased by 6%. In the absence of an up-regulated NCX, the simulated $[Ca^{2+}]_i$ transient was characterized by a 58% increase in diastolic $[Ca^{2+}]_i$, a 2.6-fold increase in $\Delta[Ca^{2+}]_i$ and a 2-fold increase in the SR Ca^{2+} content. There was a small decrease of 2% in the RT_{50}.

In the absence of both compensatory mechanisms, $\Delta[Ca^{2+}]_i$, diastolic $[Ca^{2+}]_i$ and SR Ca^{2+} content all remained higher than the KO values, by 86%, 41% and 76%, respectively. There was a small 3% increase in RT_{50}, indicating a minimal effect of the perturbation on the rate of decay of the $[Ca^{2+}]_i$ transient. The above results suggest that while increasing I_{CaL} increased systolic $[Ca^{2+}]_i$ and NCX up-regulation decreased diastolic $[Ca^{2+}]_i$, the overall effects of the co-existence of these two compensatory mechanisms appeared to be decreasing diastolic $[Ca^{2+}]_i$ while also decreasing systolic $[Ca^{2+}]_i$. Furthermore, as the RT_{50} of the transient was not found to be significantly increased in either the KO-NCX or the KO-ICaL-NCX model, these compensatory mechanisms may not be as critical for facilitating the decay of the transient as hypothesized previously [4].

3.4.5 Efficiency of Other Possible Compensatory Mechanisms

We have shown in the previous section that the increase in I_{CaL} is an important compensatory mechanism for enhancing systolic $[Ca^{2+}]_i$. It remains to investigate whether changes in systems other than up-regulation the NCX could also maintain diastolic $[Ca^{2+}]_i$ to the level observed experimentally in the KO. Possible candidates included: (1) a decrease in the persistent Na^+ current (I_{Nab}), which would reduce $[Na^+]_i$ and in turn provide a greater thermodynamic drive for Ca^{2+} extrusion through NCX to lower

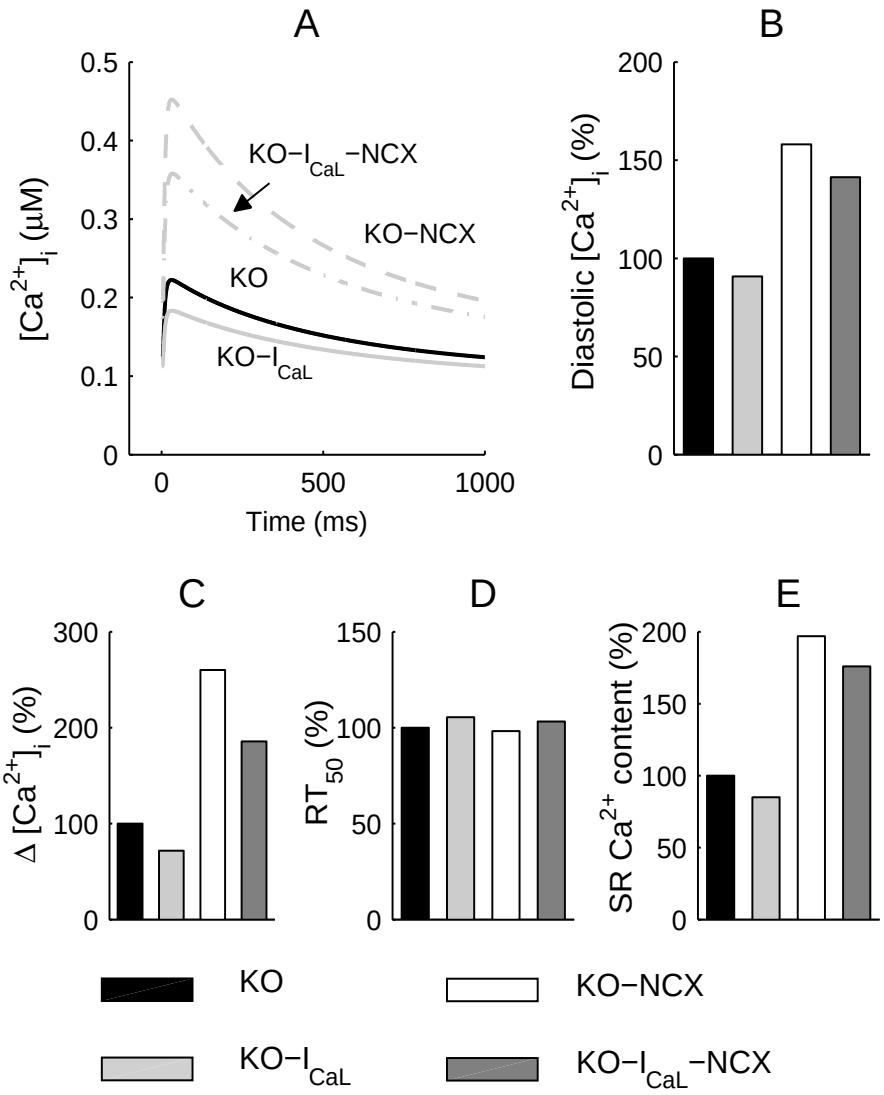

FIGURE 3.7: In-silico perturbations to the KO model. A: Simulated $[\mathrm{Ca}^{2+}]_\mathrm{i}$ transients at 1 Hz in the KO, KO-$\mathrm{I_{CaL}}$ and KO-NCX and KO-$\mathrm{I_{CaL}}$-NCX models. B-E: Diastolic $[\mathrm{Ca}^{2+}]_\mathrm{i}$ level (B), magnitude of the $[\mathrm{Ca}^{2+}]_\mathrm{i}$ transient ($\Delta[\mathrm{Ca}^{2+}]_\mathrm{i}$) (C), $\mathrm{RT_{50}}$ of the transient (D) and SR Ca^{2+} content (E) in the KO, KO-$\mathrm{I_{CaL}}$ and KO-NCX models

diastolic $[\mathrm{Ca}^{2+}]_\mathrm{i}$; (2) a decrease in SR Ca^{2+} leak which could potentially decrease diastolic $[\mathrm{Ca}^{2+}]_\mathrm{i}$, enhance SR Ca^{2+} load and thus increase systolic $[\mathrm{Ca}^{2+}]_\mathrm{i}$; and (3) an increase in the activity of NKA which would lower $[\mathrm{Na}^{+}]_\mathrm{i}$ hence enhancing NCX activity and lowering diastolic $[\mathrm{Ca}^{2+}]_\mathrm{i}$.

To test these alternative mechanisms at 6 Hz stimulation frequency, we set up the control model which was the KO model but without up-regulation of NCX. Then for each of the above candidate mechanisms, we varied the conductance of the persistent Na^+ channel (G_{Nab}), the rate of SR Ca^{2+} leak (V_{leak}), the maximum NKA pump current (I_{NKA}^{max}), respectively, as well as the maximum exchanger rate (V_{NCX}^{max}) for comparison, while all other components were kept unchanged. We then examined the peak and diastolic $[Ca^{2+}]_i$ as a function of the relative change in the conductance, as shown in Fig 3.8.

In Fig 3.8A, the x-axis is plotted as the logarithm (base 10) of the ratio between the parameter value and its original value. Zero indicates the parameter value is the same as its original value. Positive values indicate an increase in the parameter value (x = 1 corresponds to a 10-fold increase). Negative values indicate a decrease in the parameter value (x = -1 means the parameter value is 10% of the control value). The gray lines indicate the peak and diastolic $[Ca^{2+}]_i$ levels measured experimentally in the KO at 6 Hz, which can be considered as the target values that have been shown to be sufficient for maintaining cardiac function at the 4 week time point.

These results show that decreasing G_{Nab} and V_{leak} had very moderate effects on diastolic $[Ca^{2+}]_i$, which remained significantly higher than the target value even when conductances were decreased to almost zero, whereas, in contrast, increases in the activities of NKA and NCX sufficiently reduced diastolic $[Ca^{2+}]_i$. Furthermore, the rate of decrease in diastolic $[Ca^{2+}]_i$ with increasing V_{NCX}^{max} was significantly faster with the target diastolic value being reached when V_{NCX}^{max} was between 3 and 5 times its control value. The effect of increasing I_{NKA}^{max} had a similar effect to NCX initially. However, after a 5-fold increase in I_{NKA}^{max} (x = 0.7), the rate of decrease in diastolic $[Ca^{2+}]_i$ was reduced and diastolic $[Ca^{2+}]_i$ did not decrease to the target value until I_{NKA}^{max} was 50 times its control value (x = 1.7). It is significant to note that, as V_{NCX}^{max} continues to increase, the difference between peak and diastolic $[Ca^{2+}]_i$ became smaller, indicating a progress

reduction in $\Delta[Ca^{2+}]_i$ and thus an anticipated reduction in systolic funtion that potenially limits the viability of increases in V_{NCX}^{max} as a compensatory mechanism for continued loss of SERCA2 function.

A similar analysis was also carried out to test the sensitivity of peak and diastolic $[Ca^{2+}]_i$ to the total concentration (B_{max}) and affinity ($K_{d,buffer}$) of the intracellular Ca^{2+} buffers, which were originally set to 109 and 0.6 μM, respectively, in both the FF and KO models. As shown in Fig. 3.8B, a decrease in the buffering power by either decreasing B_{max} or increasing $K_{d,buffer}$ led to a lower diastolic $[Ca^{2+}]_i$ and a higher peak $[Ca^{2+}]_i$. Experimentally observed diastolic $[Ca^{2+}]_i$ was reached with a 70% decrease in B_{max} or a 7-fold increase in $K_{d,buffer}$. Further reductions in B_{max} led to alternans, while $K_{d,buffer}$ could be increased up to 13-fold with sustainable $[Ca^{2+}]_i$ transients.

3.5 Discussion

The process of SR Ca^{2+} uptake through SERCA plays a key role in determining the rate of decay of the $[Ca^{2+}]_i$ transient and hence relaxation, which in turn is crucial for diastolic filling. Ca^{2+} uptake into the SR also replenishes SR Ca^{2+} store so that Ca^{2+} can be released again during the next cardiac cycle. The current simulation study demonstrated that given the observed decrease in SERCA activity, sustained $[Ca^{2+}]_i$ transients could be maintained in the KO model. Simulated $[Ca^{2+}]_i$ transient characteristics in the FF and KO models were consistent with experimental observations in the FF and KO cardiomyocytes. In the following sections, we discuss the relationship between protein expression and functional activity based our analysis of the $[Ca^{2+}]_i$ transients in the KO cardiomyocytes, the changes in Ca^{2+} dynamics in the KO model and the roles of the compensatory mechanisms.

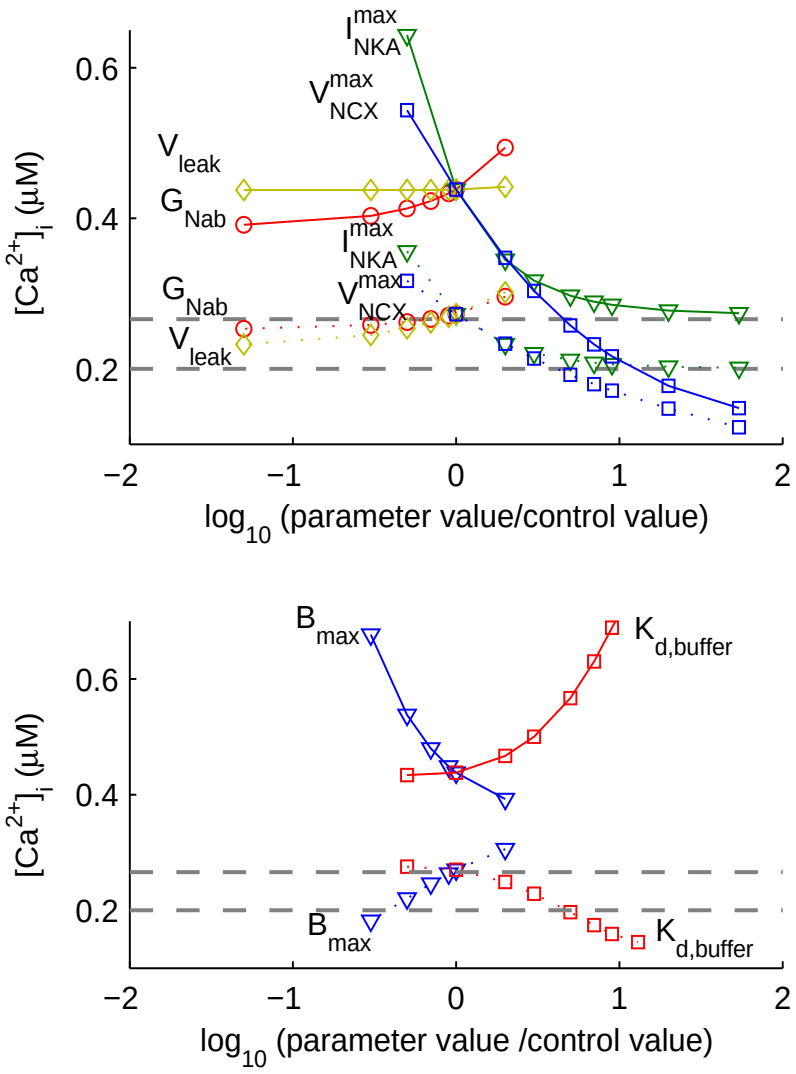

FIGURE 3.8: A. Changes in peak (solid lines) and diastolic (dotted lines) $[Ca^{2+}]_i$ in response to changes in the conductances of the persistent Na^+ current (G_{Nab}), the SR Ca^{2+} leak flux (V_{leak}), the maximum Na^+/K^+ ATPase current (I^{max}_{NKA}) and the NCX (V^{max}_{NCX}). Dashed lines indicate the experimentally meausred peak and diastolic $[Ca^{2+}]_i$ in the KO cardiomyocytes. B. Changes in peak (solid lines) and diastolic (dotted lines) $[Ca^{2+}]_i$ in response to changes in total buffer concentration (B_{max}) and affinity ($K_{d,buffer}$).

3.5.1 Functional Activities of the Ca^{2+} Handling Proteins in the KO Cardiomyocytes

Previously, it has been shown that less than 5% SERCA2 protein was expressed in myocardial tissue from the KO, compared to the FF [4]. In addition, the protein levels

of NCX, PMCA were found to increase by 31 and 45% respectively. In the current study, the functional activities of NCX and PMCA in the FF and KO cardiomyocytes was examined based on the rate of decay of the caffeine-induced $[Ca^{2+}]_i$ transient, which in turn were used in conjunction with the decay of the field-stimulated transient to examine SERCA activity. Through the application of this method, sarcolemmal Ca^{2+} extrusion was calculated to have increased over 3-fold, and SERCA activity was found to have decreased by 67% (Fig. 3.2B inset). Direct quantitative characterisation of the relationship between protein expression and function using experimental methods remains challenging. Previously, our experimental collaborators in Oslo (see Section 3.2) measured thapsigargin-sensitive ^{32}P-incorporation in left ventricular myocardial tissue homogenates, which showed SERCA activity in the KO mice was approximately 15% of the FF level [4], supporting a nonlinear relationship between expression levels and function.

The nonlinear correlation between the expression and activity of the Ca^{2+} handling proteins has also been reported by other groups. For example, Schwinger et al. [171] found a nonlinear correlation between expression and activity of the SERCA protein in their study of patients with dilated cardiomyopathy. Schmidt et al. [170] also observed reduced SERCA activity in failing human myocardium compared to nonfailing heart without any difference in SERCA protein level. One possible explanation for such differences could be that an excessive amount of SERCA protein may be present in the normal mouse which is not functional under physiological conditions [125].

3.5.2 Rate of Decay of $[Ca^{2+}]_i$ Transient in the KO Cardiomyocytes

Another interesting finding from the model is while the RT_{50} of the simulated $[Ca^{2+}]_i$ transient at 1 Hz in the KO model was more than double of that in the FF model, it was only moderately increased at 6 Hz indicating a much less profound lusitropic effect of SERCA

knockout at more physiological pacing frequencies. The reason for the aforementioned reduced lusitropic effect of SERCA knockout at 6 Hz can, however, be explained using a simplified theoretical analysis of Ca^{2+} dynamics during the decay phase of the transient, proposed by Bers and Berlin [22]. This method is based on the fact that the rate of $[Ca^{2+}]_i$ decline does not only depend on the rate of Ca^{2+} removal from the cytosol but also on the properties of intracellular Ca^{2+} buffering. Assuming that Ca^{2+} transport by SERCA is the main contributor to $[Ca^{2+}]_i$ decline in the wildtype mouse, the rate of decay of the total Ca^{2+} concentration in the cytosol ($[Ca^{2+}]_{tot}$) can be written as

$$\frac{d[Ca^{2+}]_{tot}}{dt} = J_{SERCA} = \frac{-V_{up}}{1 + (\frac{K_{m,up}}{[Ca^{2+}]_i})^2} \tag{3.1}$$

$[Ca^{2+}]_{tot}$ is related to $[Ca^{2+}]_i$ via Eq. 2.4. Thus Eqs. 2.4 and 3.1 can then be combined to give the rate of decay of $[Ca^{2+}]_i$:

$$\frac{d[Ca^{2+}]_i}{dt} = \frac{-V_{up} \cdot [Ca^{2+}]_i \cdot (1 + K_{d,buffer}/[Ca^{2+}]_i)^2}{K_{d,buffer} \cdot B_{max} \cdot [1 + (K_{m,up}/[Ca^{2+}]_i)^2]} \tag{3.2}$$

Rearranging Eq. 3.2 and integrating gives the time taken for $[Ca^{2+}]_i$ to decay from its value at time t_0 to its value at time t can be expressed as:

$$\begin{aligned} t - t_0 \;=\; & \frac{B_{max}}{V_{up}} \cdot [\frac{2K_{m,up}^2}{K_{d,buffer}^2} \cdot \ln(\frac{[Ca^{2+}]_i + K_{d,buffer}}{[Ca^{2+}]_i}) - \\ & \frac{K_{d,buffer}}{[Ca^{2+}]_i + K_{d,buffer}} \cdot (1 + \frac{K_{m,up}^2 \cdot (K_{d,buffer} + 2[Ca^{2+}]_i)}{K_{d,buffer}^2 \cdot [Ca^{2+}]_i})] \end{aligned} \tag{3.3}$$

where the right hand side is evaluated for $[Ca^{2+}]_i$ at times t and t_0. Therefore, the RT_{50} of a $[Ca^{2+}]_i$ transient can be obtained by evaluating Eq. 3.3 for $[Ca^{2+}]_i$ at the peak of the transient ($[Ca^{2+}]_p$) and $[Ca^{2+}]_i$ at 1/2·($[Ca^{2+}]_p$ + diastolic $[Ca^{2+}]_i$).

Substitution of the parameter values for the FF and KO models (B_{max} = 109 μM, $K_{d,buffer}$ = 0.6 μM, V_{up} = 0.19 μM/ms (FF 1 Hz), 0.521 μM/ms (FF 6 Hz), 0.067 μM/ms

(KO 1 Hz), 0.202 μM/ms (KO 6 Hz) μM/ms and $K_{m,up}$ = 0.412 μM) and the diastolic $[Ca^{2+}]_i$ values (0.125 μM at 1 Hz, 0.2 μM at 6 Hz) into Eq. 3.3 gives the estimated RT_{50} of the $[Ca^{2+}]_i$ transient as a function of peak $[Ca^{2+}]_i$, as shown in Fig. 3.9A. According to the above theoretical analysis, the shift in RT_{50} between FF and KO models is much greater at 1 Hz than at 6 Hz, which qualitatively agrees with what is observed experimentally [4].

The sensitivity of RT_{50} to changes in the buffering parameters was also analysed using the above approach. Experimental data on buffering properties in mouse ventricular myocytes are sparse, but rat data are available. In rat cardiac myocytes, Diaz et al. [48] measured B_{max} to be 160 μM with a $K_{d,buffer}$ of 0.3 μM, while Berlin et al. [17] reported an average B_{max} of 123 μM with cell-to-cell variations from 68 to 158 μM and an average $K_{d,buffer}$ of 0.96 μM with variations from 0.55 to 1.57 μM. We therefore independently varied B_{max} from 60 to 160 μM and $K_{d,buffer}$ from 0.3 to 1.6 μM. The predited RT_{50} at the experimentally observed peak $[Ca^{2+}]_i$ levels for the range of B_{max} and $K_{d,buffer}$ values are shown in Fig. 3.9B and C. It can be seen that an increase in the buffering power, by either increasing B_{max} or decreasing $K_{d,buffer}$, led to a slower rate of decay (longer RT_{50}). Nevertheless, within the range of B_{max} and $K_{d,buffer}$ examined, the qualitative trend of a smaller shift in RT_{50} at 6 Hz than at 1 Hz is maintained regardless of the choice of the buffering parameter values.

It is also interesting to note that, with a more simplistic model framework which did not include FDAR, Trafford et al. [197] were able to demonstrate the reduced lusitropic effect of SERCA KO at 6 Hz. To explain this result using the approach of Bers and Berlin [22], we ran the FF and KO models with a constant V_{up} value, set to its level at 1 Hz. The decay of the simulated $[Ca^{2+}]_i$ transients at 6 Hz were slower in both the FF and KO models, compared to the case with FDAR (FF: 59 *versus* 48 ms, KO: 68 *versus* 60 ms), as a consequence of the slower SERCA uptake rate. However, the difference in RT_{60}

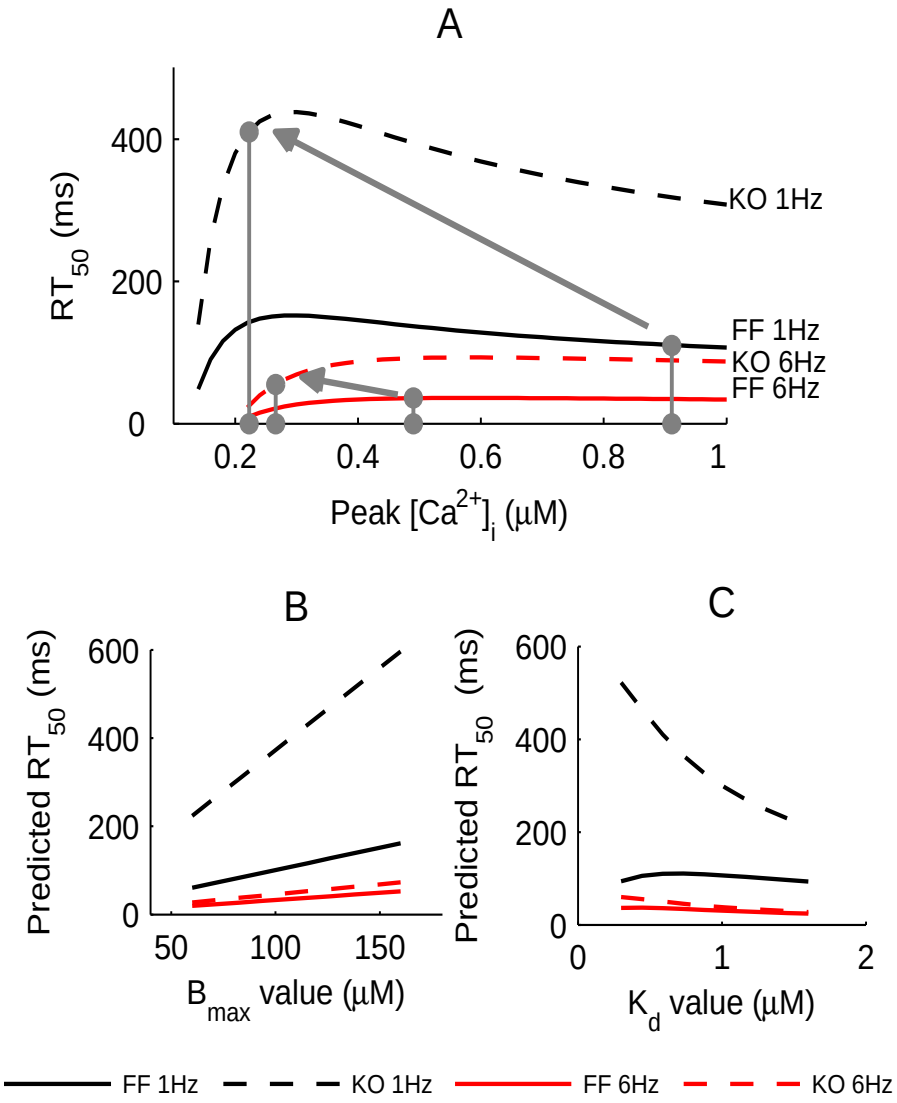

FIGURE 3.9: A. Theoretical analysis of the decay kinetics of the $[Ca^{2+}]_i$ transient, showing the RT_{50} of the transient as a function of peak $[Ca^{2+}]_i$ for the FF and KO models. The circles correspond to the experimentally measured peak $[Ca^{2+}]_i$ and the predicted RT_{50} values. B. Sensitivity of rate of $[Ca^{2+}]_i$ decay to the total buffer concentration (B_{max}). Predicted RT_{50} was obtained by substituting the appropriate parameter values into Eq. 3.3. C. Sensitivity of rate of $[Ca^{2+}]_i$ decay to the affinity of the buffers ($K_{d.buffer}$)

between the FF and KO models remained smaller at 6 Hz than at 1 Hz (6 Hz: 59 *versus* 68 ms, 1 Hz: 119 *versus* 267 ms). Substituting the appropriate parameter values into Eq. 3.3 yielded a qualitatively similar relationship (Fig. 3.10) between RT_{50} and peak $[Ca^{2+}]_i$ as that in Fig. 3.9. This result indicates that the reduced lusitropic impact of SERCA KO

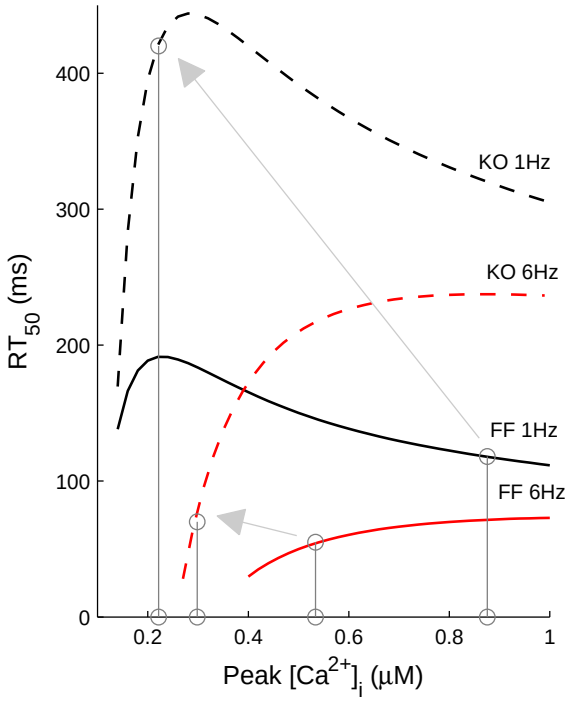

FIGURE 3.10: Analysis of the RT_{50} of $[Ca^{2+}]_i$ transients in the FF and KO models without FDAR. The circles corresponding to the simulated peak $[Ca^{2+}]_i$ and the predicted RT_{50} values.

at a higher pacing frequency may not involve FDAR.

Finally, it is important to note that although a useful analysis tool, the approach of Bers and Berlin does not take into account the effect of NCX and PMCA on relaxation time which is likely to play an important role in the KO model.

3.5.3 Contributions of the Compensatory Mechanisms

Simulations with graded reductions in V_{up} showed that at a physiologically relavant pacing frequency for the mouse, diastolic $[Ca^{2+}]_i$ rose sharply with decreasing V_{up}, while systolic $[Ca^{2+}]_i$ did not change significantly. This observation points to the potential role of the compensatory mechanisms in lowering diastolic $[Ca^{2+}]_i$. Indeed, results from the three perturbation studies (KO-I_{CaL}, KO-NCX and KO-I_{CaL}-NCX) support this hypothesis. We found that increasing I_{CaL} alone increased systolic $[Ca^{2+}]_i$ while

up-regulating NCX alone decreased diastolic $[Ca^{2+}]_i$, as one would expect. However, the combined effects of the two compensatory mechanisms in simulations appeared to be a decrease in diastolic $[Ca^{2+}]_i$ at the expense of a decrease in systolic $[Ca^{2+}]_i$. These results suggest that maintaining a physiological diastolic $[Ca^{2+}]_i$ may be more important than the need to maintain systolic $[Ca^{2+}]_i$ in the KO mice. In fact, elevated diastolic $[Ca^{2+}]_i$ has been reported previously in failing heart preparations [170, 76, 77, 23, 24]. Schmidt et al. [170] found that in failing human myocardium where SERCA function was impaired, diastolic $[Ca^{2+}]_i$ was approximately 40% higher compared to the control at low pacing frequencies, and increased to almost 100% higher following an increase in stimulation frequency. The elevated diastolic $[Ca^{2+}]_i$ was in turn associated with increased generation of diastolic tension in the same preparations, an effect which also increased significantly with increasing stimulation frequency, as well as a decreased systolic tension and a negative force-frequency relationship [170]. The level of increase in diastolic $[Ca^{2+}]_i$ observed in the study of Schmidt et al. is in the same range as that in the KO-NCX model (50%), suggesting the higher diastolic $[Ca^{2+}]_i$ could be of significant physiological relevance to cardiac function, if it had indeed occurred in the KO mice. It is worth noting the differences between the FF model with reduced SERCA activity and the KO-ICaL-NCX model. PMCA activity was kept at the FF level in the former but at the KO level in the latter. In the former, I_{CaL} parameters were kept unchanged with the same values as in the FF model, while in the latter, I_{CaL} was clamped to have the same time course as that seen in the original FF model.

We have further demonstrated that, of the many cellular systems that can lower diastolic $[Ca^{2+}]_i$ in the presence of impaired SERCA activity, up-regulations of NCX and NKA as well as lowering Ca^{2+} buffering power are the three compensatory mechanisms capable of sufficiently reducing diastolic $[Ca^{2+}]_i$ to match its level in the FF controls. For both NCX and NKA, the decrease in diastolic $[Ca^{2+}]_i$ with increasing transporter activity occurs at the expense of a reduced systolic $[Ca^{2+}]_i$. On the other hand, a decrease

in the buffering power lowered diastolic $[Ca^{2+}]_i$ while also increasing systolic $[Ca^{2+}]_i$. Experimentally, diastolic $[Ca^{2+}]_i$ was seen to be maintained in the KO cardiomyocytes while systolic $[Ca^{2+}]_i$ was significantly decreased, compared to the FF values. These observations are consistent with the effects of up-regulation of NCX or NKA, but not with lowering buffering power.

Simulation results in Fig. 3.8A and B suggest that in the KO model, a physiological diastolic $[Ca^{2+}]_i$ can be reached, independently, with (1) a 50-fold increase in NKA activity, (2) a 70% reduction in total buffer concentration (or a 7-fold decrease in the affinity of the buffer), or (3) a 3-fold increase in NCX activity. The limitation of up-regulating NKA is that the rate of decrease in diastolic $[Ca^{2+}]_i$ was progressively slowed following increases in I_{NKA}^{max} over its control value. While the reduction in buffering power may be a feasible solution in this model, experimental evidence suggests troponin C contributes to approximately 50% of total fast Ca^{2+} buffering [19, 59]. Therefore, this compensatory mechanism may necessitate a decrease in troponin concentration or its Ca^{2+}-binding affinity. These effects are likely to have further detrimental consequences on myocardial contraction in the KO cardiomyocytes where the size of the $[Ca^{2+}]_i$ transient is already severely reduced. Compared to up-regulation of NKA and decreasing buffering power, a 3-fold increase in NCX activity thus may be the most effective compensatory mechanism. However, this mechanism is not without constraint, as the reduction in $[Ca^{2+}]_i$ transient amplitude becomes progressively more severe with further increases in V_{NCX}^{max}, suggesting there may exist a balance point which optimises both diastolic and systolic $[Ca^{2+}]_i$ levels. Therefore, with continued reduction in SERCA activity beyond the 4-week time point, as confirmed by our SERCA2 KO study at the 7-week time point [125], cardiac pump function may be compromised without additional compensatory mechanisms such as up-regulation of NKA and reduction of buffering power.

In human models of HF, the important role of NCX in maintaining diastolic function

has been confirmed clinically by Hassenfuss et al. [85], who found preserved diastolic function in HF patients with increased NCX protein level. In contrast, patients with unchanged NCX protein level had severely compromised diastolic function. Therefore, results from our in-silico study are consistent with these previous findings and suggest that in the presence of impaired SERCA function, the up-regulation of NCX in the KO mice is important for maintaining diastolic $[\mathrm{Ca}^{2+}]_{\mathrm{i}}$ level and diastolic function. Maintaining diastolic $[\mathrm{Ca}^{2+}]_{\mathrm{i}}$ levels may additionally have important implications in regards to signalling. For example, CaMKII which is activated by $[\mathrm{Ca}^{2+}]_{\mathrm{i}}$, has been implicated in triggering hypertrophy and HF [208, 216]. Thus, the maintenance of diastolic $[\mathrm{Ca}^{2+}]_{\mathrm{i}}$ levels by NCX up-regulation possibly may also underlie the surprising absence of hypertrophy in KO animals [4, 125].

Chapter 4

Sodium Accumulation in SERCA KO Induced Heart Failure

4.1 Introduction

In Chapter 3, we studied SERCA2 KO mice at 4 weeks following gene deletion, when surprisingly normal cardiac function was observed. At the 7-week time point, however, these animals developed end-stage HF. In addition to a progressive reduction in SERCA2 level and further up-regulation of compensatory mechanisms, $[\mathrm{Na}^+]_\mathrm{i}$ elevation was also observed in 7-week KO cardiomyocytes [125]. As mentioned in Chapter 1, Ca^{2+} dynamics are closely linked to Na^+ homeostasis, as the concentration gradient of [Na^+] across the sarcolemma, together with the membrane potential, provides the driving force for Ca^{2+} transport through NCX. The maintenance of the Na^+ concentration gradient is in turn achieved via an ATP-consuming process of Na^+ extrusion through the NKA. Therefore, $[\mathrm{Na}^+]_\mathrm{i}$ accumulation has the potential to have a profound impact on both Ca^{2+} handling and metabolism.

In this chapter, we apply a modelling analysis to investigate, for the first time, the important changes over time in Ca^{2+} handling in SERCA KO cardiomyocytes that lead

to the eventual progression into HF. In particular, we compare total ATP consumption per cardiac cycle in the FF, 4-week and 7-week KO mice models, investigate the mechanisms for $[\mathrm{Na}^+]_\mathrm{i}$ elevation in the 7-week KO compared to the FF and 4-week KO, and analyse the sensitivity of each model to metabolic imbalance. Finally we examine the differential effects of compensatory mechanisms on total ATP consumption between the 4-week and 7-week time points.

4.2 Materials and Methods

All experimental measurements described below were provided by collaborators, Louch W. E., Jan, M. A., Christensen, G. and Sejersted, O.M., from the Institute for Experimental Medical Research, Oslo University Hospital Ullevål in Norway.

4.2.1 Animal Care

This study was approved by the Norwegian National Committee for Animal Welfare under the Norwegian Animal Welfare Act, which conforms to the *Guide for the Care and Use of Laboratory Animals* published by the US National Institutes of Health (NIH publication No. 85-23, revised 1996). Inducible, cardiomyocyte-specific disruption of the *Serca2* gene was attained by employing *Serca2*$^{flox/flox}$ Tg(αMHC-MerCreMer) mice (KO) [4]. Gene excision in 8-10 week old mice was accomplished by inclusion of tamoxifen powder (RM1 FG SQC, 811004, Scanbur BK) in the feed (100 mg/200 g) for 7 days [6, 125]. *Serca2*$^{flox/flox}$ mice (FF) served as controls [4, 5]. Tamoxifen treatment results in Serca2 gene excision exclusively in the cardiomyocytes of KO animals [4]. Hearts were harvested at 4 and 7 weeks following tamoxifen administration.

4.2.2 Cardiomyocyte Experiments

Cardiomyocytes were isolated by retrograde perfusion of the heart with enzyme-containing solutions [4, 124]. Isolated cells were then plated on laminin-coated coverslips and placed in a perfusion chamber on the stage of an inverted microscope. Intracellular $[Ca^{2+}]_i$ was measured in myocytes loaded with fluo-4 AM (Invitrogen Molecular Probes, Eugene, OR, USA). $[Ca^{2+}]_i$ transients were elicited by field stimulation (3 ms biphasic pulse, 25% above threshold) during perfusion with HEPES Tyrode solution containing (in mM): 140 NaCl, 1 $CaCl_2$, 0.5 $MgCl_2$, 5.0 HEPES, 5.5 glucose, 0.4 NaH_2PO_4 and 5.4 KCl (pH 7.4, 37°C). In these experiments, an LSM 510 microscope (Zeiss GmbH, Jena, Germany) was used to record $[Ca^{2+}]_i$ transients in line-scan mode [140].

SR function was assessed by whole-cell fluorescence (Photon Technology International, Monmouth Junction, NJ, USA) recordings of intracellular $[Ca^{2+}]_i$. SR Ca^{2+} content was estimated by rapidly switching to an extracellular solution containing 10 mM caffeine and measuring the magnitude of the elicited Ca^{2+} release. The SR-dependent component of the $[Ca^{2+}]_i$ transient was calculated by comparing the magnitude of $[Ca^{2+}]_i$ transients in the presence and absence of caffeine. The difference in the declining phase of the $[Ca^{2+}]_i$ transient under these two conditions was used to estimate rate constants for $[Ca^{2+}]_i$ re-uptake (SERCA activity) and extrusion [141]. The contribution of NCX and PMCA to Ca^{2+} extrusion was estimated by comparing the declining phase of caffeine-elicited $[Ca^{2+}]_i$ transients in the presence and absence of 5 mM Ni^{2+}.

Patch-clamp experiments were conducted with an Axoclamp 2B amplifier (Axon Instruments, Foster City, CA, USA), pCLAMP software (Axon Instruments), and low resistance pipettes (1-2 MΩ). APs were triggered by injecting a 3-ms depolarising current in cells patch-clamped with a pipette solution containing (in mM): 120 K-aspartate, 0.5 $MgCl_2$, 6 NaCl, 0.06 EGTA, 10 HEPES, 10 glucose, 25 KCl, and 4 K2-ATP (pH

7.2). L-type Ca^{2+} current was elicited by 200 ms voltage steps from -50 mV to a range of potentials, with an internal solution containing (in mM) 130 CsCl, 0.33 $MgCl_2$, 4 Mg-ATP, 0.06 EGTA, 10 HEPES, and 20 TEA, and an extracellular solution containing (in mM) 20 CsCl, 1 $MgCl_2$, 135 NaCl, 10 Hepes, 10 D-glucose, 4 4-aminopyridine, and 1 $CaCl_2$ [4, 125]. NKA currents were obtained by elevating extracellular [K^+] from 0 mM to 5.4 mM, and contributions of the α_1 and α_2 NKA isoforms were distinguished based on differential sensitivity to ouabain bloackade [125, 190].

Intracellular [Na^+] was estimated in cells loaded with SBFI AM (Invitrogen Molecular Probes, Eugene, OR, USA), using whole-cell photometry as described [190]. Intracellular pH was determined by confocal microscopy in cells loaded with SNARF-1 AM (Invitrogen). SNARF was excited at 543 nm, and pH was calculated from the ratio of fluorescence at 580 and 640 nm using a calibration curve obtained in permeabilised cells.

4.2.3 Statistics

Cardiomyocyte data are expressed as mean values $\pm$ SEM. Statistical significance was calculated using paired or unpaired t-tests, and P values$<$0.05 were considered significant.

4.3 Model Development

4.3.1 Justification for the Addition of a Subsarcolemmal Compartment

In Chapter 3, we presented a mathematical modelling study of Ca^{2+} dynamics in the FF and 4-week KO cardiomyocytes. In that work, the FF and 4-week KO models were developed using the C57BL/6 framework developed in Chapter 2, which does not include the sub-sarcolemmal compartment and will be referred to as the lumped framework (the cytosolic and sub-sarcolemmal spaces were lumped into one cytosolic space). In

the lumped framework, all transmembrane currents are uniformly distributed and most Ca^{2+} handling proteins such as NCX and PMCA are regulated by cytosolic Ca^{2+} concentration. Such framework enabled parameterisation of Ca^{2+} handling mechanisms as explicit functions of $[Ca^{2+}]_i$ and the resulting simulated Ca^{2+} dynamics were found to be in good agreement with experimental observations requiring no further addition to model complexity. However, during parameterisation of the 7-week KO model, simulated $[Ca^{2+}]_i$ transient using the lumped framework was significantly higher than experimental measurements. This result motivated the detailed calculations of Ca^{2+} fluxes into and out of the cytosol, combined with thermodynamics consideration of NCX function as presented below. Such analysis revealed that, while it was sufficient to model the FF and 4-week KO results using the lumped framework, a more detailed model of Ca^{2+} handling with a sub-sarcolemmal space was required to capture the behavior of the 7-week KO.

During a $[Ca^{2+}]_i$ transient, peak $[Ca^{2+}]_i$ is reached within approximately 40 ms and the size of a $[Ca^{2+}]_i$ transient ($\Delta[Ca^{2+}]_i$) is determined by the net Ca^{2+} flux into the cytosol during this initial period as well as intracelular Ca^{2+} buffering properties. The net Ca^{2+} flux into the cytosol can in turn be calculated as the difference between total Ca^{2+} entry through LCCs and SR Ca^{2+} release, and Ca^{2+} removal through SERCA, NCX and PMCA. In the FF cardiomyocytes, assuming most of the Ca^{2+} entry and SR Ca^{2+} release occur within the first 40 ms of the cardiac cycle, Ca^{2+} entry through LCCs could be estimated from the integral of the LCC current (I_{CaL}) recorded during an AP clamp (0.096 pC/pF), yielding approximately 3.3 μM of Ca^{2+}. SR Ca^{2+} release could be estimated from the integral of SR Ca^{2+} uptake since Ca^{2+} release and uptake must be balanced over each cardiac cycle. Using the experimentally recorded $[Ca^{2+}]_i$ transient and fitted parameter values for SERCA to approximate and integrate the time course of Ca^{2+} uptake, the estimated total SR Ca^{2+} release and SR Ca^{2+} uptake during the first 40 ms were 37.7 and 4.4 μM, respectively, yielding a net SR Ca^{2+} release of 33.3 μM. Therefore, without taking into account of Ca^{2+} extrusion through NCX and PMCA

during the first 40 ms, the net Ca^{2+} flux into the cytosol had an estimated value of 36.6 μM.

On the other hand, given the observed $[Ca^{2+}]_i$ transient in the FF cardiomyocytes, the actual increase in the total concentration of Ca^{2+} ($\Delta[Ca^{2+}]_{total}$) can be calculated as:

$$\Delta[Ca^{2+}]_{total} = \left(\frac{B_{max} \cdot [Ca^{2+}]_p}{K_{d,buffer} + [Ca^{2+}]_p} + [Ca^{2+}]_p\right) - \left(\frac{B_{max} \cdot [Ca^{2+}]_d}{K_{d,buffer} + [Ca^{2+}]_d} + [Ca^{2+}]_d\right) \tag{4.1}$$

where B_{max} and $K_{d,buffer}$ denote the total concentration and Ca^{2+} affinity of buffers, respectively, $[Ca^{2+}]_p$ and $[Ca^{2+}]_d$ are the peak and diastolic $[Ca^{2+}]_i$, respectively. With a diastolic $[Ca^{2+}]_i$ of 0.113 ± 0.025 μM, a $\Delta[Ca^{2+}]_i$ of 0.343 ± 0.065 μM, and estimated B_{max} and $K_{d,buffer}$ values of 109 and 0.6 μM, respectively, $\Delta[Ca^{2+}]_{total}$ was calculated to be between 24.3 and 35.4 μM. The above calculations demonstrated that the net Ca^{2+} flux into the cytosol, without taking into account of Ca^{2+} extrusion, was close to the actual $\Delta[Ca^{2+}]_{total}$ required. This made it possible to use the lumped model framework for the FF model, in which NCX and PMCA sensed cytosolic Ca^{2+} concentration and only a small amount of Ca^{2+} extrusion occurred during the first 40 ms.

From similar calculations carried out with the 4-week and 7-week KO data, it was found that, in the 4-week KO, the net Ca^{2+} flux into the cytosol (13.7 μM) was close to the actual $\Delta[Ca^{2+}]_{total}$ (7.63 - 13.62 μM). However, this was the not the case for the 7-week KO, in which there was a significant mismatch between net Ca^{2+} flux into the cytosol (13.87 μM) and $\Delta[Ca^{2+}]_{total}$ required (5.09 - 7.38 μM), suggesting additional Ca^{2+} removal through trans-sarcolemmal Ca^{2+} extrusion.

As outlined in Section 1.1.3 “Intracellular Calcium Handling Mechanisms”, Ca^{2+} extrusion through NCX is thermodynamically favoured when the reversal potential of the exchanger (E_{NCX}) is more positive than the transmembrane potential (V_m). E_{NCX} is in turn governed by the Nernst potentials for Ca^{2+} (E_{Ca}) and Na^+ (E_{Na}). When the

lumped framework was used, E_{NCX} could be calculated using Eq. 1.2, where E_{Na} and E_{Ca} can in turn be calculated from Eq. 1.1. Here, $[Na^+]_i$ and $[Ca^{2+}]_i$ are the bulk cytosolic concentrations of Na^+ and Ca^{2+}, respectively. Using the experimentally measured $[Na^+]_i$ and $[Ca^{2+}]_i$ transients, E_{Na} and E_{Ca} during the first 40 ms of the cardiac cycle were estimated, as shown in Fig. 4.1A, for the FF, 4-week KO and 7-week KO. It can be seen that E_{Na} was similar between the FF and 4-week KO, but decreased significantly in the 7-week KO compared to the FF level, due to the 5 mM elevation in $[Na^+]_i$. On the other hand, the decrease in the $[Ca^{2+}]_i$ transient led to a gradual rise in E_{Ca}. The resulting E_{NCX} and APs reconstructed from the average recorded APDs (APD_{20} APD_{50} and APD_{70}) are shown in Fig. 4.1B. The shaded areas where E_{NCX} is below V_m indicate the duration of NCX in reverse mode. For the FF and 4-week KO, NCX operated in forward Ca^{2+} extrusion mode during the most of the 40 ms. In contrast, for the 7-week KO, NCX mostly operated in reverse mode, as a result of both the decrease in E_{NCX} and the prolonged AP. This meant that using the lumped framework, there was little Ca^{2+} extrusion during the first 40 ms of the cardiac cycle as governed by the thermodynamics of the exchanger, such that total Ca^{2+} flux into the cytosol exceeded the actual $\Delta[Ca^{2+}]_{total}$. As a result, simulated $[Ca^{2+}]_i$ transient would inevitably be greater than that observed experimentally.

The above analysis thus motivated the addition of subsarcolemmal space, so that transmembrane proteins sense ion concentrations in their respective sub-spaces. In this framework, $[Ca^{2+}]_i$ transient in the 7-week KO can be accurately matched as $[Ca^{2+}]_{jc}$ and $[Ca^{2+}]_{sl}$ rise much faster and higher than $[Ca^{2+}]_i$ thus driving NCX into the Ca^{2+} extrusion mode much earlier (see Fig. 4.2).

A subsarcolemmal compartment was thus incorporated into the previously developed mathematical framework of Ca^{2+} dynamics and APs in murine ventricular myocytes [118], following the approach of Shannon et al. [178]. Such addition allowed differentially distributed proteins in the cell membrane to sense ion concentrations in their re-

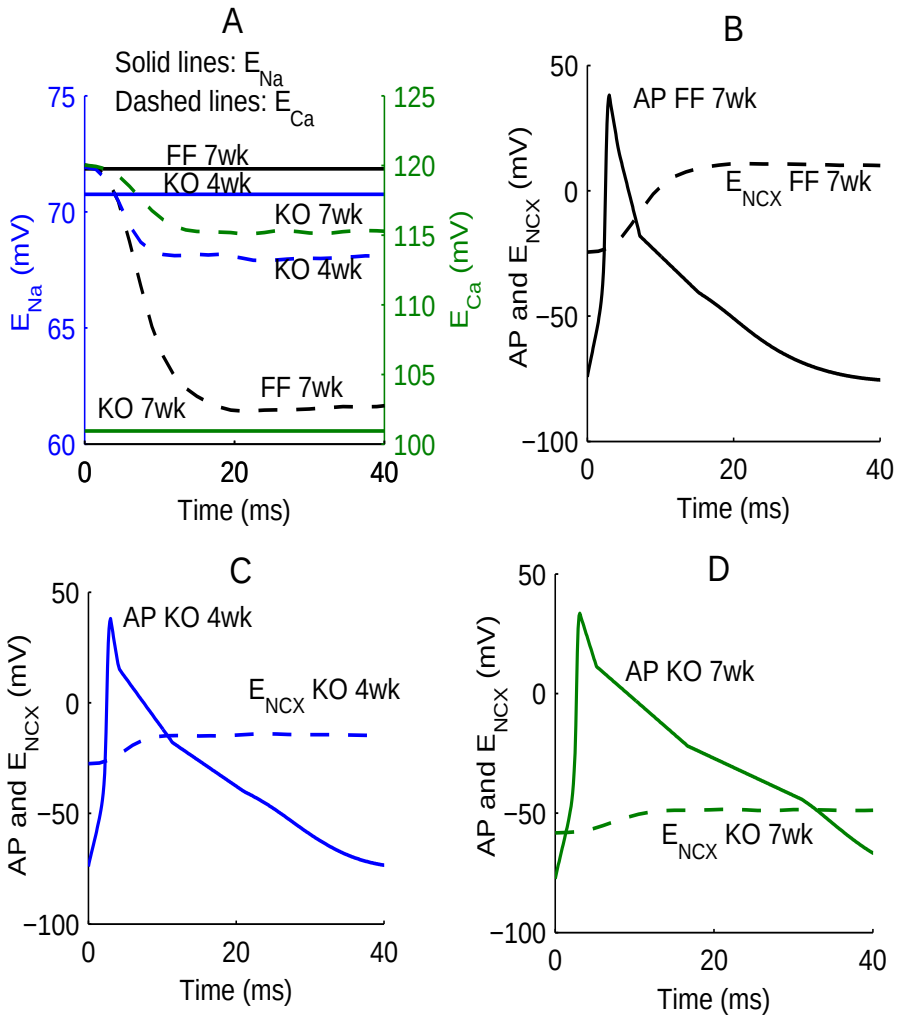

FIGURE 4.1: A: Reversal potentials for Na^+ (E_{Na}) and Ca^{2+} (E_{Ca}) estimated from the experimentally measured $[Na^+]_i$ and $[Ca^{2+}]_i$ in the FF, 4-week and 7-week KO during a cardiac cycle at 1 Hz. B-D: NCX reversal potential (E_{NCX}) calculated as $3\times E_{Na}$-$2\times E_{Ca}$ for the FF (B), 4-week (C) and 7-week KO (D) models, and their respective APs reconstructed from experimentally measured average APDs. The durations in which the transmembrane potential is greater than E_{NCX} indicate Ca^{2+} influx through NCX is thermodynamically favoured.

spective sub-spaces that could be substantially different from the bulk cytosolic concentration during an AP, as shown in Fig. 4.2. Since the formulation of Shannon et al. [178] was originally developed for rabbit ventricular myocytes, some modifications were made based on experimental data from mice and rats. These include changes to the geometrical parameters, diffusion parameters and distribution of the ion channels, as explained below.

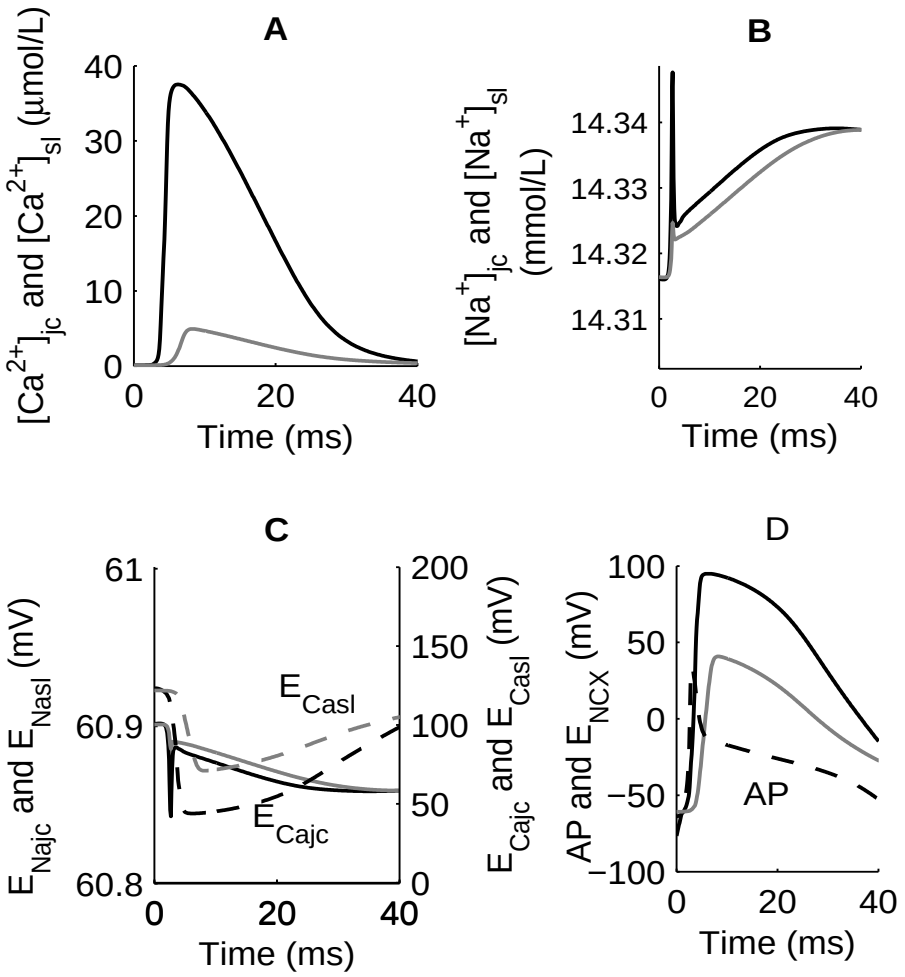

FIGURE 4.2: A: Simulated $[Ca^{2+}]_{jc}$ (black) and $[Ca^{2+}]_{sl}$ (grey) at 1 Hz in the 7-week KO model using the framework with a subsarcolemmal compartment. B. Simulated $[Na^{+}]_{jc}$ (black) and $[Na^{+}]_{sl}$ (grey) at 1 Hz in the 7-week KO model using the framework with a subsarcolemmal compartment. C: Reversal potentials for Na^{+} (E_{Na}) (solid lines) and Ca^{2+} (E_{Ca}) (dashed lines) in the junctional (black) and sarcolemmal membranes (grey), calculated from the simulated concentrations in A and B. B: NCX reversal potential (E_{NCX}) in the junctional (black) and sarcolemmal (grey) membranes, calculated as $3\times E_{Na}$-$2\times E_{Ca}$, as well as the simulated AP.

4.3.2 Geometrical Considerations

The cell membrane is divided into two areas: the junctional membrane (A_{jc}), i.e. the area occupied by transverse tubules (T-tubules), and the surface sarcolemmal area (A_{sl}). In mouse ventricular myocytes, formamide-induced detubulation in mouse ventricular

myocytes has been reported to result in a 30% reduction in membrane capacitance [18]. Therefore in our model, the areas of the junctional membrane (A_{jc}) and the surface sarcolemma (A_{sl}) were set to be 30 and 70% of the total cell membrane area (A_{tot}:1.47 $\times$ 10^{-4} cm^2), respectively.

The cell volume (2.2×10^{-5} μL) [148] is separated into five compartments, four of which (junctional space or dyadic space (referred to as jc here), junctional SR (JSR), network SR (NSR) and the cytosolic space (cyt)) are the same as those in Chapter 2. An additional subsarcolemmal space (sl), located directly underneath the surface sarcolemma area and occupying 2% of the cell volume, was added to the model.

4.3.3 Diffusion Parameters

Following the approach of Shannon et al. [178], the rate of diffusion of ions (Na^+ and Ca^{2+}) from space jc to space sl was defined as:

$$J_{I_{jcsl}} = D_{I_{jcsl}} \cdot A_{jcsl} \cdot \frac{[I]_{jc} - [I]_{sl}}{\Delta x_{jcsl}} \tag{4.2}$$

where $D_{I_{jcsl}}$ is the diffusion coefficient for the ion, A_{jcsl} is the interface area between the junction space and the subsarcolemmal space, Δx_{jcsl} is the distance between the centres of the two compartments, and $[I]_{jc} - [I]_{sl}$ is the difference in ion concentrations. Similarly, the rate of diffusion of ions from space sl to space cyt was defined as:

$$J_{I_{slcyt}} = D_{I_{slcyt}} \cdot A_{slcyt} \cdot \frac{[I]_{sl} - [I]_{i}}{\Delta x_{slcyt}} \tag{4.3}$$

The diffusion coefficients for Na^+ and Ca^{2+} ions in equations 4.2 and 4.3 were set to the same values as those in the Shannon et al. model [178], as listed in the

Appendices. The diffusion distances and interface areas were adjusted from the values used by Shannon et al., according to the differences in geometry. Each junction was considered to be a disk with a radius of 0.16 μm with a height of 0.015 μm [178]. The cross-sectional area is therefore 0.08 μm^2. Given that A_{jc} is equal to 4410 μm^2 (30% of A_{tot}), the total number of junctions is thus approximately 55000. This yielded an even spacing of 0.78 μm between junctions, which is 35% smaller compared to the 1.2 μm spacing in the Shannon et al. model. Therefore, the distance of diffusion to the middle of the SL compartment was reduced by 35% from 0.5 to 0.325 μm (See Fig 1.B in [178]. The side area of a junction is 0.015 μm^2, giving a total interface area of 8.3×10^{-6} cm^2 for diffusion from junctional space to subsarcolemmal space. The distance of diffusion from the subsarcolemmal space to the cytosol was kept unchanged from the value used by Shannon et al. (0.45 μm), and the interface area was approximated by the area of the surface sarcolemma (1.03×10^{-4} cm^2, 70% of A_{tot}).

The addition of the subsarcolemmal compartment with the aforementioned Ca^{2+} diffusion parameters resulted in an approximately ten-fold increase in the magnitude of $[Ca^{2+}]_{jc}$, compared to the lumped model. However, coorperative binding of Ca^{2+} to RyR with a hill coefficient of 4 for transition from state C_1 to state O_1 and 3 for transition from state O_1 to state O_2 in the model meant that the resulting forward rate constants would be approximately 10^4 and 10^3 times faster, respectively. This resulted in a significantly prolonged opening time of the RyRs and instability of the model (the proportion of RyRs in state C dropped transiently to just below zero in some simulations). We therefore adjusted the Ca^{2+}-sensitivity of the RyR to ensure the proper functioning of the channel, as suggested by Jafri et al. [98].

K^+ ion dynamics were not compartmentalised, following the approach of Shannon et al. [178].

4.3.4 Differential Distribution of Transmembrane Ion Channels

In adult mouse heart, two isoforms of the NKA α-subunit (α_1 and α_2) have been found, which are distributed differentially in the T-tubule and surface sarcolemmal membranes. In the study by Berry et al. [18], preferential inhibition of the high ouabain affinity α_2 subunits in control and detubulated mouse ventricular myocytes revealed that the current densities of $I_{NKA,\alpha1}$ and $I_{NKA,\alpha2}$ in the T-tubules are 1.37 and 5.57 times greater, respectively, than those in the surface sarcolemma. In our model, $I_{NKA,\alpha1}$ and $I_{NKA,\alpha2}$ were computed separately, and the data by Berry et al. [18] were used to define the maximum $I_{NKA,\alpha1}$ and $I_{NKA,\alpha2}$ in the junctional and sarcolemma areas in the model ($I^{max}_{NKA,\alpha1}$(jc) = 1.236·$I^{max}_{NKA,\alpha1}$, $I^{max}_{NKA,\alpha1}$(sl) = 0.899 ·$I^{max}_{NKA,\alpha1}$, $I^{max}_{NKA,\alpha2}$(jc) = 2.35 ·$I^{max}_{NKA,\alpha2}$, $I^{max}_{NKA,\alpha2}$(sl) = 0.422· $I^{max}_{NKA,\alpha2}$).

The current density of NCX in the junctinal membrane was found to be three times greater than that in the surface sarcolemma, based on I_{NCX} measurements from detubulated rat ventricular myocytes [46]. Yang et al. [211] also found very little NCX current in detubulated rat ventricular myocytes, indicating the majority of the channels are located on the T-tubules. Therefore, the maximum NCX activity on the junctional membrane was set to be three times greater than on the surface sarcolemma (V^{max}_{NCX}(jc) = 1.93·V^{max}_{NCX}, V^{max}_{NCX}(sl) = 0.6·V^{max}_{NCX}).

The distribution of LCCs has been assessed by Scriven et al. [172] in rat ventricular myocytes. Using indirect immunofluorescence, it was found that the majority of LCCs are located on the T-tubules, with very little immunolabelling on the surface sarcolemma. In another study in rat ventricular myocytes [100], detubulation revealed that LCC density is 8.7 times greater on the T tubules than on the surface membrane (P_{CaL}(sl) = 0.1·P_{CaL}(jc). Therefore, in our model, the permeability of the channels on the junctional membrane is nine times greater than on the surface sarcolemma. It was also assumed in the model that,

Ca^{2+}-induced-Ca^{2+} release is only triggered by Ca^{2+} entry through the LCCs located on the junctional membrane.

The distribution of the fast Na^{+} channels on the cell membrane was assumed to be uniform in our model, consistent with the observations by two different groups [211, 31] both in rat ventricular myocytes. The distribution of PMCA is currently unknown, although Ca^{2+} extrusion through PMCA was found to be present in detubulated rat ventricular myocytes [211]. This protein was thus assumed to be uniformly distributed on the cell membrane. Relatively few studies have been carried out on the distribution of K^{+} channels, which were also assumed to be uniformly distributed.

4.3.5 Buffering

Ca^{2+} buffering parameters in the junctional space, cytosolic space and the SR were kept the same as those in our previous models in Chapter 3. Buffering parameters for the additional subsarcolemmal space were the same as those used in the junctional and cytosolic spaces. However, it is worth noting that while there are membrane-bound buffers in the junctional and sub-sarcolemmal spaces, tropinin, the major contributor to Ca^{2+} buffering, is not present in these compartments. Therefore, this simplified buffering description may overestimate the amount of Ca^{2+} buffering inside the cell. Nevertheless, since the volumes of junctional and sub-sarcolemmal spaces are small compared to the cytosolic volume, buffering in these two compartments make relatively minor contributions to the total Ca^{2+} buffering capacity, and thus would not have a significant effect on the overall simulated $[Ca^{2+}]_i$ transient. This assumption was confirmed via a sensitivity analysis in which Ca^{2+} buffering in the junctional space and sub-sarcolemmal spaces was set to zero in the FF model, showing minimal changes in the simulated $[Ca^{2+}]_i$ transient.

Experimental data on Na^{+} buffering is sparse, although in one study [47] in rabbit

ventricular myocytes Na^+ buffering capacity has been reported to be very low (approximately 1.3). In our model, Na^+ buffering was included following the same formulations and parameter values as those in the Shannon et al. model [178].

4.3.6 Model Parameterisation

The Na^+/K^+-ATPase (FF and 4-week KO)

In the current study, I_{NKA} in the FF and 7-week KO cardiomycytes were measured in dialyzed cells ($[Na^+]_i$ = 50 mM) under whole-cell voltage clamping at -50 mV holding potential. The current was activated by switching from a K^+-free to K^+-containing external solution (5.4 mM $[K^+]_o$), and $I_{NKA,\alpha1}$ and $I_{NKA,\alpha2}$ were differentiated using ouabain which blocks the α_2 isoform.

Before fitting the NKA formulations to our I_{NKA} measurements, a range of existing experimental data from mice, and in some cases rats, were used to define the voltage- and $[Na^+]_i$-dependent properties of the current. The voltage-dependence of $I_{NKA,\alpha1}$ and $I_{NKA,\alpha2}$ was parameterised to experimental measurements by Swift et al. [190] in rat ventricular myocytes at 37 ^oC, as shown in Fig. 4.3. The activation of NKA by intracellular Na^+ has been studied by various groups, and a wide range of values for the affinity constant (K_m) have been reported. For example, the mean K_m values for rat ventricular myocytes at physiological temperatures range from 10.2 mM [47], 17.0 mM [46] to 40 mM [186]. These differences may, at least partially, be explained by variations in actual subsarcolemmal [Na^+] which may not always be accurately controlled by the [Na^+] in the pipette solution. In normal mouse ventricular myocytes, Berry et al. [18] measured total, α_1 and α_2-mediated Na^+ effluxes as a function of $[Na^+]_i$ at 35 ^oC. The Na^+ affinity of the total NKA function was equal to 16.6 $\pm$ 0.2 mM with similar K_m values for the α_1 and α_2 subunits (16.6 $\pm$ 0.8 and 16.7 $\pm$ 2.6 mM, respectively). The hill coefficient (nH_{NKA}) of total NKA function was equal to 2.3 $\pm$ 0.1, with values of 2.3 $\pm$

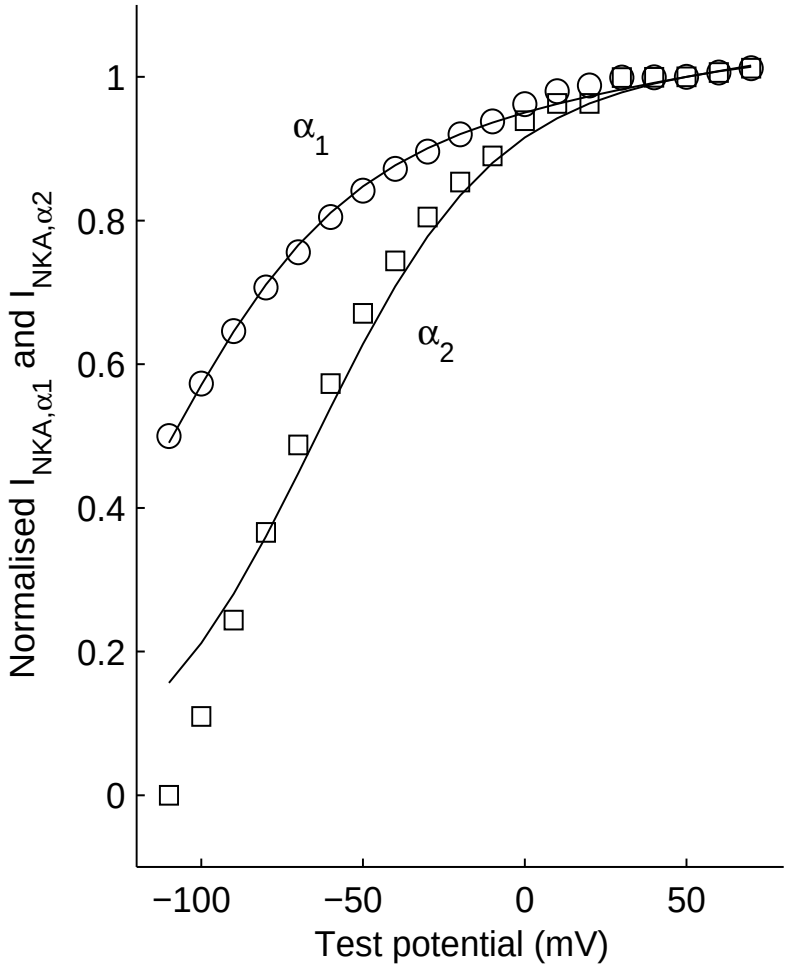

FIGURE 4.3: Experimentally measured I-V relationship of the α_1 (circles) and α_2 (squares) isoforms of NKA in rat ventricular myocytes [190]. Superimposed (solid lines) are the fitted I-V relationship.

0.1 and 4.1 $\pm$ 0.8, for the α_1 and α_2 subunits, respectively. In another study, Han et al. [81] reported a K_m of 18.3 $\pm$ 2.7 mM and an nH_{NKA} of 2.8 $\pm$ 0.2 for the overall NKA function in mouse ventricular myocytes at room temperature.

Based on the experimental evidence above, the K_m and nH_{NKA} values for the α_1 and α_2 subunits were set to be equal in the FF model. Various combinations of K_m and nH values within the range of experimental data were then tested in whole cell simulations and the resulting $[Na^+]_i$ levels compared with experimentally observed level in FF cardiomy-

ocytes ($[Na^+]_i$ = 9.6 $\pm$ 1.4 mM). For each combination, we first parameterised $I^{max}_{NKA,\alpha1}$ and $I^{max}_{NKA,\alpha2}$ based on our measurements of $I_{NKA,\alpha1}$ (2.61 $\pm$ 0.10 pA/pF) and $I_{NKA,\alpha2}$ (0.81 $\pm$ 0.09 pA/pF) in dialyzed cells at -50 mV. The models of α_1 and α_2 NKA isoforms were then incorporated into the previously developed model framework [118] for simulations of $[Na^+]_i$ under field-stimulations at 1 Hz. As shown in Fig. 4.4, experimentally measured $[Na^+]_i$ value was only matched with high nH and high K_m values. For this reason, we set nH to 3 and K_m to 21 mM in our model, with fitted $I^{max}_{NKA,\alpha1}$ and $I^{max}_{NKA,\alpha2}$ equal to 5.2 and 1.95 pA/pF, respectively. NKA parameters for the 4-week KO model were kept identical to those in the FF model.

The Na+/K$^+$-ATPase (7-week KO)

In KO cardiomyocytes, $I_{NKA,\alpha1}$ and $I_{NKA,\alpha2}$ during voltage-clamp experiments were decreased from their FF values of 2.61 $\pm$ 0.10 and 0.81 $\pm$ 0.09 pA/pF, respectively, to 2.35 $\pm$ 0.10 and 0.45 $\pm$ 0.06 pA/pF, respectively. At the same time, $[Na^+]_i$ level during 1 Hz field-stimulation was also higher (14.6 $\pm$ 1.1 mM) compared to the FF (9.6 $\pm$ 1.4 mM), which was initially thought to result only from NKA down-regulation. However, when $I^{max}_{NKA,\alpha1}$ and $I^{max}_{NKA,\alpha1}$ were fitted to experimental measurements ($I^{max}_{NKA,\alpha1}$(7-week KO) = 4.4 pA/pF and $I^{max}_{NKA,\alpha2}$ (7-week KO) = 0.9 pA/pF), simulated $[Na^+]_i$ under 1 Hz field-stimulations was increased by about 2 mM from the FF value, as shown in Fig. 4.4.

We hypothesized two mechanisms could potentially explain the additional increases in $[Na^+]_i$. The first mechanism could be a decrease in the Na^+ affinity of NKA (an increase in K_m). This means a higher $[Na^+]_i$ level would be required to achieve the same level of Na^+ efflux, which should be equal to Na^+ influx at steady state [47]. The effect of K_m on $[Na^+]_i$, with NKA down-regulation kept at the experimentally observed levels, is shown in Fig. 4.5A, demonstrating an almost linear increase in $[Na^+]_i$ with increasing K_m. Experimentally measured level of $[Na^+]_i$ was matched with K_m equal to 29 mM.

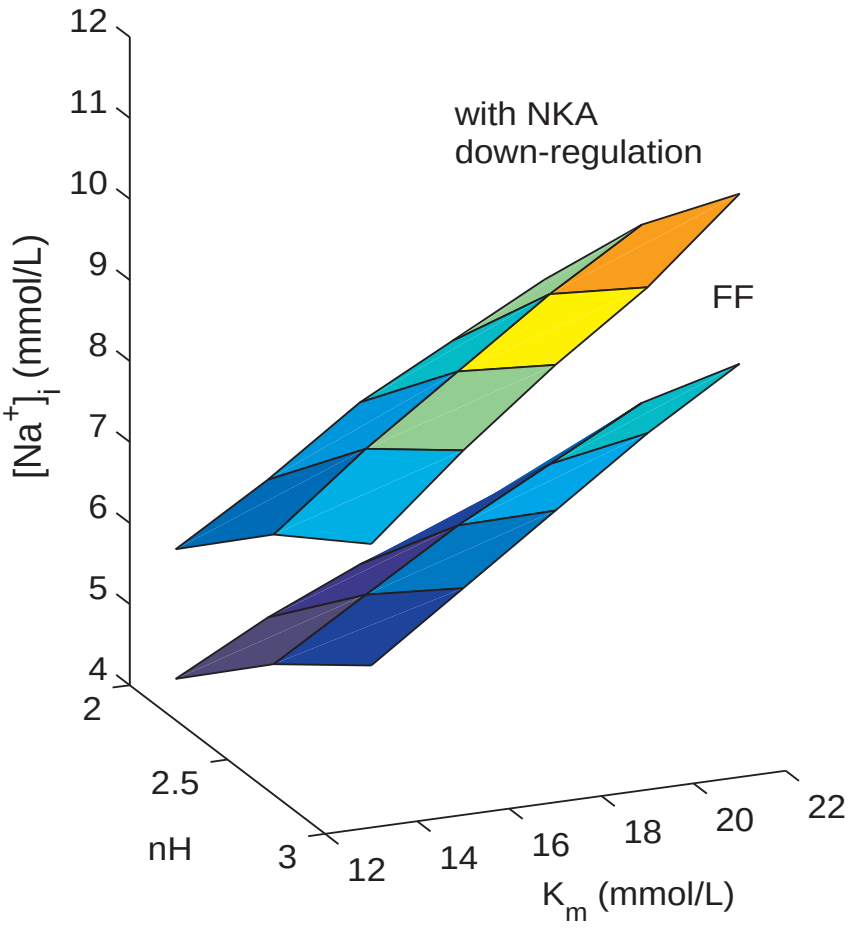

FIGURE 4.4: Simulated $[Na^+]_i$ at 1 Hz pacing frequency with various combinations of the Na^+ affinity (K_m) and the hill coefficient (nH_{NKA}). For FF, $I^{max}_{NKA,\alpha1}$ and $I^{max}_{NKA,\alpha2}$ were fitted to experimentally measurd $I_{NKA,\alpha1}$ and $I_{NKA,\alpha2}$, respectively (see explanation in text). The effect of NKA-downregulation was examined by adjusting $I^{max}_{NKA,\alpha1}$ and $I^{max}_{NKA,\alpha2}$ to match the experimentally observed reductions in $I_{NKA,\alpha1}$ and $I_{NKA,\alpha2}$.

The second mechanism could be an increase in Na^+ influx, possibly through mechanisms such as the fast Na^+ channels, the persistent Na^+ channels and the Na^+/H^+ exchanger (NHE). However, since increases in fast and persistent Na^+ currents were not observed experimentally [125], they were not considered as likely explanations. On the other hand, intracellular acidosis has the potential to cause a substantial increase in Na^+ influx through NHE and hence $[Na^+]_i$ elevation, as demonstrated in Fig. 4.5B. This model

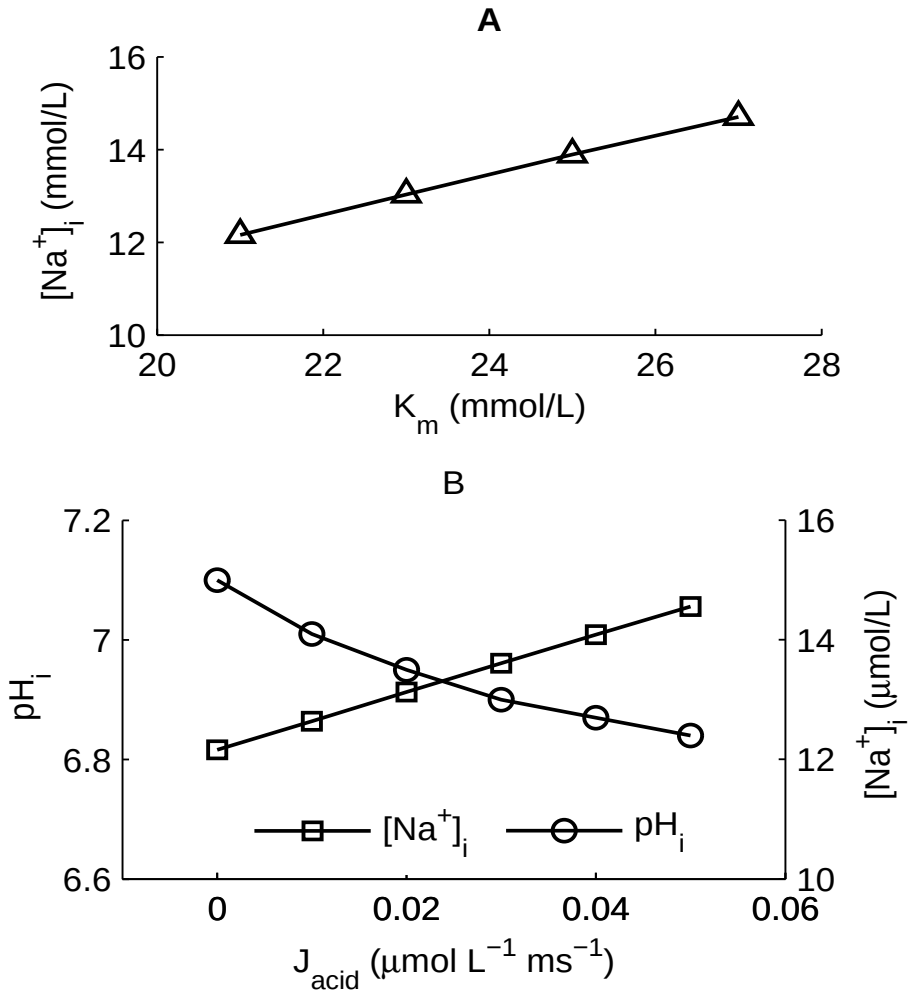

FIGURE 4.5: A. Simulated $[\mathrm{Na}^+]_\mathrm{i}$ at 1 Hz pacing frequency as a function of the Na^+ affinity of NKA. B. Simulated $\mathrm{pH_i}$ (circles) and $[\mathrm{Na}^+]_\mathrm{i}$ (squares) as a function of the size of the intracellular acid source.

prediction prompted additional experimental measurements of $\mathrm{pH_i}$, which revealed significantly increased acidity in KO 7-week cardiomyocytes with $\mathrm{pH_i}$ reduced to 6.91 ± 0.07 (*vs* 7.19 ± 0.08 in FF, $P<0.05$).

Intracellular pH Regulation

A previously developed model of intracellular pH regulation for rat ventricular myocytes [145] was introduced into the FF, 4-week and 7-week KO models. Fluxes through the Na^+/bicarbonate cotransporter and anion exchanger were set to zero in all three models,

since all our experiments were conducted using bicarbonate-free external perfusion solutions containing HEPES. Extracellular ion concentrations and pH were adjusted according to the experimental setup (see Materials and Methods). To fit the parameters for NHE we made use of the fact that total Na^+ influx and efflux per cardiac cycle must be balanced at steady state. Specifically, we first estimated the integral (over one cardiac cycle) of the Na^+ efflux through NKA and Na^+ influx through non-NHE channels in the FF and 7-week KO models by running the models, with $[\mathrm{Na}^+]_\mathrm{i}$ set to be constant at the experimentally measured value (FF: 9.6 mM , 7-week KO: 14.6 mM) and with the parameterised Ca^{2+} handling components (outlined below). The integral of the Na^+ influx through NHE in each model was then taken as the difference between the integrals of Na^+ efflux and non-NHE Na^+ influx. Since the rate of Na^+ influx through NHE does not change significantly during each cardiac cycle, it could then be approximated from the calculated integral (FF model: 0.0047 μM/ms and 7-week KO model: 0.051 μM/ms). Finally, the affinity of NHE to proton (K_i = 0.411 μM in all three models) and the hill coefficient (nH_{NHE} = 2.905 in all three models) were fitted to the above estimated Na^+ influx rates, at the experimentally observed pH_i levels in the FF and 7-week KO models. In addition, proton influx through PMCA in exchange for Ca^{2+} extrusion was accounted for in the model, assuming a stoichiometry of $1\mathrm{Ca}^{2+}$:$2\mathrm{H}^+$ [146].

Intracellular acidosis in the 7-week KO model was induced by the introduction of an acid flux from an intracellular acid-producing source (J_{acid} was set to 0.045 μM/ms), which could be attributed to compromised metabolism such as glycolysis. To maintain charge balance, an equal amount of intracellular anion flux (J_A) was also introduced. Build-up of $[A^-]_i$ was prevented by including a constant-field sarcolemmal flux extruding A^- from the cytosol which was taken into account when calculating changes in transmembrane potential. The membrane permeability to A^- was set to be 1×10^{-7} cm/s , such that the electrogenic transmembrane flux of A^- did not result in a significant change. It was also assumed that the A^- ions extruded from the cell was rapidly transported away from the

cell such that $[A^-]_o$ was approximately zero.

Parameterisation of NCX, PMCA, SERCA and L-type Calcium Current

In Chapter 2, we described a method for parameterising NCX, PMCA and SERCA directly using experimentally measured $[Ca^{2+}]_i$ transients in the presence of caffeine and during field stimulations, provided that Ca^{2+} fluxes through NCX and PMCA are functions of cytosolic Ca^{2+} concentrations. In the current model, NCX and PMCA respond to sub-space (subsarcolemmal and junction spaces) Ca^{2+} concentrations. As a result, parameterisation of NCX, PMCA and SERCA for the current model required solving a system of ordinary differential equations and matching the resulting decay of $[Ca^{2+}]_i$ to that measured experimentally, as explained below.

Generally speaking, the dynamics of Ca^{2+} concentrations in the cytosolic ($[Ca^{2+}]_i$), subsarcolemmal ($[Ca^{2+}]_{sl}$) and junctional spaces ($[Ca^{2+}]_{jc}$) during the later decay phase of a $[Ca^{2+}]_i$ transient can be described as:

$$\frac{d[Ca^{2+}]_i}{dt} = B_i \cdot (\frac{J_{Ca,slcyt}}{V_{cyt}} - J_{SERCA}) \tag{4.4}$$

$$\frac{d[Ca^{2+}]_{sl}}{dt} = B_{sl} \cdot (-\frac{J_{Ca,slcyt}}{V_{sl}} + \frac{J_{Ca,jcsl}}{V_{sl}} + J_{Casl}) \tag{4.5}$$

$$\frac{d[Ca^{2+}]_{jc}}{dt} = B_{jc} \cdot (-\frac{J_{Ca,jcsl}}{V_{jc}} + J_{Cajc}) \tag{4.6}$$

where V_{cyt}, V_{sl} and V_{jc} are the volumes of the cytosolic, subsarcolemmal and junctional spaces, respectively; J_{serca} is the rate of net uptake through SERCA; $J_{Ca,jcsl}$ and $J_{Ca,slcyt}$, calculated according to Eqs. 4.2-4.3, are the rates of Ca^{2+} diffusion from junctional space to subsarcolemmal space, and from subsarcolemmal space to cytosol, respectively; J_{Casl} and J_{Cajc} are the total fluxes of Ca^{2+} across the surface sarcolemmal membrane and the

junctional membrane, respectively. Finally, B_i, B_{sl} and B_{jc} account for Ca^{2+} buffering in the cytosol, subsarcolemmal and junctional spaces and are calculated as:

$$B_i = (1 + \frac{B_{max} \cdot K_d}{(K_d + [Ca^{2+}]_i)^2})^{-1} \tag{4.7}$$

$$B_{sl} = (1 + \frac{B_{max} \cdot K_d}{(K_d + [Ca^{2+}]_{sl})^2})^{-1} \tag{4.8}$$

$$B_{jc} = (1 + \frac{B_{max} \cdot K_d}{(K_d + [Ca^{2+}]_{sl})^2})^{-1} \tag{4.9}$$

During the decay phase of a caffeine-induced $[Ca^{2+}]_i$ transient, J_{SERCA} in Eq. 4.4 is equal to zero. J_{Casl} and J_{Cajc} are the sums of Ca^{2+} fluxes through NCX and PMCA located on the surface sarcolemma and junctional membrane, respectively, and taking into account a small background Ca^{2+} flux. Given initial values of $[Ca^{2+}]_i$, $[Ca^{2+}]_{sl}$ and $[Ca^{2+}]_{jc}$, Eqs. 4.4-4.6 can thus be solved to give the time course of decay of $[Ca^{2+}]_i$. The relative contributions of NCX and PMCA were calculated as the ratio between the integrals of the simulated J_{NCX} and J_{PMCA}.

For parameterisation, initial $[Ca^{2+}]_i$ was set equal to experimentally measured $[Ca^{2+}]_i$ at 100 ms post-peak during the caffeine-induced $[Ca^{2+}]_i$ transient. Initial $[Ca^{2+}]_{sl}$ and $[Ca^{2+}]_{jc}$ were first assumed to be equal to $[Ca^{2+}]_i$, assuming Ca^{2+} movement across the different compartments occur on a much faster time scale than Ca^{2+} removal fluxes. Maximum NCX activity (V_{NCX}^{max}), maximum Ca^{2+} current through PMCA (I_{PMCA}^{max}) and the Ca^{2+} affinity of PMCA ($K_{m,PMCA}$) were parameterised to minimise the cost function, which takes into account both the difference between simulated and experimentally measured decay of $[Ca^{2+}]_i$, and the difference between the simulated and experimentally estimated contributions of NCX and PMCA. During fitting, the concentrations of $[Na^+]$ in the different compartments were set to be equal to the experimentally measured cytosolic

$[Na^+]$ (FF and 4-week KO: $[Na^+]_{jc}$ = $[Na^+]_{sl}$ = $[Na^+]_i$ = 9.6 mM, 7-week KO: $[Na^+]_{jc}$ = $[Na^+]_{sl}$ = $[Na^+]_i$ = 14.6 mM).

During the decay phase of a field-stimulated $[Ca^{2+}]_i$ transient at 1 Hz, J_{SERCA} in Eq. 4.4 is non-zero, and V_{NCX}^{max}, I_{PMCA}^{max} and $K_{m,PMCA}$ fitted from above were treated as constants in Eqs. 4.4-4.6. The experimentally measured decay of $[Ca^{2+}]_i$ can thus be used to parameterise the maximum uptake rate of SERCA (V_{up}), its Ca^{2+} affinity ($K_{m,up}$), and the small SR Ca^{2+} leak flux (J_{leak}, assumed to be constant during fitting), with initial $[Ca^{2+}]_i$, $[Ca^{2+}]_{sl}$ and $[Ca^{2+}]_{jc}$ set equal to the experimentally measured $[Ca^{2+}]_i$ at 90 ms post-peak.

The above fitted NCX, PMCA and SERCA parameter values were then incorporated into the fitting of the LCC, using the same approach as described in Chapter 2.

The assumption of equal initial Ca^{2+} concentrations in the subsarcolemmal, junctional and cytosolic spaces were then tested by incorporating the above parameter values into the whole-cell framework as shown in Fig 4.6 (A-B for FF, C-D for KO). It can be seen that during most of the decay phase of the simulated transients, $[Ca^{2+}]_{jc}$ and $[Ca^{2+}]_{sl}$ were not equal to, but were linearly related to $[Ca^{2+}]_i$. Interpolation of the linear relationship at the experimentally measured $[Ca^{2+}]_i$ level thus would give a more accurate initial $[Ca^{2+}]_{jc}$ and $[Ca^{2+}]_{sl}$ values for parameterisation. Table 4.1 shows the initially fitted parameter values with $[Ca^{2+}]_{jc}$ and $[Ca^{2+}]_{sl}$ assumed to be equal to $[Ca^{2+}]_i$, and then with interpolated $[Ca^{2+}]_{jc}$ and $[Ca^{2+}]_{sl}$ values.

A similar approach was used for parameterisation of NCX, PMCA, SERCA and the L-type Ca^{2+} current in the KO model. Since caffeine-induced $[Ca^{2+}]_i$ transient in the KO cardiomyoycytes is very small in magnitude, we chose to use experimentally measured field-stimulated $[Ca^{2+}]_i$ transient (0.5 Hz) in the presence of caffeine to parameterise NCX and PMCA for the KO. Table 4.1 compares the final fitted parameter values between the

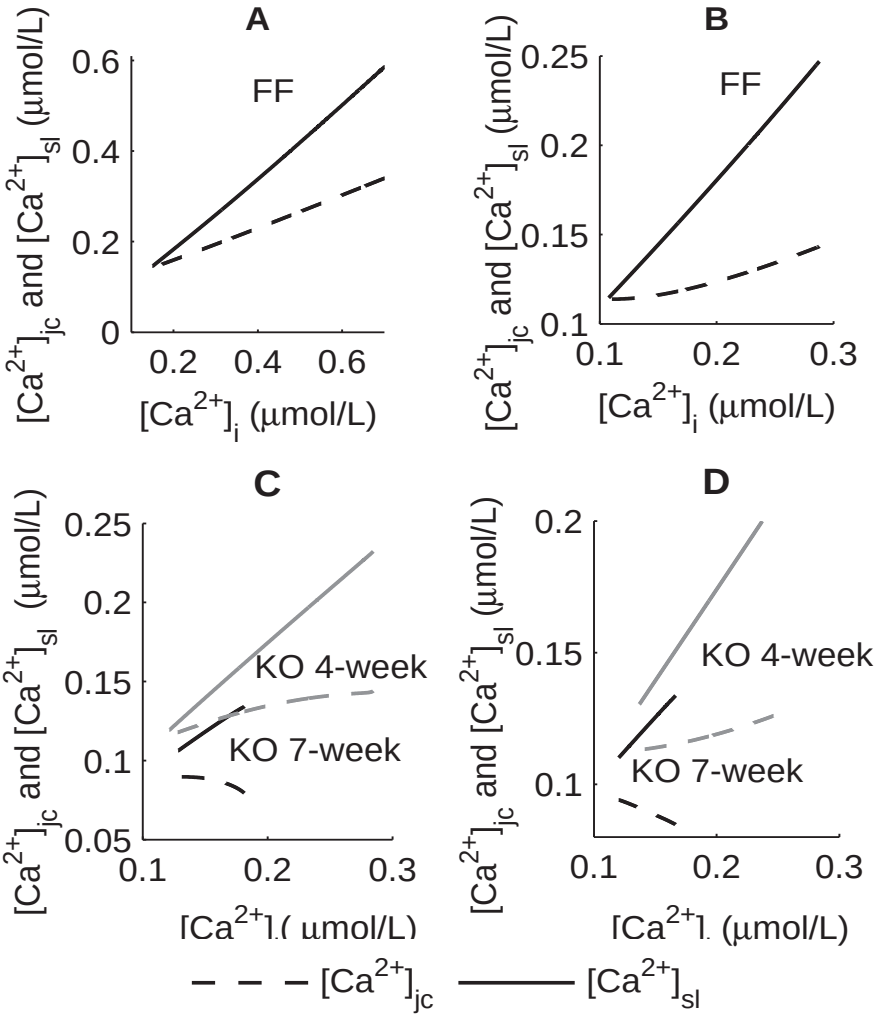

FIGURE 4.6: A. Simulated relationship between $[\mathrm{Ca}^{2+}]_{\mathrm{sl}}$ (solid lines), $[\mathrm{Ca}^{2+}]_{\mathrm{jc}}$ (dashed lines) and $[\mathrm{Ca}^{2+}]_{\mathrm{i}}$ during the decay phase of a caffeine-induced $[\mathrm{Ca}^{2+}]_{\mathrm{i}}$ transient in the FF model. B. Simulated relationship between $[\mathrm{Ca}^{2+}]_{\mathrm{sl}}$ (solid lines), $[\mathrm{Ca}^{2+}]_{\mathrm{jc}}$ (dashed lines) and $[\mathrm{Ca}^{2+}]_{\mathrm{i}}$ during the decay phase of field-stimulated $[\mathrm{Ca}^{2+}]_{\mathrm{i}}$ transient at 1 Hz in the FF model. C. Simulated relationship between $[\mathrm{Ca}^{2+}]_{\mathrm{sl}}$ (solid lines), $[\mathrm{Ca}^{2+}]_{\mathrm{jc}}$ (dashed lines) and $[\mathrm{Ca}^{2+}]_{\mathrm{i}}$ in the KO 4-week model, during the decay phase of a caffeine-induced $[\mathrm{Ca}^{2+}]_{\mathrm{i}}$ transient, and in the KO 7-week model during the decay phase of a field-stimulated $[\mathrm{Ca}^{2+}]_{\mathrm{i}}$ transient at 0.5 Hz in the presence of caffeine. D. Simulated relationship between $[\mathrm{Ca}^{2+}]_{\mathrm{sl}}$ (solid lines), $[\mathrm{Ca}^{2+}]_{\mathrm{jc}}$ (dashed lines) and $[\mathrm{Ca}^{2+}]_{\mathrm{i}}$ in the KO 4-week and KO 7-week models, during the decay phase of a field-stimulated $[\mathrm{Ca}^{2+}]_{\mathrm{i}}$ transient at 1 Hz.

FF and the KO models.

TABLE 4.1: Fitted parameter values for NCX, PMCA and SERCA. First fit was obtained by setting initial $[Ca^{2+}]_{jc}$ and $[Ca^{2+}]_{sl}$ equal to the experimentally measured level of $[Ca^{2+}]_i$ at approximately 100 ms post-peak $[Ca^{2+}]_i$. Second fit was obtained by using the intepolated $[Ca^{2+}]_{jc}$ and $[Ca^{2+}]_{sl}$ values, according to the relationship in Fig. 4.6, as initial conditions.

	FF		KO	
	First fit	Second fit	First fit	Second fit
V_{NCX}^{max} (μM/ms)	1.1009	1.1591	6.4554	6.4116
I_{PMCA}^{max} (pA/pF)	0.3509	0.5644	1.1299	1.1231
$K_{m,PMCA}$ (μM)	0.2544	0.3506	0.3506 (fixed)	0.3506 (fixed)
V_{up} (μM/ms)	0.35	0.35	0.07	0.07
$K_{m,up}$ (μM)	0.4928	0.4928	0.4928 (fixed)	0.4928 (fixed)

4.4 Results

4.4.1 Validation

Simulated $[Ca^{2+}]_i$ transients at 1 Hz in the FF, 4-week KO, and 7-week KO models are shown in Fig. 4.7A. Key characteristics are summarised in Table 4.2. Briefly, simulated diastolic $[Ca^{2+}]_i$ in the FF, 4-week KO and 7-week KO models were 0.092, 0.123 and 0.126 μM, respectively, compared to experimental values of 0.113±0.025, 0.127±0.014 and 0.108±0.014 μM, respectively, with no statistically significant changes. The magnitude of simulated $[Ca^{2+}]_i$ transient ($\Delta[Ca^{2+}]_i$) reduced by a further 37% between the 4-week and the 7-week time points leading to a total 75% reduction in $\Delta[Ca^{2+}]_i$ at 7-week compared to the FF. This is in agreement with the 85% reduction between the FF and 7-week KO measured experimentally. The RT_{50} of simulated $[Ca^{2+}]_i$ increased 1.2-fold between 4-week and 7-week KO models, and in the 7-week KO model RT_{50} was 2.5-fold longer

than that in the FF model. Similarly, experimentally measured RT_{50} increased 1.3-fold between 4-week and 7-week KO, and 2.2-fold between FF and 7-week KO.

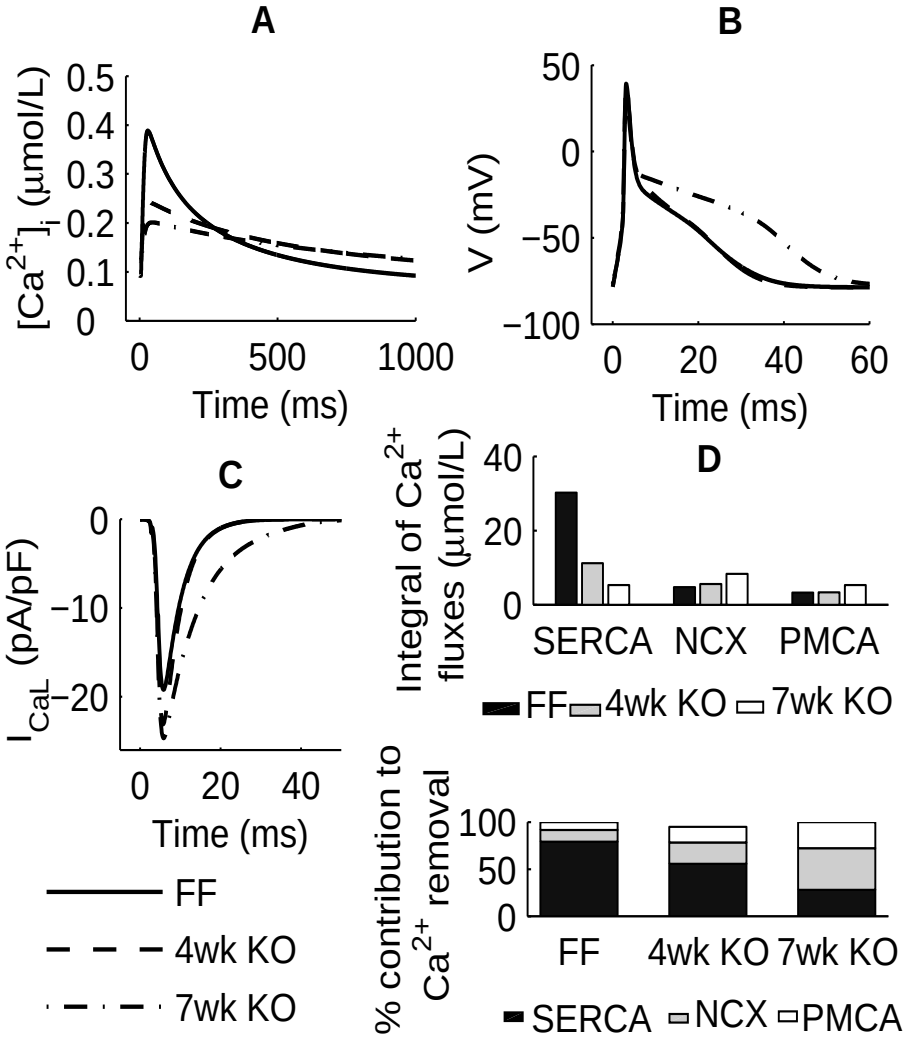

FIGURE 4.7: Simulation results from the FF, KO 4-week and KO 7-week models during an cardiac cycle at 1 Hz. A: $[\mathrm{Ca}^{2+}]_{\mathrm{i}}$ transients paced. B. Top panel: APs. Bottom panel: Time courses of $\mathrm{I}_{\mathrm{CaL}}$ during an AP. C: Ca^{2+} fluxes through SERCA, NCX and PMCA. D. Top panel: Integrals of Ca^{2+} fluxes through SERCA, NCX and PMCA. Bottom panel: Percentage contributions of SERCA, NCX and PMCA to Ca^{2+} removal.

Simulated AP repolarisation, shown in Fig. 4.7B, was slightly prolonged in the 4-week KO and became significantly slower in the 7-week KO model, in agreement with experimental measurements. Experimentally we observed no changes in resting

$[Ca^{2+}]_i$ Transient	FF		KO 4-week		KO 7-week	
and AP Characteristics	Experiment	Model	Experiment	Model	Experiment	Model
Diastolic $[Ca^{2+}]_i$ at 1 Hz (μM)	0.113±0.025	0.092	0.127±0.014	0.123	0.108±0.014	0.126
Magtnidue at 1 Hz (μM)	0.343±0.065	0.297	0.098±0.031	0.119	0.051±0.008	0.075
RT_{50} at 1 Hz (ms)	151±14	138	285±18	281	332±27	342
Δ $[Ca^{2+}]_i$ (caffeine-induced) (μM)	0.612±0.058	0.723	0.17±0.04	0.153	0.025±0.009	0.020
Integral of I_{CaL} (voltage clamp) (pC/pF)	0.111±0.009	0.165	0.205±0.020	0.237	0.243±0.015	0.27
% contribution of SERCA	87.7±1.3	79.1	62.5±7.5	55.7	33.7±0.4	28.1
% contribution of NCX	7±0.9	12.4	23.3±7.3	27.7	39.9±6.0	44.0
% contribution of PMCA	5.4±0.7	8.5	14.3±3.7	16.6	26.4±3.3	27.8
APD_{20} (ms)	4.3±0.2	4.1	4.1±0.3	4.1	5.2±0.7	4.0
APD_{50} (ms)	7.2±0.8	6.3	11.4±2.5	7.4	16.7±3.3	14.4
APD_{70} (ms)	15.3±3.2	18.6	16.8±2.4	19.0	31.0±5.6	35.7
$[Na^+]_i$ (mM)	9.6±1.4	9.8	Unchanged from FF values	10.0	14.6±1.1	14.3
pH_i	7.19±0.08	7.13	Unchanged from FF values	7.12	6.91±0.07	6.85

TABLE 4.2: Comparison between experimental measured and simulated $[Ca^{2+}]_i$ transients and APDs.

membrane potential and transient outward K^+ current measurements [125] between FF and 7-week KO cardiomyocytes. In addition, AP prolongation in 7-week KO was found to be sensitive to nifedipine, suggesting that prolongation may result primarily from augmented I_{CaL}. Therefore, parameter values for the various K^+ channels were kept identical between models. Simulated peak I_{CaL} increased progressively from 19.2 pA/pF in the FF model to 24.7 pA/pF in 7-week KO models, as shown in Fig. 4.7C. Inactivation of the current was significantly slowed in the 7-week KO, and the integral of the current increased from 0.15 pC/pF in the FF model to 0.32 pC/pF in the 7-week KO model,

compared to experimental values of 0.11 and 0.38 pC/pF, respectively.

The percentage contribution of SERCA, shown in Fig. 4.7D, was calculated as the ratio between the integral of net Ca^{2+} uptake flux through SERCA and the integral of all Ca^{2+} removal fluxes through SERCA, NCX and PMCA (Fig. 4.7D top panel). SERCA contribution decreased from 79.1 $\%$ in the FF model to 55.7 $\%$ in the 4-week KO model and 28.2 $\%$ in the 7-week KO model, compared to experimental values of 87.7, 62.5 and 33.7 $\%$, respectively (Fig. 4.7D bottom panel).

Simulated $[\mathrm{Na}^{+}]_{\mathrm{i}}$ was 4.7 mM higher in the 7-week KO model than that in the FF model, consistent with the average 5.0 mM increase observed experimentally. Finally, simulated $\mathrm{pH_i}$ decreased from 7.19 $\pm$ 0.08 in the FF to 6.85 in the 7-week KO model, in agreement with experimental values of 7.19$\pm$0.08 and 6.91$\pm$0.07, respectively.

4.4.2 ATP Consumption per Cardiac Cycle

Intracelluar acidosis in HF is attributed to a compromised metabolic state [199], thus prompting an analysis of simulated total amount of ATP used for ion transport per cardiac cycle in the model. The rate of ATP consumption by each of the major Ca^{2+} handling processes was calculated from the simulated fluxes of Ca^{2+} through SERCA and PMCA, and the flux of Na^{+} through NKA, taking into account the stoichiometry of each transporter (SERCA 2Ca^{2+}:1ATP, PMCA 1Ca^{2+}:1ATP and NKA 3Na^{+}:1ATP). The ATP consumption per cardiac cycle was then calculated as the integral of the rate of ATP consumption. As shown in Fig. 4.8A, total ATP consumption changed from 41.0 to 31.1 to 52.7 μM in the FF, 4-week and 7-week KO models, respectively. The decrease between the FF and 4-week KO models was primarily attributed to a decrease in ATP consumption by SERCA, while the increase between the 4-week and 7-week KO models was due to a significant increase in ATP consumption by NKA in the presence of a continued decrease

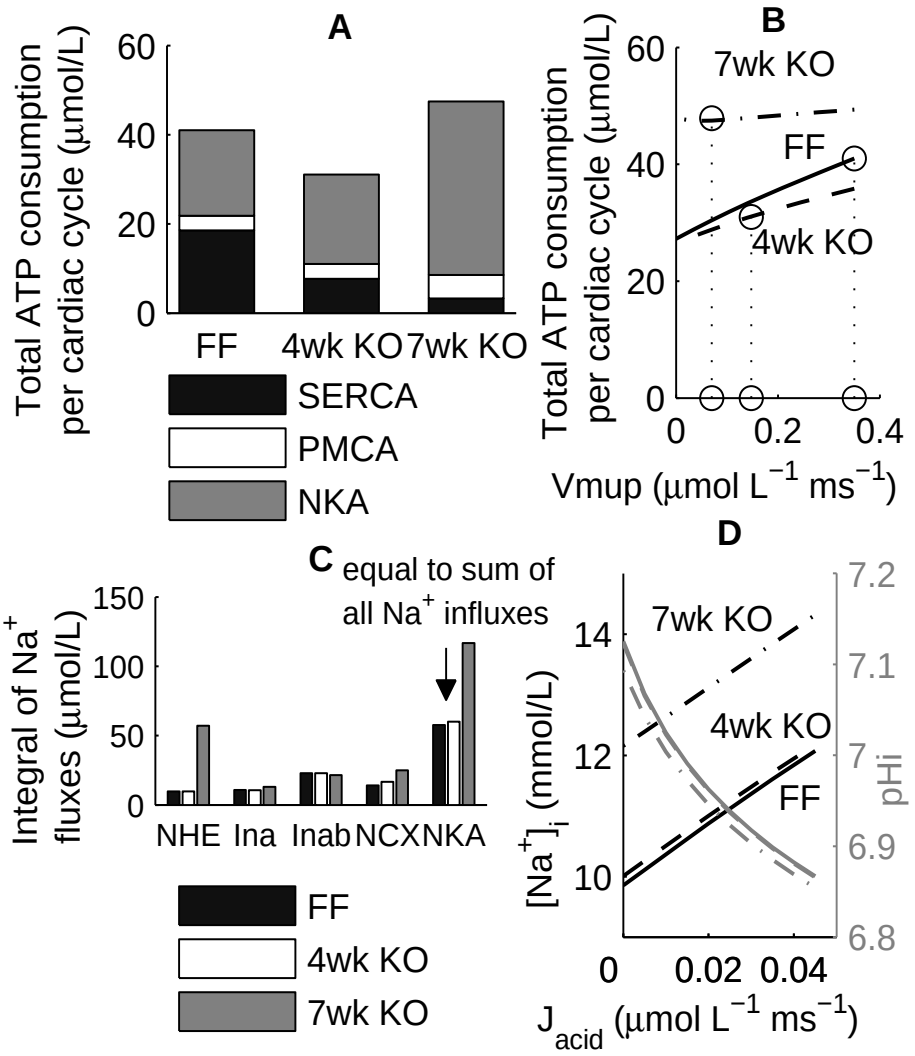

FIGURE 4.8: ATP consumption and Na^+ homeostasis in the FF, 4-week and 7-week models. A: ATP consumption per cardiac cycle by SERCA, PMCA and NKA, and total consumption. B: Total ATP consumption as a function of varying V_{up}. C: Magnitudes of Na^+ influxes and efflux. D: Changes in $[\mathrm{Na}^+]_i$ as a function of the magnitude of J_{acid}.

in ATP consumption by SERCA.

To evaluate the dependence of total ATP consumption on the maximum uptake rate of SERCA (V_{up}), a sensitivity analysis was performed on each model with V_{up} varied from the FF value (0.35 μM/ms) to zero while keeping all other parameters unchanged, as shown in Fig. 4.8B. It can be seen that ATP consumption in the 7-week KO model stayed consistently higher than that in the FF and 4-week KO models. Since the higher

ATP consumption by NKA in the 7-week model was due to an elevated $[Na^+]_i$, we then compared the various Na^+ fluxes in all three models.

4.4.3 Sodium Homeostasis

As shown in Fig. 4.8C, the simulated integrals over each cardiac cycle of Na^+ influx through NCX and NHE increased by 8.4 and 47.4 μM, respectively, between the 4-week and 7-week time points. Therefore, over 80% of the increase in Na^+ influx in the 7-week KO was due to increased Na^+ flux through NHE, activated by intracellular acidosis. In our model, the extent of acidosis was determined by the magnitude of the intracellular acid source term (J_{acid}), which in HF may be associated with lactic acid production from anaerobic metabolism due to a compromised metabolic state [2]. To examine the effects of J_{acid} on Na^+ homeostasis, a range of J_{acid} magnitudes were introduced in all three models, as shown in Fig. 4.8D. For a given level of J_{acid}, $[Na^+]_i$ in the 7-week KO remained approximately 2 mM higher than the FF and 4-week KO values due to NCX up-regulation and a reduced maximum NKA activity, indicating a reduced capacity of the 7-week KO to maintain a physiological $[Na^+]_i$ in response to metabolic imbalance.

4.4.4 Effects of Compensatory Changes on ATP Consumption

To examine whether a decrease in ATP production or an increase in demand contributed to acidosis in the 7-week KO, we investigated the changes in ATP consumption in the 4-week and 7-week KO models as a result of adaptations in response to changes in SERCA activity. For both models, V_{up} was varied between zero and 120% of the 4-week value (0.148 μM/ms) without metabolic imbalance, i.e. J_{acid} set to zero, in order to assess changes in ATP demand due to adaptive changes alone. For a given V_{up}, an adaptive change in maximum NCX (V_{NCX}^{max}) or PMCA (I_{PMCA}^{max}) activity was introduced such that simulated diastolic $[Ca^{2+}]_i$ remained unchanged, assuming that diastolic $[Ca^{2+}]_i$ may drive compensatory mechanisms [117]. Specifically, a decrease in V_{up} would lead to an elevated dias-

tolic $[Ca^{2+}]_i$ without compensatory changes. By up-regulating NCX or PMCA, diastolic $[Ca^{2+}]_i$ could be maintained, although at a cost of a lower systolic $[Ca^{2+}]_i$. Furthermore, PMCA up-regulation led to additional H^+ influx which would be extruded via NHE in exchange for Na^+. Therefore, both compensatory mechanisms directly or indirectly cause an increased Na^+ influx, Na^+ elevation and thus increased ATP consumption by NKA.

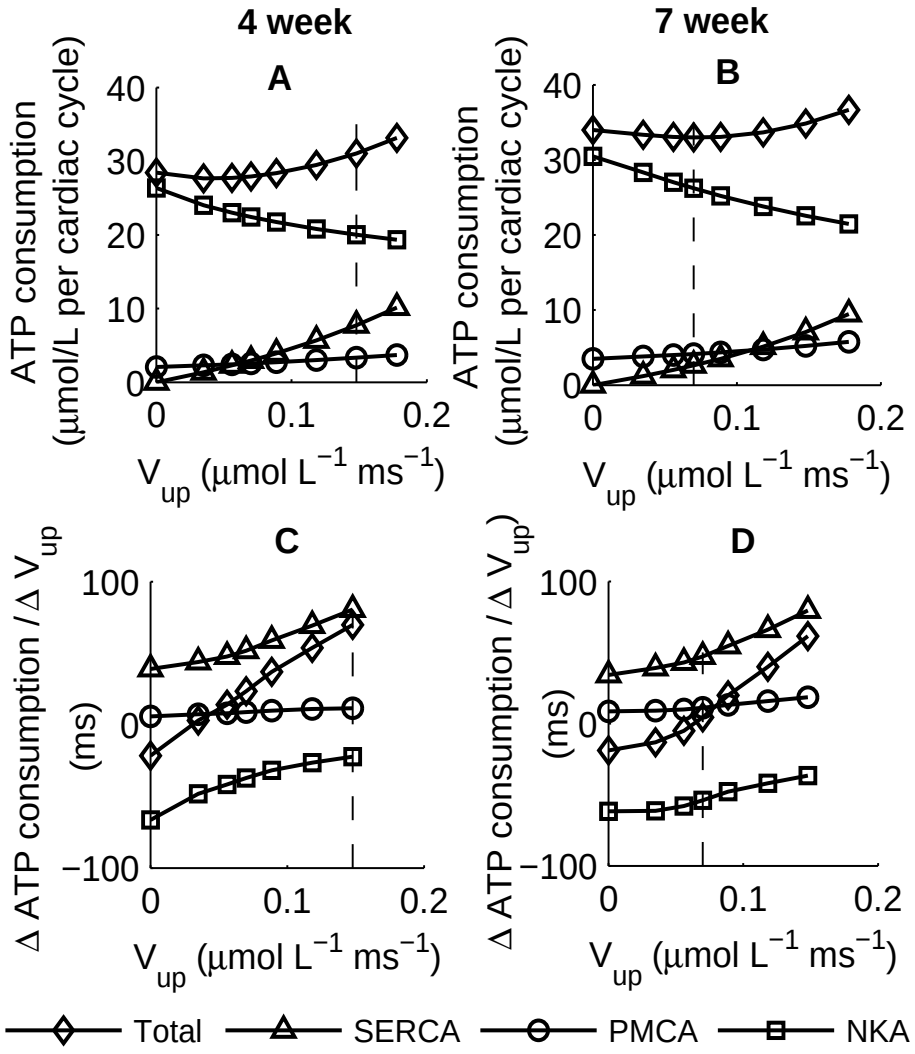

FIGURE 4.9: Effects of NCX adaptation to maintain constant diastolic $[Ca^{2+}]_i$ on ATP consumption as a function of V_{up}. A: ATP consumption per cardiac cycle by SERCA, PMCA and NKA, and total consumption in the 4-week KO model. B: ATP consumption per cardiac cycle by SERCA, PMCA and NKA and total consumption in the 7-week KO model. C: The rates of change in ATP consumption by different processes plotted in A. See text for details. D: The rates of change in ATP consumption by different processes plotted in B.

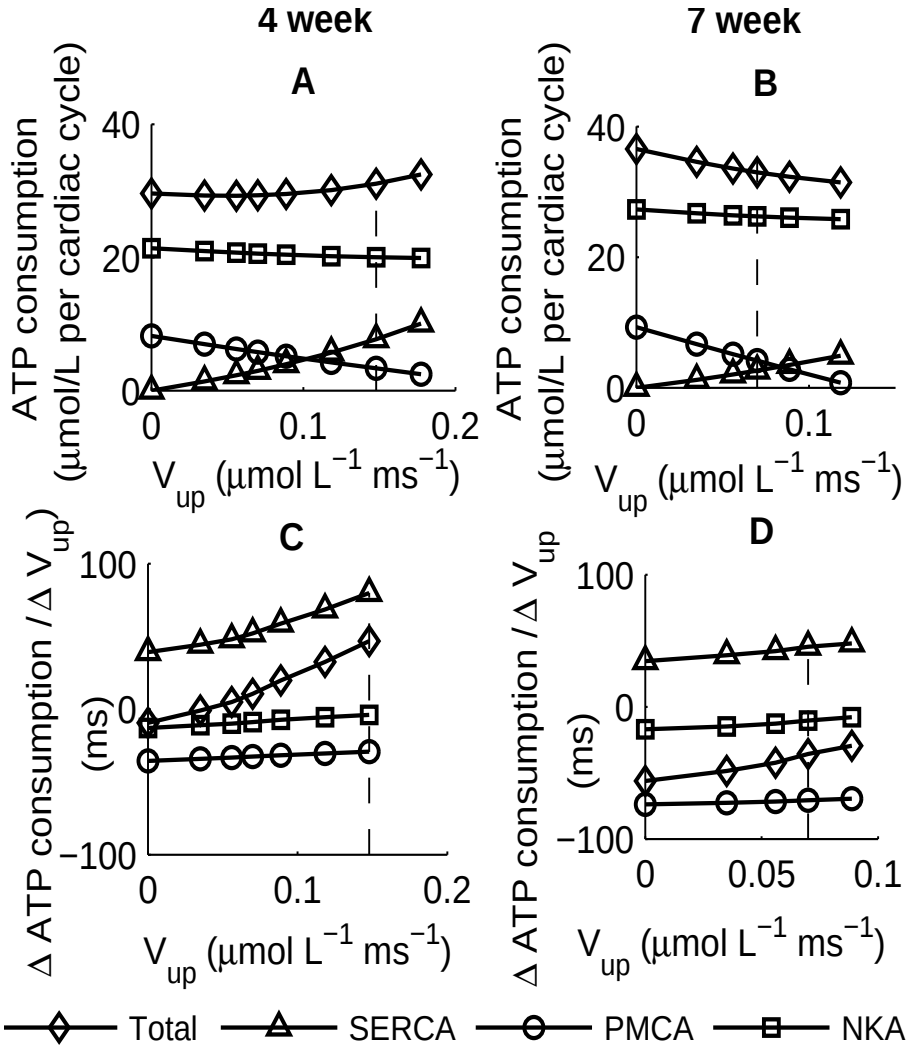

FIGURE 4.10: Effects of PMCA adaptation to maintain constant diastolic $[\mathrm{Ca}^{2+}]_{\mathrm{i}}$ on ATP consumption as a function of $\mathrm{V_{up}}$. A: ATP consumption per cardiac cycle by SERCA, PMCA and NKA, and total consumption in the 4-week KO model. B: ATP consumption per cardiac cycle by SERCA, PMCA and NKA and total consumption in the 7-week KO model. C: The rates of change in ATP consumption by different processes plotted in A. See text for details. D: The rates of change in ATP consumption by different processes plotted in B.

Fig. 4.9A and B show total ATP consumption as a function of $\mathrm{V_{up}}$ for the 4-week and 7-week KO models, respectively, with NCX adaptation. In both cases, decreasing $\mathrm{V_{up}}$ resulted in an increase in ATP consumption by NKA, and a decrease in consumption by SERCA; while relatively little changes occurred for PMCA. The corresponding rates of change in ATP consumption are plotted in Fig. 4.9C and D, for the 4-week and 7-week

time points, respectively. The rate of change in ATP consumption at a given V_{up} was calculated as the change in ATP consumption as V_{up} was decreased from its previous value to the current value, normalised to the magnitude of reduction in V_{up}. Therefore, a positive value indicates a decrease in ATP consumption with decreasing V_{up}, whereas a negative value indicates the opposite trend. This analysis demonstrated that for both models, the rate of decrease in ATP consumption by SERCA was initially faster than the corresponding rate of increase for NKA thus leading to an initial overall decrease in ATP consumption. As V_{up} continued to decrease (V_{up}<0.035 μM/ms in the 4-week KO model and <0.07 μM/ms in the 7-week KO model), the rate of increase in ATP consumption by NKA became increasingly faster exceeding the rate of decrease for SERCA and total ATP consumption started to increase. The dotted lines on Fig. 4.10 indicate the experimentally observed V_{up} levels.

In the case of PMCA adaptation, as shown in Fig. 4.10, at 4 weeks total ATP consumption decreased with decreasing SERCA activity, as the rate of decrease in ATP consumption by SERCA was greater than the combined rate of increases in consumption by PMCA and NKA, except at very low V_{up} levels (V_{up} <0.035 μM/ms). At 7 weeks however, total ATP consumption increased monotonically with decreasing SERCA activity, as the combined rate of increases in ATP consumption by NKA and PMCA were greater than the rate of decrease in consumption by SERCA.

4.5 Discussion

Decreased SERCA function and increased NCX function have been frequently demonstrated in studies of HF in both human and animal models [85, 159]. In this chapter, our goal was to analyse Ca^{2+} handling in the 7-week SERCA KO mice, and to elucidate the key differences between 4-week and 7-week time points which may underline the eventual progression into HF.

4.5.1 Effects of Compensatory Mechanisms on $[Ca^{2+}]_i$ Transient

During parameterisation, the maximum uptake rate of SERCA was found to be further decreased from 40% of the FF value at 4-week time point to 20% at 7-week time point, while transsarcolemmal Ca^{2+} fluxes were found to be moderately increased at the 4-week time point and significantly further up-regulated at 7 weeks. At the 4-week time point these compensatory increases may have been sufficient to maintain both diastolic and systolic $[Ca^{2+}]_i$ at physiologically tolerable levels, but further up-regulation of NCX and PMCA to the levels seen in the 7-week KO maintains diastolic $[Ca^{2+}]_i$ but more severely compromises systolic $[Ca^{2+}]_i$, thereby contributing to the progression to systolic HF.

Experimental measurements revealed that in the 7-week KO, the maximum activity of NKA was found to be decreased by approximately 10% and 40% for the α_1 and α_2 isoforms, respectively. NKA down-regulation is thought to increase cardiac contractility by elevating $[Na^+]_i$ which in turn decreases Ca^{2+} extrusion through NCX and enhances SR Ca loading [21, 200]. Simulation results from our model (Fig. 4.11) showed that moderate reductions in NKA activity enhanced peak $[Ca^{2+}]_i$ and the size of the $[Ca^{2+}]_i$ transient in the FF model. However, the same level of reduction in NKA activity in the 7-week KO model resulted in a greater increase in $[Na^+]_i$ and diastolic $[Ca^{2+}]_i$, as well as a much smaller increase in $\Delta[Ca^{2+}]_i$, which are likely to have detrimental effects on diastolic function.

4.5.2 ATP Consumption in the FF, 4-week and 7-week KO

Simulation results in Fig. 4.8C and D suggested that total ATP consumption per cardiac cycle by Ca^{2+} handling processes was decreased at the 4-week time point compared to the FF, due to decreased consumption by SERCA as both maximum uptake rate of SERCA and the size of the $[Ca^{2+}]_i$ transient were dramatically decreased. However, at the 7-week time point, despite further reduction in ATP consumption by SERCA, total consumption

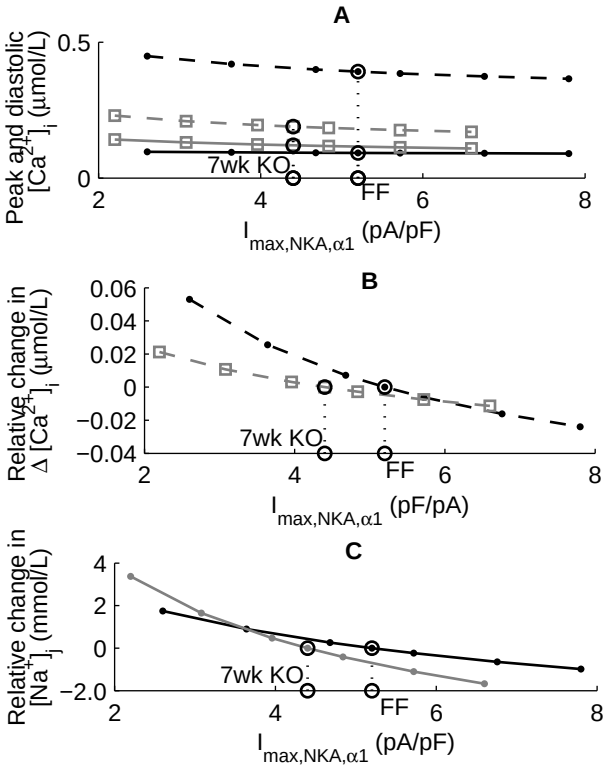

FIGURE 4.11: A: Simulated peak and diastolic $[\mathrm{Ca}^{2+}]_\mathrm{i}$ (A), $\Delta[\mathrm{Ca}^{2+}]_\mathrm{i}$ (B) and $[\mathrm{Na}^{+}]_\mathrm{i}$ (C) in the FF and 7-week KO models, with graded NKA down-regulation.

increased. This was due to dramatically increased ATP consumption by NKA resulting from a two-fold increase in total Na^{+} influx. Such an increase in Na^{+} influx was due to increased influx through NCX and NHE, with NHE contributing to 80% of the total increase.

4.5.3 Effects of Adaptations on ATP Consumption

The simulation results shown in Fig. 4.9 demonstrate that increased ATP demand may play a role in triggering intracellular acidosis in the 7-week KO. In the 4-week KO model with a physiological $\mathrm{pH_i}$ level, diastolic $[\mathrm{Ca}^{2+}]_\mathrm{i}$ may be maintained by compensatory NCX up-regulation, without incurring additional metabolic cost, as long as $\mathrm{V_{up}}$ for SERCA was greater than 10% of the FF value. As presented above, this was because the combined rate of decrease in ATP consumption by SERCA and PMCA was greater than

the rate of increase in consumption by NKA. The aforementioned minimum threshold was well below the experimentally observed SERCA activity in the 4-week KO. As V_{up} fell below this minimum, total ATP consumption increased with decreasing SERCA function, as the rate of increase in ATP consumption by NKA became greater than the combined rate of decrease in consumption by SERCA and PMCA. The parabolic shape in the relationship between ATP consumption and V_{up} suggested there may be a critical SERCA level, above which effective compensatory changes without a net metabolic cost are permitted. A qualitatively similar trend was observed in the 7-week model, although at this time point the experimentally observed SERCA activity was at the minimum (corresponding to 20% of FF value) of the aforementioned parabola and further decreases in SERCA level led to increased total ATP consumption. This indicated differential effects of NCX up-regulation on ATP consumption in the 4-week and 7-week KO models. As a result, a decrease in SERCA activity was associated with decreasing ATP consumption at the early stage of SERCA KO and then increasing ATP consumption with further SERCA loss.

The above analysis was carried out with J_{acid} set to zero in order to assess the effects of NCX up-regulation alone. In the presence of further metabolic imbalance as observed experimentally in the 7-week KO, the increase in ATP demand would inevitably result in an even greater burden on metabolic response. Several other studies have also suggested the role of Na^+ homeostasis in the regulation of mitochondria function [122, 130, 160]. Specifically, an elevated $[Na^+]_i$ has been shown to blunt mitochondrial Ca^{2+} uptake by activating mitochondrial Na^+/Ca^{2+} exchanger [122, 160]. Compromised Ca^{2+} accumulation in turn has been associated with net oxidation of NADH during increased work [122] and thus impaired matching process of energy supply and demand [130].

Therefore, we postulate that in the 7-week KO, a reinforcing cycle may underlie the eventual development into HF. As shown in Fig. 4.12, adaptive increases in NCX func-

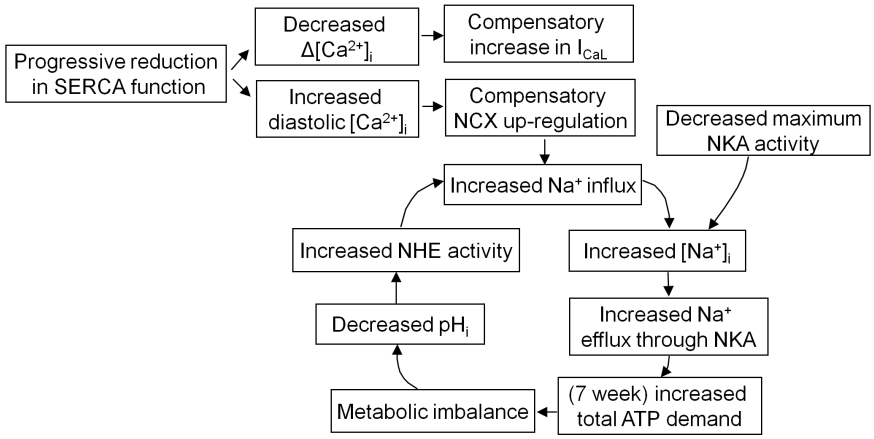

FIGURE 4.12: Progressive reductions in SERCA function eventually results in a reinforcing cycle involving Ca^{2+} handling, $[\mathrm{Na}^{+}]_{\mathrm{i}}$ accumulation and metabolic imbalance.

tion lead to $[\mathrm{Na}^{+}]_{\mathrm{i}}$ elevation and increased ATP demand by NKA. Metabolic imbalance resulting in anaerobic metabolism in turn leads to proton production thus enhancing NHE activity and hence further Na^{+} influx. Increased Na^{+} influx must be balanced by increased Na^{+} efflux through NKA, thereby leading to an even greater ATP consumption and further exacerbation of metabolic imbalance.

In the case of PMCA adaptation, as shown in Fig 4.10, total ATP consumption decreased with decreasing SERCA activity at 4 weeks but increased at 7 weeks. It can thus be reasoned that PMCA adaptation alone may initially be a feasible compensatory mechanism but later become detrimental in cells which were already metabolically compromised.

Chapter 5

Conclusions, Limitations and Future Directions

5.1 Summary

In this thesis, a data-driven biophysically-based model of Ca^{2+} dynamics in murine ventricular myocytes was developed, motivated by the need to provide a species- and temperature-consistent framework to enable quantitative studies of Ca^{2+} handling in experimental transgenic mouse models that ultimately develop HF. This framework was subsequently used to investigate cardiac electrophysiology function through time following SERCA2 gene knockout in mice at the 4-weeks and 7-weeks time points.

The first contribution of this thesis is the development of the model of Ca^{2+} dynamics in the ventricular myocytes of C57BL/6 mice, as presented in Chapter 2. To achieve this goal, where available consistent experimental data sources from mouse were applied using a parameterisation methodology developed to establish a transparent link between data and parameter values. The model was validated against a range of experimental measurements including frequency response of Ca^{2+} dynamics, AP morphology, the dependence of AP duration on cycle length and electrical restitution. This framework

allowed characterisation of key Ca^{2+} handling parameters using a set of data from standard experimental procedures. As a case study, transgenic mice over-expressing the canine NCX isoform was investigated using our model. Simulation results indicated that observations from genetic modifications were species-dependent, and in the case where species variation in the NCX isoform was eliminated, acute over-expression of NCX led to a net loss of Ca^{2+} from the cell which lowered both SR Ca^{2+} load and systolic $[\mathrm{Ca}^{2+}]_{\mathrm{i}}$ transient magnitude. This result further supported the need to use a species-specific model that takes into account the species-dependent variations, to help interpret experimental observations and elucidate the underlying mechanisms that may be difficult to observe directly.

The second contribution of this thesis is to quantitatively examine time-dependent changes in Ca^{2+} handling in SERCA2 KO mice using modelling, thereby revealing interaction between early compensatory mechanisms, metabolism and the final development of HF, as presented in Chapters 3 and 4. In Chapter 3, the Ca^{2+} handling components were re-parameterised using experimental data from SERCA2 KO mice at a 4-week time point, using a similar approach as for the C57BL/6 mice in Chapter 2. The model confirmed the experimental observation that sustained $[\mathrm{Ca}^{2+}]_{\mathrm{i}}$ transients can be maintained at this time point, despite severely impaired SERCA function. The importance of the compensatory mechanisms observed in the KO cardiomyocytes was investigated using the model, which demonstrated that the combined effect of the increased L-type Ca^{2+} current and NCX activity was to lower diastolic $[\mathrm{Ca}^{2+}]_{\mathrm{i}}$ which was highly sensitive to changes in SERCA activity at physiological relevant pacing frequencies. In-silico investigation into other possible compensatory mechanisms identified NCX as a viable and effective mechanism for lowering diastolic $[\mathrm{Ca}^{2+}]_{\mathrm{i}}$ although at the cost of a lower systolic $[\mathrm{Ca}^{2+}]_{\mathrm{i}}$.

The effects of further reductions in SERCA activity beyond the 4-week time point were investigated in Chapter 4. To do this, the above framework was extended to include

a more detailed description of Ca^{2+} dynamics in the sub-sarcolemmal compartment, which were fitted to experimental measurements from the FF, 4-week and 7-week KO cardiomyocytes. The 7-week KO model showed that the experimentally observed $[\mathrm{Na}^{+}]_{\mathrm{i}}$ elevation at this time point was due to increased Na^{+} influxes through the NCX and NHE, with the latter exacerbated by intracellular acidosis. We found that as SERCA function decreased the total ATP consumed for maintaining ionic homeostasis decreased, until SERCA reached approximately 20% of its initial value, whereby total ATP consumption began to increase as SERCA function decreased. This occurred as the rate of increase in ATP consumption by NKA for the extrusion of the additional Na^{+} brought in through up-regulated NCX eventually surpassed the rate of decrease in ATP consumption by SERCA and PMCA thus leading to an overall increase in ATP consumption. The critical point where the cell can no longer compensate for SERCA loss without increasing ATP consumption may represent the transition point to HF. In the event of intracellular acidosis and hence metabolic imbalance, a reinforcing cycle may be initiated involving Na^{+} accumulation, a mismatch between ATP demand and supply, an increasingly compromised metabolism, a decreased pH_{i} and finally an even greater $[\mathrm{Na}^{+}]_{\mathrm{i}}$ elevation.

To facilitate transparent and unambiguous dissemination of the results of this thesis, we have made the models available on the CellML website (www.cellml.org). For the C57BL/6 model framework, the metadata links to the experimental datasets used for parameterisation, a full explanation of the datasets and how they are linked with each model component are also provided.

5.2 Model Limitations

While this thesis provides important contributions to the understanding of Ca^{2+} handling in the normal and failing heart, the following paragraphs address the limitations of this study and their implications.

For the development of the C57BL/6 model, experimental measurements of the outward K^+ currents obtained at physiological temperatures are less abundant than those at room temperature. In some cases this necessitates the use of data from multiple mouse strains. These different genetic backgrounds are known to have different AP characteristics [34, 205]. These differences are likely to be less than differences observed between species but still need to be considered. This model is thus only an approximation of the C57BL/6 murine cardiac myocyte based on the currently available data and will need further updating as new data from C57BL/6 LV myocytes become available.

The C57BL/6 model includes a component of CaMKII-regulatory pathway to account for FDAR. Apart from being involved in FDAR, CaMKII is thought to regulate several other Ca^{2+} transport proteins including RyR and the LCCs. Most studies on CaMKII have been done using acute CaMKII over-expression and endogenous or exogenous activation of CaMKII. For example, Maier et al. [134] found a 4-fold increase in resting Ca^{2+} leak from the SR and a decrease in SR Ca^{2+} content in transgenic mice over-expressing CaMKII compared with WT littermates. In another study [74], endogenous CaMKII activation in mice was seen to increase Ca^{2+} spark frequency in both WT and PLB knockout mice. Although the exact level of interactions between CaMKII and RyR under physiological conditions is not clear and was not directly observed in our experiments, we tested the sensitivity of our model to increases in SR Ca^{2+} leak rate and the rate of SR Ca^{2+} release. Doubling the rate of SR Ca^{2+} release (V_{rel}) from 4.5 to 9 ms^{-1} led to no change in the magnitude of the transient at 3 Hz, but a 19% decrease in the time to peak and a 10% decrease SR Ca^{2+} content. This was consistent with experimental observations that changes in the open probability of RyR only had a transient effect on the size of the $[Ca^{2+}]_i$ transient [54, 55]. On the other hand, doubling the rate of SR Ca^{2+} leak (V_{leak}) from 3×10^{-5} to 6×10^{-5} ms^{-1} resulted in a 13% decrease in the magnitude of the transient, a 20% decrease in the SR Ca^{2+} content and no change

in the time to peak. Therefore, CaMKII regulation of RyR release at higher pacing frequencies may be important if SR leak rate is increased significantly, and this may be included in the model once quantitative experimental data becomes available in the future.

The modulation of LCC by CaMKII has also been reported by several groups. Generally, CaMKII is thought to facilitate I_{CaL} with repeated depolarisations (see review by Maier and Bers [133]). More recently, I_{CaL} in ventricular myocytes from mice with CaMKII over-expression have been reported to have a higher peak and slower decline [134]. In rabbit ventricular myocytes, acute CaMKII over-expression led to an increase in peak I_{CaL} and a prolongation of the inactivation kinetics without causing statistically significant changes in $[Ca^{2+}]_i$ transient [107]. At 3 Hz, increased activity of CaMKII should be expected to facilitate I_{CaL}, however both Dibb et al. [49] and Antoons et al. [7] have reported progressive reductions in peak I_{CaL} with increasing frequency in rat and mouse ventricular myocytes respectively. Thus since the physiological role of I_{CaL} facilitation is still debatable [133], it was not included into our model formulation.

For the model of SERCA2 KO at the 4-week time point, parameterisation of NCX and PMCA formulations in the KO model was based on the assumption that a 45% increase in PMCA expression level observed experimentally led to the same percentage increase in its activity. The validity of this assumption requires further investigation, such as an additional experiment measuring caffeine-induced $[Ca^{2+}]_i$ transients in the presence of an NCX inhibitor. Given the lack of availability of this data, we tested the sensitivity of our model results to changes in the ratio between J_{NCX} and J_{PMCA} in the KO model. The key finding that NCX up-regulation was important for maintaining diastolic $[Ca^{2+}]_i$ in the KO model was not found to be sensitive to the above assumption.

In the model of SERCA2 KO at the 4-week time point, SERCA activities in the FF and KO cardiomyocytes were obtained from analysing the decay of field-stimulated $[Ca^{2+}]_i$

transients at 1 and 6 Hz. While the analysis was based on the assumptions of no changes in buffering properties and negligible mitochondrial Ca^{2+} transport, the method has been consistently validated and represents the standard method for functionally characterising Ca^{2+} uptake through SERCA. For example, Shannon et al. [177] used this method in their study of $[Ca^{2+}]_i$ decline in voltage-clamped rabbit ventricular myocytes. Picht et al. [156] used the same method for characterising the frequency-dependent changes in SERCA activity in mouse ventricular myocytes. Li et al. [116] also characterised Ca^{2+} transport in PLB KO mice using this method. Additional examples supporting the validity of our approach can be found in many other studies [127, 155, 194, 203]. Studies using SR vesicles prepared from cardiac tissue can provide an alternative method to characterise SERCA function. However, these preparations compromise the cellular environment and thus also the complex regulatory mechanisms. Therefore, results from these studies require careful interpretation and can not readily provide a quantitative relationship between protein density and function.

For the model of SERCA2 KO at the 7-week time point, we proposed that lactic acid production through anaerobic metabolism may underlie the observed acidosis in the KO cardiomyocytes. The validity of this assumption requires further investigation. Consistent with our assumption, previous work by Allen et al. on ferret hearts showed that when oxidative phosphorylation was inhibited while also inhibiting glycolysis, the development of acidosis could be prevented [3]. However, Eisner et al. found that stimulation of lactic acid production had no effect on pH_i in isolated rat ventricular myocytes [56]. They further used modelling to demonstrate that lactic acid production only resulted in a transient reduction in pH_i which recovered as protons were extruded by the pH-regulating mechanisms. Therefore, acidosis in the SERCA2 KO cardiomyocytes may not be a result of impaired anaerobic metabolism alone and that aerobic metabolism is also affected, consistent with the observation of Eisner et al..

In all the models presented in this thesis, intracellular Ca^{2+} buffering was accounted for using the framework of rapid equilibrium approximation developed by Wagner and Keizer [204] and fitted by Trafford and Eisner [196] to data obtained from ferret ventricular myocytes at room temperature. The validity of the rapid equilibrium approximation has been examined in detail by Wagner and Keizer [204], and has since been widely applied and acknowledged as a reasonable approximation to buffering properties in studies of Ca^{2+} handling [17, 116, 156]. We have chosen this approach as a kinetic buffering model would involve additional parameters that can not be sufficiently constrained from available experimental data.

The formulation of intracellular Ca^{2+} buffering proposed by Trafford et al. [196] was based on experimental data from ferret ventricular myocytes at room temperature using fluo-3 as the Ca^{2+} indicator. Whether there are significant differences in buffering properties between mice and ferrets is unclear. To estimate the differences between ferret and murine Ca^{2+} buffering we used simultaneous measurements of caffeine-induced $[\mathrm{Ca}^{2+}]_{\mathrm{i}}$ transients and the $\mathrm{I_{NCX}}$ current in murine ventricular myocytes at room temperature performed by Adachi-Akahane et al. [1] to estimate the murine cardiac myocyte Ca^{2+} buffering curve. The buffering curve obtained from the Adachi-Akahane et al. [1] data was in close agreement with the Trafford and Eisner buffering curve for $[\mathrm{Ca}^{2+}]_{\mathrm{i}}$ below 0.5 μM, and slightly lower at higher $[\mathrm{Ca}^{2+}]_{\mathrm{i}}$ levels. Since in most cases, the observed $[\mathrm{Ca}^{2+}]_{\mathrm{i}}$ transient in our sample has a peak at or below 0.5 μM, the use of ferret buffering parameters would seem to provide a reasonable approximation until specific buffering measurements in murine hearts at physiological temperatures become available.

The difference in buffering due to the choice of Ca^{2+} indicators can be estimated as follows. According to Trafford et al. [196], fluo-3 has a $\mathrm{K_{d,buffer}}$ of 0.4 μM. In the presence of 16 μM of the dye in the cytoplasm during their experiments, its buffering capacity for $[\mathrm{Ca}^{2+}]_{\mathrm{i}}$ between 0 and 1 μM is shown in the Fig. 5.1. In our experiment, with

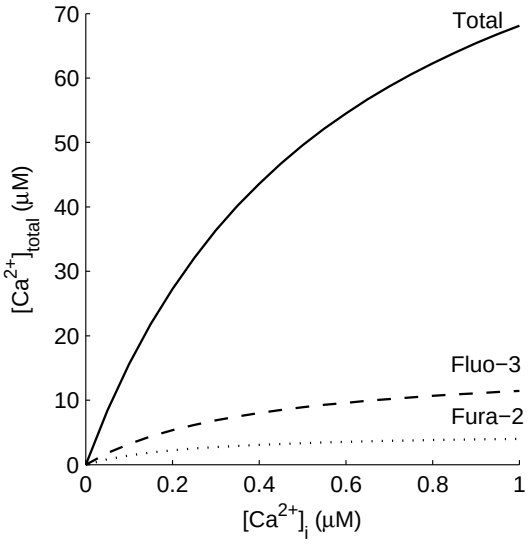

FIGURE 5.1: Difference in the buffering effects between Fluo-3 and Fura-2. "Total" indicates the total amount of buffering calculated according to the equation proposed by Trafford et al. [196]. "Fluo-3" and "Fura-2" represent the buffering effect of each Ca^{2+} indicator respectively.

a 5 μM concentration of fura-2 and a $K_{d,buffer}$ of approximately 0.25 μM, the buffering capacity of fura-2, is lower compared to fluo-3. For example, at $[\mathrm{Ca}^{2+}]_i$ equal to 0.5 μM which is the level of systolic $[\mathrm{Ca}^{2+}]_i$ at 0.5 Hz, the concentrations of Ca^{2+} bound to fura-2 and fluo-3 are approximately 3.3 and 8.9 μM, and the concentration of Ca^{2+} bound to the intrinsic buffers is approximately 52 μM according to the B_{max} (114 μM) and $K_{d,buffer}$ (0.59 μM) values estimated by Trafford et al. [196]. Therefore, the contribution of fura-2 and fluo-3 to the total buffering capacity is 6% and 15% respectively. Based on the assumption that intrinsic buffering capacity in ferret and mouse is similar, this indicates a slight overestimation of the total buffering capacity in mouse due to the different buffering capacity of the dye.

Intracellular Ca^{2+} buffering was assumed unchanged with SERCA2 KO, although the reductions in the expression and activity of SERCA may result in a decrease in the overall Ca^{2+} buffering property. Such a decrease would mean a decrease in the change of the total Ca^{2+} concentration for the same level of change in $[\mathrm{Ca}^{2+}]_i$. This means that

during the decay phase of the $[Ca^{2+}]_i$ transient, less Ca^{2+} would need to be removed from the cytosol to achieve the same decrease in $[Ca^{2+}]_i$. Under such circumstances, the activities of Ca^{2+} removal mechanisms may be overestimated in the current KO model. To investigate whether this could fully explain the proportionally higher SERCA activity found in our study, we tested how much buffering would need to change to yield an 85% reduction in SERCA activity as measured in myocardial tissue homogenate at the 4-week time point. The result was a 62% reduction in the maximum buffering activity, which is significantly greater than the reported total percentage contribution (approximately 19%) of SERCA to total buffering [19]. In addition, the situation is further complicated by the possible alterations in the Ca^{2+} binding properties of the myofilaments, as mentioned previously, since troponin C is another important fast Ca^{2+} buffer with a similar Ca^{2+} binding affinity to SERCA, and contributes to approximately 46% and 29% of fast and total buffering respectively [19, 66]. Furthermore, our sensitivity study on the rate of decay of the transient suggests that the reduced lusitropic effect of SERCA KO at a higher pacing frequency presented in the study at the 4-week time point is independent of the choice of buffering parameters.

Care should be taken when extrapolating Ca^{2+} handling properties observed in isolated myocytes to *in vivo* functions. Normal contractions at a physiological pacing frequency (10 Hz) could not be sustained in isolated myocytes, thus we could only obtain $[Ca^{2+}]_i$ transients at lower pacing frequencies (up to 3 Hz for C57BL/6 mice, and up to 6 Hz for SERCA2 FF and KO mice). This could be due to a number of factors including cell damage during isolation, loss of structural integrity and compromised metabolic properties [180, 183]. It is therefore possible that other aspects of Ca^{2+} handling properties not discussed above are also affected.

5.3 Future Work

Computational models incorporate a vast range of available experimental data sets into a consistent framework for quantitative analyses, and can often be reused in other relevant contexts. For example, existing published models can be adopted for studies that investigate a different phenomenon on a similar scale, or combined with other models within a common framework to create a new model on a larger scale.

There are a number of extensions to the modelling work presented here, some of which are still on-going. The C57BL/6 model framework has been used to investigate the effects of SR Ca^{2+} leak on Ca^{2+} dynamics in mice with neuronal NO synthase (nNOS) KO, in collaboration with Lim et al. [119]. Recent experimental evidence suggested NO may modulate RyRs function and disruption of nNOS-derived NO signalling was observed to cause an attenuated SR Ca^{2+} leak which became more evident at higher SR Ca^{2+} content [120]. However, it is unclear whether the reduction in SR Ca^{2+} leak contributes to the increases in $[\mathrm{Ca}^{2+}]_{\mathrm{i}}$ transient magnitude and SR Ca^{2+} content observed experimentally in nNOS KO mice, in the presence of reduced SERCA activity and enhanced $\mathrm{I}_{\mathrm{CaL}}$. To investigate this question, a sensitivity analysis was performed based on the C57BL/6 framework with reparameterisation of the model using experimental data from the WT and nNOS KO mice. In this analysis, the effects of varying degrees of reduction in SR Ca^{2+} leak on $[\mathrm{Ca}^{2+}]_{\mathrm{i}}$ transient magnitude and SR Ca^{2+} content were examined at a range of $[\mathrm{Ca}^{2+}]_{\mathrm{o}}$ and pacing frequencies. Simulation results suggested that decreased SR Ca^{2+} leak may facilitate SR Ca^{2+} loading in nNOS KO mice and this inotropic effect appeared to be more significant at the lower pacing frequencies and lower $[\mathrm{Ca}^{2+}]_{\mathrm{o}}$ levels.

The C57BL/6 model framework has also been used to help examine another genetically modified mouse model lacking an LCC auxiliary protein Rem, which is thought to regulate LCC function [132]. Experimentally measured $[\mathrm{Ca}^{2+}]_{\mathrm{i}}$ transients were smaller

in Rem KO ventricular myocytes, even though I_{CaL} had a +4 mV shift in steady-state activation and a 25% increase in maximum conductance. To examine the implications of changes in I_{CaL}, parameters for I_{CaL} were fitted to experimental measurements obtained from the WT and Rem KO, including the voltage-dependence of activation and inactivation kinetics, the current-voltage relationship, and the decay kinetics of the current. All other parameters for the WT and Rem KO models were kept the same as those in the C57BL/6 model. Simulation results confirmed the experimental observation of a lower $[Ca^{2+}]_i$ transient magnitude, and indicated that despite having a greater peak I_{CaL} and similar inactivation kinetics under voltage-clamp conditions compared to the WT, the +4 mV shift in activation in the Rem KO was sufficient to alter I_{CaL} dynamics during an AP, resulting an overall reduced Ca^{2+} entry.

In another study, the model of cardiac electrophysiology for the SERCA2 FF and KO mice has been coupled to a cellular mechanical model by Land et al. [111], enabling investigations into the effects of altered myofilament Ca^{2+} sensitivity on cellular contractility. The coupled cellular electro-mechanics model is in turn embedded into a detailed three-dimensional finite-element model of the intact mouse heart, using anatomically accurate geometry and microstructure information obtained through high resolution confocal images. Such a model can shed further light on the effects of SERCA2 KO on cardiac function at the whole-organ level.

Finally, the model of cardiac electrophysiology for the C57BL/6 mouse has been used in an on-going study of genotype-phenotype mapping by Vik et al. [201], in which *in silico* genetic variations are represented by parametric variations, which propagate through the model to generate multivariate phenotypes for the AP and $[Ca^{2+}]_i$ transient. Statistical analysis was then applied to the resulting genotype-to-phenotype map to reveal the correlations between low-dimensional genetic variations and high-dimensional phenotypes.

5.4 Conclusions

To conclude, the heart is a complex system in which multiple inter-dependent pathways are intricately tuned to maintain cardiac function. At the cellular level, the regulation of intracellular Ca^{2+} dynamics is one of the most important factors contributing to normal myocardial contraction. While a dynamic and delicate balance of Ca^{2+} fluxes and electrophysiological properties is essential for generating a physiological $[\mathrm{Ca}^{2+}]_{\mathrm{i}}$ transient, the system also responds with robust adaptation to short- and long-term perturbations. Genetically modified mice are a useful tool for probing each Ca^{2+} handling component within this complex system, yet the compensatory mechanisms that occur following a genetic modification make it difficult to understand the overall effects on cardiac electrophysiology and global Ca^{2+} dynamics. In this context, experimental date-driven mathematical models that take into account the species- and temperature-dependent nature of Ca^{2+} handling provide a unique opportunity to incorporate a vast range of available data into a model for an integrated investigation. We have demonstrated that such models can be used to quantitatively characterise changes in the functional activities of Ca^{2+} handling components and the effects of compensatory mechanisms which would otherwise be difficult to study experimentally. In addition, using such models to track changes in cardiac electrophysiology through time, we have been able to reveal how early compensatory mechanisms become detrimental at a later stage and ultimately result in the development of HF.

Appendix A

List of Publications

The work presented in this thesis has led to a number of publications, as listed below.

The model framework of calcium handling in ventricular myocyctes of C57BL/6 mouse heart, as presented in Chapter 2, has been published in the American Journal of Physiology.

L. Li, S. A. Niederer, W. Idigo, Y. H. Zhang, P. Swietach, B. Casadei, and N. P. Smith. A mathematical model of the murine ventricular myocyte: a data-driven biophysically based approach applied to mice overexpressing the canine NCX isoform. ***American Journal of Physiology. Heart and circulatory physiology*****, 299(4):H1045–1063, 2010.**

The study on calcium handling in SERCA2 KO mice at the 4-week time point, as presented in Chapter 3, has been published in the Biophysical Journal.

L. Li, W. E. Louch, S. A. Niederer, K. B. Andersson, G. Christensen, O. M. Sejersted, and N. P. Smith. Calcium dynamics in the ventricular myocytes of SERCA2 knowkout mice: a modelling study. ***Biophysical Journal*****, 100(2):332–331, 2010.**

The study on calcium handling, sodium homeostasis and ATP consumption for ion

transport in SERCA2 KO mice at the 7-week time point, as presented in Chapter 4, is currently under review with the Biophysical Journal.

L. Li, W. E. Louch, S. A. Niederer, J. M. Aronsen, G. Christensen, O. M. Sejersted, and N. P. Smith. Sodium accumulation in SERCA knockout induced heart failure. *Biophysical Journal*, 102(9):2039–2048, 2012.

The four extensions to the current study, as described in the chapter "Conclusions, Limitations and Future Directions ", are presented in the following papers.

1. Study on the effects of a decrease in SR Ca^{2+} leak in nNOS KO mice:

G. Lim, L. Li, N. P. Smith, B. Casadei, et al. nNOS gene disruption reduces the diastolic calcium leak from the ryanodine receptor: implications for excitation-contraction coupling. *In preparation*.

2. Study on changes in the LCCs in Rem KO mice:

J. Magyar, C. Kiper, G. Sievert, W. Cai, S. M. Crump, L. Li, N. Smith, D. A. Andrews, and J. Satin. Rem-GTPase regulates cardiac myocyte L-type calcium current. *Cardiovascular Research. Under review*.

3. Study on genotype-phenotype mapping:

J. O. Vik, A. B. Gjuvsland, L. Li, K. Tøndel, S. Niederer, N. P. Smith, P. J. Hunter, and S. W. Omholt. Genotype-phenotype map characteristics of an in silico heart cell. *Frontiers in Physiology*, 2(106), 2011.

4. Development of a coupled cell electro-mechanics model and a whole-organ electro-mechanics model of mouse heart.

S. Land, S. A. Niederer, Ø. Nordbø, E. Espe, W. E Louch, S. Omholt and N. P. Smith. An electromechanical model of the mouse heart. *In preparation*.

Appendix B

List of Parameters, Their Values and the Corresponding Experimental Data Source and Temperature for the C57BL/6 Model

RT: room temperature. *: indicates experiment was carried out in the current study. Direct: indicates parameter value was fitted directly to experimental data. Indirect: indicates parameter value was fitted indirectly to experimentally observed ensemble behaviour as explained in the text. Estimated: indicates the same parameter value from a previous model was adopted.

Parameter	Definition	Value	Species	T(^{o}C)	Fitting(source)
C_m	Specific membrane capacitance (μF/cm^2)	1.0		Physical constant	
F	Faraday constant (C/mmol)	96.5		Physical constant	
T	Absolute temperature (K)	310		Physical constant	
R	Ideal gas constant (J·mol^{-1}·K^{-1})	8.314		Physical constant	
A_{cap}	Capacitive membrane area (cm^{-2})	1.387×10^{-4}	Murine	35	Measured (*)

Continued on next page

Table B.1 – continued from previous page

Parameter	Definition	Value	Species	T(^{o}C)	Fitting(source)
V_{myo}	Myoplasmic volume (μL)	2.2×10^{-5}	Murine	37	Measured ([148])
V_{JSR}	Juctional SR volume (μL)	7.7×10^{-8}	Murine	-	Measured ([28])
V_{NSR}	Network SR volume (μL)	2.31×10^{-7}	Murine	-	Measured ([28])
V_{ds}	Dyadic space volume (μL)	2.2×10^{-8}	-	-	Estimated ([19])
B_{max}	Max. buffering capacity (μM)	109	Ferret	RT	Direct [196]
Kd_{buffer}	Affinity of buffer to Ca^{2+} (μM)	0.6	Ferret	RT	Direct [196]
V_{NCX}^{max}	NCX: max. exchange rate (pA/pF)	3.939	Murine	35	Direct (*)
$K_{m,Cao}$	NCX: affinity to extracellular Ca^{2+} (mM)	1.4	Murine	35	Estimated (*)
$K_{m,Cai}$	NCX : affinity to intracellular Ca^{2+} (mM)	0.0036	Murine	35	Estimated (*)
$K_{m,Nai}$	NCX : affinity to intracellular Na^{+} (mM)	12	Murine	35	Estimated (*)
k_{sat}	NCX: saturation factor	0.27	Murine	35	Estimated (*)
η	NCX: V_m-dependence factor	0.35	Murine	35	Estimated (*)
K_{mallo}	NCX: allosteric regulation (μM)	0	Murine	RT	Measured ([206])
f_0	CaMKII: initial fractional occupancy (%)	5	Canine	37	Estimated [95]
$K_{m,CaM}$	CaMKII: $[Ca^{2+}]_i$ for half activation (μM))	0.7	na	na	Estimated ([215]
α	CaMKII: autophosphorylation rate (ms^{-2})	0.05	Canine	37	Estimated ([95])
β	CaMKII: dephosphorylation rate (ms^{-1})	0.0002	Murine	35	Estimated (*)
$K_{m,up}$	SERCA : affinity to Ca^{2+} (μM)	0.412	Murine	35	Direct (*)
$\overline{V_{up}}$	SERCA: max. uptake rate in the absence of CaMKII (μM/ms)	0.396	Murine	35	Direct (*)
$K_{m,CaMK}$	SERCA: half-saturation coefficient for CaMKII	1.224	Murine	35	Direct (*)
n_{CaMK}	SERCA: Hill coefficient for interaction with CaMKII	2.583	Murine	35	Direct (*)
nH	SERCA: Hill coefficient for binding to Ca^{2+}	2	na	RT	Direct ([129])
$\overline{\Delta V_{up,CaMK}}$	SERCA: max. CaMKII-dependent increase in V_{up}	2.998	Murine	35	Direct (*)
V_{leak}	SR leak: rate constant (ms^{-1})	3×10^{-5}	Murine	35	Indirect (*)

Continued on next page

Table B.1 – continued from previous page

Parameter	Definition	Value	Species	T(^{o}C)	Fitting(source)
P_{CaL}	LCC: permeability of the channel (ms^{-1})	2.5	Murine	35	Direct (*)
Φ_L	LCC: proportion of time closed in open mode	1.798	Murine	35	Direct (*)
t_L	LCC: time switching between C and O states (ms)	1.5	Murine	35	Direct (*)
V_L	LCC: potential when half LCC open (mV)	0	Murine	35	Direct (*)
ΔV_L	LCC: width of opening potentials (mV)	6.45	Murine	35	Direct (*)
K_L	LCC: concentration at inactivation (μM)	0.3	Murine	35	Direct (*)
τ_L	LCC: inactivation time (ms)	1150	Murine	35	Direct (*)
a	LCC: biasing to make inactivation function of V	0.0625	Murine	35	Estimated (*)
b	LCC: biasing to make inactivation function of V	0.4	Murine	30	Indirect ([7])
C_1	LCC: V-dependent inactivation constant 1 (mV)	33	Murine	37	Direct ([143])
C_2	LCC: V-dependent inactivation constant 2 (mV)	8.23	Murine	37	Direct ([143])
C_3	LCC: V-dependent inactivation constant 3 (ms)	0.1	G-P	37	Estimated ([98])
C_4	LCC: V-dependent inactivation constant 4 (mV)	40	G-P	37	Estimated ([98])
C_5	LCC: V-dependent inactivation constant 5 (mV)	6	G-P	37	Estimated ([98])
C_6	LCC: V-dependent inactivation constant 6 (ms)	8	Murine	35	Direct (*)
C_7	LCC: V-dependent inactivation constant 7 (ms)	315	Murine	37	Direct ([143])
C_8	LCC: V-dependent inactivation constant 8 (mV)	30	Murine	35	Direct (*)
C_9	LCC: V-dependent inactivation constant 9 (mV)	4	Murine	35	Direct (*)
$G_{kto,f}$	$I_{kto,f}$: max. conductance of the channel (mS/μF)	0.535	Murine	32	Direct ([53])
G_{kur}	I_{kur}: max. conductance of the channel (mS/μF)	0.250	0.250	32	Direct ([53])
G_{kss}	I_{kss}: max. conductance of the channel (mS/μF)	0.060	Murine	32	Direct ([53])
G_{kr}	Ik_r: max. conductance of the channel (mS/μF)	0.0165	Murine	32	Direct ([115])
G_{ks}	I_{ks}: max. conductance of the channel (mS/μF)	0.00575	Murine	RT	Estimated ([27])
G_{k1}	I_{k1}: max. conductance of the channel (mS/μF)	0.35	Murine	36	Direct ([105])

Continued on next page

Table B.1 – continued from previous page

Parameter	Definition	Value	Species	T(^{o}C)	Fitting(source)
V_{rel}	RyR: max. Ca^{2+} permeability (ms^{-1})	4.5	Murine	RT	Estimated ([27])
k_a^+	RyR: P_{C1} - P_{O1} rate constant (μM^{-4}/ms)	0.006075	Murine	RT	Estimated ([27])
k_a^-	RyR: P_{O1} - P_{C1} rate constant (ms^{-1})	0.07125	Murine	RT	Estimated ([27])
k_b^+	RyR: P_{O1} - P_{O2} rate constant (μM^{-3}/ms)	0.00405	Murine	RT	Estimated ([27])
k_b^-	RyR: P_{O2} - P_{O1} rate constant (ms^{-1})	0.965	Murine	RT	Estimated ([27])
k_c^+	RyR: P_{O1} - P_{C2} rate constant (ms^{-1})	0.009	Murine	RT	Estimated ([27])
k_c^-	RyR: P_{C2} - P_{O1} rate constant (ms^{-1})	0.0008	Murine	RT	Estimated ([27])
n	RyR: Ca^{2+} cooperativity parameter P_{C1} - P_{O1}	4.0	Murine	RT	Estimated ([27])
m	RyR: Ca^{2+} cooperativity parameter P_{O1} - P_{O2}	3.0	Murine	RT	Estimated ([27])
$A_{P_{RyR}}$	P_{RyR}: Ca^{2+} release modulating constant A (ms^{-1})	-0.01	Murine	35	Indirect (*)
$B_{P_{RyR}}$	P_{RyR}: Ca^{2+} release modulating constant B (ms^{-1})	-2.0	Murine	35	Indirect (*)
τ_{tr}	Time constant for transfer from NSR to JSR (ms)	20	Murine	RT	Estimated ([27])
τ_{xfer}	Time constant for transfer from dyad space to cytosol (ms)	8.0	Murine	RT	Estimated ([27])
$CSQN_{tot}$	CSQN: total concentration in JSR (mM)	50	na	na	Estimated ([19])
K_m^{CSQN}	CSQN: affinity to Ca^{2+} (mM)	0.63	na	na	Estimated ([19])
$K_{m,Na}$	Na^+/K^+ pump: affinity to Na^+ (mM)	16.6	Murine	35	Direct ([18])
I_{NaK}^{max}	Na^+/K^+ pump: max. exchange current (pA/pF)	2.486	Murine	35	Direct ([18])
$K_{m,PMCA}$	PMCA: affinity of the pump to Ca^{2+} (μM)	0.289	Murine	35	Direct (*)
I_{PMCA}^{max}	PMCA: max. pump current (pA/pF)	0.096	Murine	35	Direct (*)
G_{Cab}	I_{Cab}: max. conductance of the channel (mS/μF)	0.00070	Murine	35	Indirect (*)
G_{Na}	I_{Na}: max. conductance of the channel (mS/μF)	16	Murine	37	Indirect ([44])
G_{Nab}	I_{Nab}: max. conductance of the channel (mS/μF)	0.0026	Murine	RT	Estimated [44])
$G_{Cl,Ca}$	$I_{Cl,Ca}$: max. conductance of the channel (mS/μF)	10	Murine	RT	Estimated ([27])
$K_{m,Cl}$	$I_{Cl,Ca}$: half saturation constant for the current (μM)	10	Murine	RT	Estimated ([27])

Continued on next page

Table B.1 – continued from previous page

Parameter	Definition	Value	Species	T(^{o}C)	Fitting(source)
E_{Cl}	$I_{Cl,Ca}$: reversal potential for the current (mV)	-40	Murine	RT	Estimated ([27])

Appendix C

Mathematical Formulations for the C57BL/6 Model Framework

All model equations were directly generated from cellml (www.cellml.org) using the Cellular Open Resource (COR: http://cor.physiol.ox.ac.uk/) to remove chance of errors.

cell

$$past = \lfloor \frac{time}{stim_{period}} \rfloor \cdot stim_{period}$$

$$i_{Stim} = \begin{cases} stim_{amplitude} & \text{if } (time - past \geq stim_{offset}) \text{ and } (time - past \leq stim_{offset} + stim_{duration}) \\ 0 & \text{otherwise} \end{cases}$$

$$\frac{\mathrm{d}V}{\mathrm{d}time} = -(i_{CaL} + i_{PMCA} + i_{NCX} + i_{Cab} + i_{Na} + i_{Nab} + i_{NKA} + i_{Kto_f} + i_{Kto_s} + i_{K1} + i_{Ks} + i_{Kur} + i_{Kss} + i_{Kr} + i_{ClCa} + i_{Stim})$$

L_type_calcium_current

$$FVRT = \frac{F \cdot V}{R \cdot T}$$

$$FVRT_{Ca} = 2 \cdot FVRT$$

$$expVL = e^{\frac{V - V_L}{\delta_{V_L}}}$$

$$\alpha_p = \frac{expVL}{t_L \cdot (expVL + 1)}$$

$$\alpha_m = \frac{\phi_L}{t_L}$$

$$\epsilon_p = \frac{expVL + a}{\tau_L \cdot K_L \cdot (expVL + 1)}$$

$$\epsilon_m = \frac{b \cdot (expVL + a)}{\tau_L \cdot (b \cdot expVL + a)}$$

$$y_{gate_{inf}} = \frac{1}{1 + e^{\frac{V + LCC_{C1}}{LCC_{C2}}}} + \frac{LCC_{C3}}{1 + e^{\frac{-V + LCC_{C4}}{LCC_{C5}}}}$$

$$y_{gate_\tau} = LCC_{C6} + \frac{LCC_{C7}}{1 + e^{\frac{V + LCC_{C8}}{LCC_{C9}}}}$$

L_type_calcium_current (continued)

$$C = 1 - O - I$$

$$\frac{\mathrm{d}O}{\mathrm{d}time} = \alpha_p \cdot C - \alpha_m \cdot O$$

$$\frac{\mathrm{d}I}{\mathrm{d}time} = \epsilon_p \cdot Cads \cdot C - \epsilon_m \cdot I$$

$$\frac{\mathrm{d}y_{gate}}{\mathrm{d}time} = \frac{y_{gate_{inf}} - y_{gate}}{y_{gate_\tau}}$$

$$i_{CaL} = \begin{cases} \dfrac{-P_{CaL} \cdot 2 \cdot Vds \cdot F}{Acap \cdot Cm} \cdot O \cdot y_{gate} \cdot FVRT_{Ca} \cdot \left(Cao \cdot e^{-FVRT_{Ca}} - Cads\right) & \text{if } |FVRT_{Ca}| > 0.000,01 \\ \dfrac{-P_{CaL} \cdot 2 \cdot Vds \cdot F}{Acap \cdot Cm} \cdot O \cdot y_{gate} \cdot 0.000,01 \cdot \left(Cao \cdot e^{-0.000,01} - Cads\right) & \text{otherwise} \end{cases}$$

calcium_activated_chloride_current

$$i_{ClCa} = \frac{G_{ClCa} \cdot O_{ClCa} \cdot Cai}{Cai + Km_{Cl}} \cdot (V - E_{Cl})$$

$$O_{ClCa} = \frac{0.2}{1 + e^{\frac{-(V-46.7)}{7.8}}}$$

calcium_background_current

$$i_{Cab} = G_{Cab} \cdot (V - E_{CaN})$$

$$E_{CaN} = \frac{R \cdot T}{2 \cdot F} \cdot \ln \frac{Cao}{Cai}$$

$$J_{Cab} = \frac{-i_{Cab} \cdot Acap \cdot Cm}{2 \cdot Vmyo \cdot F}$$

calcium_concentration

$$J_{total} = \frac{-(i_{Cab} + i_{PMCA} - 2 \cdot i_{NCX}) \cdot Acap \cdot Cm}{2 \cdot Vmyo \cdot F}$$

$$\frac{\mathrm{d}Cai}{\mathrm{d}time} = Bi \cdot \left(J_{leak} + J_{xfer} - \frac{(i_{Cab} + i_{PMCA} - 2 \cdot i_{NCX}) \cdot Acap \cdot Cm}{2 \cdot Vmyo \cdot F} - J_{serca}\right)$$

$$\frac{\mathrm{d}Cads}{\mathrm{d}time} = Bss \cdot \left(\frac{J_{rel} \cdot VJSR}{Vds} - \left(\frac{J_{xfer} \cdot Vmyo}{Vds} + \frac{i_{CaL} \cdot Acap \cdot Cm}{2 \cdot Vds \cdot F}\right)\right)$$

$$\frac{\mathrm{d}CaJSR}{\mathrm{d}time} = BJSR \cdot (J_{tr} - J_{rel})$$

$$\frac{\mathrm{d}CaNSR}{\mathrm{d}time} = \frac{(J_{serca} - J_{leak}) \cdot Vmyo}{VNSR} - \frac{J_{tr} \cdot VJSR}{VNSR}$$

$$Bi = \left(1 + \frac{Bmax \cdot Kd_{buffer}}{\left(Kd_{buffer} + Cai\right)^2}\right)^{-1}$$

$$Bss = \left(1 + \frac{Bmax \cdot Kd_{buffer}}{\left(Kd_{buffer} + Cads\right)^2}\right)^{-1}$$

$$BJSR = \left(1 + \frac{CSQN_{tot} \cdot Km_{CSQN}}{\left(Km_{CSQN} + CaJSR\right)^2}\right)^{-1}$$

$$CaSR = \frac{\frac{CaJSR \cdot CSQN_{tot}}{CaJSR + Km_{CSQN}} \cdot VJSR}{Vmyo} + \frac{CaNSR \cdot VNSR}{Vmyo}$$

calcium_fluxes

$$J_{rel} = V_{rel} \cdot (P_{O1} + P_{O2}) \cdot (CaJSR - Cads) \cdot P_{RyR}$$

$$J_{leak} = V_{leak} \cdot (CaNSR - Cai)$$

$$J_{tr} = \frac{CaNSR - CaJSR}{\tau_{tr}}$$

$$J_{xfer} = \frac{Cads - Cai}{\tau_{xfer}}$$

$$fb = \frac{f0 \cdot (1 - ft) \cdot 1}{1 + \frac{Km_{CaM}}{Cads}}$$

calcium_fluxes (continued)

$$\frac{\mathrm{d}ft}{\mathrm{d}time} = alpha \cdot fb \cdot (fb + ft) - beta \cdot ft$$

$$fa = fb + ft$$

$$Vup = \left(\frac{\delta_{VupCaMK_{max}} \cdot fa^{n_{CaMK}}}{Km_{CaMK}^{n_{CaMK}} + fa^{n_{CaMK}}} + 1\right) \cdot vmup_{init}$$

$$J_{serca} = \frac{Vup \cdot Cai^{nH}}{Km_{up}^{nH} + Cai^{nH}}$$

$$\frac{\mathrm{d}P_{RyR}}{\mathrm{d}time} = A_{PRyR} \cdot P_{RyR} + \frac{B_{PRyR} \cdot i_{CaL}}{i_{CaL_{max}}} \cdot e^{\frac{-(V-5)^2}{648}}$$

calcium_pump_current

$$i_{PMCA} = \frac{i_{PMCA_{max}} \cdot Cai^2}{Km_{PMCA}^2 + Cai^2}$$

$$J_{PMCA} = \frac{-i_{PMCA} \cdot Acap \cdot Cm}{2 \cdot Vmyo \cdot F}$$

fast_sodium_current

$$i_{Na} = G_{Na} \cdot O_{Na} \cdot (V - E_{Na})$$

$$E_{Na} = \frac{R \cdot T}{F} \cdot \ln \frac{0.9 \cdot Nao + 0.1 \cdot Ko}{0.9 \cdot Nai + 0.1 \cdot Ki}$$

$$C_{Na3} = 1 - (O_{Na} + C_{Na1} + C_{Na2} + IF_{Na} + I1_{Na} + I2_{Na} + IC_{Na2} + IC_{Na3})$$

$$\frac{\mathrm{d}C_{Na2}}{\mathrm{d}time} = \alpha_{Na11} \cdot C_{Na3} + \beta_{Na12} \cdot C_{Na1} + \alpha_{Na3} \cdot IC_{Na2} - (\beta_{Na11} \cdot C_{Na2} + \alpha_{Na12} \cdot C_{Na2} + \beta_{Na3} \cdot C_{Na2})$$

$$\frac{\mathrm{d}C_{Na1}}{\mathrm{d}time} = \alpha_{Na12} \cdot C_{Na2} + \beta_{Na13} \cdot O_{Na} + \alpha_{Na3} \cdot IF_{Na} - (\beta_{Na12} \cdot C_{Na1} + \alpha_{Na13} \cdot C_{Na1} + \beta_{Na3} \cdot C_{Na1})$$

$$\frac{\mathrm{d}O_{Na}}{\mathrm{d}time} = \alpha_{Na13} \cdot C_{Na1} + \beta_{Na2} \cdot IF_{Na} - (\beta_{Na13} \cdot O_{Na} + \alpha_{Na2} \cdot O_{Na})$$

$$\frac{\mathrm{d}IF_{Na}}{\mathrm{d}time} = \alpha_{Na2} \cdot O_{Na} + \beta_{Na3} \cdot C_{Na1} + \beta_{Na4} \cdot I1_{Na} + \alpha_{Na12} \cdot IC_{Na2} -$$

$$(\beta_{Na2} \cdot IF_{Na} + \alpha_{Na3} \cdot IF_{Na} + \alpha_{Na4} \cdot IF_{Na} + \beta_{Na12} \cdot IF_{Na})$$

$$\frac{\mathrm{d}I1_{Na}}{\mathrm{d}time} = \alpha_{Na4} \cdot IF_{Na} + \beta_{Na5} \cdot I2_{Na} - (\beta_{Na4} \cdot I1_{Na} + \alpha_{Na5} \cdot I1_{Na})$$

$$\frac{\mathrm{d}I2_{Na}}{\mathrm{d}time} = \alpha_{Na5} \cdot I1_{Na} - \beta_{Na5} \cdot I2_{Na}$$

$$\frac{\mathrm{d}IC_{Na2}}{\mathrm{d}time} = \alpha_{Na11} \cdot IC_{Na3} + \beta_{Na12} \cdot IF_{Na} + \beta_{Na3} \cdot C_{Na2} - (\beta_{Na11} \cdot IC_{Na2} + \alpha_{Na12} \cdot IC_{Na2} + \alpha_{Na3} \cdot IC_{Na2})$$

$$\frac{\mathrm{d}IC_{Na3}}{\mathrm{d}time} = \beta_{Na11} \cdot IC_{Na2} + \beta_{Na3} \cdot C_{Na3} - (\alpha_{Na11} \cdot IC_{Na3} + \alpha_{Na3} \cdot IC_{Na3})$$

$$\alpha_{Na11} = \frac{3.802}{0.102,7 \cdot e^{\frac{-(V+2.5)}{17}} + 0.2 \cdot e^{\frac{-(V+2.5)}{150}}}$$

$$\alpha_{Na12} = \frac{3.802}{0.102,7 \cdot e^{\frac{-(V+2.5)}{15}} + 0.23 \cdot e^{\frac{-(V+2.5)}{150}}}$$

$$\alpha_{Na13} = \frac{3.802}{0.102,7 \cdot e^{\frac{-(V+2.5)}{12}} + 0.25 \cdot e^{\frac{-(V+2.5)}{150}}}$$

$$\beta_{Na11} = 0.191,7 \cdot e^{\frac{-(V+2.5)}{20.3}}$$

$$\beta_{Na12} = 0.2 \cdot e^{\frac{-(V-2.5)}{20.3}}$$

$$\beta_{Na13} = 0.22 \cdot e^{\frac{-(V-7.5)}{20.3}}$$

$$\alpha_{Na3} = 7 \cdot 10^{-7} \cdot e^{\frac{-(V+7)}{7.7}}$$

$$\beta_{Na3} = 0.008,4 + 0.000,02 \cdot (V + 7)$$

$$\alpha_{Na2} = \frac{1}{0.188,495 \cdot e^{\frac{-(V+7)}{16.6}} + 0.393,956}$$

$$\beta_{Na2} = \frac{\alpha_{Na13} \cdot \alpha_{Na2} \cdot \alpha_{Na3}}{\beta_{Na13} \cdot \beta_{Na3}}$$

$$\alpha_{Na4} = \frac{\alpha_{Na2}}{1,000}$$

$$\beta_{Na4} = \alpha_{Na3}$$

$$\alpha_{Na5} = \frac{\alpha_{Na2}}{95,000}$$

$$\beta_{Na5} = \frac{\alpha_{Na3}}{50}$$

fast_transient_outward_K_I

$$i_{Kto_f} = G_{Kto_f} \cdot ato_f^3 \cdot ito_f \cdot (V - E_K)$$
$$E_K = \frac{R \cdot T}{F} \cdot \ln \frac{Ko}{Ki}$$
$$itof_{ss} = \frac{1}{1 + e^{\frac{V+51.4}{5}}}$$
$$\tau_{ito_f} = 9.664,5 + \frac{10.936,2}{1 + e^{\frac{V+51.4}{5}}}$$
$$\frac{\mathrm{d}ato_f}{\mathrm{d}time} = \alpha_a \cdot \left(1 - ato_f\right) - \beta_a \cdot ato_f$$
$$\frac{\mathrm{d}ito_f}{\mathrm{d}time} = \frac{itof_{ss} - ito_f}{\tau_{ito_f}}$$
$$\alpha_a = 0.180,64 \cdot e^{0.035,77 \cdot (V+45)}$$
$$\beta_a = 0.395,6 \cdot e^{-0.062,37 \cdot (V+45)}$$

non_inactivating_steady_state_K_I

$$i_{Kss} = G_{Kss} \cdot aKss \cdot iKss \cdot (V - E_K)$$
$$\frac{\mathrm{d}aKss}{\mathrm{d}time} = \frac{ass - aKss}{\tau_{Kss}}$$
$$\frac{\mathrm{d}iKss}{\mathrm{d}time} = 0$$
$$\tau_{Kss} = 39.3 \cdot e^{-0.05 \cdot V} + 13.17$$

potassium_concentration

$$\frac{\mathrm{d}Ki}{\mathrm{d}time} = \frac{-\left(i_{Stim} + i_{Kto_f} + i_{Kto_s} + i_{K1} + i_{Ks} + i_{Kss} + i_{Kur} + i_{Kr} - 2 \cdot i_{NKA}\right) \cdot Acap \cdot Cm}{Vmyo \cdot F}$$

rapid_delayed_rectifier_K_I

$$i_{Kr} = G_{Kr} \cdot O_K \cdot \left(V - \frac{R \cdot T}{F} \cdot \ln \frac{0.98 \cdot Ko + 0.02 \cdot Nao}{0.98 \cdot Ki + 0.02 \cdot Nai}\right)$$
$$C_{K0} = 1 - (C_{K1} + C_{K2} + O_K + I_K)$$
$$\frac{\mathrm{d}C_{K2}}{\mathrm{d}time} = kf \cdot C_{K1} + \beta_{a1} \cdot O_K - (kb \cdot C_{K2} + \alpha_{a1} \cdot C_{K2})$$
$$\frac{\mathrm{d}C_{K1}}{\mathrm{d}time} = \alpha_{a0} \cdot C_{K0} + kb \cdot C_{K2} - (\beta_{a0} \cdot C_{K1} + kf \cdot C_{K1})$$
$$\frac{\mathrm{d}O_K}{\mathrm{d}time} = \alpha_{a1} \cdot C_{K2} + \beta_i \cdot I_K - (\beta_{a1} \cdot O_K + \alpha_i \cdot O_K)$$
$$\frac{\mathrm{d}I_K}{\mathrm{d}time} = \alpha_i \cdot O_K - \beta_i \cdot I_K$$
$$\alpha_{a0} = 0.022,348 \cdot e^{0.011,76 \cdot V}$$
$$\beta_{a0} = 0.047,002 \cdot e^{-0.063,1 \cdot V}$$
$$\alpha_{a1} = 0.033,5 \cdot e^{0.010,9 \cdot V}$$
$$\beta_{a1} = 0.000,068,9 \cdot e^{-0.041,78 \cdot V}$$
$$\alpha_i = 0.070,3 \cdot e^{0.028,7 \cdot (V+5)}$$
$$\beta_i = 0.006,497 \cdot e^{-0.032,68 \cdot (V+5)}$$

ryanodine_receptors

$$\frac{\mathrm{d}P_{O1}}{\mathrm{d}time} = k_{plus_a} \cdot Cads^n \cdot P_{C1} + k_{minus_b} \cdot P_{O2} + k_{minus_c} \cdot P_{C2} - \left(k_{minus_a} \cdot P_{O1} + k_{plus_b} \cdot Cads^m \cdot P_{O1} + k_{plus_c} \cdot P_{O1}\right)$$
$$P_{C1} = 1 - (P_{C2} + P_{O1} + P_{O2})$$
$$\frac{\mathrm{d}P_{O2}}{\mathrm{d}time} = k_{plus_b} \cdot Cads^m \cdot P_{O1} - k_{minus_b} \cdot P_{O2}$$
$$\frac{\mathrm{d}P_{C2}}{\mathrm{d}time} = k_{plus_c} \cdot P_{O1} - k_{minus_c} \cdot P_{C2}$$

slow_delayed_rectifier_K_I

$$i_{Ks} = G_{Ks} \cdot nKs^2 \cdot (V - E_K)$$
$$\frac{\mathrm{d}nKs}{\mathrm{d}time} = \alpha_n \cdot (1 - nKs) - \beta_n \cdot nKs$$
$$\alpha_n = \frac{0.000,004,813,33 \cdot (V + 26.5)}{1 - e^{-0.128 \cdot (V + 26.5)}}$$
$$\beta_n = 0.000,095,333,3 \cdot e^{-0.038 \cdot (V + 26.5)}$$

slow_transient_outward_K_I

$$i_{Kto_s} = g_{Kto_s} \cdot ato_s \cdot ito_s \cdot (V - E_K)$$
$$\frac{\mathrm{d}ato_s}{\mathrm{d}time} = \frac{ass - ato_s}{\tau_{ta_s}}$$
$$\frac{\mathrm{d}ito_s}{\mathrm{d}time} = \frac{iss - ito_s}{\tau_{ti_s}}$$
$$\tau_{ta_s} = 0.493 \cdot e^{-0.062,9 \cdot V} + 2.058$$
$$\tau_{ti_s} = 270 + \frac{1,050}{1 + e^{\frac{V + 45.2}{5.7}}}$$

sodium_background_current

$$i_{Nab} = G_{Nab} \cdot (V - E_{Na})$$

sodium_calcium_exchange_current

$$I_{NCX} = \frac{V_{NCX}^{max}}{1 + (\frac{K_{malfa}}{[Ca^{2+}]_i})^2} \cdot \frac{[Na^+]_i^3 \cdot [Ca^{2+}]_o \cdot e^{\frac{\eta V_m F}{RT}} - [Na^+]_o^3 \cdot [Ca^{2+}]_i \cdot e^{\frac{(\eta - 1) V_m F}{RT}}}{\left\{ \begin{array}{l} [Na^+]_i^3 \cdot (1400 + [Ca^{2+}]_o + \frac{K_{mCai} \cdot [Na^+]_o^3}{12000^3}) \\ + [Ca^{2+}]_i \cdot \left[\frac{12000^3}{K_{mCai}} \cdot (1400 + [Ca^{2+}]_o) + [Na^+]_o^3 \right] \\ + 12000^3 \cdot [Ca^{2+}]_o + K_{mCai} \cdot [Na^+]_o^3 \end{array} \right\} \cdot (1 + k_{sat} \cdot e^{\frac{(\eta - 1) V_m F}{RT}})}$$

$$J_{NCX} = \frac{i_{NCX} \cdot Acap \cdot Cm}{Vmyo \cdot F}$$

sodium_concentration

$$\frac{\mathrm{d}Nai}{\mathrm{d}time} = \frac{-(i_{Na} + i_{Nab} + 3 \cdot i_{NKA} + 3 \cdot i_{NCX}) \cdot Acap \cdot Cm}{Vmyo \cdot F}$$

sodium_potassium_pump_current

$$i_{NKA} = \frac{\frac{i_{NKA_{max}} \cdot f_{NKA} \cdot 1}{1 + \left(\frac{Km_{Na}}{Nai} \right)^{nH_{NKA}}} \cdot Ko}{Ko + Km_{Ko}}$$
$$f_{NKA} = \frac{1}{1 + 0.124,5 \cdot e^{\frac{-0.1 \cdot V \cdot F}{R \cdot T}} + 0.036,5 \cdot sigma \cdot e^{\frac{-V \cdot F}{R \cdot T}}}$$
$$sigma = \frac{1}{7} \cdot \left(e^{\frac{Nao}{67,300}} - 1 \right)$$

time_independent_K_I

$$i_{K1} = \frac{\frac{G_{K1} \cdot Ko}{Ko + 210} \cdot (V - E_K)}{1 + e^{0.089,6 \cdot (V - E_K)}}$$

ultra_rapidly_activating_delayed_rectifier_K_I

$$ass = \frac{1}{1 + e^{\frac{-(V+6.19)}{9.6}}}$$

$$iss = \frac{1}{1 + e^{\frac{V+42.1}{5.4}}}$$

$$i_{Kur} = G_{Kur} \cdot aur \cdot iur \cdot (V - E_K)$$

$$\frac{\mathrm{d}aur}{\mathrm{d}time} = \frac{ass - aur}{\tau_{aur}}$$

$$\frac{\mathrm{d}iur}{\mathrm{d}time} = \frac{iss - iur}{\tau_{iur}}$$

$$\tau_{aur} = 0.493 \cdot e^{-0.062,9 \cdot V} + 2.058$$

$$\tau_{iur} = \tau_{i_{const}} + \frac{1,000}{1 + e^{\frac{V+42.1}{5.4}}}$$

Appendix D

Parameter Values for SERCA2 FF and KO Models:4-week Study

Parameter Values for the FF Model

	Value	Unit
K_L	0.25	micromolar
LCC_{C1}	33	millivolt
LCC_{C2}	8.2	millivolt
LCC_{C3}	0.1	dimensionless
LCC_{C4}	40	millivolt
LCC_{C5}	6	millivolt
LCC_{C6}	3	millisecond
LCC_{C7}	315	millisecond
LCC_{C8}	30	millivolt
LCC_{C9}	5	millivolt
P_{CaL}	9.5	per_millisecond
V_L	-5	millivolt
a	0.3	dimensionless
b	0.4	dimensionless
δ_{V_L}	9	millivolt
$i_{CaL_{max}}$	7	picoA_per_picoF
ϕ_L	2.5	dimensionless
t_L	3	millisecond
τ_L	885.7	millisecond
E_{Cl}	-40	millivolt
Km_{Cl}	10	micromolar
g_{ClCa}	10	milliS_per_microF

Parameter Values for the FF Model (continued)

	Value	Unit
g_{Cab}	$0.000,2$	milliS_per_microF
$Bmax$	109	micromolar
$CSQN_{tot}$	$50,000$	micromolar
Kd_{buffer}	0.6	micromolar
Km_{CSQN}	630	micromolar
A_{PRyR}	-0.04	per_millisecond
B_{PRyR}	-3	per_millisecond
Km_{CaM}	0.7	micromolar
Km_{CaMK}	$0.819,1$	dimensionless
Km_{up}	$0.322,2$	micromolar
V_{leak}	$2 \cdot 10^{-5}$	per_millisecond
V_{rel}	4.5	per_millisecond
$alpha$	0.05	per_millisecond
$beta$	$0.000,2$	per_millisecond
$\delta_{VupCaMK_{max}}$	$8.076,8$	dimensionless
nH	2	dimensionless
n_{CaMK}	11.97	dimensionless
τ_{tr}	20	millisecond
τ_{xfer}	6	millisecond
$vmup_{init}$	$0.078,5$	micromolar_per_millisecond
Km_{PMCA}	$0.450,8$	micromolar
$i_{PMCA_{max}}$	$0.129,6$	picoA_per_picoF
$Acap$	$0.000,148$	cm2
Cao	$1,000$	micromolar
Cm	1	microF_per_cm2
F	96.5	coulomb_per_millimole
Ko	$5,400$	micromolar
Nao	$135,000$	micromolar
R	8.314	joule_per_mole_kelvin
T	310	kelvin
$VJSR$	$7.7 \cdot 10^{-8}$	microlitre
$VNSR$	$2.31 \cdot 10^{-7}$	microlitre
Vds	$2.2 \cdot 10^{-8}$	microlitre
$Vmyo$	$2.2 \cdot 10^{-5}$	microlitre
$stim_{amplitude}$	-15	picoA_per_picoF
$stim_{duration}$	3	millisecond
$stim_{offset}$	0	millisecond
$stim_{period}$	$1,000$	millisecond
g_{Na}	16	milliS_per_microF
g_{Kto_f}	$0.534,7$	milliS_per_microF

Parameter Values for the FF Model (continued)

	Value	Unit
g_{Kss}	$0.059,6$	milliS_per_microF
g_{Kr}	$0.016,5$	milliS_per_microF
kb	$0.036,778$	per_millisecond
kf	$0.023,761$	per_millisecond
k_{minus_a}	$0.071,25$	per_millisecond
k_{minus_b}	0.965	per_millisecond
k_{minus_c}	$0.000,8$	per_millisecond
k_{plus_a}	$0.006,075$	micromolar4_per_millisecond
k_{plus_b}	$0.004,05$	micromolar3_per_millisecond
k_{plus_c}	0.009	per_millisecond
m	3	dimensionless
n	4	dimensionless
g_{Ks}	$0.005,75$	milliS_per_microF
g_{Kto_s}	0	milliS_per_microF
g_{Nab}	$0.002,6$	milliS_per_microF
K_{mAllo}	$0.141,5$	micromolar
K_{mCai}	3.6	micromolar
K_{mCao}	$1,400$	micromolar
K_{mNai}	$12,000$	micromolar
K_{mNao}	$88,000$	micromolar
$V_{max_{NCX}}$	1.059	picoA_per_picoF
eta	0.35	dimensionless
k_{sat}	0.27	dimensionless
Km_{Ko}	$1,500$	micromolar
Km_{Na}	$16,600$	micromolar
$i_{NKA_{max}}$	2.486	picoA_per_picoF
g_{K1}	0.35	milliS_per_microF
g_{Kur}	0.25	milliS_per_microF
$\tau_{i_{const}}$	643	millisecond

Parameter Values for the KO Model

	Value	Unit
K_L	0.23	micromolar
LCC_{C1}	33	millivolt
LCC_{C2}	8.2	millivolt
LCC_{C3}	0.1	dimensionless
LCC_{C4}	40	millivolt
LCC_{C5}	6	millivolt
LCC_{C6}	3	millisecond
LCC_{C7}	315	millisecond
LCC_{C8}	19	millivolt
LCC_{C9}	2.7	millivolt
P_{CaL}	8.5	per_millisecond
V_L	-5	millivolt
a	0.3	dimensionless
b	0.4	dimensionless
δ_{V_L}	9	millivolt
$i_{CaL_{max}}$	20	picoA_per_picoF
ϕ_L	2.5	dimensionless
t_L	3	millisecond
τ_L	885.7	millisecond
E_{Cl}	-40	millivolt
Km_{Cl}	10	micromolar
g_{ClCa}	10	milliS_per_microF
g_{Cab}	0.000, 22	milliS_per_microF
$Bmax$	109	micromolar
$CSQN_{tot}$	50, 000	micromolar
Kd_{buffer}	0.6	micromolar
Km_{CSQN}	630	micromolar
A_{PRyR}	-0.04	per_millisecond
B_{PRyR}	-3	per_millisecond
Km_{CaM}	0.7	micromolar
Km_{CaMK}	0.69	dimensionless
Km_{up}	0.322, 2	micromolar
V_{leak}	$6 \cdot 10^{-5}$	per_millisecond
V_{rel}	4.5	per_millisecond
$alpha$	0.05	per_millisecond
$beta$	0.000, 2	per_millisecond
$\delta_{VupCaMK_{max}}$	13.73	dimensionless
nH	2	dimensionless
n_{CaMK}	17.86	dimensionless

Parameter Values for the KO Model (continued)

	Value	Unit
τ_{tr}	20	millisecond
τ_{xfer}	6	millisecond
$vmup_{init}$	0.017	micromolar_per_millisecond
Km_{PMCA}	0.450, 8	micromolar
$i_{PMCA_{max}}$	0.187, 9	picoA_per_picoF
$Acap$	0.000, 155	cm2
Cao	1, 000	micromolar
Cm	1	microF_per_cm2
F	96.5	coulomb_per_millimole
Ko	5, 400	micromolar
Nao	135, 000	micromolar
R	8.314	joule_per_mole_kelvin
T	310	kelvin
$VJSR$	$7.7 \cdot 10^{-8}$	microlitre
$VNSR$	$2.31 \cdot 10^{-7}$	microlitre
Vds	$2.2 \cdot 10^{-8}$	microlitre
$Vmyo$	$2.2 \cdot 10^{-5}$	microlitre
$stim_{amplitude}$	-15	picoA_per_picoF
$stim_{duration}$	3	millisecond
$stim_{offset}$	0	millisecond
$stim_{period}$	1, 000	millisecond
g_{Na}	16	milliS_per_microF
g_{Kto_f}	0.534, 7	milliS_per_microF
g_{Kss}	0.059, 6	milliS_per_microF
g_{Kr}	0.016, 5	milliS_per_microF
kb	0.036, 778	per_millisecond
kf	0.023, 761	per_millisecond
k_{minus_a}	0.071, 25	per_millisecond
k_{minus_b}	0.965	per_millisecond
k_{minus_c}	0.000, 8	per_millisecond
k_{plus_a}	0.006, 075	micromolar4_per_millisecond
k_{plus_b}	0.004, 05	micromolar3_per_millisecond
k_{plus_c}	0.009	per_millisecond
m	3	dimensionless
n	4	dimensionless
g_{Ks}	0.005, 75	milliS_per_microF
g_{Kto_s}	0	milliS_per_microF
g_{Nab}	0.002, 6	milliS_per_microF
K_{mAllo}	0.141, 5	micromolar
K_{mCai}	3.6	micromolar

Parameter Values for the KO Model (continued)

	Value	Unit
K_{mCao}	$1,400$	micromolar
K_{mNai}	$12,000$	micromolar
K_{mNao}	$88,000$	micromolar
$V_{max_{NCX}}$	$3.626,3$	picoA_per_picoF
eta	0.35	dimensionless
k_{sat}	0.27	dimensionless
Km_{Ko}	$1,500$	micromolar
Km_{Na}	$16,600$	micromolar
$i_{NKA_{max}}$	2.486	picoA_per_picoF
g_{K1}	0.35	milliS_per_microF
g_{Kur}	0.25	milliS_per_microF
$\tau_{i_{const}}$	643	millisecond

Appendix E

Mathematical Formulations for the SERCA2 FF KO Framework: 7-week Study (with Sub-sarcolemmal Compartment)

cell

$$Ajc = Atot \cdot TT_{ratio}$$

$$Asl = Atot \cdot (1 - TT_{ratio})$$

$$past = \lfloor \frac{time}{stim_{period}} \rfloor \cdot stim_{period}$$

$$i_{Stim} = \begin{cases} stim_{amplitude} & \text{if } (time - past \geq stim_{offset}) \text{ and } (time - past \leq stim_{offset} + stim_{duration}) \\ 0 & \text{otherwise} \end{cases}$$

$$\frac{\mathrm{d}V}{\mathrm{d}time} = -(i_{cl} + i_{CaL} + i_{PMCA} + i_{NCX} + i_{Cab} + i_{Na} + i_{Nab} + i_{NKA} + i_{Ktof} + i_{K1} + i_{Ks} + i_{Kur} + i_{Kss} + i_{Kr} + i_{ClCa} + i_{Stim} + i_{anion} + i_{PMCA_{proton}})$$

Cl_concentration

$$\frac{\mathrm{d}Cli}{\mathrm{d}time} = \frac{(i_{ClCa} + i_{cl}) \cdot Atot \cdot Cm}{Vmyo \cdot F} + Jche + Jae$$

L_type_calcium_current

$$FVRT = \frac{F \cdot V}{R \cdot T}$$

$$FVRT_{Ca} = 2 \cdot FVRT$$

$$expVL = e^{\frac{V - V_L}{\delta_{V_L}}}$$

L_type_calcium_current (continued)

$$\alpha_p = \frac{expVL}{t_L \cdot (expVL + 1)}$$

$$\alpha_m = \frac{\phi_L}{t_L}$$

$$\epsilon_p = \frac{expVL + a}{\tau_L \cdot K_L \cdot (expVL + 1)}$$

$$\epsilon_m = \frac{b \cdot (expVL + a)}{\tau_L \cdot (b \cdot expVL + a)}$$

$$y_{gate_{inf}} = \frac{1}{1 + e^{\frac{V + LCC_{C1}}{LCC_{C2}}}} + \frac{LCC_{C3}}{1 + e^{\frac{-V + LCC_{C4}}{LCC_{C5}}}}$$

$$y_{gate_\tau} = LCC_{C6} + \frac{LCC_{C7}}{1 + e^{\frac{V + LCC_{C8}}{LCC_{C9}}}}$$

$$Cjc = 1 - Ojc - Ijc$$

$$Csl = 1 - Osl - Isl$$

$$\frac{\mathrm{d}Ojc}{\mathrm{d}time} = \alpha_p \cdot Cjc - \alpha_m \cdot Ojc$$

$$\frac{\mathrm{d}Osl}{\mathrm{d}time} = \alpha_p \cdot Csl - \alpha_m \cdot Osl$$

$$\frac{\mathrm{d}Ijc}{\mathrm{d}time} = \epsilon_p \cdot Cjc \cdot Cajc - \epsilon_m \cdot Ijc$$

$$\frac{\mathrm{d}Isl}{\mathrm{d}time} = \epsilon_p \cdot Csl \cdot Casl - \epsilon_m \cdot Isl$$

$$\frac{\mathrm{d}y_{gate}}{\mathrm{d}time} = \frac{y_{gate_{inf}} - y_{gate}}{y_{gate_\tau}}$$

$$i_{CaL_{jc}} = \begin{cases} \dfrac{-P_{CaL} \cdot 2 \cdot F}{Ajc \cdot Cm} \cdot Ojc \cdot y_{gate} \cdot FVRT_{Ca} \cdot \dfrac{\left(Cao \cdot e^{-FVRT_{Ca}} - Cajc\right)}{1 - e^{-FVRT_{Ca}}} & \text{if } |FVRT_{Ca}| > 0.000,01 \\ \dfrac{-P_{CaL} \cdot 2 \cdot F}{Ajc \cdot Cm} \cdot Ojc \cdot y_{gate} \cdot 0.000,01 \cdot \dfrac{\left(Cao \cdot e^{-0.000,01} - Cajc\right)}{1 - e^{-0.000,01}} & \text{otherwise} \end{cases}$$

$$i_{CaL_{sl}} = \begin{cases} \dfrac{-0.1 \cdot P_{CaL} \cdot 2 \cdot F}{Asl \cdot Cm} \cdot Osl \cdot y_{gate} \cdot FVRT_{Ca} \cdot \dfrac{\left(Cao \cdot e^{-FVRT_{Ca}} - Casl\right)}{1 - e^{-FVRT_{Ca}}} & \text{if } |FVRT_{Ca}| > 0.000,01 \\ \dfrac{-0.1 \cdot P_{CaL} \cdot 2 \cdot F}{Asl \cdot Cm} \cdot Osl \cdot y_{gate} \cdot 0.000,01 \cdot \dfrac{\left(Cao \cdot e^{-0.000,01} - Casl\right)}{1 - e^{-0.000,01}} & \text{otherwise} \end{cases}$$

$$i_{CaL} = i_{CaL_{jc}} \cdot TT_{ratio} + i_{CaL_{sl}} \cdot (1 - TT_{ratio})$$

anion_flux

$$i_{anion} = \frac{\frac{p_{anion} \cdot F^2 \cdot V}{R \cdot T \cdot Cm} \cdot \left(anion_i - anion_o \cdot e^{\frac{F \cdot V}{R \cdot T}}\right)}{1 - e^{\frac{F \cdot V}{R \cdot T}}}$$

$$\frac{\mathrm{d}anion_i}{\mathrm{d}time} = \frac{i_{anion} \cdot Atot \cdot Cm}{Vmyo \cdot F} + J_{acid_{flux_{in}}}$$

calcium_activated_chloride_current

$$i_{ClCa} = \frac{g_{ClCa} \cdot O_{ClCa} \cdot Cai}{Cai + Km_{Cl}} \cdot (V - E_{Cl})$$

$$O_{ClCa} = \frac{0.2}{1 + e^{\frac{-(V - 46.7)}{7.8}}}$$

calcium_background_current

$$E_{Ca_{jc}} = \frac{R \cdot T}{2 \cdot F} \cdot \ln \frac{Cao}{Cajc}$$

$$E_{Ca_{sl}} = \frac{R \cdot T}{2 \cdot F} \cdot \ln \frac{Cao}{Casl}$$

$$i_{Cab_{jc}} = g_{Cab} \cdot \left(V - E_{Ca_{jc}}\right)$$

$$i_{Cab_{sl}} = g_{Cab} \cdot \left(V - E_{Ca_{sl}}\right)$$

$$i_{Cab} = i_{Cab_{jc}} \cdot TT_{ratio} + i_{Cab_{sl}} \cdot (1 - TT_{ratio})$$

calcium_background_current (continued)

$$J_{Cab} = \frac{-i_{Cab} \cdot Atot \cdot Cm}{2 \cdot Vmyo \cdot F}$$

calcium_concentration

$$JCa_{sl} = \frac{-\left(i_{Cab_{sl}} + i_{PMCA_{sl}} - 2 \cdot i_{NCX_{sl}} + i_{CaL_{sl}}\right) \cdot Asl \cdot Cm}{2 \cdot Vsl \cdot F}$$

$$JCa_{jc} = \frac{-\left(i_{Cab_{jc}} + i_{PMCA_{jc}} - 2 \cdot i_{NCX_{jc}} + i_{CaL_{jc}}\right) \cdot Ajc \cdot Cm}{2 \cdot Vjc \cdot F}$$

$$\frac{\mathrm{d}Casl}{\mathrm{d}time} = Bsl \cdot \left(JCa_{sl} - \frac{JCa_{slcyt} \cdot Vmyo}{Vsl} + JCa_{jcsl}\right)$$

$$\frac{\mathrm{d}Cajc}{\mathrm{d}time} = Bjc \cdot \left(JCa_{jc} - \frac{JCa_{jcsl} \cdot Vsl}{Vjc} + \frac{J_{rel} \cdot VJSR}{Vjc}\right)$$

$$\frac{\mathrm{d}Cai}{\mathrm{d}time} = Bi \cdot \left(J_{leak} + JCa_{slcyt} - J_{serca}\right)$$

$$\frac{\mathrm{d}CaJSR}{\mathrm{d}time} = BJSR \cdot \left(J_{tr} - J_{rel}\right)$$

$$\frac{\mathrm{d}CaNSR}{\mathrm{d}time} = \frac{\left(J_{serca} - J_{leak}\right) \cdot Vmyo}{VNSR} - \frac{J_{tr} \cdot VJSR}{VNSR}$$

$$Bi = \left(1 + \frac{Bmax \cdot Kd_{buffer}}{\left(Kd_{buffer} + Cai\right)^2}\right)^{-1}$$

$$Bsl = \left(1 + \frac{Bmax \cdot Kd_{buffer}}{\left(Kd_{buffer} + Casl\right)^2}\right)^{-1}$$

$$Bjc = \left(1 + \frac{Bmax \cdot Kd_{buffer}}{\left(Kd_{buffer} + Cajc\right)^2}\right)^{-1}$$

$$BJSR = \left(1 + \frac{CSQN_{tot} \cdot Km_{CSQN}}{\left(Km_{CSQN} + CaJSR\right)^2}\right)^{-1}$$

$$CaSR = \frac{\frac{CaJSR \cdot CSQN_{tot}}{CaJSR + Km_{CSQN}} \cdot VJSR}{Vmyo} + \frac{CaNSR \cdot VNSR}{Vmyo}$$

calcium_fluxes

$$\tau_{Ca_{jcsl}} = \left(\frac{\tau_{Ca_{jcsl_{const}}}}{Vsl}\right)^{-1}$$

$$\tau_{Ca_{slcyt}} = \left(\frac{\tau_{ca_{slcyt_{const}}}}{Vmyo}\right)^{-1}$$

$$JCa_{jcsl} = \frac{Cajc - Casl}{\tau_{Ca_{jcsl}}}$$

$$JCa_{slcyt} = \frac{Casl - Cai}{\tau_{Ca_{slcyt}}}$$

$$J_{rel} = V_{rel} \cdot \left(P_{O1} + P_{O2}\right) \cdot \left(CaJSR - Cajc\right) \cdot P_{RyR}$$

$$J_{leak} = V_{leak} \cdot \left(CaNSR - Cai\right)$$

$$P_{open} = \left(P_{O1} + P_{O2}\right) \cdot P_{RyR}$$

$$J_{tr} = \frac{CaNSR - CaJSR}{\tau_{tr}}$$

$$J_{serca} = \frac{Vup \cdot Cai^{nH}}{Km_{up}^{nH} + Cai^{nH}}$$

$$J_{netup} = J_{serca} - J_{leak}$$

$$\frac{\mathrm{d}P_{RyR}}{\mathrm{d}time} = A_{PRyR} \cdot P_{RyR} + \frac{B_{PRyR} \cdot i_{CaL}}{i_{CaL_{max}}} \cdot e^{\frac{-(V-5)^2}{648}}$$

calcium_pump_current

$$i_{PMCA_{sl}} = \frac{i_{PMCA_{max}} \cdot Casl^2}{Km_{PMCA}^2 + Casl^2}$$

$$i_{PMCA_{jc}} = \frac{i_{PMCA_{max}} \cdot Cajc^2}{Km_{PMCA}^2 + Cajc^2}$$

$$i_{PMCA} = i_{PMCA_{jc}} \cdot TT_{ratio} + i_{PMCA_{sl}} \cdot \left(1 - TT_{ratio}\right)$$

calcium_pump_current (continued)

$$J_{PMCA_{sl}} = \frac{-i_{PMCA} \cdot Asl \cdot Cm}{2 \cdot Vsl \cdot F}$$
$$J_{PMCA_{jc}} = \frac{-i_{PMCA} \cdot Ajc \cdot Cm}{2 \cdot Vjc \cdot F}$$
$$J_{PMCA_{total}} = \frac{J_{PMCA_{sl}} \cdot Vsl}{Vmyo} + \frac{J_{PMCA_{jc}} \cdot Vjc}{Vmyo}$$
$$i_{PMCA_{proton}} = -i_{PMCA}$$
$$J_{PMCA_{proton}} = -J_{PMCA_{total}} \cdot 2$$

chloride_current_constant_field

$$i_{cl} = \begin{cases} \dfrac{\dfrac{p_{cl} \cdot F^2 \cdot V}{R \cdot T \cdot Cm} \cdot \left(Cli - Clo \cdot e^{\frac{F \cdot V}{R \cdot T}} \right)}{1 - e^{\frac{F \cdot V}{R \cdot T}}} & \text{if } |FVRT| > 0.000,01 \\ \dfrac{\dfrac{p_{cl} \cdot F \cdot 0.000,01}{Cm} \cdot \left(Cli - Clo \cdot e^{0.000,01} \right)}{1 - e^{0.000,01}} & \text{otherwise} \end{cases}$$

fast_sodium_current

$$i_{Na} = i_{Na_{jc}} \cdot TT_{ratio} + i_{Na_{sl}} \cdot (1 - TT_{ratio})$$
$$i_{Na_{jc}} = g_{Na} \cdot O_{Na} \cdot \left(V - E_{Na_{jc}} \right)$$
$$i_{Na_{sl}} = g_{Na} \cdot O_{Na} \cdot \left(V - E_{Na_{sl}} \right)$$
$$E_{Na_{jc}} = \frac{R \cdot T}{F} \cdot \ln \frac{0.9 \cdot Nao + 0.1 \cdot Ko}{0.9 \cdot Najc + 0.1 \cdot Ki}$$
$$E_{Na_{sl}} = \frac{R \cdot T}{F} \cdot \ln \frac{0.9 \cdot Nao + 0.1 \cdot Ko}{0.9 \cdot Nasl + 0.1 \cdot Ki}$$
$$C_{Na3} = 1 - (O_{Na} + C_{Na1} + C_{Na2} + IF_{Na} + I1_{Na} + I2_{Na} + IC_{Na2} + IC_{Na3})$$
$$\frac{\mathrm{d}C_{Na2}}{\mathrm{d}time} = \alpha_{Na11} \cdot C_{Na3} + \beta_{Na12} \cdot C_{Na1} + \alpha_{Na3} \cdot IC_{Na2} - (\beta_{Na11} \cdot C_{Na2} + \alpha_{Na12} \cdot C_{Na2} + \beta_{Na3} \cdot C_{Na2})$$
$$\frac{\mathrm{d}C_{Na1}}{\mathrm{d}time} = \alpha_{Na12} \cdot C_{Na2} + \beta_{Na13} \cdot O_{Na} + \alpha_{Na3} \cdot IF_{Na} - (\beta_{Na12} \cdot C_{Na1} + \alpha_{Na13} \cdot C_{Na1} + \beta_{Na3} \cdot C_{Na1})$$
$$\frac{\mathrm{d}O_{Na}}{\mathrm{d}time} = \alpha_{Na13} \cdot C_{Na1} + \beta_{Na2} \cdot IF_{Na} - (\beta_{Na13} \cdot O_{Na} + \alpha_{Na2} \cdot O_{Na})$$
$$\frac{\mathrm{d}IF_{Na}}{\mathrm{d}time} = \alpha_{Na2} \cdot O_{Na} + \beta_{Na3} \cdot C_{Na1} + \beta_{Na4} \cdot I1_{Na} + \alpha_{Na12} \cdot IC_{Na2} -$$
$$(\beta_{Na2} \cdot IF_{Na} + \alpha_{Na3} \cdot IF_{Na} + \alpha_{Na4} \cdot IF_{Na} + \beta_{Na12} \cdot IF_{Na})$$
$$\frac{\mathrm{d}I1_{Na}}{\mathrm{d}time} = \alpha_{Na4} \cdot IF_{Na} + \beta_{Na5} \cdot I2_{Na} - (\beta_{Na4} \cdot I1_{Na} + \alpha_{Na5} \cdot I1_{Na})$$
$$\frac{\mathrm{d}I2_{Na}}{\mathrm{d}time} = \alpha_{Na5} \cdot I1_{Na} - \beta_{Na5} \cdot I2_{Na}$$
$$\frac{\mathrm{d}IC_{Na2}}{\mathrm{d}time} = \alpha_{Na11} \cdot IC_{Na3} + \beta_{Na12} \cdot IF_{Na} + \beta_{Na3} \cdot C_{Na2} - (\beta_{Na11} \cdot IC_{Na2} + \alpha_{Na12} \cdot IC_{Na2} + \alpha_{Na3} \cdot IC_{Na2})$$
$$\frac{\mathrm{d}IC_{Na3}}{\mathrm{d}time} = \beta_{Na11} \cdot IC_{Na2} + \beta_{Na3} \cdot C_{Na3} - (\alpha_{Na11} \cdot IC_{Na3} + \alpha_{Na3} \cdot IC_{Na3})$$
$$\alpha_{Na11} = \frac{3.802}{0.102,7 \cdot e^{\frac{-(V+2.5)}{17}} + 0.2 \cdot e^{\frac{-(V+2.5)}{150}}}$$
$$\alpha_{Na12} = \frac{3.802}{0.102,7 \cdot e^{\frac{-(V+2.5)}{15}} + 0.23 \cdot e^{\frac{-(V+2.5)}{150}}}$$
$$\alpha_{Na13} = \frac{3.802}{0.102,7 \cdot e^{\frac{-(V+2.5)}{12}} + 0.25 \cdot e^{\frac{-(V+2.5)}{150}}}$$
$$\beta_{Na11} = 0.191,7 \cdot e^{\frac{-(V+2.5)}{20.3}}$$
$$\beta_{Na12} = 0.2 \cdot e^{\frac{-(V-2.5)}{20.3}}$$
$$\beta_{Na13} = 0.22 \cdot e^{\frac{-(V-7.5)}{20.3}}$$
$$\alpha_{Na3} = 7 \cdot 10^{-7} \cdot e^{\frac{-(V+7)}{7.7}}$$
$$\beta_{Na3} = 0.008,4 + 0.000,02 \cdot (V + 7)$$
$$\alpha_{Na2} = \frac{1}{0.188,495 \cdot e^{\frac{-(V+7)}{16.6}} + 0.393,956}$$
$$\beta_{Na2} = \frac{\alpha_{Na13} \cdot \alpha_{Na2} \cdot \alpha_{Na3}}{\beta_{Na13} \cdot \beta_{Na3}}$$

fast_sodium_current (continued)

$$\alpha_{Na4} = \frac{\alpha_{Na2}}{1,000}$$
$$\beta_{Na4} = \alpha_{Na3}$$
$$\alpha_{Na5} = \frac{\alpha_{Na2}}{95,000}$$
$$\beta_{Na5} = \frac{\alpha_{Na3}}{50}$$

fast_transient_outward_K_I

$$i_{Kto_f} = g_{Kto_f} \cdot ato_f^3 \cdot ito_f \cdot (V - E_K)$$
$$E_K = \frac{R \cdot T}{F} \cdot \ln \frac{Ko}{Ki}$$
$$itof_{iss} = \frac{1}{1 + e^{\frac{V+51.4}{5}}}$$
$$\tau_{ito_f} = 9.664,5 + \frac{10.936,2}{1 + e^{\frac{V+51.4}{5}}}$$
$$\frac{\mathrm{d}ato_f}{\mathrm{d}time} = \alpha_a \cdot \left(1 - ato_f\right) - \beta_a \cdot ato_f$$
$$\frac{\mathrm{d}ito_f}{\mathrm{d}time} = \frac{itof_{iss} - ito_f}{\tau_{ito_f}}$$
$$\alpha_a = 0.180,64 \cdot e^{0.035,77 \cdot (V + \alpha_{a_{const}})}$$
$$\beta_a = 0.395,6 \cdot e^{-0.062,37 \cdot (V + \alpha_{b_{const}})}$$

non_inactivating_steady_state_K_I

$$i_{Kss} = g_{Kss} \cdot aKss \cdot iKss \cdot (V - E_K)$$
$$\frac{\mathrm{d}aKss}{\mathrm{d}time} = \frac{ass - aKss}{\tau_{Kss}}$$
$$\frac{\mathrm{d}iKss}{\mathrm{d}time} = 0$$
$$\tau_{Kss} = 39.3 \cdot e^{-0.05 \cdot V} + 13.17$$

pH_regulation

$$k_{r2_{che}} = \frac{k_{f2_{che}} \cdot k_{f1_{che}}}{k_{r1_{che}}}$$
$$K_{OH_{che}} = 10^{-\left(14 - pK_{H_{che}}\right)} \cdot 1,000,000$$
$$Ho = 10^{-pHo} \cdot 1,000,000$$
$$OHo = 10^{-14+pHo} \cdot 1,000,000$$
$$JCO2 = 0$$
$$Jnbc = 0$$
$$Hi = 10^{-pH_i} \cdot 1,000,000$$
$$\alpha_{r1_{nhe}} = \frac{\frac{Nai}{K_{Na_{nhe}}} \cdot k_{r1_{nhe}}}{\left(1 + \frac{Nai}{K_{Na_{nhe}}}\right) \cdot \left(1 + \frac{Hi}{K_{H_{nhe}}}\right)}$$
$$\alpha_{f2_{nhe}} = \frac{\frac{Hi}{K_{H_{nhe}}} \cdot k_{f2_{nhe}}}{\left(1 + \frac{Nai}{K_{Na_{nhe}}}\right) \cdot \left(1 + \frac{Hi}{K_{H_{nhe}}}\right)}$$
$$Jnhe = \frac{\frac{1,000 \cdot Hi^{nH_{nhe}}}{Hi^{nH_{nhe}} + K_{i_{nhe}}^{nH_{nhe}}} \cdot \left(\alpha_{f1_{nhe}} \cdot \alpha_{f2_{nhe}} - \alpha_{r1_{nhe}} \cdot \alpha_{r2_{nhe}}\right)}{\alpha_{f1_{nhe}} + \alpha_{f2_{nhe}} + \alpha_{r1_{nhe}} + \alpha_{r2_{nhe}}}$$
$$OHi = 10^{-14+pH_i} \cdot 1,000,000$$

pH_regulation (continued)

$$\beta_{f_{1_{che}}} = \frac{k_{f_{1_{che}}} \cdot K_{Cl_{che}} \cdot OHi}{K_{OH_{che}} \cdot K_{Cl_{che}} + K_{Cl_{che}} \cdot OHi + K_{OH_{che}} \cdot Cli}$$

$$\beta_{r_{1_{che}}} = \frac{k_{r_{1_{che}}} \cdot K_{Cl_{che}} \cdot OHo}{K_{OH_{che}} \cdot K_{Cl_{che}} + K_{Cl_{che}} \cdot OHo + K_{OH_{che}} \cdot Clo}$$

$$\beta_{f_{2_{che}}} = \frac{k_{f_{2_{che}}} \cdot K_{OH_{che}} \cdot Clo}{K_{OH_{che}} \cdot K_{Cl_{che}} + K_{Cl_{che}} \cdot OHo + K_{OH_{che}} \cdot Clo}$$

$$\beta_{r_{2_{che}}} = \frac{k_{r_{2_{che}}} \cdot K_{OH_{che}} \cdot Cli}{K_{OH_{che}} \cdot K_{Cl_{che}} + K_{Cl_{che}} \cdot OHi + K_{OH_{che}} \cdot Cli}$$

$$Jexch_{che} = \frac{\beta_{f_{1_{che}}} \cdot \beta_{f_{2_{che}}} - \beta_{r_{1_{che}}} \cdot \beta_{r_{2_{che}}}}{\beta_{f_{1_{che}}} + \beta_{r_{1_{che}}} + \beta_{f_{2_{che}}} + \beta_{r_{2_{che}}}}$$

$$Jche = 1,000 \cdot Jexch_{che}$$

$$Jae = 0$$

$$\beta_i = \ln 10 \cdot \left(10^{-pH_i} \cdot 1,000 + \frac{10^{pK1-pH_i} \cdot B1}{\left(1 + 10^{pK1-pH_i}\right)^2} + \frac{10^{pK2-pH_i} \cdot B2}{\left(1 + 10^{pK2-pH_i}\right)^2} \right)$$

$$Jhyd = 0$$

$$\frac{\mathrm{d}pH_i}{\mathrm{d}time} = \frac{-1}{\beta_i} \cdot \left(Jche - Jnhe + J_{acid_{flux_{in}}} + Jhyd + J_{PMCA_{proton}} \right)$$

potassium_concentration

$$\frac{\mathrm{d}Ki}{\mathrm{d}time} = \frac{-\left(i_{Stim} + i_{Kto_f} + i_{K1} + i_{Ks} + i_{Kss} + i_{Kur} + i_{Kr} - 2 \cdot i_{NKA}\right) \cdot Atot \cdot Cm}{Vmyo \cdot F}$$

rapid_delayed_rectifier_K_I

$$i_{Kr} = g_{Kr} \cdot O_K \cdot \left(V - \frac{R \cdot T}{F} \cdot \ln \frac{0.98 \cdot Ko + 0.02 \cdot Nao}{0.98 \cdot Ki + 0.02 \cdot Nai} \right)$$

$$C_{K0} = 1 - (C_{K1} + C_{K2} + O_K + I_K)$$

$$\frac{\mathrm{d}C_{K2}}{\mathrm{d}time} = kf \cdot C_{K1} + \beta_{a1} \cdot O_K - (kb \cdot C_{K2} + \alpha_{a1} \cdot C_{K2})$$

$$\frac{\mathrm{d}C_{K1}}{\mathrm{d}time} = \alpha_{a0} \cdot C_{K0} + kb \cdot C_{K2} - (\beta_{a0} \cdot C_{K1} + kf \cdot C_{K1})$$

$$\frac{\mathrm{d}O_K}{\mathrm{d}time} = \alpha_{a1} \cdot C_{K2} + \beta_i \cdot I_K - (\beta_{a1} \cdot O_K + \alpha_i \cdot O_K)$$

$$\frac{\mathrm{d}I_K}{\mathrm{d}time} = \alpha_i \cdot O_K - \beta_i \cdot I_K$$

$$\alpha_{a0} = 0.022,348 \cdot e^{0.011,76 \cdot V}$$

$$\beta_{a0} = 0.047,002 \cdot e^{-0.063,1 \cdot V}$$

$$\alpha_{a1} = 0.033,5 \cdot e^{0.010,9 \cdot V}$$

$$\beta_{a1} = 0.000,068,9 \cdot e^{-0.041,78 \cdot V}$$

$$\alpha_i = 0.070,3 \cdot e^{0.028,7 \cdot (V+5)}$$

$$\beta_i = 0.006,497 \cdot e^{-0.032,68 \cdot (V+5)}$$

ryanodine_receptors

$$\frac{\mathrm{d}P_{O1}}{\mathrm{d}time} = k_{plus_a} \cdot Cajc^n \cdot P_{C1} + k_{minus_b} \cdot P_{O2} + k_{minus_c} \cdot P_{C2} - \left(k_{minus_a} \cdot P_{O1} + k_{plus_b} \cdot Cajc^m \cdot P_{O1} + k_{plus_c} \cdot P_{O1}\right)$$

$$P_{C1} = 1 - (P_{C2} + P_{O1} + P_{O2})$$

$$\frac{\mathrm{d}P_{O2}}{\mathrm{d}time} = k_{plus_b} \cdot Cajc^m \cdot P_{O1} - k_{minus_b} \cdot P_{O2}$$

$$\frac{\mathrm{d}P_{C2}}{\mathrm{d}time} = k_{plus_c} \cdot P_{O1} - k_{minus_c} \cdot P_{C2}$$

slow_delayed_rectifier_K_I

$$i_{Ks} = g_{Ks} \cdot nKs^2 \cdot (V - E_K)$$

slow_delayed_rectifier_K_I (continued)

$$\frac{\mathrm{d}nKs}{\mathrm{d}time} = \alpha_n \cdot (1 - nKs) - \beta_n \cdot nKs$$
$$\alpha_n = \frac{0.000,004,813,33 \cdot (V + 26.5)}{1 - e^{-0.128 \cdot (V + 26.5)}}$$
$$\beta_n = 0.000,095,333,3 \cdot e^{-0.038 \cdot (V + 26.5)}$$

sodium_background_current

$$i_{Nab_{jc}} = g_{Nab} \cdot \left(V - E_{Na_{jc}}\right)$$
$$i_{Nab_{sl}} = g_{Nab} \cdot \left(V - E_{Na_{sl}}\right)$$
$$i_{Nab} = i_{Nab_{jc}} \cdot TT_{ratio} + i_{Nab_{sl}} \cdot (1 - TT_{ratio})$$

sodium_calcium_exchange_current

$$i_{NCX_{jc}} = \frac{1.93 \times V_{NCX}^{max}}{1 + (\frac{K_{mallo}}{[Ca^{2+}]_{jc}})^2} \cdot \frac{[Na^+]_{jc}^3 \cdot [Ca^{2+}]_o \cdot e^{\frac{\eta V_m F}{RT}} - [Na^+]_o^3 \cdot [Ca^{2+}]_{jc} \cdot e^{\frac{(\eta-1) V_m F}{RT}}}{\left\{ \begin{array}{l} [Na^+]_{jc}^3 \cdot (1400 + [Ca^{2+}]_o + \frac{K_{mCai} \cdot [Na^+]_o^3}{12000^3}) \\ + [Ca^{2+}]_{jc} \cdot \left[\frac{12000^3}{K_{mCai}} \cdot (1400 + [Ca^{2+}]_o) + [Na^+]_o^3\right] \\ + 12000^3 \cdot [Ca^{2+}]_o + K_{mCai} \cdot [Na^+]_o^3 \end{array} \right\} \cdot (1 + k_{sat} \cdot e^{\frac{(\eta-1) V_m F}{RT}})}$$

$$i_{NCX_{sl}} = \frac{0.6 \times V_{NCX}^{max}}{1 + (\frac{K_{mallo}}{[Ca^{2+}]_{sl}})^2} \cdot \frac{[Na^+]_{sl}^3 \cdot [Ca^{2+}]_o \cdot e^{\frac{\eta V_m F}{RT}} - [Na^+]_o^3 \cdot [Ca^{2+}]_{sl} \cdot e^{\frac{(\eta-1) V_m F}{RT}}}{\left\{ \begin{array}{l} [Na^+]_{sl}^3 \cdot (1400 + [Ca^{2+}]_o + \frac{K_{mCai} \cdot [Na^+]_o^3}{12000^3}) \\ + [Ca^{2+}]_{sl} \cdot \left[\frac{12000^3}{K_{mCai}} \cdot (1400 + [Ca^{2+}]_o) + [Na^+]_o^3\right] \\ + 12000^3 \cdot [Ca^{2+}]_o + K_{mCai} \cdot [Na^+]_o^3 \end{array} \right\} \cdot (1 + k_{sat} \cdot e^{\frac{(\eta-1) V_m F}{RT}})}$$

$$i_{NCX} = i_{NCX_{jc}} \cdot TT_{ratio} + i_{NCX_{sl}} \cdot (1 - TT_{ratio})$$
$$J_{NCX_{sl}} = \frac{i_{NCX_{sl}} \cdot Asl \cdot Cm}{Vsl \cdot F}$$
$$J_{NCX_{jc}} = \frac{i_{NCX_{jc}} \cdot Ajc \cdot Cm}{Vjc \cdot F}$$
$$J_{NCX_{total}} = \frac{J_{NCX_{sl}} \cdot Vsl}{Vmyo} + \frac{J_{NCX_{jc}} \cdot Vjc}{Vmyo}$$

sodium_concentration

$$dNa_{jct_{buf}} = kon \cdot Najc \cdot \left(Bmax_{jct} - Najc_{buf}\right) - koff \cdot Najc_{buf}$$
$$dNa_{SL_{buf}} = kon \cdot Nasl \cdot \left(Bmax_{SL} - Nasl_{buf}\right) - koff \cdot Nasl_{buf}$$
$$\frac{\mathrm{d}Najc_{buf}}{\mathrm{d}time} = dNa_{jct_{buf}}$$
$$\frac{\mathrm{d}Nasl_{buf}}{\mathrm{d}time} = dNa_{SL_{buf}}$$
$$\tau_{Na_{jcsl}} = \left(\frac{\tau_{Na_{jcsl_{const}}}}{Vsl}\right)^{-1}$$
$$\tau_{Na_{slcyt}} = \left(\frac{\tau_{Na_{slcyt_{const}}}}{Vmyo}\right)^{-1}$$

sodium_concentration (continued)

$$JNa_{slcyt} = \frac{Nasl - Nai}{\tau_{Na_{slcyt}}}$$

$$JNa_{jcsl} = \frac{Najc - Nasl}{\tau_{Na_{jcsl}}}$$

$$\frac{\mathrm{d}Nai}{\mathrm{d}time} = JNa_{slcyt} + Jnhe + Jnbc$$

$$\frac{\mathrm{d}Nasl}{\mathrm{d}time} = \frac{-\left(i_{Na_{sl}} + i_{Nab_{sl}} + 3 \cdot i_{NKA_{sl}} + 3 \cdot i_{NCX_{sl}}\right) \cdot Asl \cdot Cm}{Vsl \cdot F} - \frac{JNa_{slcyt} \cdot Vmyo}{Vsl} + JNa_{jcsl} - dNa_{SL_{buf}}$$

$$\frac{\mathrm{d}Najc}{\mathrm{d}time} = \frac{-\left(i_{Na_{jc}} + i_{Nab_{jc}} + 3 \cdot i_{NKA_{jc}} + 3 \cdot i_{NCX_{jc}}\right) \cdot Ajc \cdot Cm}{Vjc \cdot F} - \frac{JNa_{jcsl} \cdot Vsl}{Vjc} - dNa_{jct_{buf}}$$

sodium_potassium_pump_current

$$i_{NKA_{alpha1_{jc}}} = \frac{\frac{1.236 \cdot i_{NKA_{max_{alpha1}}} \cdot f_{NKA_{alpha1}} \cdot 1}{1 + \left(\frac{Km_{Na_{alpha1}}}{Najc}\right)^{nH_{NKAalpha1}}} \cdot Ko}{Ko + Km_{Ko}}$$

$$i_{NKA_{alpha1_{sl}}} = \frac{\frac{0.899 \cdot i_{NKA_{max_{alpha1}}} \cdot f_{NKA_{alpha1}} \cdot 1}{1 + \left(\frac{Km_{Na_{alpha1}}}{Nasl}\right)^{nH_{NKAalpha1}}} \cdot Ko}{Ko + Km_{Ko}}$$

$$i_{NKA_{alpha2_{jc}}} = \frac{\frac{2.35 \cdot i_{NKA_{max_{alpha2}}} \cdot f_{NKA_{alpha2}} \cdot 1}{1 + \left(\frac{Km_{Na_{alpha2}}}{Najc}\right)^{nH_{NKAalpha2}}} \cdot Ko}{Ko + Km_{Ko}}$$

$$i_{NKA_{alpha2_{sl}}} = \frac{\frac{0.422 \cdot i_{NKA_{max_{alpha2}}} \cdot f_{NKA_{alpha2}} \cdot 1}{1 + \left(\frac{Km_{Na_{alpha2}}}{Nasl}\right)^{nH_{NKAalpha2}}} \cdot Ko}{Ko + Km_{Ko}}$$

$$i_{NKA_{jc}} = i_{NKA_{alpha1_{jc}}} + i_{NKA_{alpha2_{jc}}}$$

$$i_{NKA_{sl}} = i_{NKA_{alpha1_{sl}}} + i_{NKA_{alpha2_{sl}}}$$

$$i_{NKA_{alpha1}} = i_{NKA_{alpha1_{jc}}} \cdot TT_{ratio} + i_{NKA_{alpha1_{sl}}} \cdot (1 - TT_{ratio})$$

$$i_{NKA_{alpha2}} = i_{NKA_{alpha2_{jc}}} \cdot TT_{ratio} + i_{NKA_{alpha2_{sl}}} \cdot (1 - TT_{ratio})$$

$$i_{NKA} = i_{NKA_{jc}} \cdot TT_{ratio} + i_{NKA_{sl}} \cdot (1 - TT_{ratio})$$

$$f_{NKA_{alpha1}} = \frac{1}{1 + 0.294,6 \cdot e^{\frac{-0.1 \cdot V \cdot F}{R \cdot T}} + 0.016,4 \cdot sigma \cdot e^{\frac{-V \cdot F}{R \cdot T}}}$$

$$f_{NKA_{alpha2}} = \frac{1}{1 + 0.124,5 \cdot e^{\frac{-0.1 \cdot V \cdot F}{R \cdot T}} + 0.089 \cdot sigma \cdot e^{\frac{-V \cdot F}{R \cdot T}}}$$

$$sigma = \frac{1}{7} \cdot \left(e^{\frac{Nao}{67,300}} - 1\right)$$

$$J_{Na_{NKA}} = \frac{i_{NKA} \cdot 3 \cdot Atot \cdot Cm}{F \cdot Vmyo}$$

time_independent_K_I

$$i_{K1} = \frac{\frac{g_{K1} \cdot Ko}{Ko + 210} \cdot (V - E_K)}{1 + e^{0.089,6 \cdot (V - E_K)}}$$

ultra_rapidly_activating_delayed_rectifier_K_I

$$ass = \frac{1}{1 + e^{\frac{-(V+15)}{20}}}$$

$$iss = \frac{1}{1 + e^{\frac{V+42.1}{5.4}}}$$

$$i_{Kur} = g_{Kur} \cdot aur \cdot iur \cdot (V - E_K)$$

$$\frac{\mathrm{d}aur}{\mathrm{d}time} = \frac{ass - aur}{\tau_{aur}}$$

ultra_rapidly_activating_delayed_rectifier_K_I (continued)

$$\frac{\mathrm{d}iur}{\mathrm{d}time} = \frac{iss - iur}{\tau_{iur}}$$

$$\tau_{aur} = 0.493 \cdot e^{-0.062,9 \cdot V} + \tau_{a_{const}}$$

$$\tau_{iur} = \tau_{i_{const}} + \frac{1,000}{1 + e^{\frac{V+42.1}{5.4}}}$$

Appendix F

Parameter Values for SERCA2 FF and KO Models in the 7-week Study

Parameter Values for the FF Model

	Value	Unit
K_L	0.8	micromolar
LCC_{C1}	33	millivolt
LCC_{C2}	8.23	millivolt
LCC_{C3}	0.1	dimensionless
LCC_{C4}	40	millivolt
LCC_{C5}	6	millivolt
LCC_{C6}	5	millisecond
LCC_{C7}	315	millisecond
LCC_{C8}	30	millivolt
LCC_{C9}	4.5	millivolt
P_{CaL}	$1.55 \cdot 10^{-7}$	microlitre_per_millisecond
V_L	-5	millivolt
a	0.3	dimensionless
b	0.4	dimensionless
δ_{V_L}	8	millivolt
$i_{CaL_{max}}$	7	picoA_per_picoF
ϕ_L	2.5	dimensionless
t_L	8	millisecond
τ_L	400	millisecond
$anion_o$	0	micromolar
p_{anion}	$1 \cdot 10^{-7}$	cm_per_second
E_{Cl}	-40	millivolt

Parameter Values for the FF Model (continued)

	Value	Unit
Km_{Cl}	10	micromolar
g_{ClCa}	10	milliS_per_microF
g_{Cab}	$0.000,4$	milliS_per_microF
$Bmax$	109	micromolar
$CSQN_{tot}$	$50,000$	micromolar
Kd_{buffer}	0.6	micromolar
Km_{CSQN}	630	micromolar
A_{PRyR}	-0.2	per_millisecond
B_{PRyR}	-3	per_millisecond
Km_{up}	$0.492,8$	micromolar
V_{leak}	$2 \cdot 10^{-5}$	per_millisecond
V_{rel}	4.5	per_millisecond
Vup	0.35	micromolar_per_millisecond
nH	2	dimensionless
$\tau_{Ca_{jcsl_{const}}}$	$4.188 \cdot 10^{-7}$	microlitre_per_millisecond
$\tau_{ca_{slcyt_{const}}}$	$2.79 \cdot 10^{-6}$	microlitre_per_millisecond
τ_{tr}	20	millisecond
Km_{PMCA}	$0.350,6$	micromolar
$i_{PMCA_{max}}$	$0.564,4$	picoA_per_picoF
$Atot$	$0.000,147$	cm2
Cao	$1,000$	micromolar
Clo	$148,400$	micromolar
Cm	1	microF_per_cm2
F	96.5	coulomb_per_millimole
Ko	$5,400$	micromolar
Nao	$140,000$	micromolar
R	8.314	joule_per_mole_kelvin
T	310	kelvin
TT_{ratio}	0.3	dimensionless
$VJSR$	$7.7 \cdot 10^{-8}$	microlitre
$VNSR$	$2.31 \cdot 10^{-7}$	microlitre
Vjc	$2.2 \cdot 10^{-8}$	microlitre
$Vmyo$	$2.2 \cdot 10^{-5}$	microlitre
Vsl	$4.4 \cdot 10^{-7}$	microlitre
$stim_{amplitude}$	-15	picoA_per_picoF
$stim_{duration}$	3	millisecond
$stim_{offset}$	0	millisecond
$stim_{period}$	$1,000$	millisecond
p_{cl}	$1.3 \cdot 10^{-8}$	cm_per_second
g_{Na}	16	milliS_per_microF

Parameter Values for the FF Model (continued)

	Value	Unit
$\alpha_{a_{const}}$	45	millivolt
$\alpha_{b_{const}}$	45	millivolt
g_{Kto_f}	0.4	milliS_per_microF
g_{Kss}	0.059, 6	milliS_per_microF
$B1$	84, 200	micromolar
$B2$	29, 400	micromolar
$J_{acid_{flux_{in}}}$	0	micromolar_per_millisecond
$K_{Cl_{che}}$	18, 000, 000	micromolar
$K_{H_{nhe}}$	0.000, 177, 8	micromolar
$K_{Na_{nhe}}$	21, 490	micromolar
$K_{i_{nhe}}$	0.411, 1	micromolar
$\alpha_{f_{1_{nhe}}}$	0.001, 97	per_millisecond
$\alpha_{r_{2_{nhe}}}$	0.000, 818	per_millisecond
$k_{f_{1_{che}}}$	0.004, 29	per_millisecond
$k_{f_{2_{che}}}$	0.068, 1	per_millisecond
$k_{f_{2_{nhe}}}$	0.014, 15	per_millisecond
$k_{r_{1_{che}}}$	0.25	per_millisecond
$k_{r_{1_{nhe}}}$	1.172, 4	per_millisecond
nH_{nhe}	2.905, 3	dimensionless
pHo	7.4	dimensionless
$pK1$	6.03	dimensionless
$pK2$	7.57	dimensionless
$pK_{H_{che}}$	7.95	dimensionless
g_{Kr}	0.016, 5	milliS_per_microF
kb	0.036, 778	per_millisecond
kf	0.023, 761	per_millisecond
k_{minus_a}	0.071, 25	per_millisecond
k_{minus_b}	0.965	per_millisecond
k_{minus_c}	0.000, 8	per_millisecond
k_{plus_a}	$6.075 \cdot 10^{-6}$	micromolar4_per_millisecond
k_{plus_b}	$4.05 \cdot 10^{-6}$	micromolar3_per_millisecond
k_{plus_c}	0.009	per_millisecond
m	3	dimensionless
n	4	dimensionless
g_{Ks}	0.005, 75	milliS_per_microF
g_{Nab}	0.002, 6	milliS_per_microF
$I_{NCX_{max}}$	1.159, 1	picoA_per_picoF
K_{mAllo}	0	micromolar
K_{mCai}	3.6	micromolar
K_{mCao}	1, 400	micromolar

Parameter Values for the FF Model (continued)

	Value	Unit
K_{mNai}	$12,000$	micromolar
K_{mNao}	$88,000$	micromolar
eta	0.35	dimensionless
k_{sat}	0.27	dimensionless
$Bmax_{SL}$	$1,650$	micromolar
$Bmax_{jct}$	$3,700$	micromolar
$koff$	0.001	per_millisecond
kon	$1 \cdot 10^{-7}$	per_micromolar_per_millisecond
$\tau_{Na_{jcsl_{const}}}$	$2.78 \cdot 10^{-6}$	microlitre_per_millisecond
$\tau_{Na_{slcyt_{const}}}$	$4.09 \cdot 10^{-5}$	microlitre_per_millisecond
Km_{Ko}	$1,500$	micromolar
$Km_{Na_{alpha1}}$	$21,000$	micromolar
$Km_{Na_{alpha2}}$	$21,000$	micromolar
$i_{NKA_{max_{alpha1}}}$	5.2	picoA_per_picoF
$i_{NKA_{max_{alpha2}}}$	1.95	picoA_per_picoF
$nH_{NKAalpha1}$	3	dimensionless
$nH_{NKAalpha2}$	3	dimensionless
g_{K1}	0.35	milliS_per_microF
g_{Kur}	0.45	milliS_per_microF
$\tau_{a_{const}}$	2.058	millisecond
$\tau_{i_{const}}$	643	millisecond

Parameter Values for the 4-week KO Model

	Value	Unit
K_L	0.7	micromolar
LCC_{C1}	33	millivolt
LCC_{C2}	8.23	millivolt
LCC_{C3}	0.1	dimensionless
LCC_{C4}	40	millivolt
LCC_{C5}	6	millivolt
LCC_{C6}	5	millisecond
LCC_{C7}	315	millisecond
LCC_{C8}	24	millivolt
LCC_{C9}	4.5	millivolt
P_{CaL}	$1.6 \cdot 10^{-7}$	microlitre_per_millisecond
V_L	-5	millivolt
a	0.3	dimensionless
b	0.4	dimensionless
δ_{V_L}	8	millivolt
$i_{CaL_{max}}$	20	picoA_per_picoF
ϕ_L	2.5	dimensionless
t_L	6	millisecond
τ_L	450	millisecond
$anion_o$	0	micromolar
p_{anion}	$1 \cdot 10^{-7}$	cm_per_second
E_{Cl}	-40	millivolt
Km_{Cl}	10	micromolar
g_{ClCa}	10	milliS_per_microF
g_{Cab}	$0.000,4$	milliS_per_microF
$Bmax$	109	micromolar
$CSQN_{tot}$	$50,000$	micromolar
Kd_{buffer}	0.6	micromolar
Km_{CSQN}	630	micromolar
A_{PRyR}	-0.2	per_millisecond
B_{PRyR}	-3	per_millisecond
Km_{up}	$0.492,8$	micromolar
V_{leak}	$3 \cdot 10^{-5}$	per_millisecond
V_{rel}	4.5	per_millisecond
Vup	$0.147,9$	micromolar_per_millisecond
nH	2	dimensionless
$\tau_{Ca_{jcsl_{const}}}$	$4.188 \cdot 10^{-7}$	microlitre_per_millisecond
$\tau_{ca_{slcyt_{const}}}$	$2.79 \cdot 10^{-6}$	microlitre_per_millisecond
τ_{tr}	20	millisecond

Constants (continued)

	Value	Unit
Km_{PMCA}	$0.350,6$	micromolar
$i_{PMCA_{max}}$	$0.621,4$	picoA_per_picoF
$Atot$	$0.000,147$	cm2
Cao	$1,000$	micromolar
Clo	$148,400$	micromolar
Cm	1	microF_per_cm2
F	96.5	coulomb_per_millimole
Ko	$5,400$	micromolar
Nao	$140,000$	micromolar
R	8.314	joule_per_mole_kelvin
T	310	kelvin
TT_{ratio}	0.3	dimensionless
$VJSR$	$7.7 \cdot 10^{-8}$	microlitre
$VNSR$	$2.31 \cdot 10^{-7}$	microlitre
Vjc	$2.2 \cdot 10^{-8}$	microlitre
$Vmyo$	$2.2 \cdot 10^{-5}$	microlitre
Vsl	$4.4 \cdot 10^{-7}$	microlitre
$stim_{amplitude}$	-15	picoA_per_picoF
$stim_{duration}$	3	millisecond
$stim_{offset}$	0	millisecond
$stim_{period}$	$1,000$	millisecond
p_{cl}	$1.3 \cdot 10^{-8}$	cm_per_second
g_{Na}	16	milliS_per_microF
$\alpha_{a_{const}}$	45	millivolt
$\alpha_{b_{const}}$	45	millivolt
g_{Kto_f}	0.4	milliS_per_microF
g_{Kss}	$0.059,6$	milliS_per_microF
$B1$	$84,200$	micromolar
$B2$	$29,400$	micromolar
$J_{acid_{flux_{in}}}$	0	micromolar_per_millisecond
$K_{Cl_{che}}$	$18,000,000$	micromolar
$K_{H_{nhe}}$	$0.000,177,8$	micromolar
$K_{Na_{nhe}}$	$21,490$	micromolar
$K_{i_{nhe}}$	$0.411,1$	micromolar
$\alpha_{f_{1_{nhe}}}$	$0.001,97$	per_millisecond
$\alpha_{r_{2_{nhe}}}$	$0.000,818$	per_millisecond
$k_{f_{1_{che}}}$	$0.004,29$	per_millisecond
$k_{f_{2_{che}}}$	$0.068,1$	per_millisecond
$k_{f_{2_{nhe}}}$	$0.014,15$	per_millisecond
$k_{r_{1_{che}}}$	0.25	per_millisecond

Constants (continued)

	Value	Unit
$k_{r_{1_{nhe}}}$	$1.172,4$	per_millisecond
nH_{nhe}	$2.905,3$	dimensionless
pHo	7.4	dimensionless
$pK1$	6.03	dimensionless
$pK2$	7.57	dimensionless
$pK_{H_{che}}$	7.95	dimensionless
g_{Kr}	$0.016,5$	milliS_per_microF
kb	$0.036,778$	per_millisecond
kf	$0.023,761$	per_millisecond
k_{minus_a}	$0.071,25$	per_millisecond
k_{minus_b}	0.965	per_millisecond
k_{minus_c}	$0.000,8$	per_millisecond
k_{plus_a}	$6.075 \cdot 10^{-6}$	micromolar4_per_millisecond
k_{plus_b}	$4.05 \cdot 10^{-6}$	micromolar3_per_millisecond
k_{plus_c}	0.009	per_millisecond
m	3	dimensionless
n	4	dimensionless
g_{Ks}	$0.005,75$	milliS_per_microF
g_{Nab}	$0.002,6$	milliS_per_microF
$I_{NCX_{max}}$	$1.656,3$	picoA_per_picoF
K_{mAllo}	0	micromolar
K_{mCai}	3.6	micromolar
K_{mCao}	$1,400$	micromolar
K_{mNai}	$12,000$	micromolar
K_{mNao}	$88,000$	micromolar
eta	0.35	dimensionless
k_{sat}	0.27	dimensionless
$Bmax_{SL}$	$1,650$	micromolar
$Bmax_{jct}$	$3,700$	micromolar
$koff$	0.001	per_millisecond
kon	$1 \cdot 10^{-7}$	per_micromolar_per_millisecond
$\tau_{Na_{jcsl_{const}}}$	$2.78 \cdot 10^{-6}$	microlitre_per_millisecond
$\tau_{Na_{slcyt_{const}}}$	$4.09 \cdot 10^{-5}$	microlitre_per_millisecond
Km_{Ko}	$1,500$	micromolar
$Km_{Na_{alpha1}}$	$21,000$	micromolar
$Km_{Na_{alpha2}}$	$21,000$	micromolar
$i_{NKA_{max_{alpha1}}}$	5.2	picoA_per_picoF
$i_{NKA_{max_{alpha2}}}$	1.95	picoA_per_picoF
$nH_{NKAalpha1}$	3	dimensionless
$nH_{NKAalpha2}$	3	dimensionless

Constants (continued)

	Value	Unit
g_{K1}	0.35	milliS_per_microF
g_{Kur}	0.45	milliS_per_microF
$\tau_{a_{const}}$	2.058	millisecond
$\tau_{i_{const}}$	643	millisecond

Parameter Values for the 7-week KO Model

	Value	Unit
K_L	0.5	micromolar
LCC_{C1}	33	millivolt
LCC_{C2}	8.2	millivolt
LCC_{C3}	0.1	dimensionless
LCC_{C4}	40	millivolt
LCC_{C5}	6	millivolt
LCC_{C6}	10	millisecond
LCC_{C7}	315	millisecond
LCC_{C8}	26	millivolt
LCC_{C9}	4.5	millivolt
P_{CaL}	$1.75 \cdot 10^{-7}$	microlitre_per_millisecond
V_L	-5	millivolt
a	0.3	dimensionless
b	0.4	dimensionless
δ_{V_L}	8	millivolt
$i_{CaL_{max}}$	20	picoA_per_picoF
ϕ_L	2.5	dimensionless
t_L	10	millisecond
τ_L	400	millisecond
$anion_o$	0	micromolar
p_{anion}	$1 \cdot 10^{-7}$	cm_per_second
E_{Cl}	-40	millivolt
Km_{Cl}	10	micromolar
g_{ClCa}	10	milliS_per_microF
g_{Cab}	$0.000,4$	milliS_per_microF
$Bmax$	109	micromolar
$CSQN_{tot}$	$50,000$	micromolar
Kd_{buffer}	0.6	micromolar
Km_{CSQN}	630	micromolar
A_{PRyR}	-0.2	per_millisecond
B_{PRyR}	-3	per_millisecond
Km_{up}	$0.492,8$	micromolar
V_{leak}	$2 \cdot 10^{-5}$	per_millisecond
V_{rel}	4.5	per_millisecond
Vup	0.07	micromolar_per_millisecond
nH	2	dimensionless
$\tau_{Ca_{jcsl_{const}}}$	$4.188 \cdot 10^{-7}$	microlitre_per_millisecond
$\tau_{ca_{slcyt_{const}}}$	$2.79 \cdot 10^{-6}$	microlitre_per_millisecond
τ_{tr}	20	millisecond

Parameter Values for the 7-week KO Model (continued)

	Value	Unit
Km_{PMCA}	$0.350,6$	micromolar
$i_{PMCA_{max}}$	$1.123,1$	picoA_per_picoF
$Atot$	$0.000,147$	cm2
Cao	$1,000$	micromolar
Clo	$148,400$	micromolar
Cm	1	microF_per_cm2
F	96.5	coulomb_per_millimole
Ko	$5,400$	micromolar
Nao	$140,000$	micromolar
R	8.314	joule_per_mole_kelvin
T	310	kelvin
TT_{ratio}	0.3	dimensionless
$VJSR$	$7.7 \cdot 10^{-8}$	microlitre
$VNSR$	$2.31 \cdot 10^{-7}$	microlitre
Vjc	$2.2 \cdot 10^{-8}$	microlitre
$Vmyo$	$2.2 \cdot 10^{-5}$	microlitre
Vsl	$4.4 \cdot 10^{-7}$	microlitre
$prepulses_{number}$	$1,000,000$	dimensionless
$stim_{amplitude}$	-15	picoA_per_picoF
$stim_{duration}$	3	millisecond
$stim_{offset}$	0	millisecond
$stim_{period}$	$1,000$	millisecond
p_{cl}	$1.3 \cdot 10^{-8}$	cm_per_second
g_{Na}	16	milliS_per_microF
$\alpha_{a_{const}}$	45	millivolt
$\alpha_{b_{const}}$	45	millivolt
g_{Kto_f}	0.4	milliS_per_microF
g_{Kss}	$0.059,6$	milliS_per_microF
$B1$	$84,200$	micromolar
$B2$	$29,400$	micromolar
$J_{acid_{flux_{in}}}$	0.045	micromolar_per_millisecond
$K_{Cl_{che}}$	$18,000,000$	micromolar
$K_{H_{nhe}}$	$0.000,177,8$	micromolar
$K_{Na_{nhe}}$	$21,490$	micromolar
$K_{i_{nhe}}$	$0.411,1$	micromolar
$\alpha_{f_{1_{nhe}}}$	$0.001,97$	per_millisecond
$\alpha_{r_{2_{nhe}}}$	$0.000,818$	per_millisecond
$k_{f_{1_{che}}}$	$0.004,29$	per_millisecond
$k_{f_{2_{che}}}$	$0.068,1$	per_millisecond
$k_{f_{2_{nhe}}}$	$0.014,15$	per_millisecond

Parameter Values for the 7-week KO Model (continued)

	Value	Unit
$k_{r1_{che}}$	0.25	per_millisecond
$k_{r1_{nhe}}$	1.172, 4	per_millisecond
nH_{nhe}	2.905, 3	dimensionless
pHo	7.4	dimensionless
$pK1$	6.03	dimensionless
$pK2$	7.57	dimensionless
$pK_{H_{che}}$	7.95	dimensionless
g_{Kr}	0.016, 5	milliS_per_microF
kb	0.036, 778	per_millisecond
kf	0.023, 761	per_millisecond
k_{minus_a}	0.071, 25	per_millisecond
k_{minus_b}	0.965	per_millisecond
k_{minus_c}	0.000, 8	per_millisecond
k_{plus_a}	$6.075 \cdot 10^{-6}$	micromolar4_per_millisecond
k_{plus_b}	$4.05 \cdot 10^{-6}$	micromolar3_per_millisecond
k_{plus_c}	0.009	per_millisecond
m	3	dimensionless
n	4	dimensionless
g_{Ks}	0.005, 75	milliS_per_microF
g_{Nab}	0.002, 6	milliS_per_microF
$I_{NCX_{max}}$	6.411, 6	picoA_per_picoF
K_{mAllo}	0	micromolar
K_{mCai}	3.6	micromolar
K_{mCao}	1, 400	micromolar
K_{mNai}	12, 000	micromolar
K_{mNao}	88, 000	micromolar
eta	0.35	dimensionless
k_{sat}	0.27	dimensionless
$Bmax_{SL}$	1, 650	micromolar
$Bmax_{jct}$	3, 700	micromolar
$koff$	0.001	per_millisecond
kon	$1 \cdot 10^{-7}$	per_micromolar_per_millisecond
$\tau_{Na_{jcsl_{const}}}$	$2.78 \cdot 10^{-6}$	microlitre_per_millisecond
$\tau_{Na_{slcyt_{const}}}$	$4.09 \cdot 10^{-5}$	microlitre_per_millisecond
Km_{Ko}	1, 500	micromolar
$Km_{Na_{alpha1}}$	21, 000	micromolar
$Km_{Na_{alpha2}}$	21, 000	micromolar
$i_{NKA_{max_{alpha1}}}$	4.4	picoA_per_picoF
$i_{NKA_{max_{alpha2}}}$	0.9	picoA_per_picoF
$nH_{NKAalpha1}$	3	dimensionless

Parameter Values for the 7-week KO Model (continued)

	Value	Unit
$nH_{NKAalpha2}$	3	dimensionless
g_{K1}	0.35	milliS_per_microF
g_{Kur}	0.45	milliS_per_microF
$\tau_{a_{const}}$	2.058	millisecond
$\tau_{i_{const}}$	643	millisecond

References

[1] S. Adachi-Akahane, L. Lu, Z. Li, J. S. Frank, K. D. Philipson, and M. Morad. Calcium signaling in transgenic mice overexpressing cardiac Na^{+}-Ca^{2+} exchanger. *The Journal of General Physiology*, 109:717–729, 1997.

[2] G. Agnetti, N. Kaludercic, L. A. Kane, S. T. Elliott, Y. Guo, K. Chakir, D. Samantapudi, N. Paolocci, G. F. Tomaselli, D. A. Kass, and J. E. Van Eyk. Modulation of mitochondrial proteome and improved mitochondrial function by biventricular pacing of dyssynchronous failing hearts. *Circulation. Cardiovascular Genetics*, 3(1):78–87, 2010.

[3] D. G. Allen, P. G. Morris, C. H. Orchard, and J. S. Pirolo. A nuclear magnetic resonance study of metabolism in the ferret heart during hypoxia and inhibition of glycolysis. *The Journal of Physiology*, 361(1):185–204, 1985.

[4] K. B. Andersson, J. A. K. Birkeland, A. V. Finsen, W. E. Louch, I. Sjaastad, Y. Wang, J. Chen, J. D. Molkentin, K. R. Chien, O. M. Sejersted, and G. Christensen. Moderate heart dysfunction in mice with inducible cardiomyocyte-specific excision of the serca2 gene. *Journal of Molecular and Cellular Cardiology*, 47(2):180 – 187, 2009.

[5] K. B. Andersson, A. V. Finsen, C. Sjaland, L. H. Winer, I. Sjåastad, A. Ødegaard, W. E. Louch, Y. Wang, J. Chen, K. R. Chien, O. M. Sejersted, and G. Christensen.

Mice carrying a conditional Serca2^{flox} allele for the generation of Ca^{2+} handling-deficient mouse models. *Cell Calcium*, 46(3):219–225, 2009.

[6] K. B. Andersson, L. H. Winer, H. K. Mørk, J. D. Molkentin, and F. Jaisser. Tamoxifen administration routes and dosage for inducible cre-mediated gene disruption in mouse hearts. *Transgenic Research*, 2009.

[7] G. Antoons, K. Mubagwa, I. Nevelsteen, and K. R. Sipido. Mechanisms underlying the frequency dependence of contraction and $[Ca^{2+}]_i$ transients in mouse ventricular myocytes. *The Journal of Physiology*, 543:889–898, 2002.

[8] C. Armstrong and F. Bezanilla. Inactivation of the sodium channel. II. Gating current experiments. *Journal of General Physiology*, 70:567 – 590, 1977.

[9] L. C. Baker, B. London, B.-R. Choi, G. Koren, and G. Salama. Enhanced dispersion of repolarization and refractoriness in transgenic mouse hearts promotes reentrant ventricular tachycardia. *Circulation Research*, 86:396–407, 2000.

[10] J. Barhanin, F. Lesage, E. Guillemare, M. Fink, M. Lazdunski, and G. Romey. K_vLQT1 and IsK (minK) proteins associate to form the I_{KS} cardiac potassium current. *Nature*, 384:78–80, 1996.

[11] R. A. Bassani, J. W. Bassani, and D. M. Bers. Mitochondrial and sarcolemmal Ca^{2+} transport reduce $[Ca^{2+}]_i$ during caffeine contractures in rabbit cardiac myocytes. *The Journal of Physiology*, 453(1):591–608, 1992.

[12] R. A. Bassani, J. W. M. Bassani, and D. M. Bers. Relaxation in ferret ventricular myocytes: role of the sarcolemmal Ca ATPase. *Pflügers Archiv European Journal of Physiology*, 430(4):573 – 578, 1995.

[13] R. A. Bassani and D. M. Bers. Na-Ca Exchange is required for rest-decay but not for rest-potential of twitches in rabbit and rat ventricular myocytes. *Journal of Molecular and Cellular Cardiology*, 26(10):1335 – 1347, 1994.

[14] R. A. Bassani, A. Mattiazzi, and D. M. Bers. CaMKII is responsible for activity-dependent acceleration of relaxation in rat ventricular myocytes. *American Journal of Physiology. Heart and Circulatory Physiology*, 268(2):H703–712, 1995.

[15] F. Bazanilla and C. Armstrong. Inactivation of the sodium channel. I. Sodium current experiments. *Journal of General Physiology*, 70:549 – 566, 1977.

[16] G. W. Beeler and H. Reuter. Reconstruction of the action potential of ventricular myocardial fibres. *The Journal of Physiology*, 268(1):177–210, 1977.

[17] J. R. Berlin, J. W. Bassani, and D. M. Bers. Intrinsic cytosolic calcium buffering properties of single rat cardiac myocytes. *Biophysical Journal*, 67(4):1775 – 1787, 1994.

[18] R. G. Berry, S. Despa, W. Fuller, D. M. Bers, and M. J. Shattock. Differential distribution and regulation of mouse cardiac Na^+/K^+-ATPase alpha1 and alpha2 subunits in T-tubule and surface sarcolemmal membranes. *Cardiovascular Research*, 73:92–100, 2007.

[19] D. M. Bers. *Excitation-contraction coupling and cardiac contractile force*. Kluwer Academic Publishers, 2 edition, 2001.

[20] D. M. Bers. Calcium cycling and signaling in cardiac myocytes. *Annual Review of Physiology*, 70(1):23–49, 2008.

[21] D. M. Bers, W. H. Barry, and S. Despa. Intracellular Na^+ regulation in cardiac myocytes. *Cardiovascular Research*, 57(4):897–912, 2003.

[22] D. M. Bers and J. R. Berlin. Kinetics of $[Ca]_i$ decline in cardiac myocytes depend on peak $[Ca]_i$. *American Journal of Physiology. Cell Physiology*, 268(1):C271–277, 1995.

[23] D. J. Beuckelmann, M. Nabauer, and E. Erdmann. Intracellular calcium handling in isolated ventricular myocytes from patients with terminal heart failure. *Circulation*, 85(3):1046–1055, 1992.

[24] D. J. Beuckelmann, M. Nabauer, C. Kruger, and E. Erdmann. Altered diastolic $[Ca^{2+}]_i$ handling in human ventricular myocytes from patients with terminal heart failure. *American Heart Journal*, 129(4):684–689, 1995.

[25] S. C. Beuve, P. D. Allen, G. Dambrin, F. Rannou, I. Marty, P. Trouvé, V. Bors, A. Pavie, I. Gandgjbakch, and D. Charlemagne. Cardiac calcium release channel (ryanodine receptor) in control and cardiomyopathic human hearts: mRNA and protein contents are differentially regulated. *Journal of Molecular and Cellular Cardiology*, 29(4):1237 – 1246, 1997.

[26] M. P. Blaustein and W. J. Lederer. Sodium/calcium exchange: its physiological implications. *Physiology Reviews*, 79(3):763–854, 1999.

[27] V. E. Bondarenko, G. P. Szigeti, G. C. L. Bett, S.-J. Kim, and R. L. Rasmusson. Computer model of action potential of mouse ventricular myocytes. *American Journal of Physiology. Heart and circulatory physiology*, 287(3):H1378–1403, 2004.

[28] E. H. Bossen, J. Sommer, and R. A. Waugh. Comparative stereology of mouse atria. *Tissue Cell*, 13, 1981.

[29] C. J. Brandl, N. M. Green, B. Korczak, and D. H. MacLennan. Two Ca^{2+} ATPase genes: homologies and mechanistic implications of deduced amino acid sequences. *Cell*, 44(4):597 – 607, 1986.

[30] A. P. Braun and H. Schulman. The multifunctional calcium/calmodulin-dependent protein kinase: from form to function. *Annuals Reviews in Physiology*, 57:417 – 335, 1995.

[31] F. Brette and C. H. Orchard. Density and sub-cellular distribution of cardiac and neuronal sodium channel isoforms in rat ventricular myocytes. *Biochemical and Biophysical Research Communications*, 348(3):1163 – 1166, 2006.

[32] A. M. Brillantes, P. Allen, T. Takahashi, S. Izumo, and A. R. Marks. Differences in cardiac calcium release channel (ryanodine receptor) expression in myocardium from patients with end-stage heart failure caused by ischemic versus dilated cardiomyopathy. *Circulation Research*, 71(1):18–26, 1992.

[33] J. Brouillette, R. B. Clark, W. R. Giles, and C. l. Fiset. Functional properties of K^+ currents in adult mouse ventricular myocytes. *The Journal of Physiology*, 559:777–798, 2004.

[34] J. Brouillette, K. Rivard, E. Lizotte, and C. Fiset. Sex and strain differences in adult mouse cardiac repolarization: importance of androgens. *Cardiovascular Research*, 65:148–157, 2005.

[35] M. Cannell. Numerical analysis of ryanodine receptor activation by L-type channel activity in the cardiac muscle diad. *Biophysical Journal*, 73:112–122, jul 1997.

[36] H. Cheng, W. J. Lederer, and M. B. Cannell. Calcium sparks: elementary events underlying excitation-contraction coupling in heart muscle. *Science*, 262(5134):740–744, 1993.

[37] T. C. Chiello, C. Cabo, J. Coromilas, J. Kurokawa, R. S. Kass, and A. L. Wit. Electrophysiological consequences of human I_{Ks} channel expression in adult murine heart. *American journal of physiology. Heart and circulatory physiology*, 284(1):H168–H175, 2003.

[38] C. E. Clancy and Y. Rudy. Linking a genetic defect to its cellular phenotype in a cardiac arrhythmia. *Nature*, 400:566–569, 1999.

[39] C. E. Clancy and Y. Rudy. Cellular consequences of HERG mutations in the long QT syndrome: precursors to sudden cardiac death. *Cardiovascular Research*, 50(2):301–313, 2001.

[40] D. M. Clarke, T. W. Loo, G. Inesi, and D. H. MacLennan. Location of high affinity Ca^{2+}-binding sites within the predicted transmembrahe domain of the sarcoplasmic reticulum Ca^{2+}-ATPase. *Nature*, 339:476–478, 1989.

[41] R. Clayton and A. Panfilov. A guide to modelling cardiac electrical activity in anatomicaly detailed ventricles. *Progress in Biophsics and Molecular Biology*, 96:19 – 43, 2008.

[42] E. J. Crampin and N. P. Smith. A dynamic model of excitation-contraction coupling during acidosis in cardiac ventricular myocytes. *Biophysical Journal*, 90(9):3074–3090, 2006.

[43] F. del Monte and R. J. Hajjar. Targeting calcium cycling proteins in heart failure through gene transfer. *The Journal of Physiology*, 546(1):49–61, 2003.

[44] S. Demolombe, G. Lande, F. Charpentier, M. A. van Roon, M. J. B. van den Hoff, G. Toumaniantz, I. Baro, G. Guihard, N. Le Berre, A. Corbier, J. de Bakker, T. Opthof, A. Wilde, A. F. M. Moorman, and D. Escande. Transgenic mice overexpressing human KvLQT1 dominant-negative isoform Part I: Phenotypic characterisation. *Cardiovascular Research*, 50:314–327, 2001.

[45] J. DeSantiago, L. S. Maier, and D. M. Bers. Frequency-dependent acceleration of relaxation in the heart depends on CaMKII, but not phospholamban. *Journal of Molecular and Cellular Cardiology*, 34(8):975 – 984, 2002.

[46] S. Despa, F. Brette, O. C.H., and D. M. Bers. Na/Ca exchange and Na/K-ATPase function are equally concentrated in transverse tubules of rat ventricular myocytes. *Biophysical Journal*, 85(5):3388–3396, 2003.

[47] S. Despa, M. A. Islam, S. M. Pogwizd, and D. M. Bers. Intracellular [Na^+] and Na^+ pump rate in rat and rabbit ventricular myocytes. *he Journal of Physiology*, 539(1):133–143, 2002.

[48] M. E. Diaz, A. W. Trafford, and D. A. Eisner. The role of intracellular Ca buffers in determining the shape of the systolic Ca transient in cardiac ventricular myocytes. *Pflügers Archiv European Journal of Physiology*, 442:96–100, 2001.

[49] K. M. Dibb, D. A. Eisner, and A. W. Trafford. Regulation of systolic $[Ca^{2+}]_i$ and cellular Ca^{2+} flux balance in rat ventricular myocytes by SR Ca^{2+}, L-type Ca^{2+} current and diastolic $[Ca^{2+}]_i$. *The Journal of Physiology*, 585(2):579–592, 2007.

[50] K. M. Dibb, H. K. Graham, L. A. Venetucci, D. A. Eisner, and A. W. Trafford. Analysis of cellular calcium fluxes in cardiac muscle to understand calcium homeostasis in the heart. *Cell Calcium*, 42(4-5):503 – 512, 2007.

[51] D. DiFrancesco and D. Noble. A model of cardiac electrical activity incorporating ionic pumps and concentration changes. *Philosophical Transactions of the Royal Society of London. B, Biological Sciences*, 307(1133):353–398, 1985.

[52] I. M. Dixon, S. L. Lee, and N. S. Dhalla. Nitrendipine binding in congestive heart failure due to myocardial infarction. *Circulation Research*, 66(3):782–788, 1990.

[53] W. H. DuBell, W. J. Lederer, and T. B. Rogers. K^+ currents responsible for repolarization in mouse ventricle and their modulation by $FK-506$ and rapamycin. *American Journal of Physiology. Heart and circulatory physiology*, 278:H886–897, 2000.

[54] D. A. Eisner, H. S. Choi, M. E. Diaz, S. C. O'Neill, and A. W. Trafford. Integrative analysis of calcium cycling in cardiac muscle. *Circulation Research*, 87:1087–1094, 2000.

[55] D. A. Eisner, C. H. George, G. L. Smith, A. W. Trafford, and L. A. Venetucci. How does CaMKIIδ phosphorylation of the cardiac ryanodine receptor contribute to inotropy? *Proceedings of the National Academy of Sciences*, 107(31):E123, 2010.

[56] D. A. Eisner, G. L. Smith, and S. C. O'Neill. The effects of lactic acid production on contraction and intracellular pH during hypoxia in cardiac muscle. *Basic Research in Cardiology*, 88:421–429, 1993.

[57] A. M. Evans and M. B. Cannell. The role of L-type Ca^{2+} current and Na^{+} current-stimulated Na/Ca exchange in triggering SR calcium release in guinea-pig cardiac ventricular myocytes. *Cardiovascular Research*, 35(2):294–302, 1997.

[58] G. Faber. Action potential and contractility changes in $[Na^{+}]_i$ overloaded cardiac myocytes: a simulation study. *Biophysical Journal*, 78:2392–2404, may 2000.

[59] A. Fabiato. Calcium-induced release of calcium from the cardiac sarcoplasmic reticulum. *American Journal of Physiology. Cell Physiology*, 245(1):C1–14, 1983.

[60] A. Fabiato and F. Fabiato. Contractions induced by a calcium-triggered release of calcium from the sarcoplasmic reticulum of single skinned cardiac cells. *The Journal of Physiology*, 249(3):469–495, 1975.

[61] A. Fabiato and F. Fabiato. Calcium release from the sarcoplasmic reticulum. *Circ Res*, 40(2):119–129, 1977.

[62] A. M. Feldman, E. O. Weinberg, P. E. Ray, and B. H. Lorell. Selective changes in cardiac gene expression during compensated hypertrophy and the transition to cardiac decompensation in rats with chronic aortic banding. *Circulation Research*, 73(1):184–192, 1993.

[63] M. Fink, W. R. Giles, and D. Noble. Contributions of inwardly rectifying K^{+} currents to repolarization assessed using mathematical models of human ventricu-

lar myocytes. *Philosophical Transactions of the Royal Society A: Mathematical, Physical and Engineering Sciences*, 364:1207 – 1222, 2006.

[64] M. S. Finkel, L. Shen, R. C. Romeo, C. V. Oddis, and G. Salama. Radioligand binding of inotropic effects of ryanodine in the cardiomyopathic Syrian hamster. *Journal of Cardiovascular Pharmacology*, 19(4):610–617, 1992.

[65] C. H. Fry, T. Powell, V. W. Twist, and J. P. T. Ward. Net calcium exchange in adult rat ventricular myocytes: an assessment of mitochondrial calcium accumulating capacity. *Proceedings of the Royal Society of London. Series B. Biological Sciences*, 223(1231):223–238, 1984.

[66] W. Gao, P. Backx, M. Azan-Backx, and E. Marban. Myofilament Ca^{2+} sensitivity in intact versus skinned rat ventricular muscle. *Circulation Research*, 74(3):408–415, 1994.

[67] W. D. Gao, N. G. Perez, and E. Marban. Calcium cycling and contractile activation in intact mouse cardiac muscle. *The Journal of Physiology*, 507(1):175–184, 1998.

[68] J. I. Goldhaber, L.-H. Xie, T. Duong, C. Motter, K. Khuu, and J. N. Weiss. Action potential duration restitution and alternans in rabbit ventricular myocytes: the key role of intracellular calcium cycling. *Circulation Research*, 96(4):459–466, 2005.

[69] E. Goldman, David. Potential, impedance, and rectification in membranes. *Journal of General Physiology*, 27(1):37–60, 1943.

[70] A. M. Gómez, H. H. Valdivia, H. Cheng, M. R. Lederer, L. F. Santana, M. B. Cannell, S. A. McCune, R. A. Altschuld, and W. J. Lederer. Defective excitation-contraction coupling in experimental cardiac hypertrophy and heart failure. *Science*, 276(5313):800–806, 1997.

[71] C. J. Grantham and M. B. Cannell. Ca^{2+} influx during the cardiac action potential in guinea pig ventricular myocytes. *Circulation Research*, 79(2):194–200, 1996.

[72] J. Greenstein and R. Winslow. An integrative model of the cardiac ventricular myocyte incorporating local control of Ca^{2+} release. *Biophysical Journal*, 83:2918–2945, dec 2002.

[73] G. Grynkiewicz, M. Poenie, and R. Y. Tsien. A new generation of Ca^{2+} indicators with greatly improved fluorescence properties. *Journal of Biological Chemistry*, 260(6):3440–3450, 1985.

[74] T. Guo, T. Zhang, R. Mestril, and D. M. Bers. Ca^{2+}/Calmodulin-dependent protein kinase II phosphorylation of ryanodine receptor does affect calcium sparks in mouse ventricular myocytes. *Circulation Research*, 99:398–406, 2006.

[75] W. Guo, H. Li, B. London, and J. M. Nerbonne. Functional consequences of elimination of Ito,f and Ito,s : early afterdepolarizations, atrioventricular block, and ventricular arrhythmias in mice lacking Kv1.4 and expressing a dominant-negative Kv4 alpha subunit. *Circulation Research*, 87:73–79, 2000.

[76] J. K. Gwathmey, L. Copelas, R. MacKinnon, F. J. Schoen, M. D. Feldman, W. Grossman, and J. P. Morgan. Abnormal intracellular calcium handling in myocardium from patients with end-stage heart failure. *Circulation Research*, 61(1):70–76, 1987.

[77] J. K. Gwathmey and R. J. Hajjar. Relation between steady-state force and intracellular [Ca^{2+}] in intact human myocardium. Index of myofibrillar responsiveness to Ca^{2+}. *Circulation*, 82(4):1266–1278, 1990.

[78] S. Gyorke and M. Fill. Ryanodine receptor adaptation: control mechanism of Ca^{2+}-induced Ca^{2+} release in heart. *Science*, 260(5109):807–809, 1993.

[79] R. W. Hadley and J. R. Hume. An intrinsic potential-dependent inactivation mechanism associated with calcium channels in guinea-pig myocytes. *The Journal of Physiology*, 389(1):205–222, 1987.

[80] D. Hagemann, M. Kuschel, T. Kuramochi, W. Zhu, H. Cheng, and R.-P. Xiao. Frequency-encoding Thr17 phospholamban phosphorylation is independent of Ser16 phosphorylation in cardiac myocytes. *Journal of Biological Chemistry*, 275(29):22532–22536, 2000.

[81] F. Han, J. Bossuyt, S. Despa, A. L. Tucker, and D. M. Bers. Phospholemman phosphorylation mediates the protein kinase C-dependent effects on Na^+/K^+ pump function in cardiac myocytes. *Circulation Research*, 99(12):1376–1383, 2006.

[82] P. I. Hanson, M. T., S. L., and S. H. Dual role of calmodulin in autophosphorylation of multifunctional CaM kinase may underlie decoding of calcium signals. *Neuron*, 12(5):943 – 956, 1994.

[83] G. Hasenfuss. Animal models of human cardiovascular disease, heart failure and hypertrophy. *Cardiovascular Research*, 39(1):60–76, 1998.

[84] G. Hasenfuss, H. Reinecke, R. Studer, M. Meyer, B. Pieske, J. Holtz, C. Holubarsch, H. Posival, H. Just, and H. Drexler. Relation between myocardial function and expression of sarcoplasmic reticulum Ca^{2+}-ATPase in failing and nonfailing human myocardium. *Circulation Research*, 75(3):434–442, 1994.

[85] G. Hasenfuss, W. Schillinger, S. E. Lehnart, M. Preuss, B. Pieske, L. S. Maier, J. Prestle, K. Minami, and H. Just. Relationship between Na^+-Ca^{2+}-exchanger protein levels and diastolic function of failing human myocardium. *Circulation*, 99:641–648, 1999.

[86] S. N. Hatem, J. S. Sham, and M. Morad. Enhanced Na^+-Ca^{2+} exchange activity in cardiomyopathic Syrian hamster. *Circulation Research*, 74(2):253–261, 1994.

[87] J. He, L. G. Ogden, L. A. Bazzano, S. Vupputuri, C. Loria, and P. K. Whelton. Risk factors for congestive heart failure in US men and women: NHANES I epidemiologic follow-up study. *Archives of Internal Medicine*, 161(7):996–1002, 2001.

[88] S. A. Henderson, J. I. Goldhaber, J. M. So, T. Han, C. Motter, A. Ngo, C. Chantawansri, M. R. Ritter, M. Friedlander, D. A. Nicoll, J. S. Frank, M. C. Jordan, K. P. Roos, R. S. Ross, and K. D. Philipson. Functional adult myocardium in the absence of Na^+-Ca^{2+} exchange: cardiac-specific knockout of NCX1. *Circulation Research*, 95(6):604–611, 2004.

[89] R. Hinch, J. L. Greenstein, A. J. Tanskanen, L. Xu, and R. L. Winslow. A simplified local control model of calcium-induced calcium release in cardiac ventricular myocytes. *Biophysical Journal*, 87:3723 – 3768, 2004.

[90] Y. Hirano, H. A. Fozzard, and C. T. January. Characteristics of L- and T-type Ca^{2+} currents in canine cardiac Purkinje cells. *American Journal of Physiology - Heart and Circulatory Physiology*, 256(5):H1478–H1492, 1989.

[91] A. L. Hodgkin and A. F. Huxley. A quantitative description of membrane current and its application to conduction and excitation in nerve. *Journal of Physiology*, 117:500 – 544, 1952.

[92] A. L. Hodgkin and B. Katz. The effect of sodium ions on the electrical activity of the giant axon of the squid. *The Journal of Physiology*, 108(1):37–77, 1949.

[93] S. Huke and D. M. Bers. Temporal dissociation of frequency-dependent acceleration of relaxation and protein phosphorylation by CaMKII. *Journal of Molecular and Cellular Cardiology*, 42(3):590 – 599, 2007.

[94] T. J. Hund, J. P. Kucera, N. F. Otani, and Y. Rudy. Ionic charge conservation and long-term steady state in the Luo-Rudy dynamic cell model. *Biophysical Journal*, 81(6):3324–3331, 2001.

[95] T. J. Hund and Y. Rudy. Rate dependence and regulation of action potential and calcium transient in a canine cardiac ventricular cell model. *Circulation*, 110:3168 – 3174, 2004.

[96] P. J. Hunter, P. A. McNaughton, and D. Noble. Analytical models of propagation in excitable cells. *Progress in Biophysics and Molecular Biology*, 30(2-3):99 – 144, 1975.

[97] J. P. Imredy and D. T. Yue. Mechanism of Ca^{2+}-sensitive inactivation of L-type Ca^{2+} channels. *Neuron*, 12(6):1301 – 1318, 1994.

[98] M. Jafri, J. Rice, and R. Winslow. Cardiac Ca^{2+} dynamics: The roles of ryanodine receptor adaptation and sarcoplasmic reticulum load. *Biophysical Journal*, 74:1149–1168, 1998.

[99] C. Johansson, R. Koopmann, M. B. Vennstr Ouml, and K. Benndorf. Accelerated inactivation of voltage-dependent K^+ outward current in cardiomyocytes from thyroid hormone receptor alpha1-deficient mice. *Journal of Cardiovascular Electrophysiology*, 13:44–50, 2002.

[100] M. Kawai, M. Hussain, and C. H. Orchard. Excitation-contraction coupling in rat ventricular myocytes after formamide-induced detubulation. *American Journal of Physiology. Heart and Circulatory Physiology*, 277(2):H603–H609, 1999.

[101] J. Keener and J. Sneyd. *Mathematical Physiology*. Spinger Science+Business Mddia Inc., 1998.

[102] J. Keizer and L. Levine. Ryanodine receptor adaptation and Ca^{2+}-induced Ca^{2+} release-dependent Ca^{2+} oscillations. *Biophysical Journal*, 71:3477–3487, 1996.

[103] J. Kimura, A. Noma, and H. Irisawa. Na-Ca exchange current in mammalian heart cells. *Nature*, 319:596–597, 1986.

[104] B. C. Knollmann, P. Kirchhof, S. G. Sirenko, H. Degen, A. E. Greene, T. Schober, J. C. Mackow, L. Fabritz, J. D. Potter, and M. Morad. Familial hypertrophic cardiomyopathy-linked mutant troponin T causes stress-induced ventricular tachy-

cardia and Ca^{2+}-dependent action potential remodeling. *Circulation Research*, 92:428–436, 2003.

[105] B. C. Knollmann, B. E. C. Knollmann-Ritschel, N. J. Weissman, L. R. Jones, and M. Morad. Remodelling of ionic currents in hypertrophied and failing hearts of transgenic mice overexpressing calsequestrin. *The Journal of Physiology*, 525:483–498, 2000.

[106] B. C. Knollmann, T. Schober, A. O. Petersen, S. G. Sirenko, and M. R. Franz. Action potential characterization in intact mouse heart: steady-state cycle length dependence and electrical restitution. *American Journal of Physiology. Heart and circulatory physiology*, 292:H614–621, 2007.

[107] M. Kohlhaas, T. Zhang, T. Seidler, D. Zibrova, N. Dybkova, A. Steen, S. Wagner, L. Chen, B. J. Heller, D. M. Bers, and M. L. S. Increased sarcoplasmic reticulum calcium leak but unaltered contractility by acute CaMKII overexpression in isolated rabbit cardiac myocytes. *Circulation Research*, 98:235–244, 2006.

[108] O. Kohomoto, A. J. Levi, and J. H. Bridge. Relation between reverse sodium-calcium exchange and sarcoplasmic reticulum calcium release in guinea pig ventricular cells. *Circulation Research*, 74(3):550–554, 1994.

[109] K. L. Koss and E. G. Kranias. Phospholamban: a prominent regulator of myocardial contractility. *Circulation Research*, 79(6):1059–1063, 1996.

[110] S. Kurihara and T. Sakai. Effects of rapid cooling on mechanical and electrical responses in ventricular muscle of guinea-pig. *The Journal of Physiology*, 361(1):361–378, 1985.

[111] S. Land, S. A. Niederer, O. Nordbø, E. Espe, W. E. Louch, S. Omholt, and N. P. Smith. An electromechanical model of the mouse heart. *In preparation*.

[112] J. Layland and J. C. Kentish. Positive force- and $[Ca^{2+}]_i$-frequency relationships in rat ventricular trabeculae at physiological frequencies. *American Journal of Physiology. Heart and circulatory physiology*, 276(1):H9–18, 1999.

[113] C. J. Le Peuch, J. Haiech, and J. G. Damaille. Concerted regulation of cardiac sarcoplasmic reticulum calcium transport by cyclic adenosine monophosphate dependent and calcium-calmodulin-dependent phosphorylations. *Biochemistry*, 18(23):5250 – 7, 1979.

[114] N. Leblanc and J. R. Hume. Sodium current-induced release of calcium from cardiac sarcoplasmic reticulum. *Science*, 248(4953):372–376, 1990.

[115] J. P. Lees-Miller, J. Guo, J. R. Somers, D. E. Roach, R. S. Sheldon, D. E. Rancourt, and H. J. Duff. Selective knockout of mouse ERG1 B potassium channel eliminates IKr in adult ventricular myocytes and elicits episodes of abrupt sinus bradycardia. *Molecular and Cellular Biology*, 23:1856 – 1862, 2003.

[116] L. Li, G. Chu, E. G. Kranias, and D. M. Bers. Cardiac myocyte calcium transport in phospholamban knockout mouse: relaxation and endogenous CaMKII effects. *American Journal of Physiology. Heart and Circulatory Physiology*, 274(4):H1335–1347, 1998.

[117] L. Li, W. E. Louch, S. A. Niederer, K. B. Andersson, G. Christensen, O. M. Sejersted, and N. P. Smith. Calcium dynamics in the ventricular myocytes of SERCA2 KO mice: a modelling study. *Biophysical Journal*, 100(2):332–331, 2010.

[118] L. Li, S. A. Niederer, W. Idigo, Y. H. Zhang, P. Swietach, B. Casadei, and N. P. Smith. A mathematical model of the murine ventricular myocyte: a data-driven biophysically based approach applied to mice overexpressing the canine NCX isoform. *American Journal of Physiology. Heart and circulatory physiology*, 299(4):H1045–1063, 2010.

[119] G. Lim et al. nNOS gene disruption reduces the diastolic calcium leak from the ryanodine receptor: implications for excitation-contraction coupling . *In preparation*.

[120] G. Lim, L. Venetucci, D. A. Eisner, and B. Casadei. Does nitric oxide modulate cardiac ryanodine receptor function? Implications for excitation–contraction coupling. *Cardiovascular Research*, 77(2):256–264, 2008.

[121] C. J. Limas, M.-T. Olivari, I. F. Goldenberg, T. B. Levine, D. G. Benditt, and A. Simon. Calcium uptake by cardiac sarcoplasmic reticulum in human dilated cardiomyopathy. *Cardiovascular Research*, 21(8):601–605, 1987.

[122] T. Liu, D. A. Brown, and B. O'Rourke. Role of mitochondrial dysfunction in cardiac glycoside toxicity. *Journal Molecular Cellular Cardiology*, 49(5):728–736, 2010.

[123] B. London, W. Guo, X.-h. Pan, J. S. Lee, V. Shusterman, C. J. Rocco, D. A. Logothetis, J. M. Nerbonne, and H. J. A. Targeted replacement of Kv1.5 in the mouse leads to loss of the 4-Aminopyridine-sensitive component of IK,slow and resistance to drug-induced QT prolongation. *Circulation Research*, 88:940 – 946, 2001.

[124] W. E. Louch, J. Hake, G. F. Jølle, H. K. Mørk, I. Sjaastad, G. T. Lines, and O. M. Sejersted. Control of Ca^{2+} release by action potential configuration in normal and failing murine cardiomyocytes. *Biophysical Journal*, 99(5):1377–1386, 2010.

[125] W. E. Louch, K. Hougen, H. K. Mork, F. Swift, J. M. Aronsen, I. Sjaastad, H. M. Reims, B. Roald, K. B. Andersson, G. Christensen, and O. M. Sejersted. Sodium Accumulation Promotes diastolic dysfunction in end-stage heart failure following Serca2 knockout. *The Journal of Physiology*, 588(3):465 – 478, 2010.

[126] W. E. Louch, H. K. Mørk, J. Sexton, T. A. Strømme, P. Laake, I. Sjaastad, and O. M. Sejersted. T-tubule disorganization and reduced synchrony of Ca^{2+} release

in murine cardiomyocytes following myocardial infarction. *The Journal of Physiology*, 574(2):519–533, 2006.

[127] C. M. Loughrey, G. L. Smith, and K. E. MacEachern. Comparison of Ca^{2+} release and uptake characteristics of the sarcoplasmic reticulum in isolated horse and rabbit cardiomyocytes. *American Journal of Physiology - Heart and Circulatory Physiology*, 287(3):H1149–H1159, 2004.

[128] C. Luo and Y. Rudy. A dynamic model of the cardiac ventricular action potential. I. Simulations of ionic currents and concentration changes. *Circulation Research*, 74(6):1071–1096, 1994.

[129] J. Lytton, M. Westlin, S. E. Burk, G. E. Shull, and D. H. MacLennan. Functional comparisons between isoforms of the sarcoplasmic or endoplasmic reticulum family of calcium pumps. *Journal of Biological Chemistry*, 267:14483 – 14489, 1992.

[130] C. Maack and B. O'Rourke. Excitation-contraction coupling and mitochondrial energetics. *Basic Research in Cardiology*, 102(5):369–392, 2007.

[131] D. H. MacLennan, C. J. Brandl, B. Korczak, and N. M. Green. Amino-acid sequence of a Ca^{2+} + Mg^{2+}-dependent ATPase from rabbit muscle sarcoplasmic reticulum, deduced from its complementary DNA sequence. *Nature*, 316:696–700, 1985.

[132] J. Magyar, C. Kiper, G. Sievert, W. Cai, S. M. Crump, L. Li, N. Smith, D. A. Andrews, and J. Satin. Rem-GTPase regulates cardiac myocyte L-type calcium current. *Cardiovascular Research. Under review*.

[133] L. S. Maier and D. M. Bers. Calcium, calmodulin, and calcium-calmodulin Kinase II: heartbeat to heartbeat and beyond. *Journal of Molecular and Cellular Cardiology*, 34:919–939.

[134] L. S. Maier, T. Zhang, L. Chen, J. DeSantiago, J. H. Brown, and B. D. M. Transgenic CaMKII deltaC overexpression uniquely alters cardiac myocyte Ca^{2+} handling: reduced SR Ca^{2+} load and activated SR Ca^{2+} release. *Circulation Research*, 92:904–911, 2003.

[135] S. O. Marx, S. Reiken, Y. Hisamatsu, T. Jayaraman, D. Burkhoff, N. Rosemblit, and R. Marks, Andrew. PKA hosphorylation dissociates FKBP12.6 from the calcium release channel (ryanodine receptor): defective regulation in failing hearts. *Cell*, 101(4):365–376, 2000.

[136] K. Maxwell, J. Scott, A. Omelchenko, A. Lukas, L. Lu, Y. Lu, M. Hnatowich, K. D. Philipson, and L. V. Hryshko. Functional role of ionic regulation of Na^{+}/Ca^{2+} exchange assessed in transgenic mouse hearts. *American Journal of Physiology. Heart and circulatory physiology*, 277:H2212–2221, 1999.

[137] R. E. McAllister, D. Noble, and R. W. Tsien. Reconstruction of the electrical activity of cardiac Purkinje fibres. *The Journal of Physiology*, 251(1):1–59, 1975.

[138] T. Mewes and R. Ursula. L-type calcium currents of human myocytes from ventricle of non-failing and failing hearts and from atrium. *Journal of Molecular and Cellular Cardiology*, 26(10):1307 – 1320, 1994.

[139] M. Meyer, W. Schillinger, B. Pieske, C. Holubarsch, C. Heilmann, H. Posival, G. Kuwajima, K. Mikoshiba, H. Just, and G. Hasenfuss. Alterations of sarcoplasmic reticulum proteins in failing human dilated cardiomyopathy. *Circulation*, 92(4):778–784, 1995.

[140] H. K. Mørk, I. Sjaastad, J. B. Sande, M. Periasamy, O. M. Sejersted, and W. E. Louch. Increased cardiomyocyte function and Ca^{2+} transients in mice during early congestive heart failure. *Journal of Molecular and Cellular Cardiology*, 43(2):177–186, 2007.

[141] H. K. Mørk, I. Sjaastad, O. M. Sejersted, and W. E. Louch. Slowing of cardiomyocyte Ca^{2+} release and contraction during heart failure progression in postinfarction mice. *American Journal of Physiology. Heart and circulatory physiology*, 296(4):H1069–H1079, 2009.

[142] E. Murphy and D. A. Eisner. Regulation of intracellular and mitochondrial sodium in health and disease. *Cirulation Research*, 104(3):292–303, 2009.

[143] F. Nguemo, B. K. Fleischmann, H. Schunkert, J. Hescheler, and M. Peppel. Functional expression and inactivation of L-type Ca^{2+} currents during murine heart development - implications for cardiac Ca^{2+} homeostasis. *Cellular physiology and Biochemistry*, 20:809 – 824, 2007.

[144] S. A. Niederer, M. Fink, D. Noble, and N. P. Smith. A meta-analysis of cardiac electrophysiology computational models. *Experimental Physiology*, 94(5):486–495, 2009.

[145] S. A. Niederer and N. P. Smith. A mathematical model of the slow force response to stretch in rat ventricular myocytes. *Biophysical Journal*, 92(11):4030–4044, 2007.

[146] V. Niggli and S. Erwin. Anticipating antiport in P-type ATPases. *Trends in Biochemical Sciences*, 33(4):156–160, 2007.

[147] D. Noble. A modification of the Hodgki - Huxley equations applicable to Purkinje fibre action and pacemaker potentials. *The Journal of Physiology*, 160(2):317–352, 1962.

[148] T. D. O'Connell, S. Ishizaka, A. Nakamura, P. M. Swigart, M. C. Rodrigo, G. L. Simpson, S. Cotecchia, D. G. Rokosh, W. Grossman, F. E, and P. C. Simpson. The alphaA/C- and alpha1B-adrenergic receptors are required for physiological cardiac hypertrophy in the double-knockout mouse. *The Journal of Clinical Investigation*, 111:1783 – 1791, 2003.

[149] L. H. Opie. *Heart Physiology From cell to circulation*. Lippincott Williams & Wilkins, 4 edition, 2004.

[150] B. O'Rourke and L. A. Blatter. Mitochondrial Ca^{2+} uptake: Tortoise or hare? *Journal of Molecular and Cellular Cardiology*, 46(6):767 – 774, 2009.

[151] B. O'Rourke, D. A. Kass, G. F. Tomaselli, S. Kaab, R. Tunin, and E. Marban. Mechanisms of altered excitation-contraction coupling in canine tachycardia-induced heart failure, I : experimental studies. *Circulation Research*, 84(5):562–570, 1999.

[152] S. Pandit, W. Giles, and S. Demir. A mathematical model of the electrophysiological alterations in rat ventricular myocytes in Type-I diabetes. *Biophysical Journal*, 84:832–841.

[153] M. Periasamy and A. Kalyanasundaram. Serca pump isoforms: Their role in calcium transport and disease. *Muscle & Nerve*, 35(4):430–442, 2007.

[154] M. Periasamy, T. D. Reed, L. H. Liu, Y. Ji, E. Loukianov, R. J. Paul, M. L. Nieman, T. Riddle, J. J. Duffy, T. Doetschman, J. N. Lorenz, and G. E. Shull. Impaired cardiac performance in heterozygous mice with a null mutation in the sarco(endo)plasmic reticulum Ca^{2+}-ATPase isoform 2 (SERCA2) gene . *Journal of Biological Chemistry*, 274(4):2556–2562, 1999.

[155] I. Piacentino, Valentino, C. R. Weber, X. Chen, J. Weisser-Thomas, K. B. Margulies, D. M. Bers, and S. R. Houser. Cellular basis of abnormal calcium transients of failing human ventricular myocytes. *Circulation Research*, 92(6):651–658, 2003.

[156] E. Picht, J. DeSantiago, S. Huke, M. A. Kaetzel, J. R. Dedman, and D. M. Bers. CaMKII inhibition targeted to the sarcoplasmic reticulum inhibits frequency-

dependent acceleration of relaxation and Ca^{2+} current facilitation. *Journal of Molecular and Cellular Cardiology*, 42(1):196 – 205, 2007.

[157] B. Pieske, L. S. Maier, D. M. Bers, and G. Hasenfuss. Ca^{2+} handling and sarcoplasmic reticulum Ca^{2+} content in isolated failing and nonfailing human myocardium. *Circulation Research*, 85(1):38–46, 1999.

[158] B. Pieske, L. S. Maier, I. Piacentino, Valentino, J. Weisser, G. Hasenfuss, and S. Houser. Rate dependence of $[Na^+]_i$ and contractility in nonfailing and failing human myocardium. *Circulation*, 106(4):447–453, 2002.

[159] S. M. Pogwizd, K. R. Sipido, F. Verdonck, and D. M. Bers. Intracellular Na in animal models of hypertrophy and heart failure: contractile function and arrhythmogenesis. *Cardiovascular Research*, 57:887–896, 2003.

[160] R. K. Pradhan, D. A. Beard, and R. K. Dash. A biophysically based mathematical model for the kinetics of mitochondrial Na^+-Ca^{2+} antiporter. *Biophysical Journal*, 98(2):218–231, 2010.

[161] M. Qi, T. R. Shannon, D. E. Euler, D. M. Bers, and A. M. Samarel. Downregulation of sarcoplasmic reticulum Ca^{2+}-ATPase during progression of left ventricular hypertrophy. *American Journal of Physiology. Heart and circulatory physiology*, 272(5):H2416–2424, 1997.

[162] R. F. Rakowski, D. C. Gadsby, and P. De Weer. Voltage dependence of the Na/K pump. *Journal of Membrane Biology*, 155:105–112, 1997. 10.1007/s002329900162.

[163] R. L. Rasmusson, J. W. Clark, W. R. Giles, K. Robinson, R. B. Clark, E. F. Shibata, and D. L. Campbell. A mathematical model of electrophysiological activity in a bullfrog atrial cell. *American Journal of Physiology. Heart and circulatory physiology*, 259(2):H370–389, 1990.

[164] J. P. Reeves and C. C. Hale. The stoichiometry of the cardiac sodium-calcium exchange system. *Journal of Biological Chemistry*, 259(12):7733–7739, 1984.

[165] H. Reuter, T. Han, C. Motter, K. D. Philipson, and J. I. Goldhaber. Mice overexpressing the cardiac sodium-calcium exchanger: defects in excitation–contraction coupling. *The Journal of Physiology*, 554(3):779–789, 2004.

[166] J. J. Rice, M. Saleet Jafri, and R. L. Winslow. Modeling gain and gradedness of Ca^{2+} release in the functional unit of the cardiac diadic space. *Biophysical Journal*, 77(4):1871–1884, 1999.

[167] V. Robert, P. Gurlini, V. Tosello, T. Nagai, A. Miyawaki, F. Di Lisa, and T. Pozzan. Beat-to-beat oscillations of mitochondrial [Ca^{2+}] in cardiac cells. *EMBO Journal*, 20(17):4998 – 5007, 2001.

[168] Y. Rudy and J. R. Silva. Computational biology in the study of cardiac ion channels and cell electrophysiology. *Quarterly Reviews of Biophysics*, 39(01):57 – 116, 2006.

[169] C. Schemacher, B. Konigs, M. Sigmund, B. Kohne, F. Schondube, M. Vob, B. Stein, J. Weil, and P. Hanrath. The ryanodine binding sarcoplasmic reticulum calcium release channel in nonfailing and in failing human myocardium. *Naunyn-Schmiedeberg's Archives of Pharmacology*, 353(1):80–85, 1995.

[170] U. Schmidt, R. J. Hajjar, P. A. Helm, C. S. Kim, A. A. Doye, and J. K. Gwathmey. Contribution of abnormal sarcoplasmic reticulum ATPase activity to systolic and diastolic dysfunction in human heart failure. *Journal of Molecular and Cellular Cardiology*, 30(10):1929 – 1937, 1998.

[171] R. H. Schwinger, M. Bohm, U. Schmidt, P. Karczewski, U. Bavendiek, M. Flesch, E.-G. Krause, and E. Erdmann. Unchanged protein levels of SERCA II and phospholamban but reduced Ca^{2+} uptake and Ca^{2+}-ATPase activity of cardiac sar-

coplasmic reticulum from dilated cardiomyopathy patients compared with patients with nonfailing hearts. *Circulation*, 92(11):3220–3228, 1995.

[172] D. R. L. Scriven, P. Dan, and E. D. W. Moore. Distribution of proteins implicated in excitation-contraction coupling in rat ventricular myocytes. *Biophysical Journal*, 79(5):2682–2691, 2000.

[173] C. E. Sears, S. M. Bryant, E. A. Ashley, C. A. Lygate, S. Rakovic, H. L. Wallis, S. Neubauer, D. A. Terrar, and B. Casadei. Cardiac neuronal nitric oxide synthase isoform regulates myocardial contraction and calcium handling. *Circulation Research*, 92(5):e52–59, 2003.

[174] J. S. Sham, L. R. Jones, and M. Morad. Phospholamban mediates the beta-adrenergic-enhanced Ca^{2+} uptake in mammalian ventricular myocytes. *American Journal of Physiology - Heart and Circulatory Physiology*, 261(4):H1344–H1349, 1991.

[175] J. S. K. Sham, L.-S. Song, Y. Chen, L.-H. Deng, M. D. Stern, E. G. Lakatta, and H. Cheng. Termination of Ca^{2+} release by a local inactivation of ryanodine receptors in cardiac myocytes. *Proceedings of the National Academy of Sciences of the United States of America*, 95(25):15096–15101, 1998.

[176] T. R. Shannon and D. M. Bers. Assessment of intra-SR free [Ca] and buffering in rat heart. *Biophysical Journal*, 73:1524–1531, 1997.

[177] T. R. Shannon, K. S. Ginsburg, and D. M. Bers. Quantitative sssessment of the SR Ca^{2+} leak-load relationship. *Circulation Research*, 91(7):594–600, 2002.

[178] T. R. Shannon, F. Wang, J. Puglisi, C. Weber, and D. Bers. A mathematical treatment of integrated ca dynamics within the ventricular myocytes. *Biophysical Journal*, 87(5):3351 – 3371, 2004.

[179] M. J. Shattock and D. M. Bers. Rat vs. rabbit ventricle: Ca flux and intracellular Na assessed by ion-selective microelectrodes. *American Journal of Physiology. Cell Physiology*, 256(4):C813–822, 1989.

[180] L. H. Silver, E. L. Hemwall, T. A. Marino, and S. R. Houser. Isolation and morphology of calcium-tolerant feline ventricular myocytes. *American Journal of Physiology. Heart and circulatory physiology*, 245:H891–896, 1983.

[181] H. K. Simmerman, J. H. Collins, J. L. Theibert, A. D. Wegener, and L. R. Jones. Sequence analysis of phospholamban. Identification of phosphorylation sites and two major structural domains. *Journal of Biological Chemistry*, 261(28):13333–13341, 1986.

[182] L.-S. Song, J. S. K. Sham, M. D. Stern, E. G. Lakatta, and H. Cheng. Direct measurement of SR release flux by tracking 'Ca^{2+} spikes' in rat cardiac myocytes. *The Journal of Physiology*, 512(3):677–691, 1998.

[183] A. M. Spanier and W. B. Weglicki. Ca^{2+}-tolerant adult canine myocytes: preparation and response to anoxia/acidosis. *American Journal of Physiology. Heart and circulatory physiology*, 243:H448–455, 1982.

[184] M. Stern. Theory of excitation-contraction coupling in cardiac muscle. *Biophysical Journal*, 63:497–517, Aug. 1992.

[185] M. D. Stern, L.-S. Song, H. Cheng, J. S. Sham, H. T. Yang, K. R. Boheler, and E. Ríos. Local control models of cardiac excitation–contraction coupling. *The Journal of General Physiology*, 113(3):469–489, 1999.

[186] J. R. Stimers, S. Liu, and T. A. Kinard. Effect of Nai on activity and voltage dependence of the Na/K pump in adult rat cardiac myocytes. *The Journal of Membrane Biology*, 135(1):39–47, 1993.

[187] M. K. Stokke, K. Hougen, I. Sjaastad, W. E. Louch, S. J. Briston, U. H. Enger, K. B. Andersson, G. Christensen, D. A. Eisner, O. M. Sejersted, and A. W. Trafford. Reduced SERCA2 abundance decreases the propensity for Ca^{2+} wave development in ventricular myocytes. *Cardiovascular Research*, 86(1):63–71, 2010.

[188] R. Studer, H. Reinecke, J. Bilger, T. Eschenhagen, M. Bohm, G. Hasenfuss, H. Just, J. Holtz, and H. Drexler. Gene expression of the cardiac Na^{+}-Ca^{2+} exchanger in end-stage human heart failure. *Circulation Research*, 75(3):443–453, 1994.

[189] B. Surawicz. Role of potassium channels in cycle length dependent regulation of action potential duration in mammalian cardiac Purkinje and ventricular muscle fibres. *Cardiovascular Research*, 26:1021–1029, 1992.

[190] F. Swift, N. Tovsrud, U. H. Enger, I. Sjaastad, and O. M. Sejersted. The Na^{+}/K^{+}-ATPase α_2-isoform regulates cardiac contractility in rat cardiomyocytes. *Cardiovascular Research*, 75(1):109–117, 2007.

[191] T. Takahashi, P. D. Allen, R. V. Lacro, A. R. Marks, A. R. Dennis, F. J. Schoen, W. Grossman, J. D. Marsh, and S. Izumo. Expression of dihydropyridine receptor (Ca^{2+} channel) and calsequestrin genes in the myocardium of patients with end-stage heart failure. *The Journal of Clinical Investigation*, 90(3):927–935, 9 1992.

[192] C. Terracciano, K. D. Philipson, and K. T. MacLeod. Overexpression of the Na^{+}/Ca^{2+} exchanger and inhibition of the sarcoplasmic reticulum Ca^{2+}-ATPase in ventricular myocytes from transgenic mice. *Cardiovascular Research*, 49:38–47, 2001.

[193] C. M. N. Terracciano, A. I. De Souza, K. D. Philipson, and K. T. MacLeod. Na^{+}-Ca^{2+} exchange and sarcoplasmic reticular Ca^{2+} regulation in ventricular myocytes from transgenic mice overexpressing the Na^{+}-Ca^{2+} exchanger. *The Journal of Physiology*, 512:651–667, 1998.

[194] N. Teucher, J. Prestle, T. Seidler, S. Currie, E. B. Elliott, D. F. Reynolds, P. Schott, S. Wagner, H. Kogler, G. Inesi, D. M. Bers, G. Hasenfuss, and G. L. Smith. Excessive sarcoplasmic/endoplasmic reticulum Ca^{2+}-ATPase expression causes increased sarcoplasmic reticulum Ca^{2+} uptake but decreases myocyte shortening. *Circulation*, 110(23):3553–3559, 2004.

[195] A. W. Trafford, M. E. Diaz, and D. A. Eisner. Measurement of sarcoplasmic reticulum Ca content and sarcolemmal fluxes during the transient stimulation of the systolic Ca transient produced by caffeine. *Annals of the New York Academy of Sciences*, 853(1):368–371, 1998.

[196] A. W. Trafford, M. E. Diaz, and D. A. Eisner. A novel, rapid and reversible method to measure Ca buffering and time-course of total sarcoplasmic reticulum Ca content in cardiac ventricularm myocytes. *Pflügers Archiv European Journal of Physiology*, 437:501 – 503, 1999.

[197] A. W. Trafford, W. J. Lederer, and E. A. Sobie. Keeping the beat: Life without serca – is it possible? *Journal of Molecular and Cellular Cardiology*, 47(2):171 – 173, 2009.

[198] D. Vatner, N. Sato, K. Kiuchi, R. Shannon, and S. Vatner. Decrease in myocardial ryanodine receptors and altered excitation- contraction coupling early in the development of heart failure. *Circulation*, 90(3):1423–1430, 1994.

[199] R. D. Vaughan-Jones, K. W. Spitzer, and P. Swietach. Intracellular pH regulation in heart. *Journal of Molecular Cellular Cardiology*, 46:318–331, 2009.

[200] F. Verdonck, P. G. A. Volders, M. A. Vos, and K. R. Sipido. Intracellular Na^+ and altered Na^+ transport mechanisms in cardiac hypertrophy and failure. *Journal Molecular Cellular Cardiology*, 35(1):5–25, 2003.

[201] J. O. Vik, A. B. Gjuvsland, L. Li, K. Tøndel, S. Niederer, N. P. Smith, P. J. Hunter, and S. W. Omholt. Genotype-phenotype map characteristics of an in silico heart cell. *Frontiers in Physiology*, 2(106), 2011.

[202] T. Wagenknecht, R. Grassucci, J. Frank, A. Saito, M. Inui, and S. Fleischer. Three-dimensional architecture of the calcium channel/foot structure of sarcoplasmic reticulum. *Nature*, 338:167–170, 1989.

[203] J. R. Waggoner, K. S. Ginsburg, B. Mitton, K. Haghighi, J. Robbins, D. M. Bers, and E. G. Kranias. Phospholamban overexpression in rabbit ventricular myocytes does not alter sarcoplasmic reticulum Ca transport. *American Journal of Physiology - Heart and Circulatory Physiology*, 296(3):H698–H703, March 2009.

[204] J. Wagner and J. Keizer. Effects of rapid buffers on Ca^{2+} diffusion and Ca^{2+} oscillations. *Biophysical Journal*, 67(1):447 – 456, 1994.

[205] C. Waldeyer, L. Fabritz, L. Fortmueller, J. Gerss, D. Damke, A. Blana, S. Laakmann, N. Kreienkamp, D. Volkery, G. Breithardt, and P. Kirchhof. Regional, age-dependent, and genotype-dependent differences in ventricular action potential duration and activation time in 410 Langendorff-perfused mouse hearts. *Basic Research in Cardiology*, 104:523–533, 2009.

[206] C. R. Weber, K. S. Ginsburg, K. D. Philipson, T. R. Shannon, , and D. M. Bers. Allosteric regulation of Na/Ca exchange current by cytosolic Ca in intact cardiac myocytes. *The Journal of General Physiology*, 117:119 – 132, 2001.

[207] R. E. Williams, D. A. Kass, Y. Kawagoe, P. Pak, R. S. Tunin, R. Shah, A. Hwang, and A. M. Feldman. Endomyocardial gene expression during development of pacing tachycardia- induced heart failure in the dog. *Circulation Research*, 75(4):615–623, 1994.

[208] Y. Wu, J. Temple, R. Zhang, I. Dzhura, W. Zhang, R. Trimble, D. M. Roden, R. Passier, E. N. Olson, R. J. Colbran, and M. E. Anderson. Calmodulin kinase II and arrhythmias in a mouse model of cardiac hypertrophy. *Circulation*, 106(10):1288–1293, 2002.

[209] A. Xu, C. Hawkins, and N. Narayanan. Phosphorylation and activation of the Ca^{2+}-pumping ATPase of cardiac sarcoplasmic reticulum by Ca^{2+}/calmodulin-dependent protein kinase. *Journal of Biological Chemistry*, 268:8394 – 8397, 1993.

[210] H. Xu, W. Guo, and J. M. Nerbonne. Four kinetically distinct depolarization-activated K^+ currents in adult mouse ventricular myocytes. *The Journal of General Physiology*, 113:661–678, 1999.

[211] Z. Yang, C. Pascarel, D. S. Steele, K. Komukai, F. Brette, and C. H. Orchard. Na^+-Ca^{2+} exchange activity is localized in the T-tubules of rat ventricular myocytes. *Circulation Research*, 91(4):315–322, 2002.

[212] A. Yao, Z. Su, A. Nonaka, I. Zubair, L. Lu, K. D. Philipson, J. H. B. Bridge, and W. H. Barry. Effects of overexpression of the Na^+-Ca^{2+} exchanger on $[Ca^{2+}]_i$ transients in murine ventricular myocytes. *Circulation Research*, 82(6):657–665, 1998.

[213] W. Yuan, K. S. Ginsburg, and D. M. Bers. Comparison of sarcolemmal calcium channel current in rabbit and rat ventricular myocytes. *The Journal of Physiology*, 493(3):733 – 746, 1996.

[214] A. Zarain-Herzberg, N. Afzal, V. Elimban, and N. S. Dhalla. Decreased expression of cardiac sarcoplasmic reticulum Ca^{2+}-pump ATPase in congestive heart failure due to myocardial infarction. *Molecular and Cellular Biochemistry*, 163-164:285–290, 1996.

[215] T. Zhang and J. H. Brown. Role of Ca^{2+}/calmodulin-dependent protein kinase II in cardiac hypertrophy and heart failure. *Cardiovascular Research*, 63:476 – 486, 2004.

[216] T. Zhang, L. S. Maier, N. D. Dalton, S. Miyamoto, J. Ross, John, D. M. Bers, and J. H. Brown. The δC isoform of CaMKII is activated in cardiac hypertrophy and induces dilated cardiomyopathy and heart failure. *Circulation Research*, 92(8):912–919, 2003.

[217] J. Zhou, A. Jeron, B. London, X. Han, and G. Koren. Characterization of a slowly inactivating outward current in adult mouse ventricular myocytes. *Circulation Research*, 83(8):806–814, 1998.